

ACOUSTIC TRANSDUCTION – MATERIALS AND DEVICES

Period 31 July 1996 to 31 December 1997

Annual Report

VOLUME VIII

**OFFICE OF NAVAL RESEARCH
Contract No: N00014-96-1-1173**

**APPROVED FOR PUBLIC RELEASE –
DISTRIBUTION UNLIMITED**

**Reproduction in whole or in part is permitted for any
purpose of the United States Government**

Kenji Uchino

PENNSTATE



**THE MATERIALS RESEARCH LABORATORY
UNIVERSITY PARK, PA**

19980910 008

REPORT DOCUMENTATION PAGE

Form Approved
OMB No. 0704-0188

Public reporting burden for this collection of information is estimated to average 1 hour per response, including the time for reviewing instructions, searching existing data sources, gathering and maintaining the data needed, and completing and reviewing the collection of information. Send comments regarding this burden estimate or any other aspect of this collection of information, including suggestions for reducing this burden, to Washington Headquarters Services, Directorate for Information Operations and Reports, 1215 Jefferson Davis Highway, Suite 1204, Arlington, VA 22202-4302, and to the Office of Management and Budget, Paperwork Reduction Project (0704-0188), Washington, DC 20503.

[illegible]

GENERAL INSTRUCTIONS FOR COMPLETING SF 298

The Report Documentation Page (RDP) is used in announcing and cataloging reports. It is important that this information be consistent with the rest of the report, particularly the cover and title page. Instructions for filling in each block of the form follow. It is important to *stay within the lines* to meet optical scanning requirements.

Block 1. Agency Use Only (Leave blank).

Block 2. Report Date. Full publication date including day, month, and year, if available (e.g. 1 Jan 88). Must cite at least the year.

Block 3. Type of Report and Dates Covered. State whether report is interim, final, etc. If applicable, enter inclusive report dates (e.g. 10 Jun 87 - 30 Jun 88).

Block 4. Title and Subtitle. A title is taken from the part of the report that provides the most meaningful and complete information. When a report is prepared in more than one volume, repeat the primary title, add volume number, and include subtitle for the specific volume. On classified documents enter the title classification in parentheses.

Block 5. Funding Numbers. To include contract and grant numbers; may include program element number(s), project number(s), task number(s), and work unit number(s). Use the following labels:

C - Contract	PE - Project
G - Grant	TA - Task
PE - Program Element	WU - Work Unit Accession No.

Block 6. Author(s). Name(s) of person(s) responsible for writing the report, performing the research, or credited with the content of the report. If editor or compiler, this should follow the name(s).

Block 7. Performing Organization Name(s) and Address(es). Self-explanatory

Block 8. Performing Organization Report Number. Enter the unique alphanumeric report number(s) assigned by the organization performing the report.

Block 9. Sponsoring/Monitoring Agency Name(s) and Address(es). Self-explanatory.

Block 10. Sponsoring/Monitoring Agency Report Number. (If known)

Block 11. Supplementary Notes. Enter information not included elsewhere such as: Prepared in cooperation with...; Trans. of...; To be published in.... When a report is revised, include a statement whether the new report supersedes or supplements the older report.

Block 12a. Distribution/Availability Statement. Denotes public availability or limitations. Cite any availability to the public. Enter additional limitations or special markings in all capitals (e.g. NOFORN, REL, ITAR).

DOD - See DoDD 5230.24, "Distribution Statements on Technical Documents."

DOE - See authorities.

NASA - See Handbook NHB 2200.2.

NTIS - Leave blank.

Block 12b. Distribution Code.

DOD - Leave blank.

DOE - Enter DOE distribution categories from the Standard Distribution for Unclassified Scientific and Technical Reports.

NASA - Leave blank.

NTIS - Leave blank.

Block 13. Abstract. Include a brief (Maximum 200 words) factual summary of the most significant information contained in the report.

Block 14. Subject Terms. Keywords or phrases identifying major subjects in the report.

Block 15. Number of Pages. Enter the total number of pages.

Block 16. Price Code. Enter appropriate price code (NTIS only).

Blocks 17. - 19. Security Classifications. Self-explanatory. Enter U.S. Security Classification in accordance with U.S. Security Regulations (i.e., UNCLASSIFIED). If form contains classified information, stamp classification on the top and bottom of the page.

Block 20. Limitation of Abstract. This block must be completed to assign a limitation to the abstract. Enter either UL (unlimited) or SAR (same as report). An entry in this block is necessary if the abstract is to be limited. If blank, the abstract is assumed to be unlimited.

ABSTRACT

The report documents work carried out over the period 31 July 1996 to 31 December 1997 on a Multi-University Research Initiative (MURI) program under Office of Naval Research (ONR) sponsorship. The program couples transducer materials research in the Materials Research Laboratory (MRL), design and testing studies in the Applied Research Laboratory (ARL) and vibration and flow noise control in the Center for Acoustics and Vibration (CAV) at Penn State.

The overarching project objective is the development of acoustic transduction materials and devices of direct relevance to Navy needs and with application in commercial products. The initial focus of studies is upon high performance sensors and high authority high strain actuators. This objective also carries the need for new materials, new device designs, improved drive and control strategies and a continuing emphasis upon reliability under a wide range of operating conditions.

In *Material Studies*, undoubtedly major breakthroughs have occurred in the ultra-high strain relaxor ferroelectric systems. Earlier reports of unusual piezoelectric activity in single crystal perovskite relaxors have been amply confirmed in the lead zinc niobate : lead titanate, and lead magnesium niobate : lead titanate systems for compositions of rhombohedral symmetry close to the Morphotropic Phase Boundary (MPB) in these solid solutions. Analysis of the unique properties of 001 field poled rhombohedral ferroelectric crystals suggests new intrinsic mechanisms for high strain and carries the first hints of how to move from lead based compositions. A major discovery of comparable importance is a new mode of processing to convert PVDF:TrFE copolymer piezoelectric into a relaxor ferroelectric in which electrostrictive strains of 4% have been demonstrated at high fields. Both single crystal and polymer relaxors appear to offer energy densities almost order of magnitude larger than in earlier polycrystal ceramic actuators.

Transducer Studies have continued to exploit the excellent sensitivity and remarkable versatility of the cymbal type flexensional element. Initial studies of a small cymbal arrays show excellent promise in both send and receive modes, and larger arrays are now under construction for tests at ARL. New studies in constrained layer vibration damping and in flow noise reduction are yielding exciting new results.

In *Actuator Studies*, an important advance in piezoelectric generated noise control now permits wider use of acoustic emission as a reliability diagnostic technique. Joint studies with NRL, Washington have developed a completely new d_{15} driven torsional actuator and the CAV program element has designed an exciting high strain high force inchworm.

Finite element analysis continues to be an important tool for understanding the more complex composite structures and their beam forming capability in water. *Thin and Thick Thin Film Studies* are gearing up to provide the material base for micro-tonpils arrays. New exploitation of ultra sensitive strain and permittivity measurements is providing the first reliable data of electrostriction in simple solids, and suggesting new modes for separating the polarizability contributors in dielectrics and electrostrictors.

APPENDICES

VOLUME I

GENERAL SUMMARY PAPERS

1. Ito, Y. and K. Uchino, Wiley Encyclopedia of Electrical and Electronics Engineering, J. G. Webster, Edit., (Partial Charge "Piezoelectricity"), John Wiley & Sons (1998). [in press].
2. Newnham, R.E., "Molecular Mechanisms in Smart Materials," MRS Bulletin (May 1997).
3. Swartz, S.L., T.R. Shrout, and T. Takenaka, "Electronic Ceramics R&D in the U.S., Japan, Part I: Patent History," The American Ceramic Society Bulletin 76 (8) (1997).

2.0 MATERIALS STUDIES

2.1 *Polycrystal Perovskite Ceramics*

4. Alberta, E.F., and A.S. Bhalla, "Piezoelectric Properties of $\text{Pb}(\text{InNb})_{1/2}\text{O}_3\text{-PbTiO}_3$ Solid Solution Ceramics," J. Korean Phys. Soc. 32, S1265-S1267 (February 1998).
5. Alberta, E.F. and A.S. Bhalla, "High Strain and Low Mechanical Quality Factor Piezoelectric $\text{Pb}[\text{Sc}_{1/2}\text{Nb}_{1/2}]_{0.575}\text{Ti}_{0.425}\text{O}_3$ Ceramics" (1997).
6. Zhang, Q.M. and J. Zhao, "Polarization Responses in Lead Magnesium Niobate Based Relaxor Ferroelectrics," Appl. Phys. Lett. 71 (12, 1649-1651 (1997).
7. Glazounov, A.E., J. Zhao, and Q.M. Zhang, "Effect of Nanopolar Regions on Electrostrictive Coefficients of a Relaxor Ferroelectric," Proceedings Williamsburg Meeting, Williamsburg, Virginia (1998).
8. Zhao, J. A.E. Glazounov, Q.M. Zhang, and B. Toby, "Neutron Diffraction Study of Electrostrictive Coefficients of Prototype Cubic Phase of Relaxor Ferroelectric $\text{PbMg}_{1/3}\text{Nb}_{2/3}\text{O}_3$," Appl. Phys. Lett. 72 (9), 1-3 (1998).
9. Park, S.-E., T.R. Shrout, P. Bridenbaugh, J. Rottenberg, and G.M. Loiacono, "Electric Field Induced Anisotropy in Electrostrictive $\text{Pb}(\text{Mg}_{1/3}\text{Nb}_{2/3})\text{O}_3\text{-PbTiO}_3$ Crystals," Ferroelectrics (1997).
10. You, H. and Q.M. Zhang, "Diffuse X-Ray Scattering Study of Lead Magnesium Niobate Single Crystals," Phys. Rev. Lett. 79 (20), 3950-3953 (1997).
11. Zhao, J., V. Mueller, and Q.M. Zhang, "The Influence of the External Stress on the Electromechanical Response of Electrostrictive $0.9\text{Pb}(\text{Mg}_{1/3}\text{Nb}_{2/3})\text{O}_3\text{-}0.1\text{PbTiO}_3$ in the DC Electrical Field Biased State," J. Mat. Res. (1998).

VOLUME II

12. Yoon, S.-J., A. Joshi, and K. Uchino, "Effect of Additives on the Electromechanical Properties of $\text{Pb}(\text{Zr,Ti})\text{O}_3\text{-Pb}(\text{Y}_{2/3}\text{W}_{1/3})\text{O}_3$ Ceramics," J. Am. Ceram. Soc 80 (4), 1035-39 (1997).
13. Hackenberger, W., M.-J. Pan, V. Vedula, P. Pertsch, W. Cao, C. Randall, and T. Shrout, "Effect of Grain Size on Actuator Properties of Piezoelectric Ceramics," Proceedings of the SPIE's 5th International Symposium on Smart Structures and Materials, San Diego, CA (March 1-5, 1998).

THIS PAGE LEFT INTENTIONALLY BLANK

Materials Studies—continued

14. Mueller, V. and Q.M. Zhang, "Shear Response of Lead Zirconate Titanate Piezoceramics," *J. Appl. Phys.* (1998).
15. Park, S.-E., M.-J. Pan, K. Markowski, S. Yoshikawa, and L.E. Cross, "Electric Field Induced Phase Transition of Antiferroelectric Lead Lanthanum Zirconate Titanate Stannate Ceramics," *J. Appl. Phys.* **82** (4), 1798-1803 (1997).
16. Yoshikawa, S., K. Markowski, S.-E. Park, M.-J. Pan, and L.E. Cross, "Antiferroelectric-to-Ferroelectric Phase Switching Lead Lanthanum Zirconate Stannate Titanate (PLZST) Ceramics," Proceedings of SPIE's 4th Annual Symposium on Smart Structures and Materials, San Diego, CA (March 3-6, 1997).
17. Pan, M.-J., S.-E. Park, K.A. Markowski, W.S. Hackenberger, S. Yoshikawa, and L.E. Cross, "Electric Field Induced Phase Transition in Lead Lanthanum Stannate Zirconate Titanate (PLSnZT) Antiferroelectrics: Tailoring Properties through Compositional Modification" (1997).
18. Pan, M.-J., P. Pertsch, S. Yoshikawa, T.R. Shrout, and V. Vedula, "Electroactive Actuator Materials: Investigations on Stress and Temperature Characteristics," Proceedings of the SPIE's 5th International Symposium on Smart Structures and Materials, San Diego, CA (March 1-5, 1998).
19. Pan, M.-J. and S. Yoshikawa, "Effect of Grain Size on the Electromechanical Properties of Antiferroelectric-to-Ferroelectric Phase Switching PLSnZT Ceramics" (1997).

2.2 Relaxor Ferroelectric Single Crystal Systems

20. Service, R.F., "Shape-Changing Crystals Get Shiftier," *Science* **275**, 1878 (28 March 1997).
21. Shrout, T.R., S.-E. Park, C.A. Randall, J.P. Shepard, L.B. Hackenberger, "Recent Advances in Piezoelectric Materials" (1997).
22. Park, S.-E. and T.R. Shrout, "Ultrahigh Strain and Piezoelectric Behavior in Relaxor Based Ferroelectric Single Crystals," *J. Appl. Phys.* **82** (4), 1804-1811 (1997).
23. Park, S.-E. and T. R. Shrout, "Characteristics of Relaxor-Based Piezoelectric Single Crystals for Ultrasonic Transducers," *IEEE Transactions, Ferroelectrics, and Frequency Control* **44** (5), 1140-1147 (1997).
24. Park, S.-E. and T.R. Shrout, "Relaxor Based Ferroelectric Single Crystals for Electro-Mechanical Actuators," *Mat. Res. Innov.* **1**, 20-25 (1997).
25. Park, S.-E., M.L. Mulvihill, G. Risch, and T.R. Shrout, "The Effect of Growth Conditions on the Dielectric Properties of $\text{Pb}(\text{Zn}_{1/3}\text{Nb}_{2/3})\text{O}_3$ Single Crystals," *Jpn. J. Appl. Phys.* **36**, 1154-1158 (1997).
26. Mulvihill, M.L., L.E. Cross, W. Cao, and K. Uchino, "Domain-Related Phase Transitionlike Behavior in Lead Zinc Niobate Relaxor Ferroelectric Single Crystals," *J. Am. Ceram. Soc.* **80** (6), 1462-68 (1997).
27. Park, S.-E., P.D. Lopath, K.K. Shung, and T.R. Shrout, "Relaxor-Based Single Crystal materials for Ultrasonic Transducer Applications" (1997).
28. Lopath, P.D., S.-E. Park, K.K. Shung, and T.R. Shrout, " $\text{Pb}(\text{Zn}_{1/3}\text{Nb}_{2/3})\text{O}_3/\text{PbTiO}_3$ Single Crystal Piezoelectrics for Ultrasonic Transducers" (1997).
29. Lopath, P.D., S.-E. Park, K.K. Shung, and T.R. Shrout, "Single Crystal $\text{Pb}(\text{Zn}_{1/3}\text{Nb}_{2/3})\text{O}_3/\text{PbTiO}_3$ (PZN/PT) in Medical Ultrasonic Transducers" (1997).

Materials Studies—continued

2.3 New High Strain Polymer Materials

30. Su, J., Q.M. Zhang, C.H. Kim, R.Y. Ting, and R. Capps, "Effect of Transitional Phenomena on the Electric Field Induced Strain-Electrostrictive Response of a Segmented Polyurethane Elastomer" (1997).
31. Su, J., Q.M. Zhang, and R.Y. Ting, "Space-Charge-Enhanced Electromechanical Response in Thin-Film Polyurethane Elastomers," *Appl. Phys. Lett* **71** (3), 386-388 (1997).

VOLUME III

32. Su, J., Q.M. Zhang, P.-C. Wang, A.G. MacDiarmid, K.J. Wynne, "Preparation and Characterization of an Electrostrictive Polyurethane Elastomer with Conductive Polymer Electrodes," *Polymers for Adv. Tech.* (1998).
33. Zhang, Q.M., V. Bharti, and X. Zhao, "Giant Electrostriction and Relaxor Ferroelectric Behavior in Electron Irradiated Poly(vinylidene Fluoride-Trifluoroethylene) Copolymer," *Science* (1998).

3.0 TRANSDUCER STUDIES

3.1 Cymbal : Moonie : BB Composites

34. Newnham, R.E., "Composite Sensors and Actuators" (1997).
35. Steele, B.CH., R.E. Newnham, and A.G. Evans, "Ceramics, Composites, and Intergrowth," *Current Opinion in Solid State & Materials Science* **2**, 563-565 (1997).
36. Tressler, J.F. S. Alkoy, and R.E. Newnham, "Piezoelectric Sensors and Sensor Materials" (1997).
37. Tressler, J.F., S. Alko, A. Dogan, and R.E. Newnham, "Functional Composites for Sensors, Actuators, and Transducers" (1997).
38. Dogan, A., K. Uchino, R.E. Newnham, "Composite Piezoelectric Transducer with Truncated Conical Endcaps 'Cymbal'," *IEEE Transactions on Ultrasonics, Ferroelectrics, and Frequency Control* **44** (3), 597-605 (1997).
39. Dogan, A., J.F. Fernandez, K. Uchino, and R.E. Newnham, "The 'Cymbal' Electromechanical Actuator" (1997).
40. Tressler, J.F., W. Cao, K. Uchino, and R.E. Newnham, "Ceramic-Metal Composite Transducers for Underwater Acoustic Applications" (1997).
41. Tressler, J.F. and R.E. Newnham, "Doubly Resonant Cymbal-Type Transducers," *IEEE Transactions on Ultrasonics, Ferroelectrics, and Frequency Control* **44** (5), 1175-1177 (1997).
42. Tressler, J.F., W. Cao, K. Uchino, and R.E. Newnham, "Finite Element Analysis of The Cymbal-Type Transducer" (1997).
43. Tressler, J.F., W.J. Hughes, W. Cao, K. Uchino, and R.E. Newnham, "Capped Ceramic Underwater Sound Projector" (1997).

VOLUME IV

44. Alkoy, S., P.D. Lopath, R.E. Newnham, A.-C. Hladky-Hennion, and J.K. Cochran, "Focused Spherical Transducers for Ultrasonic Imaging" (1997).
45. Alkoy, S., A. Dogan, A.-C. Hladky, P. Langlet, J.K. Cochran, and R.E. Newnham, "Miniature Piezoelectric Hollow Sphere Transducers (BBs)" (1997).
46. Zipparo, M.J., K.K. Shung, and T.R. Shrout, "Piezoceramics for High-Frequency (20 to 100 MHz) Single-Element Imaging Transducers," *IEEE Transactions on Ultrasonics, Ferroelectrics, and Frequency Control* **44** (5), 1038-1048 (1997).

3.2 *Frequency Agile Transducers*

47. Davis, C. and G.A. Lesieutre, "An Actively-Tuned Solid State Piezoelectric Vibration Absorber" (1997).
48. Davis, C.L., G.A. Lesieutre, and J. Dosch, "A Tunable Electrically Shunted Piezoceramic Vibration Absorber" (1997).
49. Lesieutre, G.A. and U. Lee, "A Finite Element for Beams Having Segmented Active Constrained Layers with Frequency-Dependent Viscoelastic Material Properties" (1997).
50. Hebert, C.A. and G.A. Lesieutre, "Rotocraft Blade Lag Damping Using Highly Distributed Tuned Vibration Absorbers," *American Institute of Aeronautics and Astronautics (AIAA 98-2001)*.
51. Lesieutre, G.A. and C.L. Davis, "Can a Coupling Coefficient of a Piezoelectric Device be Higher than Those of its Active Material?," *SPIE 4th Annual Symposium on Smart Structures and Materials, San Diego, CA (March 1997)*.

3.3 *3-D Acoustic Intensity Probes*

52. Lauchle, G.C., J.R. MacGillivray, and D.C. Swanson, "Active Control of Axial-flow Fan Noise," *J. Acoust. Soc. Am* **101** (1), 341-349 (1997).
53. McGuinn, R.S., G.C. Lauchle, and D.C. Swanson, "Low Flow-Noise Microphone for Active Noise Control Applications," *AIAA Journal* **35** (1), 29-34 (1997).
54. McGuinn, R.S., G.C. Lauchle, and D.C. Swanson, "Low Flow-Noise Pressure Measurements Using a "Hot-Mic," *AIAA -97-1665-CP*.
55. Capone, D.E., and G.C. Lauchle, "Designing a Virtual Sound-Level Meter in LabVIEW," *Education/Acoustics, LabVIEW, National Instruments*.

VOLUME V

4.0 ACTUATOR STUDIES

4.1 *Materials : Designs : Reliability*

56. Uchino, K., "Piezoelectric Actuators" (1997).
57. Uchino, K., "Overview: Materials Issues in Design and Performance of Piezoelectric Actuators," *SPIE Mtg.* (1997).
58. Uchino, K., "Shape Memory Ceramics," Chapter 8 (1997).

Actuator Studies—continued

59. Aburatani, H., S. Yoshikawa, K. Uchino, and J.W.C. deVries, "A Study of Acoustic Emission in Piezoelectric Multilayer Ceramic Actuator," *Jpn. J. Appl. Phys.* **37**, 204-209 (1998).
60. Aburatani, H. and K. Uchino, "Acoustic Emission (AE) Measurement in Piezoelectric Ceramics" (1997).
61. Aburatani, H. and K. Uchino, "The Application of Acoustic Emission (AE) Method for Ferroelectric Devices and Materials," 8th US-Japan Seminar (1997).
62. Uchino, K., "Reliability of Ceramic Actuators" (1997).

4.2 Photostrictive Actuators

63. Tonooka, K. P. Poosanaas, and K. Uchino, "Mechanism of the Bulk Photovoltaic Effect in Ferroelectrics," *Proceedings of the 5th SPIE Mtg., San Diego, CA* (1998).
64. Poosanaas, P. A. Dogan, S. Thakoor, and K. Uchino, "Dependence of Photostriction on Sample Thickness and Surface Roughness for PLZT Ceramics," *Proceedings of the 1997 IEEE Ultrasonics Symposium, Toronto, Ontario, Canada* (October 1997).
65. Poosanaas, P. A. Dogan, A.V. Prasadaraao, S. Komarneni, and K. Uchino, "Photostriction of Sol-Gel Processed PLZT Ceramics," *J. Electroceramics* **1** (1), 105-111 (1997).

VOLUME VI

66. Poosanaas, P., A. Dogan, A.V. Prasadaraao, S. Komarneni, and K. Uchino, "Effect of Ceramic Processing Methods on Photostrictive Ceramics," *J. Adv. Perf. Mat.* (1997).
67. Thakoor, S., P. Poosanaas, J.M. Morookian, A. Yavrovian, L. Lowry, N. Marzwell, J. Nelson, R.R. Neurgaonkar, and K. Uchino, "Optical Microactuation in Piezoceramics" (1997).

4.3 New Torsional Amplifier/Actuators

68. Glazounov, A.E., Q.M. Zhang, and C. Kim, "Piezoelectric Actuator Generating Torsional Displacement from Piezoelectric d_{15} Shear Response," *Appl Phys. Lett.* (1997).
69. Glazounov, A.E., Q.M. Zhang, and C. Kim, "A New Torsional Actuator Based on Shear Piezoelectric Response," *Proceedings of SPIE Smart Materials, San Diego, CA* (March 1998).

4.4 High Force Amplifiers and Inchworms

70. Uchino, K., J. Zheng, A. Joshi, S. Yoshikawa, S. Hirose, S. Takahashi, and J.W.C. deVries, "High Power Characterization of Piezoelectric Materials" (1997).
71. Uchino, K., "High Electromechanical Coupling Piezoelectrics - How High Energy Conversion Rate is Possible," *Mat. Res. Soc. Symp. Proc.* **459**, 3-14 (1997).
72. Park, S.-E., V. Vedula, M.-J. Pan, W.S. Hackenberger, P. Pertsch, and T.R. Shrout, "Relaxor Based Ferroelectric Single Crystals for Electromechanical Actuators," *Proceedings of the SPIE's 5th International Symposium on Smart Structures and Materials, San Diego, CA* (March 1998).

Actuator Studies—continued

73. Koopmann, G.H. G.A. Lesieutre, B.R. Dershem, W. Chen, and S. Yoshikawa, "Embeddable Induced Strain Actuators Using Framed 3-3 Piezoceramic Stacks: Modeling and Characterization," Proceedings of the SPIE's 4th Annual International Symposium on Smart Structures and Materials, San Diego, CA (March 1997).
74. Driesch, P.L., G.H. Koopmann, J. Dosch, and H. Iwata, "Development of a Surface Intensity Probe for Active Control Applications," IMECE, Dallas, Texas (November 1997).
75. Galante, T., J. Frank, J. Bernard, W. Chen, G.A. Lesieutre, and G.H. Koopmann, "Design, Modeling, and Performance of a High Force Piezoelectric Inchworm Motor" (1997).
76. Galante, T.P., "Design and Fabrication of a High Authority Linear Piezoceramic Actuator: The PSU H3 Inchworm," Master of Science Thesis, The Pennsylvania State University (August 1997).
77. Lesyna, M.W., "Shape Optimization of a Mechanical Amplifier for Use in a Piezoceramic Actuator," Master of Science Thesis, The Pennsylvania State University (May 1998).

VOLUME VII

78. Uchino, K., "Piezoelectric Ultrasonic Motors: Overview," J. Smart Materials and Structures—Special Issue (1997).
79. Uchino, K., "Compact Piezoelectric Ultrasonic Motors," J. Medical Ultrasonics 24 (9), 1191-92 (1997).

5.0 MODELING and CHARACTERIZATION

5.1 Finite Element Methods

80. Qi, W. and W. Cao, "Finite Element Analysis and Experimental Studies on the Thickness Resonance of Piezocomposite Transducer," Ultrasonic Imaging 18, 1-9 (1996).
81. Qi, W. and W. Cao, "Finite Element Study on Random Design of 2-2 Composite Transducer," SPIE 3037, 176-180 (1997).
82. Geng, X. and Q.M. Zhang, "Evaluation of Piezocomposites of Ultrasonic Transducer Applications—Influence of the Unit Cell Dimensions and the Properties of Constituents on the Performance of 2-2 Piezocomposites," IEEE Transactions on Ultrasonics, Ferroelectrics, and Frequency Control 44 (4), 857-872 (1997).
83. Zhang, Q. and X. Geng, "Acoustic Properties of the Interface of a Uniform Medium-2-2 Piezocomposite and the Field Distributions in the Composite," Jpn. J. Appl. Phys. 36, 6853-6861 (1997).
84. Geng, X. and Q.M. Zhang, "Analysis of the Resonance Modes and Losses in 1-3 Composites for Ultrasonic Transducer Applications," IEEE UFFC (1997).

APPENDIX 87

Crystal Orientation Dependence of Piezoelectric Properties in Lead Zirconate Titanate: Theoretical Expectation for Thin Films

Xiao-hong DU, Uma BELEGUNDU and Kenji UCHINO*

International Center for Actuators and Transducers, Materials Research Laboratory,
 The Pennsylvania State University, University Park, Pennsylvania 16802, U.S.A.

(Received April 14, 1997; accepted for publication June 12, 1997)

Crystal orientation dependence of piezoelectric properties has been calculated phenomenologically for lead zirconate titanate (PZT) in the three-dimensional space. The calculation has been made for tetragonal PZT 40/60 (40% PZ and 60% PT) and rhombohedral PZT 60/40 compositions. The maximum longitudinal piezoelectric constant d_{33} and electromechanical coupling factor k_{33} in the rhombohedral composition were found to be at 57° and 51° angles, respectively, canted from the spontaneous polarization direction. This suggests that thin film piezoelectric actuators or sensors should employ a rhombohedral composition with the perovskite [100] epitaxially-oriented configuration.

KEYWORDS: crystal orientation, thin film, lead zirconate titanate

1. Introduction

Recent developments in ferroelectric and piezoelectric thin films have been remarkable. The polarization switching and high capacitance of a thin film configuration are attractive for memory devices such as dynamic random access memories (DRAM). A combination of the piezoelectric film and a silicon diaphragm realizes integrated actuator and sensor arrays.^{1,2)}

Most of the previous researches have been done on the thin films with polycrystalline or epitaxially-grown structures with the spontaneous polarization direction normal to the film. To the author's knowledge, no investigations have been made relating to the enhancement of electromechanical properties by using specially oriented thin films.

This paper describes a theoretical approach to such enhancement of piezoelectric properties in lead zirconate titanate (PZT) thin films.

2. Analytical Background

The phenomenology theory of the lead zirconate-titanate has been systematically developed in ref. 3. Here we just use the phenomenology to derive the relations of dielectric, piezoelectric, and elastic constants between two different orientations. We shall start by expressing the elastic Gibbs free energy as a function of polarization and stress at some temperature T . For convenience, we use the Einstein summation convention, i.e. a repeated index in a term implies that the term is summed with respect to the index for all its possible values. We then have

$$\begin{aligned} \Delta G = & \frac{1}{2} \alpha_{ij} P_i P_j + \frac{1}{4} \alpha_{ijkl} P_i P_j P_k P_l \\ & + \frac{1}{6} \alpha_{ijklrs} P_i P_j P_k P_l P_r P_s - \frac{1}{2} s_{ijkl} X_{ij} X_{kl} \\ & - Q_{ijkl} P_i P_j X_{kl} + \dots \end{aligned} \quad (1)$$

where ΔG is the elastic Gibbs free energy referring to the cubic paraelectric state, P_i are the ferroelectric po-

larizations, X_{ij} are the stresses, α_{ij} , α_{ijkl} , and α_{ijklrs} are the ferroelectric stiffness at constant stress, s_{ijkl} are the elastic compliances at constant polarization, and Q_{ijkl} are the electrostrictive coefficients. Depending on the symmetry of the crystal, some of the coefficients are zero.

The electric field E_n and strain x_{nm} are obtained by taking derivatives of ΔG with respect to the polarization and stress, respectively. We have

$$\begin{aligned} E_n = \frac{\partial \Delta G}{\partial P_n} = & \alpha_{nj} P_j \\ & + \alpha_{njkl} P_j P_k P_l + \alpha_{njklrs} P_j P_k P_l P_r P_s \\ & - 2Q_{njkl} P_j X_{kl} + \dots \end{aligned} \quad (2)$$

$$x_{nm} = -\frac{\partial \Delta G}{\partial X_{nm}} = s_{nmkl} X_{kl} + Q_{ijnm} P_i P_j + \dots \quad (3)$$

From eqs. (2) and (3), the relative dielectric stiffness χ_{ij} under constant stress and the piezoelectric g constants can be expressed as

$$\begin{aligned} \chi_{nm} = \epsilon_0 \frac{\partial E_n}{\partial P_m} = & \epsilon_0 (\alpha_{nm} + 3\alpha_{nmkl} P_k P_l \\ & + 5\alpha_{nmklrs} P_k P_l P_r P_s - 2Q_{nmkl} X_{kl} + \dots) \end{aligned} \quad (4)$$

and

$$g_{nkl} \approx -\frac{\partial E_n}{\partial X_{kl}} = \frac{\partial x_{kl}}{\partial P_n} = 2Q_{njkl} P_j + \dots \quad (5)$$

where ϵ_0 is the permittivity of free space.

The transformations of the dielectric stiffness, piezoelectric constants, and elastic compliances from one orientation to another orientation correspond to a rotation of the axis system. Let $\{e_i\}$ and $\{e'_i\}$ be orthonormal bases representing the original and a new axis systems, respectively. The transformation matrix can be calculated by

$$A'_{ij} = e'_i \cdot e_j. \quad (6)$$

By applying the transformation rules of second, third, and fourth tensors respectively to the dielectric, piezoelectric, and elastic constants, ref. 4 provides all the formulas to calculate the constants in the new axis system. However, we can also obtain the constants by calculat-

*Corresponding author.

E-mail address: kenjiuchino@Alpha.mrl.psu.edu

ing each term on the right sides of eqs. (4) and (5) in the new axis system. To show the consistence of these two methods, we will derive the same formulas by calculating

$$\chi_{n'm'} = \varepsilon_0(\alpha_{n'm'} + 3\alpha_{n'm'k'l'}P_kP_l + 5\alpha_{n'm'k'l'r's'}P_kP_lP_rP_s - 2Q_{n'm'k'l'}X_{kl} + \dots) \quad (7)$$

By applying tensor operation to each term on the right side of eq. (7), we have

$$\begin{aligned} \chi_{n'm'} = \varepsilon_0(A_n^n A_m^m \alpha_{nm} + 3A_n^n A_m^m A_k^k A_l^l A_i^i A_j^j \alpha_{nmkl} P_i P_j \\ + 5A_n^n A_m^m A_k^k A_l^l A_r^r A_s^s A_i^i A_j^j \alpha_{nmklrs} P_i P_j P_r P_s - 2A_n^n A_m^m A_k^k A_l^l A_i^i A_j^j Q_{nmkl} X_{ij} + \dots). \end{aligned} \quad (8)$$

Since we choose both $\{e_i\}$ and $\{e'_i\}$ to be orthonormal, we have $A_i^i A_j^j = \delta_{ij}$, where δ_{ij} is the Kronecker delta. Then, eq. (8) can be simplified as

$$\chi_{n'm'} = A_n^n A_m^m \varepsilon_0(\alpha_{nm} + 3\alpha_{nmkl} P_k P_l + 5\alpha_{nmklrs} P_k P_l P_r P_s - 2Q_{nmkl} X_{kl} + \dots). \quad (9)$$

Consequently, we have

$$\chi_{n'm'} = A_n^n A_m^m \chi_{nm}. \quad (10)$$

Similarly, we can obtain the transformation equations for piezoelectric constants and elastic compliances

$$g_{n'k'l'} = A_n^n A_k^k A_l^l g_{nkl} \quad (11)$$

and

$$s_{n'm'k'l'} = A_n^n A_m^m A_k^k A_l^l s_{nmkl}. \quad (12)$$

The above derivation shows that although the right sides of eqs. (2) and (3) contain tensors with various orders, the constants χ_{nm} , g_{nkl} , and s_{nmkl} always abide by the transformation rules of second, third, and fourth order tensors, respectively; no matter how many terms we expand the free energy ΔG upto. In other words, if we have the constants in one orientation, we can obtain the constants in another orientation simply by applying the operations of the second, third, and fourth tensors.

The relative electric susceptibility η_{ij} and dielectric

constant ϵ_{ij} under constant stress can be obtained by

$$[\eta_{ij}] = [\chi_{ij}]^{-1} \quad (13)$$

and

$$\epsilon_{ij} = \eta_{ij} + \delta_{ij}. \quad (14)$$

The piezoelectric d constants can be calculated by

$$d_{ikl} = \varepsilon_0 \eta_{ij} g_{jkl}. \quad (15)$$

To simplify the calculations, the compressed notations are used. The details of the correspondence between the tensor forms and the matrix forms have been described in ref. 5. For the compressed notation, the constants in the new axis system can be calculated by⁴⁾

$$\epsilon' = A \epsilon A' \quad (16)$$

$$d' = A d N' \quad (17)$$

$$s' = N s N' \quad (18)$$

where $A = [A_i^j]$ and

$$N = \begin{bmatrix} a_{11}^2 & a_{12}^2 & a_{13}^2 & a_{12}a_{13} & a_{11}a_{13} & a_{11}a_{12} \\ a_{21}^2 & a_{22}^2 & a_{23}^2 & a_{22}a_{23} & a_{21}a_{23} & a_{21}a_{22} \\ a_{31}^2 & a_{32}^2 & a_{33}^2 & a_{32}a_{33} & a_{31}a_{33} & a_{31}a_{32} \\ 2a_{21}a_{31} & 2a_{22}a_{32} & 2a_{23}a_{33} & a_{22}a_{33} + a_{23}a_{32} & a_{21}a_{33} + a_{23}a_{31} & a_{21}a_{32} + a_{22}a_{31} \\ 2a_{11}a_{31} & 2a_{12}a_{32} & 2a_{13}a_{33} & a_{12}a_{33} + a_{13}a_{32} & a_{11}a_{33} + a_{13}a_{31} & a_{11}a_{32} + a_{12}a_{31} \\ 2a_{11}a_{21} & 2a_{12}a_{22} & 2a_{13}a_{23} & a_{12}a_{23} + a_{13}a_{22} & a_{11}a_{23} + a_{13}a_{21} & a_{11}a_{22} + a_{12}a_{21} \end{bmatrix}. \quad (19)$$

In eq. (19), $a_{ij} = A_i^j$, the i -th row and j -th column element in matrix A .

All the coefficients except the elastic compliances in eq. (1) have been calculated by fitting experiment data in ref. 6. It should be mentioned that all the constants in refs. 3 and 6 are the constants referring to the axis system for the cubic perovskite. For rhombohedral symmetry, this axis system is different from the conventional system where Z -axis is along $[111]$, X -axis is perpendicular to the mirror plan, and Y -axis is chosen to form a right-hand system. In our calculation, we keep $\{e_i\}$ being the convention axis system for each individual phase and start all the calculation from this axis system.

The phase diagram of the lead zirconate titanate is well known and is given in ref. 7. At a high temperature, the PZT exhibits a cubic paraelectric phase, and

as temperature decreases, either a rhombohedral or a tetragonal phase occurs depending on the composition. We have considered the compositions with 60% and 40% of PT as examples to demonstrate the piezoelectric properties of the tetragonal and rhombohedral PZT crystals, respectively.

The dielectric constants under constant stress and piezoelectric constants are calculated by using the data from ref. 6 and summarized in Tables I and II. Since the elastic compliances for PZT single crystals have not been reported, we assumed that the compliances are independent of the composition. The compliances under constant electric field of lead titanate are used for other tetragonal compositions for the first approximation (Table III from ref. 8). For the rhombohedral PZT 60/40, the average value of s_{11} and s_{33} was used as s_{11} , the av-

erage value of s_{12} and s_{13} as s_{12} , and the average value of s_{44} and s_{66} as s_{44} in the axis system for the cubic perovskite. After the axis system is rotated back to the conventional axis system for the rhombohedral $3m$ symmetry, the compliances under constant electric field are listed in Table IV. The ambiguity of elastic compliance does not inflect the calculation for the permittivity and piezoelectric constants.

Table I. Dielectric constants under constant stress and piezoelectric constants of tetragonal PZT 40/60 from ref. 6.

ϵ_{11}	ϵ_{33}	d_{33} (pC/N)	d_{31} (pC/N)	d_{15} (pC/N)
499.0	198.3	162.0	-58.9	169.0

Table II. Dielectric constants under constant stress and piezoelectric constants of rhombohedral PZT 60/40 calculated by using the data from ref. 6.

ϵ_{11}	ϵ_{33}	d_{33} (pC/N)	d_{22} (pC/N)	d_{31} (pC/N)	d_{15} (pC/N)	P_s ($\mu\text{C}/\text{cm}^2$)
529.8	296.1	70.8	75.2	-11.3	359.9	50

Table III. Compliances of PbTiO_3 under constant electric field from ref. 8.

s_{11} (1/TPa)	s_{33} (1/TPa)	s_{12} (1/TPa)	s_{13} (1/TPa)	s_{44} (1/TPa)	s_{66} (1/TPa)
7.06	21.3	-0.4	-6.27	15.4	9.62

Table IV. Compliance of rhombohedral PZT 60/40 under constant electric field calculated by using the data from ref. 8.

s_{11} (1/TPa)	s_{12} (1/TPa)	s_{13} (1/TPa)	s_{14} (1/TPa)	s_{33} (1/TPa)	s_{44} (1/TPa)	s_{66} (1/TPa)
8.55	-1.46	0.417	-5.31	6.67	27.53	20.01

To illustrate the orientation dependence of ϵ_{33} , d_{33} , and k_{33} , axis e_3 is rotated in the three-dimensional space and the corresponding ϵ'_{33} , d'_{33} , and s'_{33} are calculated by using eqs. (16)–(18). The choice of e_1 and e_2 are arbitrary since ϵ'_{33} , d'_{33} , and s'_{33} are independent from e_1 and e_2 . The electromechanical coupling factor k_{33} in the new orientation can be calculated by

$$k'_{33} = \frac{d'_{33}}{\sqrt{s'_{33}\epsilon'_{33}}}. \quad (20)$$

The results are shown in Figs. 1(a), 2(a), 2(c), 4(a), 5(a), and 5(c) when e_3 is rotated along the longitude lines and the latitude lines at steps less than 10° . The cross sections are also shown beside these figures; however, the cross sections are calculated at a reduced step of 0.1° in order to increase the accuracy of the optimal directions.

For d_{31} and k_{31} , we fix direction 3 along e_3 , but direction 1 is rotated. For each position of e_1 , the transformation matrices A and N are first calculated by using eqs. (6) and (19), then the constants in the new axis system are determined by eqs. (16)–(18). The electromechanical coupling factor k_{31} in the new orientation can be calculated by

$$k'_{31} = \frac{d'_{31}}{\sqrt{s'_{11}\epsilon'_{33}}}. \quad (21)$$

3. Results of the Calculation

The results for the tetragonal PZT 40/60 are shown in Figs. 1–3. In the figures, the distance between the origin and a point on the graph represents the absolute value

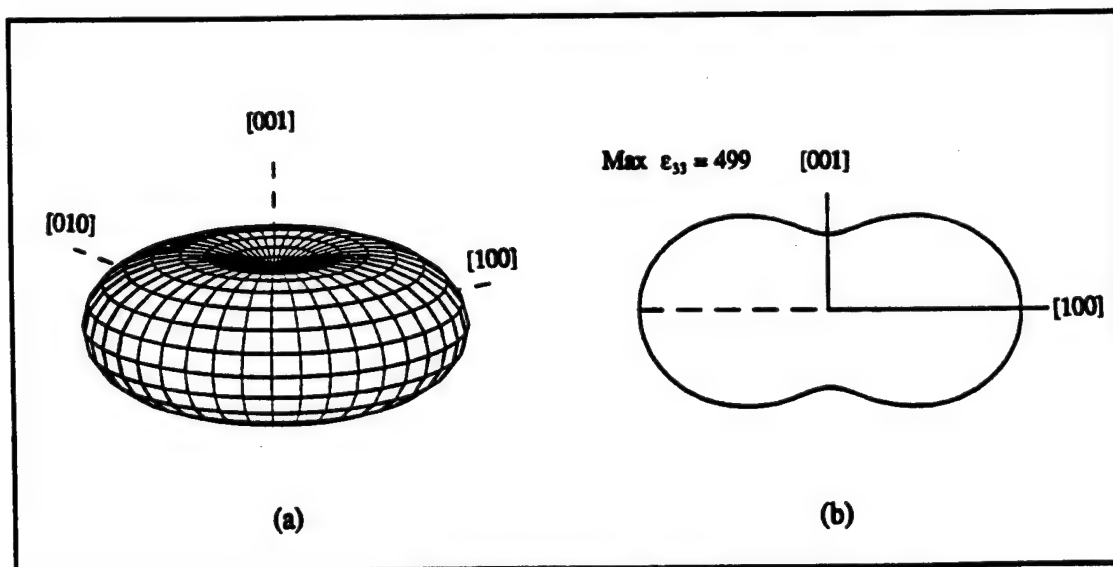


Fig. 1. (a) Dielectric constant of tetragonal PZT 40/60. (b) The cross section curve when the figure in Fig. 1(a) is cut by (010) plane. The maximum value of ϵ_{33} is in the directions perpendicular to $[001]$.

of the constant in the corresponding direction. Figure 1 shows the crystal orientation dependence of the dielectric constant. Along the polarization direction, the dielectric constant ϵ_{33} shows the minimum value. The maximum dielectric constant ϵ_{33} is obtained in the orientation perpendicular to the polarization direction, i.e. equivalent to ϵ_{11} . Figure 2 shows the orientation dependence of the longitudinal piezoelectric constant d_{33} and electromechanical coupling factor k_{33} , respectively. The maximum values occur along the polarization direction. In the orientation perpendicular to the polarization direction, the d_{33} is calculated to be zero. Figure 3 shows the orientation dependence of d_{31} and k_{31} with direction 3 along [001] which is perpendicular to the paper and direction 1 being rotated. The k_{31} value shows the maximum when axis 1 is along [110].

The results for rhombohedral PZT 60/40 are shown in Figs. 4–6, which are rather different from the tetragonal results. Figure 4 shows the orientation dependence of the dielectric constant. The maximum dielectric constant is in the orientation perpendicular to the polarization direction, and the dielectric constant becomes the minimum along the polarization direction. Figure 5 shows the orientation dependence of the longitudinal piezoelectric constant d_{33} and the electromechanical coupling factor k_{33} . The maximum values of d_{33} and k_{33} can be obtained in the directions 56.7° and 51.3° , respectively, away from the polarization direction, which is very different from the situation in the tetragonal state. Roughly speaking, along cubic perovskite [100] direction, d_{33} and k_{33} values are most enhanced. The d_{33} of 189×10^{-12} C/N for this canted angle is larger than the d_{33} along the po-

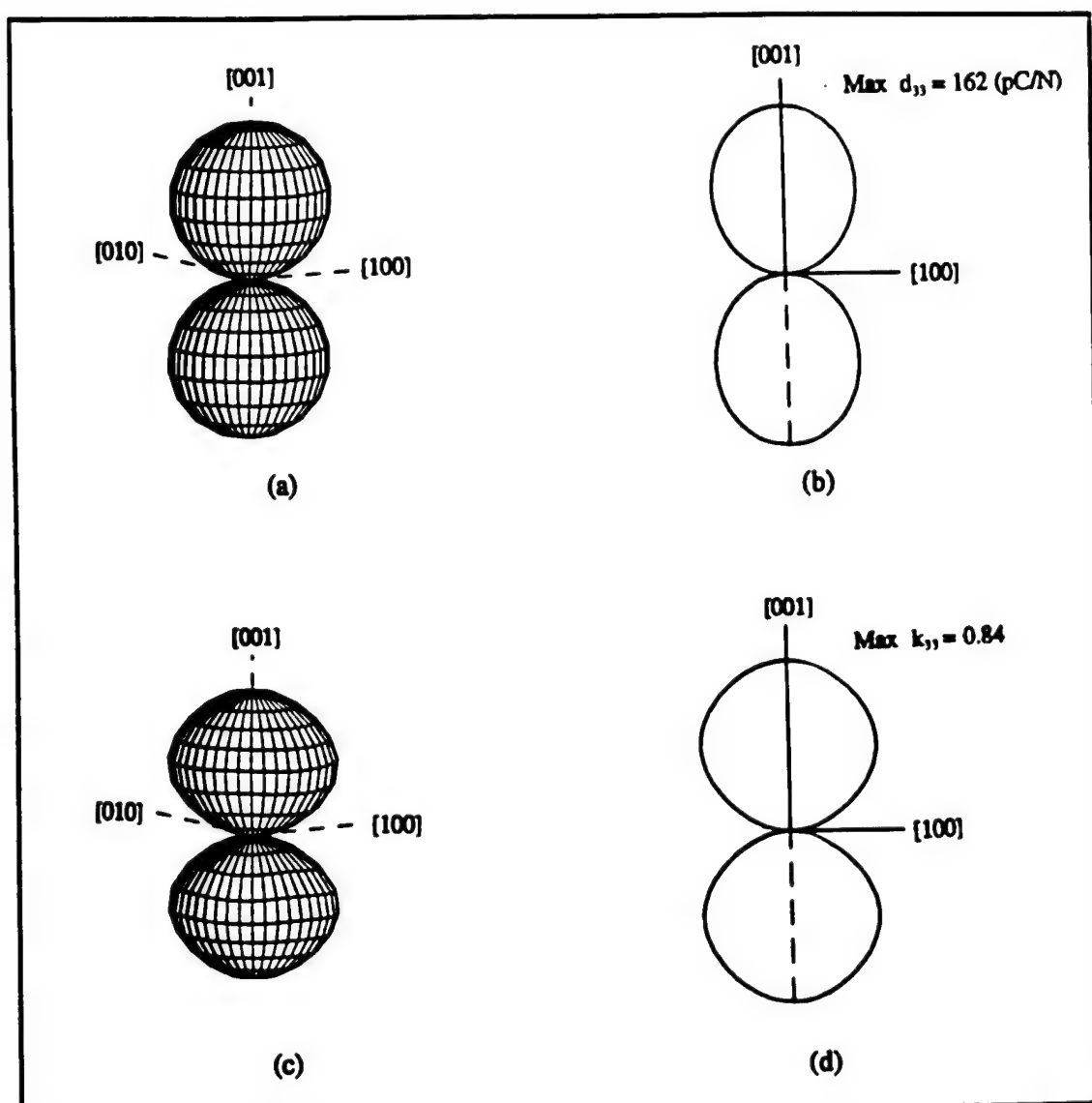


Fig. 2. (a) Piezoelectric constant d_{33} of tetragonal PZT 40/60. (b) The cross section curve when the figure in (a) is cut by (010) plane. The maximum value of d_{33} is along [001]. (c) Electromechanical coupling factor k_{33} of tetragonal PZT 40/60. (d) The cross section curve when the figure in (c) is cut by (010) plane. The maximum value of k_{33} is along [001].

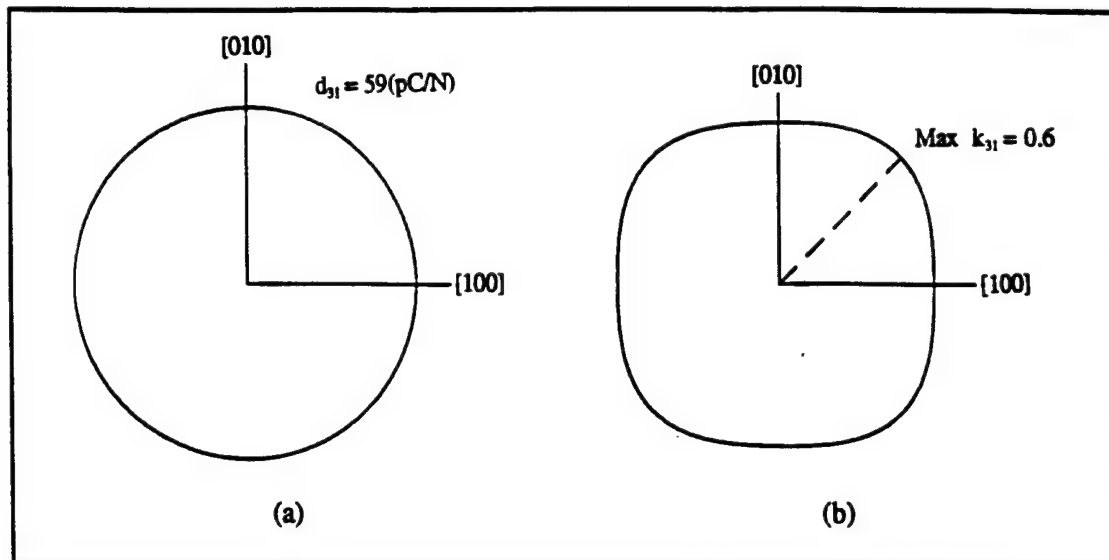


Fig. 3. (a) Piezoelectric constant d_{31} of tetragonal PZT 40/60. Axis 3 is fixed along [001] which is perpendicular to the paper and axis 1 is rotated. (b) Electromechanical coupling factor k_{31} of tetragonal PZT 40/60. Axis 3 is fixed along [001] which is perpendicular to the paper and axis 1 is rotated. k_{31} has the maximum value when axis 1 is along [110].

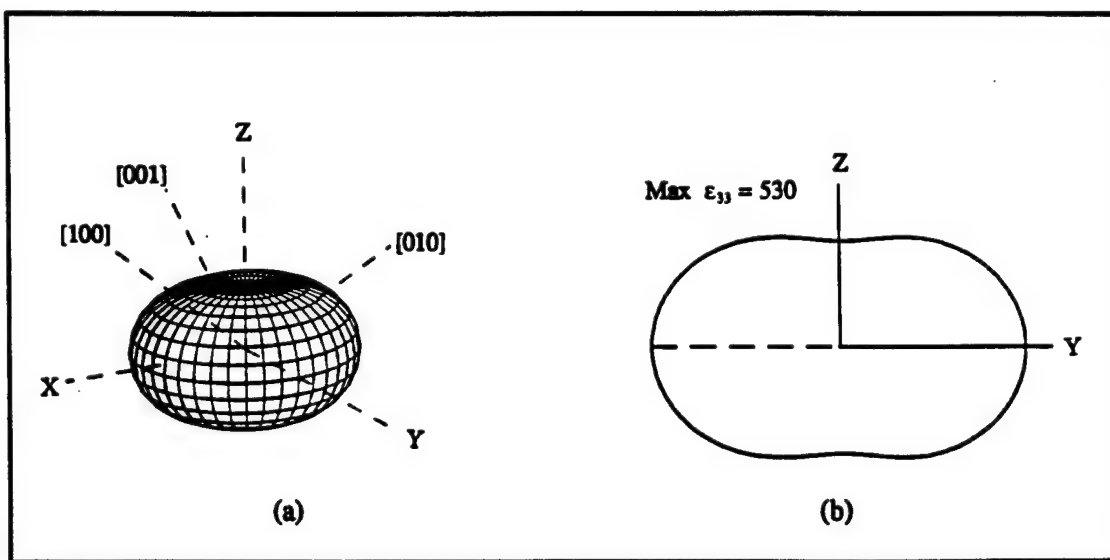


Fig. 4. (a) Dielectric constants of rhombohedral PZT 60/40. (b) The cross section curve when the figure in (a) is cut by Y-Z plane.

larization direction and also larger than the d_{33} in the tetragonal PZT 40/60. Figure 6 shows the orientation dependence of d_{31} and k_{31} with the direction 3 along Z-direction which is perpendicular to the paper and the direction 1 being rotated. Both d_{31} and k_{31} are independent of the choice of the direction 1.

4. Discussions

The above results show that the physical properties of single crystals PZT are highly dependent on the crystal orientation. Particularly, for the single crystal rhom-

bohedral PZT, the maximum values of d_{33} and k_{33} occur along the orientation close to the cubic perovskite equivalent axis [100]. Since the calculations were made using the speculated data, the canted angle to give the maximum value may be different from the experimental data. However, we believe the tendency would be true. We also believe that the composition nearer to the morphotropic phase boundary should show enhanced d values, and a similar crystal orientation dependence should be observed. Thus, PZT thin film actuators and sensors should employ a rhombohedral

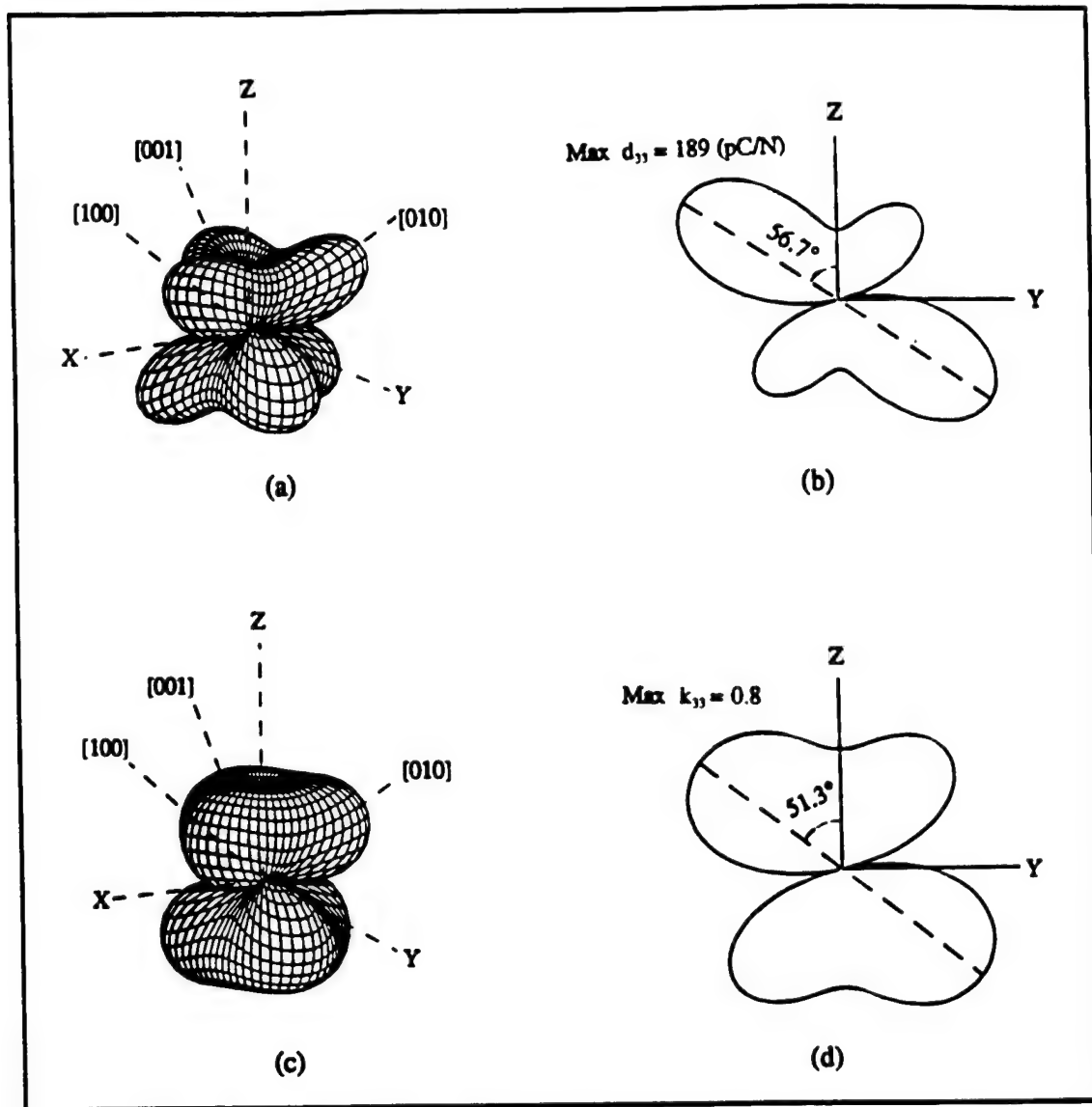


Fig. 5. (a) Piezoelectric constant d_{33} of rhombohedral PZT 60/40. (b) The cross section curve when the figure in (a) is cut by Y - Z plane. The maximum value of d_{33} is on Y - Z plane and 56.7° away from Z -axis. (c) Electromechanical coupling factor k_{33} of rhombohedral PZT 60/40. (d) The cross section curve when the figure in (c) is cut by Y - Z plane. The maximum value of k_{33} is on Y - Z plane and 51.3° away from Z -axis.

composition with the perovskite [100] epitaxially oriented configuration. It is worth to note a related piezoelectric behavior in a $\text{Pb}(\text{Zn}_{1/3}\text{Nb}_{2/3})\text{O}_3$ - PbTiO_3 system. Similar to PZT, this solid solution system shows a rhombohedral: tetragonal morphotropic phase boundary around the 0.9PZN-0.1PT composition.⁹⁾ Advantage of this system is easy fabrication of large single crystals. The rhombohedral single crystal with the composition $0.91\text{Pb}(\text{Zn}_{1/3}\text{Nb}_{2/3})\text{O}_3$ - 0.09PbTiO_3 exhibits unusually large values of d_{33} and k_{33} ($d_{33} = 1570$ pC/N and $k_{33} = 92\%$) when poled along the pseudo-cubic [100] direction.⁹⁾ For various acoustic applications, the large piezoelectric constants and high electromechanical coupling factors are the most important.¹⁰⁾ The calculation for this crystal has not been done yet. However, some interesting parallels can be drawn. From Fig. 5, the ra-

tios $d_{[111]}/d_{33(\text{Max})} \cong 0.395$, and $k_{[111]}/k_{\text{max}} \cong 0.69$. By using the experimental data for PZN-PT from ref. 9, $d_{[111]}/d_{[100]} \cong 625(\text{pC/N})/1570 \text{ pC/N} = 0.398$, and $k_{[111]}/k_{[100]} \cong 0.68/0.92 = 0.74$, which are very close to the theoretically calculated ratios for PZT.

Finally, let us consider the polarization and induced strain hysteresis curves theoretically for the rhombohedral PZT composition 60/40. Figure 7 shows the possible spontaneous polarization directions for the (111) and (100) orientation epitaxial films. The electric field E_3 is applied normal to the film. For the (111) film, polarization directions 2, 3, and 4 are equivalent and are about 70.5° away from polarization direction 1, as shown in Fig. 7(a). Other two equivalent polarization directions are (6, 7, 8) and (5). When the electrical field changes its direction from upward to downward, the domains along

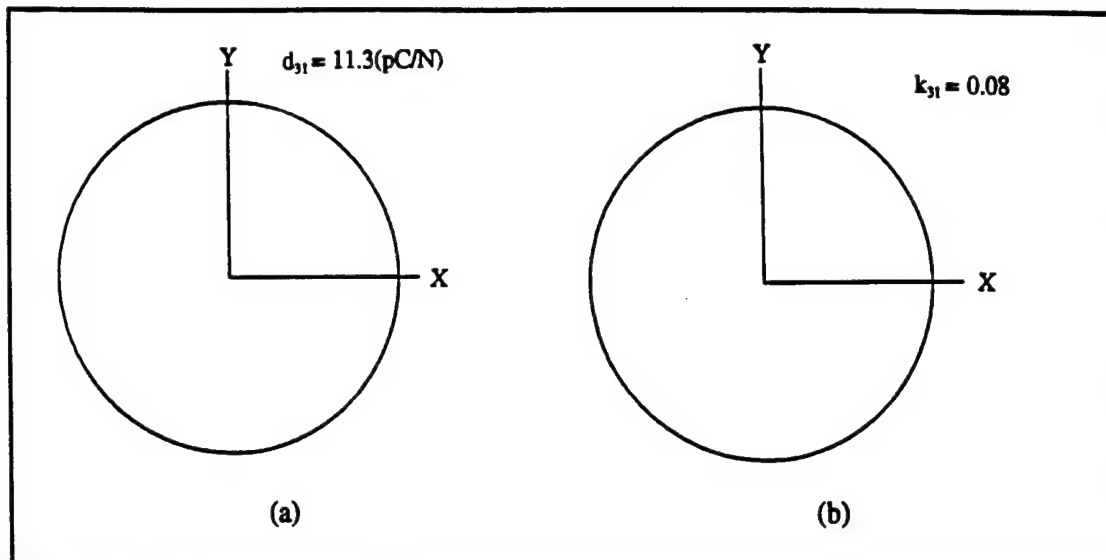


Fig. 6. (a) Piezoelectric constant d_{31} of rhombohedral PZT 60/40. Axis 3 is fixed along Z -axis which is perpendicular to the paper and axis 1 is rotated. (b) Electromechanical coupling factor k_{31} of rhombohedral PZT 60/40. Axis 3 is fixed along Z -axis which is perpendicular to the paper and axis 1 is rotated.

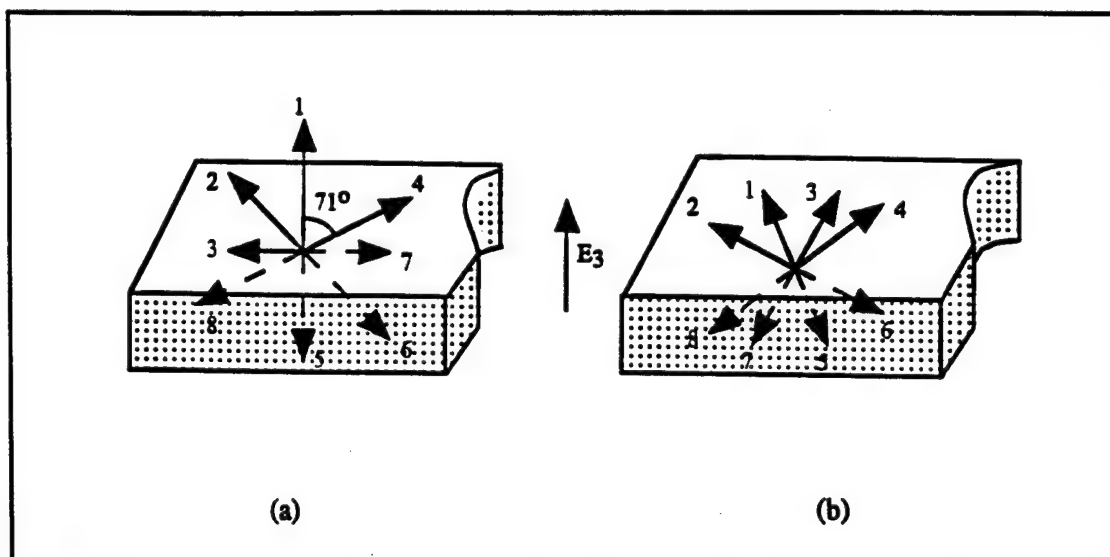


Fig. 7. Possible spontaneous polarization directions. (a) for (111) oriented films and (b) for (001) oriented films.

direction 1 will be first reversed since they are parallel to the field, while the domains along directions 2, 3, and 4 will be reversed later. Thus, the reverse-segments on the polarization and induced strain hysteresis curves are inclined as shown in Fig. 8(a). For the (100) film, there are two equivalent polarization directions, namely (1,2,3,4) and (5,6,7,8), which are about 54.7° away from the normal of the film, as shown in Fig. 7(b). When the electrical field changes its direction from upward to downward, the domains along directions 1, 2, 3, and 4 will be reversed at the same time. Consequently, the reverse-segments on the polarization and induced strain hysteresis curves are abrupt as shown in Fig. 8(b). Tak-

ing account of Fig. 7, the (100) film should have the remanent polarization $1/\sqrt{3}$ of the remanent polarization of the (111) film. The spontaneous polarization P_s for PZT 60/40 can be phenomenologically calculated⁶⁾ and is shown in Table II. Combining the information above and the constants shown in Table II, we propose the hysteresis curves as shown in Fig. 8.

Experimental proof is now under process.

Acknowledgements

The authors would like to thank the Office of Naval Research for supporting this work through contract: N00014-91-J-4145.

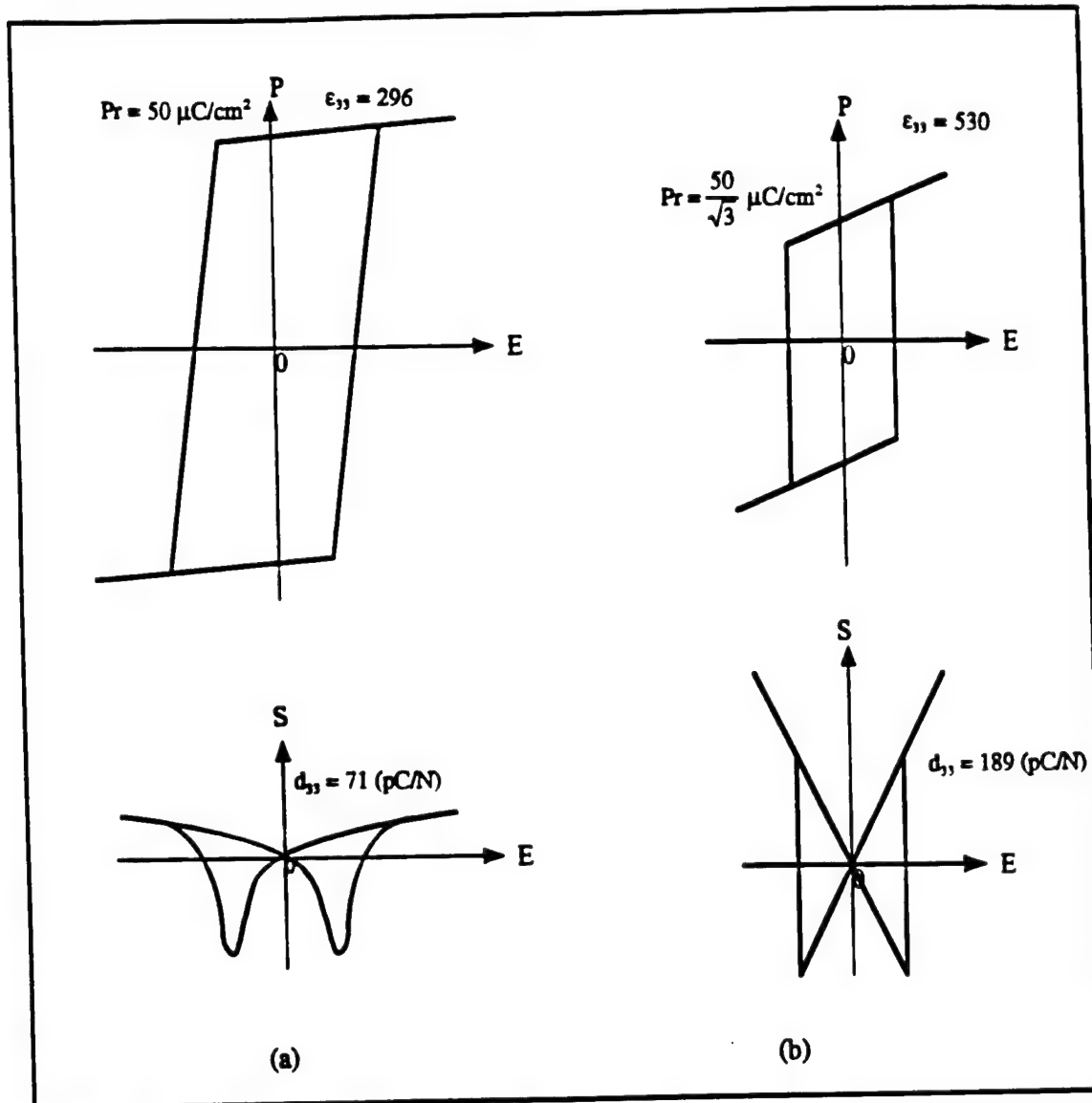


Fig. 8. Theoretical polarization and induced strain curves for the rhombohedral PZT 60/40. (a) for (111) oriented films and (b) for (001) oriented films.

- 1) M. Okuyama: Bull. Ceram. Soc. Jpn. **30** (1995) 504.
- 2) M. Sakata: Bull. Ceram. Soc. Jpn. **31** (1996) 927.
- 3) M. J. Haun, E. Furman, S. J. Jang and L. E. Cross: *Ferroelectrics* **99** (1989) 13.
- 4) W. G. Cady: *Piezoelectricity* (Dover, New York, 1964) Vol. 1, Chap. IV, p. 65.
- 5) ANSI/IEEE, IEEE Standard on Piezoelectricity, Std 176-1987 (IEEE, New York, 1987).
- 6) M. J. Haun, E. Furman, S. J. Jang and L. E. Cross: *Ferroelectrics* **99** (1989) 63.
- 7) B. Jaffe, W. J. Cook and H. Jaffe: *Piezoelectric Ceramics* (Academic Press, London, 1971).
- 8) Z. Li, M. Grimsditch, X. Xu and S.-K. Chan: *Ferroelectrics* **141** (1993) 313.
- 9) J. Kuwata, K. Uchino and S. Nomura: *Jpn. J. Appl. Phys.* **31** (1982) 1298.
- 10) Y. Yamashita: *Jpn. J. Appl. Phys.* **33** (1994) 5328.

Thin and Thick Thin Films

APPENDIX 88

THIN-FILM INTEGRATED FERROELECTRICS

L. ERIC CROSS AND S. TROLIER-MCKINSTRY, *Intercollege Materials Research Laboratory, The Pennsylvania State University, University Park, Pennsylvania, U.S.A.*

Introduction	429	3.1	Boundary Conditions for	
1. Needs for Ferroelectric			Films on Silicon	440
Films on Silicon	429	3.2	Deposition Methods	441
1.1 DRAM Applications	429	3.3	Vapor-Phase Techniques	441
1.2 FRAM Applications	430	3.4	Liquid-Phase Techniques	441
1.3 IR Thermal Imaging	430	4. Characterization of Film		
1.4 Mechanics	431	Microstructure	442	
1.5 Packaging	431	4.1 Introduction	442	
1.6 Microchemistry	431	4.2 Direct Methods	442	
2. Ferroelectric Material		4.3 Optical Methods	443	
Systems	431	5. Properties of Films on		
2.1 Properties of Bulk Materials ..	431	Silicon	443	
2.2 Symmetry Considerations	432	5.1 High-Permittivity Films		
2.3 Domains and Polarization		(DRAM)	443	
Switching	433	5.2 Hysteretic Films (FRAM)	444	
2.4 Transport Properties	434	5.3 Pyroelectric Films	446	
2.5 Perovskite-Structure		5.4 High-Energy-Density		
Systems	435	Transducers	446	
2.6 Bismuth Oxide Layer		6. Conclusions	447	
Structures	438	Glossary	448	
2.7 Alternative Systems	439	Works Cited	448	
2.8 Relaxor Ferroelectric		Further Reading	451	
Systems	439			
3. Ferroelectric Film				
Preparation	440			

INTRODUCTION

The recent explosion of research on ferroelectric thin films has led to significant advances in the processing and properties of these materials. A major driving force for this research is the advantages that accrue from integrating ferroelectric elements with integrated circuits (ICs) (especially silicon-based electronics). In particular, ferroelectric films can be optimized for high dielectric constants, hysteretic polarization behavior, and pyroelectric, electromechanical, or electro-optic properties. In this article, the potential uses of ferroelectric films, the structure and properties of ferroelectrics, the deposition methods for films, the properties of ferroelectric films on silicon, and the cur-

rent status of research around the world are reviewed.

1. NEEDS FOR FERROELECTRIC FILMS ON SILICON

1.1 DRAM Applications

One crucial need for next-generation high-density memory circuits is the development of high-dielectric-constant, low-leakage films that are compatible with silicon circuitry for ultracompact charge storage. Until recently, the standard capacitors used in integrated circuitry were either SiO₂ or silicon oxynitride thin films. However, the dielectric constants of both of these materials are quite

low ($\epsilon_r \sim 4$ and ~ 9 , respectively). Thus, as the linewidths of active devices have decreased, it has been hard to achieve a comparable reduction in capacitor size, even through the use of extremely thin layers or trench geometries. The situation is particularly severe in dynamic random-access memories (DRAM). Consequently, it is becoming imperative to integrate higher-dielectric-constant materials with Si circuitry. As a first attempt at this, several companies have switched to Ta_2O_5 ($\epsilon_r \sim 18$ –25), but for extremely high integration levels, an even higher dielectric constant will eventually be required. For this purpose, considerable research is now being directed at development of low-loss paraelectric thin films.

1.2 FRAM Applications

The possibility of developing a high-density nonvolatile ferroelectric random-access memory (FRAM), in which the polarization state of the ferroelectric thin film is used to store information, has been one of the major drivers for the explosion of effort in ferroelectric thin films. Because intrinsically the switching in ferroelectric films is extremely fast (<100 ps) (Larsen, 1995), a ferroelectric-based memory might ultimately challenge existing technologies for computer applications. In the short term, however, FRAMs are becoming competitive with other nonvolatile information storage systems on silicon such as EEPROM (electrically erasable programmable read-only memory). Potential large-volume markets include the information storage systems on "smart cards."

1.3 IR Thermal Imaging

In ferroelectric crystals and films the strong temperature dependence of the spontaneous electric polarization leads to the possibility of very strong pyroelectric effects, as the pyroelectric coefficient p is defined by

$$p = \frac{\partial P_s}{\partial T}, \quad (1)$$

where P_s is the polarization and T is the temperature.

For a thin sheet of crystal or ceramic, poled normal to the sheet and blackened on

one surface, absorbed long-wavelength infrared radiation will change the temperature, and the pyroelectric current may be used to monitor the radiation level. Such current-mode detectors can be very fast and are usable as power meters for pulsed CO_2 lasers working at $10 \mu\text{m}$. If the radiation is chopped at a frequency $\omega \sim 30$ Hz, and the element is thin and very well thermally isolated, the thermal sensitivity is given by

$$\frac{\Delta T}{W} = \frac{\eta}{(g^2 + \omega^2 c^2 t^2)^{1/2}}, \quad (2)$$

where ΔT is the temperature rise for incident IR energy W , a fraction η of which is absorbed by the detector chip; g is the effective thermal conductance to the environment; c is the volume specific heat; and t is the detector thickness. For high sensitivity the cardinal importance of low g and very small t for any given frame frequency ω is clearly apparent.

In isolated point detectors it is easy to provide excellent thermal isolation by mounting the element on an ultrathin polymer "drum head," and very inexpensive, high-sensitivity thermal IR detectors made from a wide range of ferroelectric materials are commonly used in industry.

For imaging, where the individual element is down to a pixel size of $\sim 25 \mu\text{m}$, the conflicting requirements of electrical interconnection and refined thermal isolation provide challenging problems. Present systems use hybrid technology in which the detector plane is a very thin sheet of poled ferroelectric ceramic, bump bonded to the silicon integrated interrogation circuit. With an $f1$ lens system, such imaging systems give resolution of 0.07 K in the object plane (Kulwicki *et al.*, 1992).

Currently, there is a strong push to move to integrated systems using microelectromechanical technology to form air-bridge or diaphragm thermal isolation on the silicon chip itself (Shorrocks *et al.*, 1995; Kohli *et al.*, 1995; Watton, 1994). Major problems concern the conflicting processing needs of ferroelectric films and silicon microcircuits, but the prize would be a system that could be fitted in automobiles to provide drivers with useful night vision.

1.4 Mechanics

Piezoelectricity and electrostriction entail a coupling between electrical and mechanical energy in materials. That is, if a stress is applied to the material, it responds with an electrical polarization. Conversely, if an electric field is applied, the material undergoes a strain. Piezoelectric materials find widespread use in both sensor and actuator applications. A significant research effort is now being directed toward miniaturization of piezoelectric devices for microelectromechanical systems (MEMS). For these applications, the capability of processing thin-film piezoelectrics such as $\text{Pb}(\text{Zr}_{1-x}\text{Ti}_x)\text{O}_3$ (PZT) on platinum-coated silicon allows for the integration of the active sensing or actuator elements directly with on-chip driving or receiving electronics (including all of the necessary amplification). This can significantly increase the sensitivity of devices such as microphones and hydrophone detectors (Kim, 1990; Kim and Muller, 1987). From the standpoint of actuation, it is clear that as devices are miniaturized, piezoelectric devices permit comparatively higher energy densities, compared to other means of generating displacement. Thus, as active elements are integrated, electromechanical devices become progressively more attractive.

1.5 Packaging

Ferroelectrics are widely used as high-volumetric-efficiency capacitors in the bulk form. Thus, it is not surprising that there is interest in developing thin-film ferroelectrics as decoupling capacitors for integrated-circuit applications (Schwartz *et al.*, 1994). In particular, in some applications it is possible to replace chip capacitors with higher-density thin-film integrated capacitors in order to decrease circuit noise. For example, Matsushita has reported use of $\text{Ba}_{1-x}\text{Sr}_x\text{TiO}_3$ films in GaAs MMICs for portable telephones and in conjunction with CCDs for VCRs and camcorders (Shimada *et al.*, 1995). Required properties for films used in these applications are a high dielectric constant at the use frequency, a low dielectric loss, and a high resistivity.

1.6 Microchemistry

A specialized area of MEMS that is receiving rapidly increasing interest is that associated with chemistry and biochemistry on a chip. For a number of important liquid-phase chemical reactions, there are accessible regions of the boundary conditions where the reactions can become unstable and uncontrollable. By splitting the reactants into very small reaction chambers that can be replicated by inexpensive semiconductor technology and where sensing and control circuits may be on the same chip, control time constants are drastically shortened ensuring better control, but even in the extreme case of a "runaway," the volumes involved ensure that the result is not catastrophic (Jensen, 1996).

For many biological problems it is essential to work with microliter volumes and below, so that the micropumps and microvalves accessible in MEMS become essential components. DNA sequencing by electrophoretic capillary separation is just one example where widespread use in the criminal justice system is pressing toward massive markets (Sonnenschein, 1996).

In the microchemical-biochemical systems the piezoelectric/electrostrictive components are primarily for mechanical actuation (pumps and valves), pressure flow, and temperature sensing.

2. FERROELECTRIC MATERIAL SYSTEMS

2.1 Properties of Bulk Materials

Ferroelectricity is a property of crystals; there are no ferroelectric glasses or liquids. The appearance of a polarization vector in a crystal will certainly modify the point symmetry and create a new phase. If the resulting phase is to be ferroelectric, there must be more than one equivalent equilibrium orientation for the polar vector, and it must be switchable between states by a realizable electric field.

The electrical consequence of the reorientable spontaneous electric polarization is the appearance of dielectric hysteresis in the relation between dielectric polarization and applied electric field at higher field levels

(Fig. 1). This behavior is strongly reminiscent of the ferromagnetic hysteresis between intensity of magnetization and magnetic field and led to the adoption of the name ferroelectric for these materials. From the hysteresis loop, the terms remanent polarization and coercive field are defined (Fig. 1) also by analogy with the magnetic systems. As with magnets, many ferroelectrics exhibit a phase change to a nonferroelectric (paraelectric) form at higher temperature, and the transition point is defined as the Curie temperature (T_c). Similarly above T_c one of the diagonal elements of the permittivity tensor often follows a Curie-Weiss relation of the form

$$\epsilon_{ii} = c/(T - \theta), \quad (3)$$

where θ is the Curie-Weiss temperature. However, in the dielectric case, the Curie constant c is 5 to 7 orders of magnitude larger than in the corresponding magnetic case, indicating the much "softer" ordering (weaker interaction) in the ferroelectric and leading to very high values of dielectric permittivity in the paraelectric phase above T_c . Also, unlike magnetism, the remanent polarization of a ferroelectric does not give rise to a strong permanent electric field in the sur-

rounding medium, as the bound dipolar charge at the surface is always eventually compensated by the free charges that are available in the electrical case.

2.2 Symmetry Considerations

All point symmetries other than 1, which has no symmetry to lose, may be prototypic (paraelectric) phases out of which ferroelectric species may occur. A complete cataloging of all possibilities has been given by Shuvalov (1970) and Aizu (1969), and compact notations have been presented for describing the state shifts. The tabulation for the cubic point groups is given in Table 1, adapted from Shuvalov. Taking, for example, one of the common species from point group $m3m$, the symbol

$$m3m (3) D4F 4mm \quad (4)$$

means that prototype $m3m$ has a ferroelectric state (F) that will have three (3) equivalent orientations (six vector directions) which are definite (D) along the fourfold axis (4) giving rise to six domain states, each in tetragonal point symmetry $4mm$.

A consequence of the general symmetry

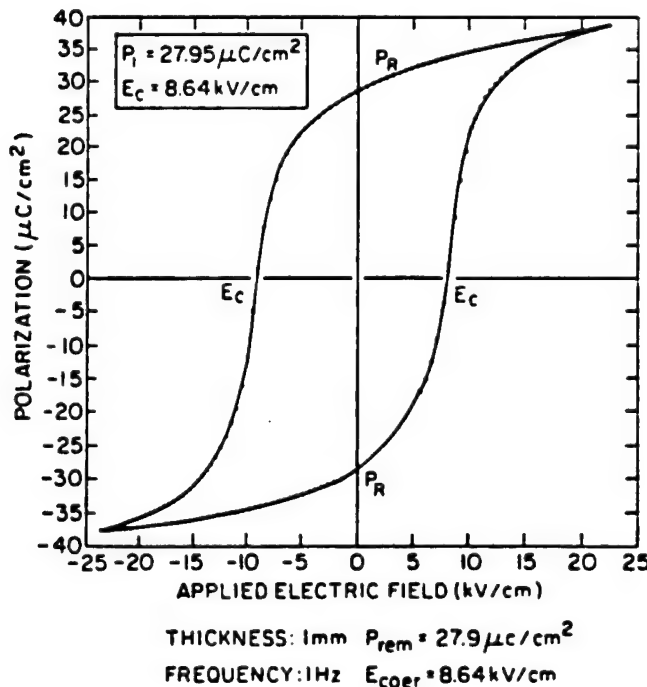


FIG. 1. Typical hysteresis between electric polarization and electric field in a ferroelectric material in its ferroelectric phase. P_R , remanent polarization. E_c , coercive field.

Table 1. Ferroelectric phases accessible from cubic point symmetries, showing the orientations and symmetries of resulting ferroelectric species.

Kind of transition—kind of ferroelectric phase	Corresponding simple form of initial phase	Order of transition
$m3m$ (3) $D4F$ $4mm$	Hexahedron (cube)	II
$m3m$ (4) $D3F$ $3mm$	Octahedron	II
$m3m$ (6) $D2F$ $mm2$	Rhombic dodecahedron	I
$m3m$ (12) $A4F$ m	Tetrahexahedron	I
$m3m$ (12) $A*2F$ m	Trigonal trioctahedron	I
$m3m$ (12) $A**2F$ m	Tetragonal trioctahedron	I
$m3m$ (24) $A1F$ 1	Hexoctahedron	I
$\bar{4}3m$ (3) $D\bar{4}F$ $mm2$	Hexahedron (cube)	I
$\bar{4}3m$ (4/2) $D3F$ $3m$	Tetrahedron	I
$\bar{4}3m$ (12/2) $A*mF$ m	Tetragonal tritetrahedron	I
$\bar{4}3m$ (12/2) $A**mF$ m	Trigonal tritetrahedron	I
$\bar{4}3m$ (24/2) $A1F$ 1	Hexatetrahedron	I
432 (3) $D4F$ 4	Hexahedron (cube)	II
432 (4) $D3F$ 3	Octahedron	II
432 (6) $D2F$ 2	Rhombic dodecahedron	I
432 (24/2) $A1F$ 1	Pentagonal trioctahedron	I
$m3$ (3) DmF $mm2$	Hexahedron (cube)	II
$m3$ (4) $D3F$ 3	Octahedron	II
$m3$ (6) AmF m	Pentagonal dodecahedron	I
$m3$ (12) $A1F$ 1	Didodecahedron	I
23 (2) $D2F$ 2	Hexahedron (cube)	I
23 (4/2) $D3F$ 3	Tetrahedron	I
23 (12/2) $A1F$ 1	Pentagonal tritetrahedron	I

arguments was the realization that there could be ferroelectric species in which the polar vector is reorientable but not reversible. An example is in the cubic group $\bar{4}3m$, i.e., $\bar{4}3m$ (12/2) AmF m . Again $\bar{4}3m$ is the prototype group. In the ferroelectric species there are 12 vector directions for ferroelectric polarization; (12/2) indicates that the orientation is redirectable but not reversible; A indicates arbitrary, but in the plane of the mirror (m), and the ferroelectric phase has monoclinic (m) symmetry.

In Shuvalov's table the corresponding simple form is the solid surface that would be formed by the normals to the full family of polar directions. In the "nature of the phase change" column, Roman II indicates that the Curie transition may be either first or second order thermodynamically, Roman I indicates that the change must be first order (discontinuous). The small symbols at the end of the letter descriptors indicate whether the sublattices in the different domain states are parallel (||) or canted.

It should be stressed that the symmetry

classification is a tabulation of the possible; i.e., all actual ferroelectrics of any symmetry must fall within this grouping. However, whether any structure of a given symmetry is actually prototypic depends on details of its atomic architecture, which are not controlled by the crystal symmetry.

2.3 Domains and Polarization Switching

Only simple proper ferroelectrics from centric prototype (paraelectric) symmetries have so far been applied to thin films, and discussion of domains and switching is confined to such crystals. In these proper ferroelectrics, the appearance of polarization leads to significant shape change driven through the phenomenon of electrostriction; i.e., the strain induced from the prototype $x_{ij(s)}$ is given by

$$x_{ij(s)} = Q_{klij} P_{k(s)} P_{l(s)}, \quad (5)$$

where Q_{klij} are the symmetry-permitted electrostriction constants and $P_{k(s)} P_{l(s)}$ are com-

ponents of the spontaneous polarization vector in the ferroelectric domain. Einstein summation convention is assumed, and the expression is expanded for repeated subscripts to get the full family of equations.

Clearly for these centric prototypes, domain inversion will not change the shape; however, for non-180° changes, the domains are strain distinct, and acceptable planes joining such domains (domain walls) will be regulated by elastic as well as electric boundary conditions. The spontaneous strains $x_{ij(s)}$ are quite large, of the order of 1% in BaTiO₃ and from 2% to 6% in tetragonal PZTs, so that the elastic constraints are strong. A tabulation of strain-preferred walls has been given by Fousek and Janovec (1969).

For BaTiO₃ and PZT the phenomenological Gibbs free energy is known, and it is possible to calculate the field level required for intrinsic coherent polarization switching within the single domain. Such calculations yield values orders of magnitude larger than the observed coercive field. Thus it is generally agreed that in bulk crystals the switching is incoherent and occurs by the motion of domain walls.

For BaTiO₃ 180° switching has been extensively studied and has shown to be by nucleation and growth of new domains, preferentially against existing walls, and not by a true sidewise motion of the wall. The presence of non-180° walls in general appears to raise the effective coercive field, but shape-changing ferroelastic switching has been much less studied.

In the randomly axed polycrystal both 180° and ferroelastic shape-changing switching must be involved, and the process varies widely between different systems. For BaTiO₃ less than 30% of the single-domain spontaneous polarization is remnant, and the response is a strong function of grain size. For PZT compositions close to the morphotropic phase boundary at the 52:48 Zr:Ti ratios, good "square loop" switching is observed. From elementary electrostatic considerations, Arlt (1996) has shown recently that grain-by-grain switching in a ceramic is impossible and that the switching nucleus must be a larger entity. Given the fact that thin films often have appreciably different grain sizes and stress states than are characteristic of bulk ceramics, it is possible that the

switching process in films will differ markedly from that observed in bulk materials.

2.4 Transport Properties

Comprehensive reviews of the electrical conduction mechanisms in ferroelectric materials have been given by Smyth (1994) and Waser (1994). As has been described there, the principal charge carriers in the perovskite oxides are electrons, holes, and oxygen vacancies. In most of the perovskites, nominally undoped materials contain an excess of acceptors from lower-valent impurities, and so act as acceptor-doped compounds. This is especially true for the lead-based materials, where lead vacancies also act as acceptor sites. These materials are insulating at room temperature on account of the existence of hole traps (Warren *et al.*, 1994). It is important to note, though, that either variations in the film stoichiometry or preparing films without sufficient oxygen present changes the defect chemistry and can lead to unacceptably high conductivity levels.

Upon application of a dc voltage to a ferroelectric capacitor, the capacitor passes a polarization current. Eventually, this transient dies away, and the current decays to the value determined by the leakage through the capacitor. At still longer times, if the applied dc field is high enough, the sample may undergo resistivity degradation and ultimately time-dependent dielectric breakdown (TDDB) (Chen *et al.*, 1994).

As has been shown by Waser and co-workers, the current initially follows the Curie-Von Schweidler law (Waser and Klee, 1992):

$$J \propto t^{-m}, \quad (6)$$

where J is the current density, t is time, and m is approximately 0.5 (actually 0.4 to 1) (Dietz and Waser, 1995). It then flattens out as the true leakage value is reached. It is important to note that the transition to the steady-state current can be quite slow ($>10^3$ s) (Chen *et al.*, 1994). Techniques for measuring this properly have been described by Dietz and Waser (1995). In particular, it has been demonstrated that stepped changes in the applied voltage (with appropriately long wait times between steps), where both charging and discharging currents are measured,

are preferable to ramped voltage experiments in determining the true leakage currents. This is especially true at low temperatures (i.e., 25 °C).

2.5 Perovskite-Structure Systems

The simple cubic perovskite ABO_3 structure is the prototype structure for many useful ferroelectric materials. Fundamentally, it consists of large 12-coordinated cations such as Na, K, Rb, Ca, Sr, Ba, Pb, etc. at the corners of a unit cell, with a smaller cation such as Ti, Sn, Zr, Nb, Ta, or W at the unit cell center octahedrally coordinated to the anions at the face centers (see Fig. 2). These octahedral units form a three-dimensional array via corner linking. The resulting structure has a high symmetry (the point group symmetry is $m\bar{3}m$). This high symmetry is extremely useful, as it implies that when the material distorts to form a ferroelectric phase, there are many equivalent differently oriented domain state polarization directions. As a result, it is possible in the randomly axed polycrystal to thread the polarization vector through the structure without major discontinuities. Consequently, large remanent polarizations can be developed, as well as substantial piezoelectric and electro-optic coefficients.

Among the technologically important materials possessing this crystal structure are the solid solutions $BaTiO_3$: $SrTiO_3$ (BST), $PbZrO_3$: $PbTiO_3$ (PZT), and $KTaO_3$: $KNbO_3$

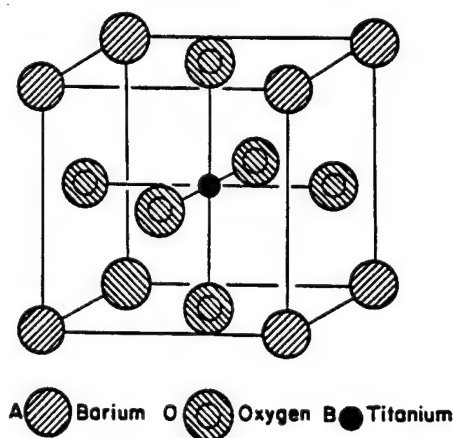


FIG. 2. Cubic form of the perovskite structure using barium titanate as a typical example.

(KTN). $BaTiO_3$ itself shows three ferroelectric phases as a function of temperature. At temperatures above ~ 135 °C, the octahedra are undistorted, and the material possesses symmetry group $m\bar{3}m$. On cooling through the Curie point, however, the Ti^{4+} ion displaces closer to one of the adjacent oxygen along the $[001]$ direction. This results in an elongation along the c axis, contraction along the a and b axes, and, most importantly, development of a spontaneous polarization along the ferroelectric c axis. This tetragonal structure is stable to ~ 5 °C, at which point the Ti^{4+} ion shifts again, along one of the $[110]$ directions of the original cubic unit cell. This leads to an orthorhombic structure with the polarization oriented along the direction of Ti^{4+} displacement. Finally, at ~ -90 °C, the TiO_6^{3-} octahedra distort again, with the Ti^{4+} ion (and hence P_s) displacing along one of the original $[111]$ directions. Each of these symmetry changes corresponds to a first-order displacive transition (see Fig. 3).

Associated with each of the transitions in $BaTiO_3$ is a maximum in the low-field dielectric permittivity as shown in Fig. 4. Fundamentally, each transition marks a temperature where two phases are similar in energy. On application of an electric field, then, the material can be distorted between the two different polytypes. This, in turn, leads to high polarizability near transition temperatures. The high dielectric permittivity even between phase transitions in ferroelectric $BaTiO_3$ is tied to the presence of the spontaneous polarization and to the existence of domain walls.

$BaTiO_3$ and $SrTiO_3$ form a complete substitutional solid solution in which the ferroelectric-paraelectric transition temperature of the compound decreases nearly linearly with Sr composition. As a result, it is possible to tailor the transition temperature as well as the dielectric properties. For DRAM applications, paraelectric BST compositions are being widely investigated because of the combination of relatively high dielectric permittivity with low dielectric loss.

The most important of the piezoelectric ceramics are found in the lead zirconate-lead titanate solid-solutions series. PZT shows a temperature-independent morphotropic phase boundary between tetragonally and rhombohedrally distorted ferroelectric

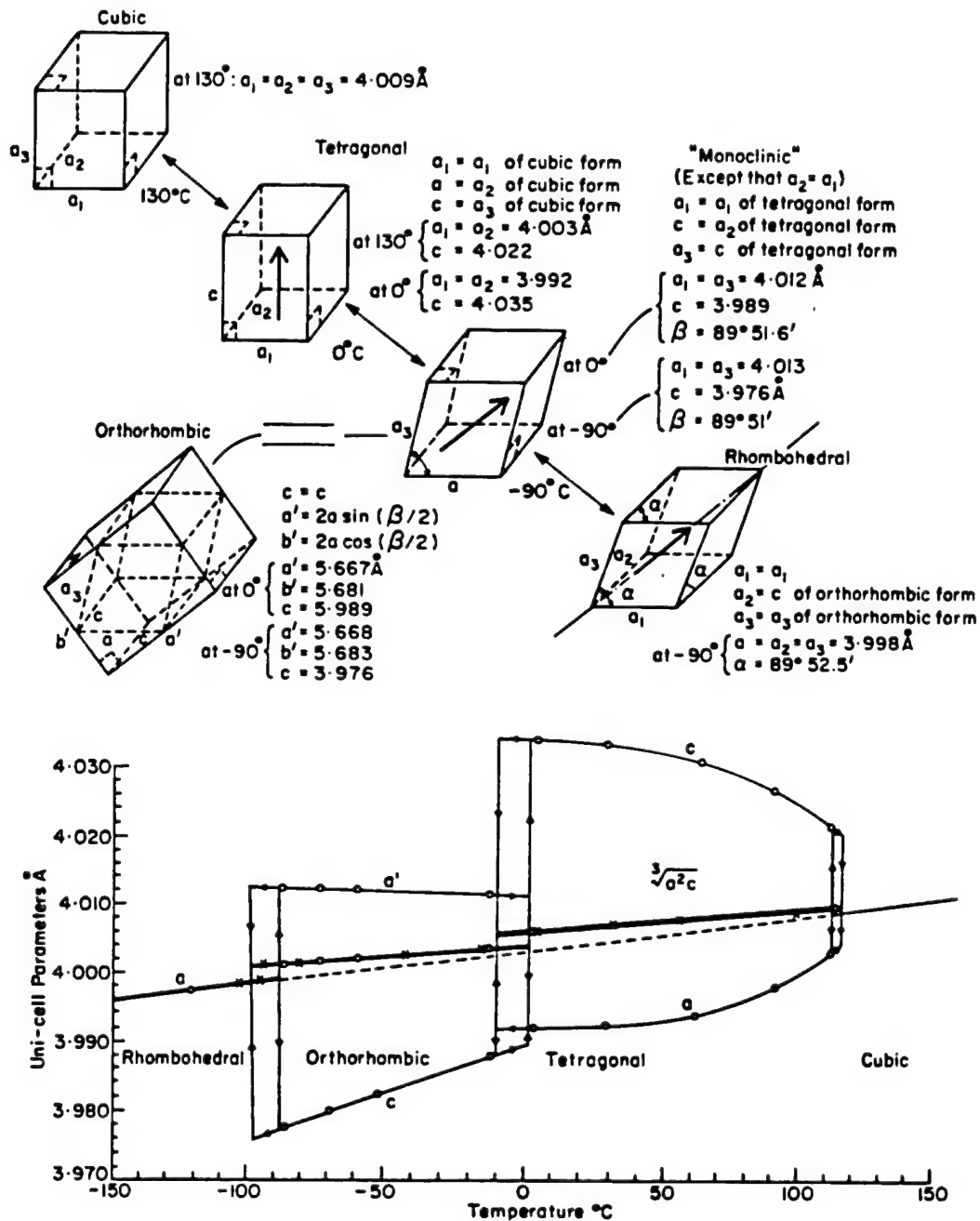


FIG. 3. Temperature dependence of the crystal structure, orientation of spontaneous polarization, and consequent electrostrictive strain in barium titanate.

phases at the Zr:Ti ratio of 52:48 as seen in Fig. 5. As a result of the large number of potential orientations for the spontaneous polarization, this material shows efficient poling and large enhancements in the dielectric

and piezoelectric properties at this composition.

Potassium niobate, KNbO_3 , is a monovalent/pentavalent analog of BaTiO_3 , in essentially the same perovskite structure. It goes

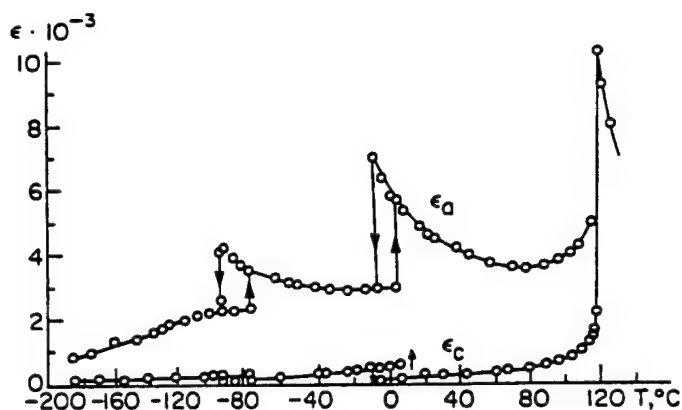


FIG. 4. Dielectric permittivity in weak electric field for a Remeika-grown α -grown single crystal of BaTiO_3 . Note that for temperatures below $\sim -90^\circ\text{C}$ the data reflect the anisotropic strain in these crystals and do not follow the symmetry of a perfect crystal.

through the same sequence of phase changes associated with the onset and reorientation of spontaneous electric polarization. In KNbO_3 , the Curie point is at 420°C , the tetragonal \rightleftharpoons orthorhombic transition is at 220°C , and the orthorhombic \rightleftharpoons rhombohedral phase change is at -10°C . Replacing Nb with Ta rapidly lowers T_c , and the sequence of change is similar to that induced in BaTiO_3 by Sr substitution.

At low concentration of Nb in KTaO_3 an

interesting new phenomenon occurs, associated with the formation of small droplets of polar phase within the high-K tantalate matrix leading to massive dielectric maxima ($K \sim 100\,000$) with strong relaxation character, behavior in many ways compatible to the relaxor ferroelectrics discussed in Sec. 2.4.

Sodium niobate, like lead zirconate, is antiferroelectric at room temperature, and as in lead zirconate, the antipolar state can be destabilized under high-electric-field switch-

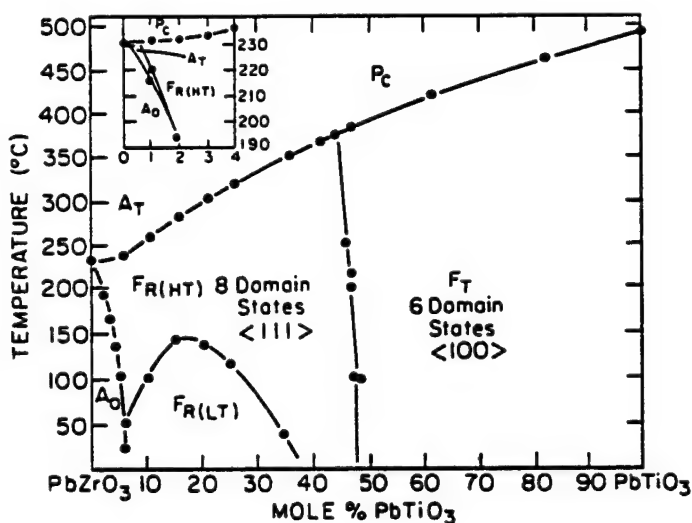


FIG. 5. Phase diagram for the $\text{PbZrO}_3\text{:PbTiO}_3$ solid-solution ferroelectric system. Note the almost vertical (morphotropic) phase boundary at the Zr/Ti 52/48 composition separating tetragonal and rhombohedral ferroelectric forms. P_c is the paraelectric prototypic cubic state. F_T is a tetragonal ferroelectric phase with six alternative domain states polarized along the $\langle 100 \rangle$ family of directions of the unit cube. F_R is a rhombohedral ferroelectric state with eight equivalent polar directions in its domain structure with polar vectors along equivalent $\langle 111 \rangle$ family of directions. The rhombohedral form has a simple high-temperature phase in which oxygen octahedra are in orthogonal array, and a low-temperature form in which the oxygen octahedra are slightly rotated about the $\langle 111 \rangle$ family of directions. A_0 is an orthorhombic antiferroelectric phase in which opposing polarizations occur on a unit cell scale.

Inset: An enlargement of the higher-temperature high-zirconate compositions showing the probable presence of a small insert of an antiferroelectric tetragonal phase (A_T).

ing to a strong ferroelectric form (Cross and Nicholson, 1955).

2.6 Bismuth Oxide Layer Structures

Particularly in the area of FRAMs, the family of bismuth oxide layer-structure ferroelectrics is also important. The bismuth

oxide layer structures are made up of sheets of perovskite-like corner-linked oxygen octahedra separated by $\text{Bi}_2\text{O}_2^{2+}$ layers (Fig. 6) (Dorrian *et al.*, 1971). The prototypic symmetry is $4/mmm$ with the $\text{Bi}_2\text{O}_2^{2+}$ sheets normal to the c axis interleaved by from one to five perovskite-like layers. In the bulk crys-

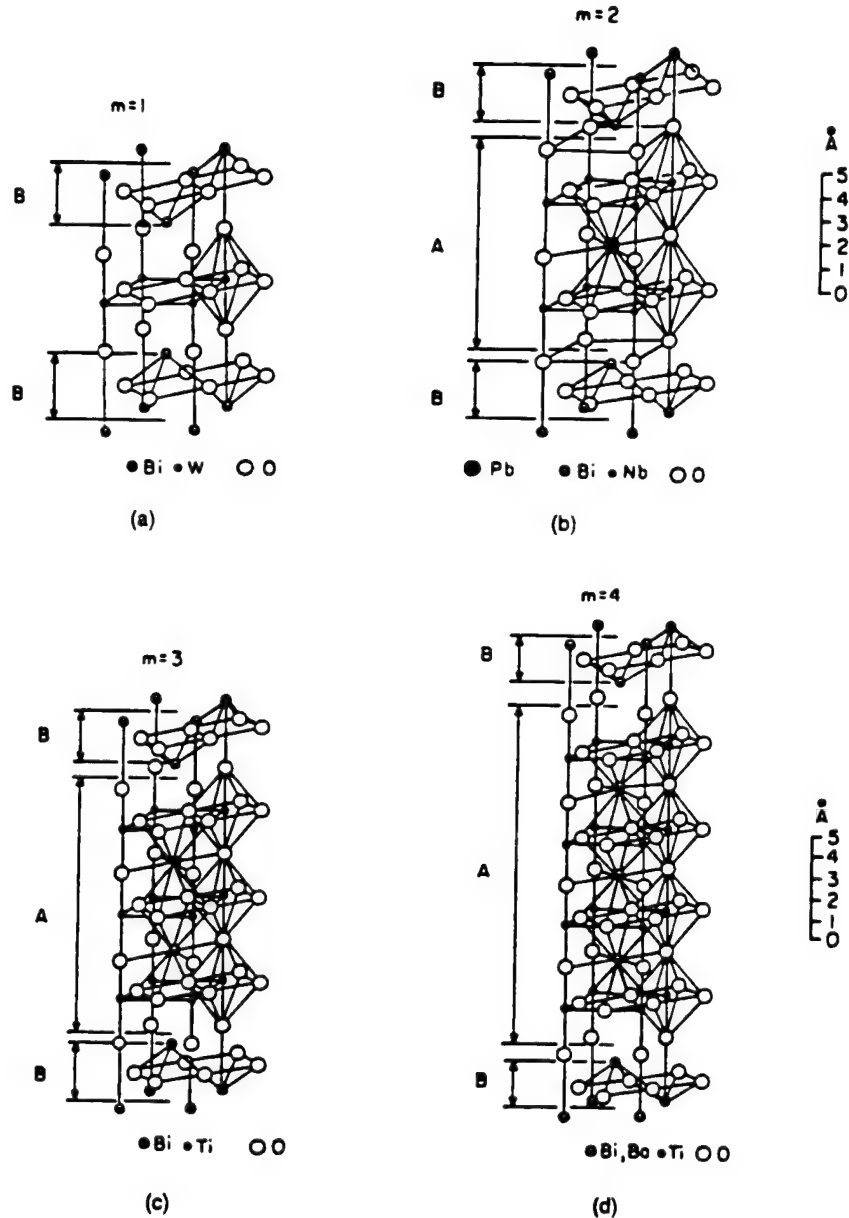


FIG. 6. Crystal structures for 1-, 2-, 3-, and 4-layer bismuth oxide layer-structure ferroelectrics. The figure shows one-half of the unit cell of (a) Bi_2WO_6 , (b) $\text{PbBi}_2\text{Nb}_2\text{O}_9$, (c) $\text{Bi}_4\text{Ti}_3\text{O}_{12}$, (d) $\text{BaBi}_4\text{Ti}_4\text{O}_{15}$ (after Aurivillius). "A" denotes perovskite-like layers; "B" denotes $(\text{Bi}_2\text{O}_2)^{2+}$ sheets.

tals there are major differences both in structure and in properties between compositions with odd (1,3,5) and even (2,4) numbers of interleaving perovskite layers. Even-layer structures retain a mirror normal to the fourfold axis in the ferroelectric phases so that the polarization vector is confined to the plane of the perovskite sheet (Newnham *et al.*, 1971), while in the one- and three-layer structures the mirror is lost, and in $\text{Bi}_4\text{Ti}_3\text{O}_{12}$ the polarization tilts out of the perovskite plane. Similarly, in properties odd-layer compounds have a single phase change on cooling, leading to a prominent dielectric anomaly. Two- and four-layer structures go through two phase changes, only one of which carries the major dielectric anomaly (Diaz-Colon, 1973).

To date, the best studied thin films have been in the $\text{Bi}_4\text{Ti}_3\text{O}_{12}$ and $\text{SrBi}_2\text{Ta}_2\text{O}_9$ compositions. The latter is particularly important, as it appears that when fabricated with simple platinum electrodes it shows lower coercivity and much lower fatigue on repeated cycling than comparable PZT films. It is difficult to see why a randomly axed polycrystal film made up from crystallites with only four in-plane domain states should have low coercivity and quite high remanent polarization, and one suspects that the processing and consequent microstructure of the film may significantly modify the bulk symmetry and properties.

2.7 Alternative Systems

In addition to these compounds there are alternative normal ferroelectric systems that are, for the most part, somewhat less well studied in thin-film form. Examples include LiNbO_3 and its tantalate analog, the tungsten bronze systems, and some of the improper ferroelectrics. LiNbO_3 is widely used as a bulk single crystal for nonlinear optical applications and as a high-temperature piezoelectric (its ferroelectric transition temperature $T_c \approx 1200^\circ\text{C}$). Thin films are amenable to wave-guiding applications and so have been pursued for optical switches and second-harmonic-generation applications. In thin films, as in bulk crystal growth, maintaining the correct stoichiometry is problematic. The tungsten bronze family of ferroelectrics is based on a relatively complex crystal structure in which oxygen octahedra are the

primary structural units (Lines and Glass, 1977). The multiple possibilities for cation disordering in these compounds, coupled with the large solid-solution regions, lead to widely tailorable dielectric, electro-optic, and electromechanical properties. Epitaxial $\text{Sr}_{5-x}\text{Ba}_x\text{Nb}_{10}\text{O}_{30}$ (SBN) films have been grown on single-crystal substrates with different Sr:Ba ratios (Trivedi *et al.*, 1996). Among improper ferroelectrics such as $\text{Gd}_2(\text{MoO}_4)_3$, the primary order parameter is not the polarization, so that the ferroelectricity is a secondary consequence of a zone-boundary structural mode (Dvorak, 1971). A study of thin films of this material might be rather useful, given the strong effect that the elastic clamping of the film to the substrate is expected to have on the properties of most ferroelectrics. In $\text{Gd}_2(\text{MoO}_4)_3$, where the elastic effects should be much more important than the electrical boundary conditions, it may be easier to isolate the importance of the film stress state.

There are ferroelectric polymers of which the odd-number nylons and polyvinylidene difluoride (PVDF) are much the most widely researched. PVDF and its copolymer with polytetrafluoroethylene (PTFE) is commercially produced in thick film sheet ($\tau > 10\ \mu\text{m}$) and finds useful piezoelectric and pyroelectric application. The material is in fact a composite between a ferroelectric crystalline form and a flexible amorphous component. The polarization levels are more than an order of magnitude less than in PZTs, but the permittivity is also low so that voltage coefficients of piezoelectric and pyroelectric response are quite attractive for large-area, low-frequency sensors.

There are also large families of ferroelectric liquid crystals, which find major application in display technologies. Since, however, they are liquids, they take the form of the containment vessel and have not been widely explored in thin-film form.

2.8 Relaxor Ferroelectric Systems

In contrast to normal ferroelectrics, relaxor ferroelectrics demonstrate a diffuse phase transition and dispersion in the low-frequency dielectric properties. The broad temperature response, in conjunction with the high dielectric constants that can be achieved in bulk ceramics, make such mate-

materials attractive as relatively temperature-stable high-volume-efficiency capacitors. To date, thin films based on relaxor ferroelectric compositions such as lead magnesium niobate (PMN) or lead scandium tantalate (PST) show lower dielectric constants than do bulk materials, though they are still clearly high enough to warrant investigation as alternative capacitor compositions. Additional areas where thin-film relaxor ferroelectrics would be attractive include pyroelectric sensors and actuators based on either electrostrictive or biased piezoelectric response. Among the compositions available, solid solutions based on the PMN-PbTiO₃ and PST-PbTiO₃ systems look particularly good.

3. FERROELECTRIC FILM PREPARATION

3.1 Boundary Conditions for Films on Silicon

Most of the interesting ferroelectrics for integration on silicon come from the perovskite and the layered perovskite families. Unfortunately, in most cases when deposited directly on silicon, these materials react at the temperatures required for processing crystalline films. The lead-based compounds, in particular, form a lead silicate glass phase when processed directly on silicon or SiO₂, which leaches lead from the ferroelectric and acts as a low-dielectric-constant barrier layer between the ferroelectric and the semiconductor. As a result, reaction-blocking chemical barrier layers between the ferroelectric and the Si are required. Development of appropriate barrier-layer and electrode schemes is currently an area of intense research. This is particularly important in memory elements where the device capacitor is placed directly over the contact plug (often poly-Si). For such a geometry, a barrier layer is required to prevent the plug material from oxidizing or reacting with the dielectric during the capacitor processing.

There are also processing temperature restrictions that must be considered in integrating ferroelectric elements with Si-based semiconductor circuitry. All of the interesting ferroelectrics are multiple-cation compositions. While this is not inherently a limitation, the fact that many of the interesting

compositions contain at least one volatile component, either Pb or Bi, limits the upper temperature to which the film can be exposed before appreciable changes in the film chemistry occur. As a result, the ferroelectric elements are typically introduced into the semiconductor after the majority of the CMOS processing has been completed. This, in turn, places restrictions on the temperature excursions allowed during the ferroelectric film processing, so that the silicon circuitry itself is not affected. This time-temperature limitation is expected to become progressively more restrictive as linewidths in the circuitry continue to fall. In order to minimize the thermal budget associated with the preparation of the ferroelectric element, rapid thermal processing (RTP) is preferred over conventional annealing for *ex situ* crystallized films. For films deposited at elevated temperatures so that they can be prepared in the desired crystalline form, routes that lower the deposition temperature are particularly attractive.

An additional parameter that must be considered, particularly for thick-film deposition, is the thermal expansion coefficient mismatch between the ferroelectric and the substrate. Since the thermal expansion coefficient of PZT does not match that of the underlying Si substrate, appreciable stresses develop during cooling from typical processing temperatures of 650 to 750 °C. Thus, particularly in thick films, the resulting stresses are large enough to cause film cracking and delamination. While this is unlikely to be a serious limitation in capacitor applications, for piezoelectric devices where large electrically induced displacements are required, larger thicknesses are necessary.

Some of the most important issues to be resolved in integrating ferroelectric (or paraelectric) capacitors into silicon-based circuitry are

1. development of appropriate electrode materials,
2. development of IC-compatible processing (including conformal coverage of non-planar surfaces as well as all of the necessary etch chemistries), and
3. maintaining the required electrical properties through all of the processing steps required to form the device.

To date, the most important electrodes

have been Ti/Pt and RuO₂. Both retain good conductivity after firing in an oxidizing atmosphere at the temperatures required for crystallization of the capacitor. They do, however, suffer from problems. Pt, in particular, frequently undergoes significant stress relief during heating (which is often accompanied by hillocking) (Bruchhaus *et al.*, 1992) along with the migration of O and Ti through the Pt layer. PZT films electroded with Pt show much higher levels of fatigue than the same films on RuO₂. In addition, no good dry-etch chemistry has been developed for Pt. RuO₂, on the other hand, leads to improved fatigue behavior but degraded leakage current values in PZT. It also has a lower conductivity than Pt, which can lead to degradation in the high-frequency response of ferroelectric capacitors. Moreover, many of the volatile Ru compounds are toxic. Additional electrode materials that have been investigated include Pd, Ir, IrO₂, SrRuO₃, CaRuO₃, La_{0.5}Sr_{0.5}CoO₃, YBa₂Cu₃O_{7-x}, and TiN.

From an equipment standpoint, since the high volatility of Pb leads to appreciable diffusion during annealing steps, it will be necessary to develop secondary, contaminated, processing lines for the ferroelectric film processing in order to avoid contaminating the CMOS fabrication equipment. This is a significant additional expense.

3.2 Deposition Methods

There are a wide variety of deposition methods that have been used to prepare ferroelectric thin films, including chemical methods such as sol-gel or metal-organic decomposition (MOD), sputtering, laser ablation, metal-organic chemical-vapor deposition (MOCVD), reactive evaporation, molecular-beam epitaxy (MBE), and liquid-phase epitaxy. Factors that may dictate the techniques chosen for a specific composition and application include

- availability of appropriate precursors,
- uniformity of coverage,
- particulate generation,
- ease of composition control,
- growth temperature limitations,
- desired residual stress level,
- required thickness and deposition rate,
- step coverage, and

- compatibility with additional processing (especially semiconductor processing).

Since the literature is by now extensive enough that it is not possible to give a comprehensive review of each of the techniques, a short review is given in the following section. More complete descriptions are contained elsewhere (Myers and Kingon, 1991; Kingon *et al.*, 1992; Myers *et al.*, 1993; Tuttle *et al.*, 1994; Desu *et al.*, 1995). It is important that all of the methods described can be used to produce high-quality films, once problems associated with film composition and film microstructure are overcome.

3.3 Vapor-Phase Techniques

There are a host of vapor-phase techniques for preparing ferroelectric films, which differ primarily in the method for generating the vapor phase. Multiple texts are available that discuss the equipment requirements and deposition mechanisms for these methods. One factor that distinguishes vapor-phase production of ferroelectric films from deposition of other materials is the fact that most ferroelectrics are multiple-cation compounds that show large degradation in properties when made nonstoichiometric. This is especially problematic because many of the useful ferroelectric compounds contain cations with vastly different sputtering yields and vapor pressures (especially Bi and Pb relative to Ti, Zr, or Ta.). Consequently, in many of the vapor-phase deposition techniques, maintenance of the film composition is nontrivial. Of the vapor-phase techniques, Table 2 summarizes the advantages and disadvantages associated with each.

3.4 Liquid-Phase Techniques

Both sol-gel and MOD techniques rely on introducing an organometallic precursor into an appropriate solvent system. This liquid is then either spun, misted, sprayed, or dip-coated onto the substrate. Following solvent evaporation, the organic phase must be removed through a pyrolysis step and the film crystallized. While good results have been obtained with furnace annealing, a consensus is developing that RTP is preferable for integrated applications, given the vastly lower thermal budget. In principle, the stoi-

Table 2. Advantages and disadvantages of vapor-phase thin-film deposition techniques.

Method	Advantages	Disadvantages
Magnetron sputtering	High deposition rate possible. IC-compatible. Good compositional flexibility.	Target chemistry changes in reactive gas environment. Preferential sputtering/resputtering of multicomponent materials.
Ion-beam sputtering	Independent control of ion current density and ion energy. Atom/ion arrival ratios controllable.	Low deposition rates.
Laser ablation	Good target/film compositional fidelity.	Boulder production. Poor thickness uniformity.
MOCVD	High deposition rate. Excellent step coverage. Large area coverage possible.	Appropriate precursors required. Precursor toxicity.
MBE	High deposition rate possible. Layer-by-layer control.	Low throughput. Low coverage areas.

chiometry of the resulting film should be identical to that of the initial solution. It is clear, however, that compositional heterogeneities can arise during gelation, pyrolysis, or crystallization, any of which may lead to some segregation of cations from an originally homogeneous precursor. Procedures for solution preparation of high-quality lead zirconate titanate, as well as other perovskite films, are well documented for a variety of solvent-precursor systems (Tuttle and Schwartz, 1996). Similarly, several reports on the deposition of $\text{Sr}_2\text{BiTa}_2\text{O}_9$ films from solution precursors are available (Huffman, 1995). Some of the significant advantages of the sol-gel techniques are good compositional tailorability, even in multiple-cation systems, large area coverage, and the capability of building up films several microns thick (Chen *et al.*, 1996). In terms of integrated ferroelectric films, sol-gel materials have been used for most of the published work on MEMS. Debits include the fact that the liquid-phase techniques do not permit conformal coverage, and they are not compatible with high-density integrated-circuit processing.

4. CHARACTERIZATION OF FILM MICROSTRUCTURE

4.1 Introduction

Demonstration of good crystallinity in thin films is not, in and of itself, a guarantee of acceptable film properties. Equally impor-

tant are the microstructure and the defect structure of the films. The role of defect structure has been discussed already. In this section, the use of microstructural characterization as an essential complement to structural and electrical characterization is described. Numerous articles describing microstructure-property relations in ferroelectric films are available in the literature (Tuttle *et al.*, 1995; Barlingay and Dey, 1992; Reaney *et al.*, 1994). Given the wide variety of data available, only generic features are covered here.

4.2 Direct Methods

Key microstructural features that can significantly affect the electrical properties include grain size, crystallite orientation, phase purity, density, and, in some cases, the depth profile of each of these parameters. In particular, the importance of phase purity and crystallographic orientation have been well described in numerous texts (Jaffe *et al.*, 1971; Herbert, 1985). Structure-sensitive probes such as x-ray diffraction and selected-area diffraction can be used to determine the phase content and to investigate the global and local crystallographic orientation, respectively. However, x-ray diffraction measurements alone are not a conclusive demonstration of single-phase films. Especially in the lead- and bismuth-based compounds, second phases can be present to levels as high as 15% before they appear in most x-ray patterns. High-resolution SEM, or TEM, particularly in conjunction with local

composition probes, can be used to identify second phases such as PbO-rich pockets, or pyrochlore surface layers in PbTiO_3 and PZT films (Tuttle *et al.*, 1996; Reaney *et al.*, 1994; Fox *et al.*, 1992). Similarly, second-phase porosity can often be identified. Such microscopy studies have been instrumental in identifying the nucleation and growth processes in ferroelectric films. Similar studies are now coming out on the compound $\text{SrBi}_2\text{Ta}_2\text{O}_9$ (Scott *et al.*, 1996).

In interpreting the film properties, a knowledge of the grain size is also important. Electron microscopy and, to a lesser extent, atomic-force microscopy (AFM) can be utilized to determine the film microstructure, including the primary grain size, directly. In general, it cannot be assumed that grains in thin films are isometric, and so measurement in cross section is required. It is also important to note that lower-resolution SEM studies often identify cluster boundaries, which may be considerably larger than the primary grain size in the material.

TEM analysis also permits investigation of the domain structure in films. Several studies have demonstrated that PZT thin films tend to show relatively high domain densities, at least once the grains are above a certain size (Reaney *et al.*, 1994; Voight *et al.*, 1993). This is consistent with the observation in bulk PZT ceramics that the domain size drops with the grain size (Kim, 1994). It is not clear, however, that these twin walls are mobile in thin films (Tuttle and Schwartz, 1996; Troler-McKinstry *et al.*, 1995a). Consequently, it may not be possible to rely, in thin films, on the extrinsic contributions to the dielectric and piezoelectric properties that are available in bulk materials.

4.3 Optical Methods

Optical methods, including wave-guiding experiments (Potter *et al.*, 1993), light scattering (Sinclair *et al.*, 1995), and spectroscopic ellipsometry (Troler-McKinstry *et al.*, 1993; Troler-McKinstry *et al.*, 1995b) can also be used to depth profile dielectric films nondestructively. These methods can be quite sensitive to small inhomogeneities in the density of the film through the film thickness. Such information is useful in electrical applications since introduction of a low-density (and hence low dielectric permittivity) layer

leads to an appreciable decrease in the effective dielectric constant, piezoelectric coefficient, and electro-optic coefficient of the film. For optical applications, such as wave guiding, identification and elimination of low-density layers is essential, as the associated refractive index discontinuities lead to unacceptable optical scattering (Fork *et al.*, 1996). Similarly, scattering centers such as rough surfaces, grain boundaries, and domain walls can significantly decrease the distance over which light can be guided. The importance of these factors is best determined by optical measurements, as a microstructure-based technique will not necessarily be a complete predictor of the scattering losses.

5. PROPERTIES OF FILMS ON SILICON

5.1 High-Permittivity Films (DRAMs)

In the area of memory applications, the drive to incorporate paraelectric materials is predicated on the need for dielectrics that permit development of gigabit memories. A good review of the requirements for memory dielectrics is given by Jones *et al.* (1995). For DRAM applications, information is kept by storing charge on a capacitor and periodically reading and resetting it (typically, around ten times per second). In such a configuration, it is imperative that the charge be retained without excessive leakage during a cycle time, and it must be large enough that α -particle events do not change the logic state. This necessitates a capacitor of at least 50–75 fF (Jones *et al.*, 1995).

Until this point, SiO_2 and $\text{SiO}_2/\text{Si}_3\text{N}_4$ have been used as the capacitor material. However, as memory density increases beyond 256 Mbit, it is difficult to achieve sufficient capacitance per element with these materials. Ta_2O_5 films, with their higher relative permittivity, permit higher densities and may be adequate for 1-Gbit DRAM. Considerable simplification of the capacitor structure would, however, be facilitated by materials of higher ϵ_r . Potential candidates include SrTiO_3 , $\text{Ba}_x\text{Sr}_{1-x}\text{TiO}_3$, or paraelectric La-doped PZT (Jones *et al.*, 1995).

The primary materials parameters that must be optimized for DRAM applications are a high storage density, a low leakage current, little resistance degradation, and sup-

pression of time-dependent dielectric breakdown (TDDB). Paraelectric compositions are preferred in these applications. Most dielectric films for DRAM applications show somewhat lower dielectric constants than their bulk counterparts, especially when prepared as layers <100 nm in thickness. However, several groups have demonstrated that it is possible to prepare films that meet the capacitance density, leakage, and breakdown strengths required for DRAMs. A listing of some of the reported efforts in DRAM manufacturing is given in Table 3. A discussion of some of the important processing integration issues is given below in the section on FRAM materials, since many of the issues are identical.

5.2 Hysteretic Films (FRAM)

In the design of ferroelectric nonvolatile memories, the polarization state of the film is used to store the ones and zeros of the binary code. In principle, such memories are nonvolatile since the remanent polarization state of the ferroelectric is not lost when power is cut off. Low-density FRAMs are attractive for applications such as smart cards and drop-in EEPROM replacements, while high-density FRAM could replace some Si-based memory in computing applications. FRAMs can be written quite rapidly, and so they offer significant advantages over other nonvolatile memories such as EEPROM. In

practice, several barriers need to be overcome before the full benefits of a high-density, nonvolatile memory based on ferroelectric films will be viable. These include

1. fatigue, i.e., loss of switchable polarization associated with repeated polarization reversals over the lifetime of the device;
2. poor retention of the written polarization direction;
3. imprint, or development of a preferred polarization state; and
4. development of IC-compatible processing.

Significant progress has been made in each of these areas over the past few years.

At present, the two best-developed candidates for this application are PZT and $\text{SrBi}_2\text{Ta}_2\text{O}_9$. For FRAM applications, PZT is attractive because of its large switchable polarization ($2P$, around $45\text{--}55 \mu\text{C}/\text{cm}^2$) and the lower temperatures required for crystallization. However, PZT films deposited on Pt electrodes suffer significant fatigue in the magnitude of the switchable polarization after the polarization has been reversed on the order of 10^7 times. This can lead to significant difficulties in distinguishing the memory state. While for a few applications this is acceptable, in computer memories it would be preferable to have $10^{12}\text{--}10^{15}$ polarization reversal cycles. Several years ago, it was demonstrated that fatigue could be eliminated in PZT films by using conductive oxide electrodes such as RuO_2 , IrO_2 , or LSCO (Au-

Table 3. Some efforts in DRAM production.

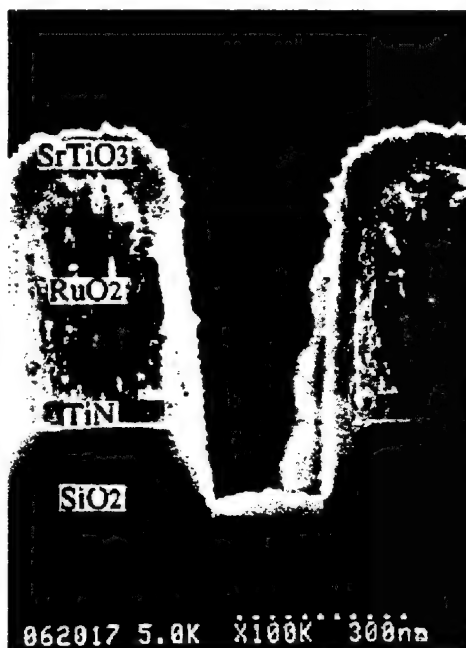
Company	Device	Dielectric/Ferroelectric	Reference
Matsushita	4-, 6-Mbit DRAM	BST	Shimada <i>et al.</i> , 1995
Matsushita	256 kbit	$\text{SrBi}_2\text{Ta}_2\text{O}_9$	Itoh <i>et al.</i> , 1995
NEC	Gbit-compatible DRAM	SrTiO_3	Lesaichere <i>et al.</i> , 1995
NEC	1-Mbit FRAM	$\text{SrBi}_2\text{Ta}_2\text{O}_9$	Scott <i>et al.</i> , 1996
Mitsubishi	4-, 9-Mbit DRAM		
	Gbit-compatible	BST	Itoh <i>et al.</i> , 1995
GEC-Marconi	4-kBit FRAM		
	silicon-on-sapphire	PZT	Bland <i>et al.</i> , 1995
GEC-Marconi	Infrared imaging	PZT	Shorrocks <i>et al.</i> , 1995
Ramtron	64-kbit shadow RAM	PZT	Bondurant, 1990
U.S. DRAM Consortium	ULSI DRAM	BST	Kington <i>et al.</i> , 1996
Samsung	64-kbit FRAM	PZT	Chung <i>et al.</i> , 1996
Samsung	USLI DRAM	BST	Hwang <i>et al.</i> , 1995
Motorola/Symetrix	FRAM	$\text{SrBi}_2\text{Ta}_2\text{O}_9$	Melnick <i>et al.</i> , 1995
SHARP	FRAM	$\text{Bi}_4\text{Ti}_3\text{O}_{12}$	Kijima <i>et al.</i> , 1996
Texas Instruments	Infrared imaging	PZT	Udayakumar, 1996
Northern Telecom	FRAM	PZT	Chivukula <i>et al.</i> , 1995
FRAM	PZT		Wakamura <i>et al.</i> , 1995

ciello and Ramesh, 1996; Nakamura *et al.*, 1994; Ramesh *et al.*, 1993). In some cases these electrodes also minimize imprint problems (Nakamura *et al.*, 1994). An alternative choice is to switch to one of the Bi-layer structure ferroelectrics like $\text{SrBi}_2\text{Ta}_2\text{O}_9$. While in polycrystalline films, the reversible polarization in this system is smaller than in the PZTs ($2P_r < 22 \mu\text{C}/\text{cm}^2$), they also show negligible fatigue out to 10^{12} cycles, even when deposited on Pt electrodes (Jones and Desu, 1996).

In addition to the materials requirements, there are many processing issues that must be addressed in order for paraelectric or ferroelectric films to be integrated into DRAM or FRAM. First, most groups are reporting memory capacitor structures similar to that shown in Fig. 7. Since the capacitor must be deposited over a $0.25\text{--}0.75 \mu\text{m}$ step in order to increase the element capacitance while maintaining a small feature size, a deposition process that enables conformal coverage is essential. For such applications, MOCVD is the method of choice. Second, each of the

materials utilized must be patternable at the required feature size, which will probably require reactive ion etching (RIE). Third, the dielectric film properties must be retained throughout the entire processing cycle. As has been discussed elsewhere (Jones and Desu, 1996), this is a significant challenge. Especially problematic is the RIE (Pan *et al.*, 1994), which can result in degradation of the ferroelectric's hysteresis loop (for FRAMs). Additional degradation can be induced when the interlevel dielectric is deposited over the patterned capacitor. Moreover, any processing step that involves significant exposure to hydrogen can lead to reduction of the ferroelectric layer, with a consequent increase in the conductivity, and a decrease in the switchable polarization. A more complete review of these effects is given by Archard *et al.* (1995).

Research in both DRAM and FRAM memories is being conducted in Japan, the United States, Europe, and Korea. Table 3 summarizes recent publications in these areas.



(a)



(b)

FIG. 7. SEM micrographs showing (a) the conformal step coverage of 1000-Å-thick SrTiO_3 films over RuO_2/TiN electrodes and (b) a high-magnification image of the MOCVD SrTiO_3 films. Pictures taken from Lesaichere *et al.* (1995).

5.3 Pyroelectric Films

As described in Sect. 1.3, thin-film pyroelectrics offer significant advantages in terms of integration with integrated circuitry and low thermal time constants relative to bulk materials (Shorrock *et al.*, 1995). For pyroelectric applications, PbTiO_3 , $(\text{Pb},\text{La})\text{TiO}_3$, $(\text{Pb},\text{Ca})\text{TiO}_3$, and PZT have been the most widely studied film compositions. Interest in the PbTiO_3 -based compounds stems from its combination of a large polarization (around $80 \mu\text{C}/\text{cm}^2$) and hence the potential for a large pyroelectric coefficient, and its relatively modest dielectric permittivity. Both factors are necessary for a substantial figure of merit (FOM). Ca or La doping serves the dual purpose of bringing the ferroelectric transition temperature closer to room temperature and increasing the electrical resistivity of the film. Taking p/ϵ as an approximate FOM for a pyroelectric detector, PZT films have been demonstrated with FOMs of $\sim 0.7 \mu\text{C}/(\text{m}^2 \text{ K})$ (Shorrock *et al.*, 1995; Kohli *et al.*, 1995), while PbTiO_3 -based films have been reported with FOMs as high as $2.9 \mu\text{C}/(\text{m}^2 \text{ K})$ (Kamada *et al.*, 1995; Seifert *et al.*, 1996).

In terms of thermal isolation, two families of device geometries have been pursued: diaphragm structures prepared by bulk Si micromachining and air-bridge arrays (Shorrock *et al.*, 1995; Polla, 1995) for higher-resolution imaging. Thin-film $(\text{Pb},\text{La})\text{TiO}_3$ pyroelectric sensors are now being used commercially in some Matsushita air-conditioning units so that the ventilation can be automatically adjusted on the basis of the number of heat sources in the room (Kamada *et al.*, 1995). There is considerable room in this field for optimization of detector properties based on both the film composition and microstructure as well as new device designs.

5.4 High-Energy-Density Transducers

The primary requirements for a thin-film transducer are that it demonstrate an appreciable controllable displacement and that it have a high energy density. Piezoelectric and electrostrictive materials are attractive from both standpoints, as large electrically induced displacements can be achieved. Moreover, on account of the high dielectric con-

stant of most ferroelectrics, they have a significant advantage in energy density over electrostatic actuators. In addition, they show much higher piezoelectric activity as well as higher piezoelectric coupling coefficients than ZnO. For many years, ZnO has been the predominant piezoelectric transducer for thin-film applications, largely because oriented thin films could be sputtered reproducibly. However, the piezoelectric activity of ZnO is modest (typically 5–10 pm/V). As a consequence, in applications where large displacements and efficient electromechanical coupling are required, ferroelectric thin films (with $d_{33} = 50\text{--}300 \text{ pm/V}$) offer significant advantages.

Among the ferroic candidates for actuator films, three distinct mechanisms can be utilized to generate a strain in the film: piezoelectricity, electrostriction, and phase switching. Fundamentally, the piezoelectric effect is the linear relationship between the applied electric field and the resultant displacement. Electrostriction, on the other hand, implies proportionality between the square of the electric field and the shape change, and is observed when piezoelectricity is absent. In practice, both of these relations are applicable over a limited electric-field range. For example, when a large alternating electric field is applied to excite piezoelectric displacement, hysteresis in the strain is observed due to domain-wall motion. While electrostrictive materials show much lower levels of hysteresis in the strain, it has been found that the strain is properly proportional to the square of the polarization rather than the square of the electric field at high field levels. Phase-switching compositions, on the other hand, rely on the electrically induced transition from an antiferroelectric phase to a ferroelectric phase. Since the volumes of the unit cells differ between the two, an appreciable surface displacement can be generated.

Thin-film actuators based on each of these mechanisms have been demonstrated over the past several years. Among the piezoelectric compositions, PZT-based materials have been the best studied. In most cases, PZT thin films show smaller effective piezoelectric coefficients than do bulk ceramics of the same composition (i.e., $d_{33} \sim 70\text{--}140 \text{ pm/V}$ for undoped PZT films where undoped bulk ceramic PZT shows a d_{33} of $\sim 220 \text{ pm/V}$). Nonetheless, this represents a significant step

up from ZnO-based devices. Comparable properties have been demonstrated by several groups, including some in the United States (Polla, 1995; Udayakumar *et al.*, 1992; Li *et al.*, 1994), Europe (Murali *et al.*, 1995), and Japan (Fujii and Watanabe, 1996). In many cases, the piezoelectric coefficients of PZT thin films can be increased if the ac driving field is superimposed over a dc bias electric field (Udayakumar *et al.*, 1992; Murali *et al.*, 1995). Thus far, a conclusive demonstration of soft PZT properties in thin films has not been reported in the literature, possibly as a result of either the small grain size or the stress state in films, either of which can restrict the domain-wall mobility (Shepard *et al.*, 1996; Damjanovich and Demartin, 1996). However, this may be obviated, at least in part, by the fact that thin films typically have high breakdown strengths (~ 1 MV/cm), and so they can be driven harder than a comparable bulk actuator.

Over the last few years, several types of MEMS actuators using ferroelectric films have been demonstrated, including micromotors (Udayakumar *et al.*, 1992; Murali *et al.*, 1995; Flynn *et al.*, 1992), pumps (Polla, 1995), acoustic imaging devices (Bernstein *et al.*, 1996), AFM components (Fujii and Watanabe, 1996), and meanderline actuators (Polla and Francis, 1996). Outstanding issues in the field include the effect of the film stress state and the film microstructure on the piezoelectric coefficients, the aging of the properties, and the long-term reliability of the structures for large-amplitude devices.

Considerably less data are available in the literature on the use of electrostrictive compositions for thin-film actuators. PMN:PbTiO₃ electrostrictive compounds show very large strain levels in bulk ceramics without the hysteretic response that is characteristic of PZT under large drive levels. If comparable properties can be achieved in thin films, such materials would be attractive for precise positioning components.

In contrast, there have been several reports on the properties of antiferroelectric-ferroelectric phase-switching materials for thin-film actuators, with the majority of the activity being centered in the United States (Gaskey *et al.*, 1995; Tani *et al.*, 1994; Yamakawa *et al.*, 1996). Square double hysteresis loops with well-defined coercive fields

have been prepared from lead zirconate and doped lead zirconate compositions (especially La- and Sn-doped materials). Of particular note is the fact that strain levels of 0.3% have been generated in films, which exceeds that available in piezoelectrically actuated materials. Such films are especially attractive in digital displacement applications where well-defined on and off states are required.

Many MEMS devices require larger surface displacements than can be generated in thin films. In such applications, thicker films are required. Preparation of thick films entails considerable care in the processing in order to prevent film cracking or delamination. Several groups have demonstrated thick piezoelectric films, largely prepared by wet-chemical methods (i.e., sol-gel or MOD). In particular, PZT films of 12 μm in thickness have been prepared on Pt-coated Si (Chen *et al.*, 1996), and up to 10 μm in thickness on ZrO₂ substrates (Brooks *et al.*, 1996).

6. CONCLUSIONS

Over the past few years, it has been clearly demonstrated that ferroelectric thin films have tremendous potential for integration with silicon-based electronics. Significant strides in appropriate materials selection, film deposition and characterization, and IC-compatible processing have been made. In particular, prototype devices have been demonstrated using ferroic films in DRAMs, FRAMs, decoupling capacitors, pyroelectric sensors, and piezoelectric or phase change transducers. Both low-density FRAMs and pyroelectric sensors are now being produced commercially.

It is clear, though, that much additional work is required in order to realize fully the benefits of ferroelectric thin films in integrated applications. For the high-density memory applications, where there are tremendous potential advantages to ferroic film incorporation, significant work still needs to be done to optimize the film properties to promote both short-term and long-term device reliability, facilitate low-temperature deposition, and improve compatibility of both the electrode and the capacitor with silicon electronics processing. In the areas of pyroelectric and piezoelectric devices, only modest efforts have been expended to date

in the development of film composition and film integration. Vendors capable of supplying a range of thin-film compositions for prototyping would also be an important boost in terms of demonstrating the viability of the technology.

GLOSSARY

Aging: The continuous change of properties in a ferroelectric as a function of time under zero external stimulus and constant temperature.

Curie Temperature: The temperature that is the boundary between ferroelectric and paraelectric phases in a ferroelectric crystal.

Curie-Weiss Temperature: If the dielectric stiffness in the paraelectric phase is of the form $\chi = \chi_0(T - \theta)$, i.e. following a Curie-Weiss law, it is the Curie-Weiss temperature θ where the extrapolated stiffness would go to zero.

Fatigue: The loss of switchable polarization as a function of the number of switching cycles between "saturated" polarization states.

Imprint: Development of a favored remanent polar state under asymmetric pulsed switching conditions.

Morphotropic Phase Boundary (MPB): A phase boundary in the phase diagram of a ferroelectric solid solution system that is nearly vertical from the composition axis; i.e., a composition close to the boundary will remain close over a wide temperature interval.

Works Cited

- Aizu, K. (1969), "Possible Species of 'Ferroelastic' Crystals and of Simultaneously Ferroelectric and Ferroelastic Crystals," *J. Phys. Soc. Jpn.* **27**, 387.
- Archard, H., Mace, H., Peccoud, L. (1995), "Device Processing and Integration of Ferroelectric Thin Films for Memory Applications," *Microelec. Eng.* **29**, 19.
- Arlt, G. (1996), in: C. A. Paz de Araujo (Chm.), *8th International Symposium on Integrated Ferroelectrics*, Tempe, Arizona, New York: Gordon and Breach.
- Auciello, O., Ramesh, R. (Eds.) (1996), Special Issue on Electroceramic Thin Films, Part I, Processing, *Mater. Res. Bull.* **21** (6), 21-58.
- Barlingay, C. K., Dey, S. K. (1992), "Observation of Sol-Gel Solid Phase Epitaxial Growth of Ferroelectric $\text{Pb}(\text{Nb,Zr,Ti})\text{O}_3$ Thin Films on Sapphire," *Appl. Phys. Lett.* **61**, 1278.
- Bernstein, J., Houston, K., Niles, L., Li, K., Chen, H., Cross, L. E., Udayakumar, K. (1996), "Integrated Ferroelectric Monomorph Transducers for Acoustic Imaging," in: C. A. Paz de Araujo (Chm.), *8th International Symposium on Integrated Ferroelectrics*, Tempe, Arizona, New York: Gordon and Breach.
- Bland, T., Ohbi, J., Patel, A., Kirby, P., Robinson, M., Kerr, J. (1995), "Integration of Sol-Gel PZT with Silicon-on-Sapphire CMOS Circuitry," *Microelec. Eng.* **29**, 29.
- Bondurant, D. (1990), "Ferroelectric RAM Memory Family for Critical Data Storage," *Ferroelectrics* **112**, 273.
- Brooks, K. G., Kohli, M., Taylor, D. V., Maeder, T., Reaney, I., Kholkin, A., Murali, P., Setter, N. (1996), in: B. Kulwicki (Ed.), *Proceedings of the International Symposium on Applications of Ferroelectrics (ISAF 96)*, New Brunswick, NJ: IEEE.
- Bruchhaus, R., Pitzer, D., Scheithaurer, U., Hoesler, W. (1992), "Investigation of Pt Bottom Electrodes for 'In-Situ' Deposited $\text{Pb}(\text{Zr,Ti})\text{O}_3$ (PZT) Thin Films," in: A. I. Kingon, E. R. Myers, B. A. Tuttle (Eds.), *Ferroelectric Thin Films II*, MRS Proceedings Vol. 243, Pittsburgh: Materials Research Society, p. 355.
- Chen, H. D., Udayakumar, K. R., Gaskey, C. J., Cross, L. E. (1996), "Fabrication and Electrical Properties of Lead Zirconate Titanate Thick Films," *J. Am. Ceram. Soc.* **79**, 2189.
- Chen, X., Kingon, A. I., Al-Shareef, H., Bellur, K. R. (1994), "Electrical Transport and Dielectric Breakdown in $\text{Pb}(\text{Zr,Ti})\text{O}_3$ Thin Films," *Ferroelectrics* **151**, 133.
- Chivukula, V., Ilowski, J., Emesh, I., McDonald, D., Leung, P., Sayer, M. (1995), "Dielectric Properties of Ferroelectric Thin Films in the Frequency Range of mHz-GHz," *Integ. Ferroelec.* **10**, 247.
- Chung, I., Kim, C. J., Chung, C. W., Yoo, I. K. (1996), "Integration of Ferroelectric Capacitors Using Multilayered Electrode," in: B. Kulwicki (Ed.), *Proceedings of the International Symposium on Applications of Ferroelectrics (ISAF 96)*, New Brunswick, NJ: IEEE.
- Cross, L. E., Nicholson, B. J. (1955), "The Optical and Electrical Properties of NaNbO_3 Single Crystals," *Philos. Mag.* **46**, 453.
- Damjanovich, D., Demartin, M. (1996), "Dependence of the Direct Piezoelectric Effect in Coarse and Fine Grain Barium Titanate Ceramics on Dynamic and Static Pressure," *Appl. Phys. Lett.* **68**, 3046.
- Desu, S. B., Ramesh, R., Tuttle, B. A., Jones, R. E., Yoo, I.-K. (1995), *Ferroelectric Thin Films V*, MRS Proceedings Vol. 433, Pittsburgh: MRS.
- Diaz-Colon, F. A. (1973), "Dielectric and Electro-Optic Properties of Mixed Bismuth Oxide Layer Structure Compounds," Ph.D. Thesis, The Pennsylvania State University, University Park, PA.

- Dietz, G. W., Waser, R. (1995), "How to Analyze Relaxation and Leakage Currents of Dielectric Thin Films: Simulation of Voltage-Step and Voltage-Ramp Techniques," *Integ. Ferroelec.* 9, 317.
- Dvorak, V. (1971), "The Origin of the Structural Phase Transition in $\text{Gd}(\text{MoO}_4)_3$," *Phys. Status Solidi B45*, 147.
- Dorrian, J. F., Newnham, R. E., Smith, D. K., Kay, M. I. (1971), "Crystal Structures of $\text{Bi}_4\text{Ti}_3\text{O}_{12}$," *Ferroelectrics* 3 (1), 17-27.
- Flynn, A. M., Tavrow, L. S., Bart, S. F., Brooks, R. A., Ehrlich, D. J., Udayakumar, K. R., Cross, L. E. (1992), "Piezoelectric Micromotors for Micro-robots," *J. Microelectromech. Syst.* 1, 44.
- Fork, D. K., Armani-Leplingard, F., Kingston, J. J. (1996), "Application of Electroceramic Thin Films to Optical Waveguide Devices," *MRS Bull.* 21 (7), 53.
- Fousek, J., Janovec, V. (1969), "The Orientation of Domain Walls in Twinned Ferroelectric Crystals," *J. Appl. Phys.* 40, 135.
- Fox, G. R., Krupanidhi, S. B., More, K. L., Allard, L. F. (1992), "Composition/Structure/Property Relations of Multi-Ion-Beam Reactive Sputtered Lead Lanthanum Titanate Thin Films: Part I, Composition and Structure Analysis," *J. Mater. Res.* 7, 3039.
- Fujii, T., Watanabe, S. (1996), "Feedback Positioning Cantilever Using a Lead Zirconate Titanate Thin Film for Force Microscopy Observations of Micropattern," *Appl. Phys. Lett.* 68, 467.
- Gaskey, C. J., Udayakumar, K. R., Chen, H. D., Cross, L. E. (1995), "'Square' Hysteresis Loops in Phase-Switching Nb-Doped Lead Zirconate Stannate Titanate Thin Films," *J. Mater. Res.* 10, 2764.
- Herbert, J. M. (1985), *Ceramic Dielectrics and Capacitors*, New York: Gordon and Breach.
- Huffman, M. (1995), "Liquid Source Misted Chemical Deposition (LMSCD)—A Critical Review," *Integ. Ferroelec.* 10, 39.
- Hwang, C. S., Park, S. O., Kang, C. S., Kang, H. K., Lee, S. I., Lee, M. Y. (1995), "Deposition of Extremely Thin $(\text{Ba},\text{Sr})\text{TiO}_3$ Thin Films for Ultra-Large-Scale Integrated Dynamic Random Access Memory Application," *Appl. Phys. Lett.* 67, 2819.
- Itoh, H., Kashiwara, K., Okudaira, T., Tsunemine, Y., Ohno, Y., Nishimura, T., Horikawa, T., Shibano, T. (1995), "Integration of BST Thin Film for DRAM Fabrication," *Integ. Ferroelec.* 11, 101.
- Jacobsen, S. C., Ramsey, M. (1994), "Microchip Capillary Electrophoresis with an Integrated Post Column Detector," *Anal. Chem.* 66, 3472.
- Jaffe, B., Cook, W. R., Jr., Jaffe, H. (1971), *Piezoelectric Ceramics*, Marietta, OH: R. A. N. Publishers.
- Jensen, K. (1996), private communication.
- Jones, R. E., Jr., Desu, S. B. (1996), "Process Integration for Nonvolatile Ferroelectric Memory Fabrication," *Mater. Res. Bull.* 21 (6), 55.
- Jones, R. E., Jr., Zurcher, P., Chu, P., Taylor, D. J., Lii, Y. T., Jiang, B., Maniar, P. D., Gillespie, S. J. (1995), "Memory Applications Based on Ferroelectric and High Permittivity Dielectric Thin Films," *Microelec. Eng.* 29, 3.
- Kamada, T., Takayama, R., Fujii, S., Degushi, T., Hirao, T. (1995), "Pyroelectric Infrared Sensors Made of La-Modified PbTiO_3 Thin Films and Their Applications," *Integ. Ferroelec.* 11, 15.
- Kijima, T., Nagata, M. M., Matsunaga, H. (1996), "Ultra Thin Fatigue Free $\text{Bi}_4\text{Ti}_3\text{O}_{12}$ Films for Nonvolatile Ferroelectric Memories," *Jpn. J. Appl. Phys.* 35 (Pt. 2B), 1246.
- Kim, E. S. (1990), "Integrated Microphone with CMOS Circuits on a Single Chip," Ph.D. Thesis, University of California, Berkeley.
- Kim, E. S., Muller, R. S. (1987), "IC-Processed Piezoelectric Microphone," *IEEE Electron. Dev. Lett.* EDL-8, 467.
- Kim, N. (1994), "Grain Size Effect on the Dielectric and Piezoelectric Properties in Compositions which are Near the Morphotropic Phase Boundary of Lead Zirconate-Titanate Based Ceramics," Ph.D. Thesis, The Pennsylvania State University, University Park, PA.
- Kington, A. I., Myers, E. R., Tuttle, B. (1992), *Ferroelectric Thin Films II*, MRS Proceedings Vol. 243, Pittsburgh: MRS.
- Kington, A. I., Streiffer, S. K., Basceri, C., Summerfeldt, S. R. (1996), "High-Permittivity Perovskite Thin Films for Dynamic Random Access Memories," *MRS Bull.* 21 (7), 46.
- Kohli, M. (1996), private communication.
- Kohli, M., Huang, Y., Maeder, T., Wuetherich, C., Bell, A., Muralt, P., Setter, N., Ryser, P., Forster, M. (1995), "Processing and Properties of Thin Film Pyroelectric Devices," *Microelec. Eng.* 29, 93.
- Kulwicki, B. M., Amin, A., Beratan, H., Hanson, C. M. (1992), "Pyroelectric Imaging," in: A. Sarari, A. Kington, G. Haertling (Eds.), *8th International Symposium on Applications of Ferroelectrics (ISAF 92)*, New Brunswick, NJ: IEEE.
- Larsen, P. (1995), private communication.
- Lesaicherre, P. Y., Tamamichi, S., Takemura, K., Yamaguchi, H., Tokoshiki, K., Miyasaka, Y., Yoshida, M., Ono, H. (1995), "A Gbit-Scale DRAM Stacked Capacitor with ECR MOCVD SrTiO_3 over RIE Patterned RuO_2/TiN Storage Nodes," *Integ. Ferroelec.* 11, 81.
- Li, J. F., Viehland, D. D., Tani, T., Lakeman, C. D. E., Payne, D. A. (1994), "Piezoelectric Properties of Sol-Gel Derived Ferroelectric and Antiferroelectric Thin Layers," *J. Appl. Phys.* 75, 442.
- Lines, M. E., Glass, A. M. (1977), *Principles and Applications of Ferroelectrics and Related Materials*, Oxford: Clarendon.
- Melnick, B. M., Gregory, J., Paz de Araujo, C. A. (1995), "Characterization of an n-channel 1T-1C Nonvolatile Memory Cell Using Ferroelectric $\text{SrBi}_2\text{Ta}_2\text{O}_9$ as the Capacitor Dielectric," *Integ. Ferroelec.* 11, 145.
- Muralt, P., Kohli, M., Maeder, T., Kholkin, A., Brooks, K., Setter, N., Luthier, R. (1995), "Fabri-

- cation and Characterization of PZT-Thin Film Vibrators for Micromotors," *Sensors Actuators A48*, 157.
- Myers, E. R., Kingon, A. I. (1991), *Ferroelectric Thin Films I*, MRS Proceedings Vol. 200, Pittsburgh: MRS.
- Myers, E. R., Tuttle, B. A., Desu, S. B., Larson, P. K. (1993), *Ferroelectric Thin Films III*, MRS Proceedings Vol. 310, Pittsburgh: MRS.
- Nakamura, T., Nakao, Y., Kamisama, A., Takasu, H. (1994), "Preparation of $\text{Pb}(\text{Zr,Ti})\text{O}_3$ Thin Films on Ir and IrO_2 Electrodes," *Jpn. J. Appl. Phys.* 33 (Pt. 1), 5211.
- Newnham, R. E., Wolfe, R. W., Dorrian, J. F. (1971), "Structural Basis of Ferroelectricity in the Bismuth Titanate Family," *Mater. Res. Bull.* 6, 1029.
- Pan, W., Desu, S. B., Yoo, I. K., Vijay, D. P. (1994), "Reactive Ion Etching of $\text{PbZr}_{1-x}\text{Ti}_x\text{O}_3$ and RuO_2 Films by Environmentally Safe Gases," *J. Mater. Res.* 9, 2976.
- Polla, D. L. (1995), "Microelectromechanical Systems Based on Ferroelectric Thin Films," *Microelec. Eng.* 29, 51.
- Polla, D. L., Francis, L. F. (1996), "Ferroelectric Thin Films in Microelectromechanical Systems Applications," *MRS Bull.* 21 (7), 59-65.
- Potter, B. G., Jr., Sinclair, M. B., Dimos, D. (1993), "Electrooptical Characterization of $\text{Pb}(\text{Zr,Ti})\text{O}_3$ Thin Films by Waveguide Refractometry," *Appl. Phys. Lett.* 63, 2180.
- Ramesh, R., Gilchrist, H., Sands, T., Keramidas, V. G., Haakenaasen, R., Fork, D. K. (1993), *Appl. Phys. Lett.* 63, 3592.
- Reaney, I. M., Brooks, K., Klissurska, R., Pawlacyk, C., Setter, N. (1994), "Use of Transmission Electron Microscopy for the Characterization of Rapid Thermally Annealed, Solution-Gel, Lead Zirconate Titanate Films," *J. Am. Ceram. Soc.* 77, 1209.
- Schwartz, R. W., Dimos, D., Lockwood, S. J., Torres, V. M. (1994), "Preparation and Properties of Sol-Gel Derived PZT Thin Films for Decoupling Capacitor Applications," *Integ. Ferroelec.* 4, 165.
- Scott, J. F., Ross, F. M., Paz de Araujo, C. A., Scott, M. C., Huffman, M. (1996), "Structure and Device Characteristics of $\text{SrBi}_2\text{Ta}_2\text{O}_9$ -Based Non-volatile Random-Access Memories," *MRS Bull.* 21 (7), 33.
- Seifert, A., Murali, P., Setter, N. (1996), private communication.
- Shepard, J. F., Jr., Trolie-McKinstry, S., Hendrickson, M. A., Zeto, R. (1996), "Properties of PZT Thin Films as a Function of In-Plane Biaxial Stress," in: B. Kulwicki (Ed.), *Proceedings of the International Symposium on Applications of Ferroelectrics (ISAF 96)*, New Brunswick, NJ: IEEE.
- Shimada, Y., Nagano, Y., Fujii, E., Azuma, M., Uemoto, Y., Sumi, T., Judai, Y., Hayashi, S., Moriawaki, N., Nakane, J., Otsuki, T., Paz de Araujo, C. A., McMillan, L. D. (1995), "Integration Technology of Ferroelectrics and the Performance of Integrated Ferroelectrics," *Integ. Ferroelec.* 11, 229.
- Shorrock, N. M., Patel, A., Walker, M. J., Parsons, A. D. (1995), "Integrated Thin Film PZT Pyroelectric Detector Arrays," *Microelec. Eng.* 29, 59.
- Shuvalov, L. A. (1970), "Symmetry Aspects of Ferroelectricity," *J. Phys. Soc. Jpn.* 38, 285.
- Sinclair, M. B., Dimos, D., Potter, B. G., Jr., Schwartz, R. W., Buchheit, C. D. (1995), "Light Scattering from Sol-Gel $\text{Pb}(\text{Zr,Ti})\text{O}_3$ Thin Films: Surface Versus Volume Scattering," *Integ. Ferroelec.* 11, 25.
- Smyth, D. M. (1994), "Ionic Transport in Ferroelectrics," *Ferroelectrics* 151, 115.
- Sonnenschein, B. (1996), "Gene Sequencers Seek to Boost the Spread of their Technology," *R&D Magazine* 38 (2), 41.
- Tani, T., Li, J. F., Viehland, D., Payne, D. A. (1994), "Antiferroelectric-Ferroelectric Switching and Induced Strains for Sol-Gel Derived Lead Zirconate Thin Layers," *J. Appl. Phys.* 75, 3017.
- Trivedi, D., Tayabati, P., Tabat, M. (1996), "Measurement of Large Electro-Optic Coefficients in Thin Films of Strontium Barium Niobate ($\text{Sr}_{0.6}\text{Ba}_{0.4}\text{Nb}_2\text{O}_6$)," *Appl. Phys. Lett.* 68, 3227.
- Trolie-McKinstry, S., Hu, H., Krupanidhi, S. B., Chindaudom, P., Vedam, K., Newnham, R. E. (1993), "Spectroscopic Ellipsometry Studies on Ion Beam Sputter Deposited $\text{Pb}(\text{Zr,Ti})\text{O}_3$ Films on Sapphire and Pt-Coated Silicon Substrates," *Thin Sol. Films* 230, 15.
- Trolie-McKinstry, S., Randall, C. A., Maria, J. P., Theis, C., Schlom, D. G., Shepard, J., Jr., Yamakawa, K. (1995a), "Size Effects and Domains in Ferroelectric Thin Film Actuators," in: S. B. Desu, R. Ramesh, B. A. Tuttle, R. E. Jones, I.-K. Yoo (Eds.), *Ferroelectric Thin Films V*, MRS Proceedings Vol. 433, Pittsburgh: MRS.
- Trolie-McKinstry, S., Chen, J., Vedam, K., Newnham, R. E. (1995b), "In situ Annealing Studies of Sol-Gel Ferroelectric Thin Films by Spectroscopic Ellipsometry," *J. Am. Ceram. Soc.* 78, 1907.
- Tuttle, B. A., Schwartz, R. W. (1996), "Solution Deposition of Ferroelectric Thin Films," *Mater. Res. Bull.* 21 (6), 49.
- Tuttle, B. A., Desu, S. B., Ramesh, R., Shiosaki, T. (1994), *Ferroelectric Thin Films IV*, MRS Proceedings Vol. 361, Pittsburgh: MRS.
- Tuttle, B. A., Garino, J. J., Voight, J. A., Headley, T. J., Dimos, D., Eatough, M. (1995), in: O. Auciello, R. Waser (Eds.), *Science and Technology of Electroceramic Thin Films*, Boston: Kluwer Academic.
- Udayakumar, K. R. (1996), private communication.
- Udayakumar, K. R., Chen, J., Flynn, A. M., Brooks, K. G., Cross, L. E., Ehrlich, D. J. (1992), "Piezoelectric Thin Film Ultrasonic Micromotors," in: A. I. Kingon, E. R. Myers, B. Tuttle (Eds.), *Ferroelectric Thin Films II*, MRS Proceedings Vol. 243, Pittsburgh: MRS.
- Voight, J. A., Tuttle, B. A., Headley, T. J., Ea-

tough, M. O., Lamppa, D. L., Goodnow, D. (1993), "Oriented Lead Zirconate Titanate Thin Films: Characterization of Film Crystallization," in: E. R. Myers, B. A. Tuttle, S. B. Desu, P. K. Larson (Eds.), *Ferroelectric Thin Films III*, MRS Proceedings Vol. 310, Pittsburgh: MRS.

Wakamura, T., Nakao, Y., Kimasawa, A., Takasu, H. (1995), "PZT on Ir Doped Pt: No Fatigue," *Integ. Ferroelec.* 11, 161.

Warren, W. L., Robertson, J., Dimos, D. B., Tuttle, B. A., Smyth, D. M. (1994), "Transient Hole Traps in PZT," *Ferroelectrics* 153, 303.

Waser, R. (1994), "Charge Transport in Perovskite-Type Titanates: Space Charge Effects in Ceramics and Films," *Ferroelectrics* 151, 125.

Waser, R., Klee, M. (1992), "Theory of Conduction and Breakdown in Perovskite Thin Films," *Integ. Ferroelec.* 2, 23.

Watton, R. (1994), "Ferroelectric Materials and IR Bolometer Arrays: From Hybrid Arrays Towards Integration," *Integ. Ferroelec.* 4, 175.

Wolfe, R. W., Newnham, R. E., Smith, D. K., Kay, M. I. (1971), "Crystal Structure of $\text{Bi}_3\text{TiNbO}_9$," *Ferroelectrics* 3, 1.

Yamakawa, K., Trolier-McKinstry, S., Dougherty, J. P. (1996), "Electrical Properties and Phase Transformations in Antiferroelectric Lead Zirconate Thin Films," in: B. Kulwicki (Ed.), *Proceedings of the International Symposium on Applications of Ferroelectrics*, New Brunswick, NJ: IEEE.

Further Reading

General Information on Ferroelectricity

Setter, N., Colla, E. L. (1993), *Ferroelectric Ceramics. Tutorial Reviews, Theory, Processing and Applications*, Boston: Birkhauser.

Xu, Yuhuan (1991), *Ferroelectric Materials and Their Applications*, Amsterdam: North-Holland.

Practical Applications of Ferroelectrics

Krupanidhi, S., Kurtz, S. K. (1990), *7th International Symposium on Applications of Ferroelectrics (ISAF 90)*, New Brunswick, NJ: IEEE.

Pandey, R. K., Liu, M., Safari, A. (1994), *9th International Symposium on Applications of Ferroelectrics (ISAF 94)*, New Brunswick, NJ: IEEE.

Safari, A., Kingon, A., Haertling, G. (1992), *8th International Symposium on Applications of Ferroelectrics (ISAF 92)*, New Brunswick, NJ: IEEE.

Specific to Ferroelectric Thin Films

Desu, S. B., Ramesh, R., Tuttle, B. A., Jones, R. E., Yoo, I. K. (Eds.) (1996), *Ferroelectric Thin Films V*, MRS Proceedings Vol. 433, Pittsburgh: MRS.

Kingon, A. I., Myers, E. R., Tuttle, B. A. (Eds.) (1992), *Ferroelectric Thin Films II*, MRS Proceedings Vol. 243, Pittsburgh: MRS.

Myers, E. R., Kingon, A. I. (Eds.) (1990), *Ferroelectric Thin Films I*, MRS Proceedings Vol. 200, Pittsburgh: MRS.

Paz de Araujo, C. A., Scott, J. F., Taylor, G. W. (1996), *Ferroelectric Thin Films: Synthesis and Basic Properties*, New York: Gordon and Breach.

Tuttle, B. A., Myers, E. R., Desu, S. B., Larsen, P. K. (1993), *Ferroelectric Thin Films III*, MRS Proceedings Vol. 310, Pittsburgh: MRS.

Tuttle, B. A., Desu, S. B., Ramesh, R., Shiosaki, T. (Eds.) (1994), *Ferroelectric Thin Films IV*, MRS Proceedings Vol. 361, Pittsburgh: MRS.

APPENDIX 89

Charge release of lanthanum-doped lead zirconate titanate stannate antiferroelectric thin films

Baomin Xu,^{a)} Paul Moses, Neelesh G. Pai, and L. Eric Cross

Intercollege Materials Research Laboratory, Pennsylvania State University, University Park, Pennsylvania 16802

(Received 21 October 1997; accepted for publication 7 December 1997)

The charge release speed and backward phase switching time of lanthanum-doped lead zirconate titanate stannate antiferroelectric thin films were investigated by directly measuring the switching current upon removal of the applied electric field. The backward switching time is about 6 ns. The maximum switching current density can reach 9400 A/cm², and more than half of the stored charge can be released in 10 ns. These results show that the obtained antiferroelectric thin films are very promising for decoupling capacitor applications in high speed multichip modules. © 1998 American Institute of Physics. [S0003-6951(98)03605-5]

Lead zirconate titanate stannate (Pb(Zr,Sn,Ti)O₃) based antiferroelectric materials have been studied extensively over the past several decades for applications as high-energy-storage capacitors and high-strain actuators/transducers.¹⁻⁶ More recently, with the development of microelectronic devices, antiferroelectric thin films have been explored for applications such as microactuators in microelectromechanical systems (MEMS), and decoupling capacitors in high speed multichip modules (MCMs).⁷⁻⁹ It has been found that there are two types of hysteresis loops in the doped Pb(Zr,Sn,Ti)O₃ system, that is, "slanted" and "square"-types, as shown in Fig. 1.⁴ Only those materials with square hysteresis loops are suitable for energy storage capacitor applications.¹ The charge storage capacity of different kinds of dielectric materials is given in Fig. 2. It can be seen that for charge storage applications, antiferroelectrics are superior to ferroelectrics because all the stored charge can be released due to absence of any remanent polarization, and superior to linear dielectrics because of their high dielectric constant and high charge storage density.¹ However, it is very difficult to obtain thin films with square hysteresis loops and zero remanent polarization.^{7,8} Just recently, our group succeeded in fabricating niobium or lanthanum-doped lead zirconate titanate stannate antiferroelectric thin films with square hysteresis loops and zero remanent polarization.^{9,10} This made it possible to use antiferroelectric thin films as decoupling capacitors in high speed multichip modules.

For high-energy-storage capacitor applications, especially for decoupling capacitor applications in high speed MCMs, one of the most important parameters is the charge release speed and backward phase switching time, but to date work reported in this area has been limited. Pan *et al.*¹¹ studied the backward phase switching of the (Pb,Lu)(Zr,Sn,Ti)O₃ bulk materials. They found the shortest switching time in their samples to be 2 μs. For antiferroelectric thin films, only Brooks *et al.*⁷ studied the phase switching time. They used the same compositions as Pan's work and found the forward phase switching time to be 300 ns. However, no data were presented about the backward phase switching time and charge release speed. On the other hand, their samples had

slanted rather than square-type hysteresis loops. In this work, the switching current-time curve upon removal of dc bias from the thin films was measured in nanosecond range. The switching current, charge release speed, and backward phase switching time of antiferroelectric thin films were investigated and reported.

The composition of the samples is Pb_{0.97}La_{0.02}(Zr_{0.85}Sn_{0.13}Ti_{0.02})O₃. The films were prepared by a modified sol-gel method using acetic acid as solvent, and were deposited on 1 in.×1 in. Pt(1500 Å)/Ti(200 Å)/SiO₂(5000 Å)/Si(0.5 mm) substrates. The film thickness is about 0.40 μm. The processing details will be reported elsewhere.¹⁰ Considering the possibility of large switching current density in these antiferroelectric thin films, a platinum top electrode with 0.10 mm in diameter was chosen in this work. The hysteresis loop of the films was measured by a modified Sawyer-Tower circuit with a frequency of 60 Hz. The result is shown in Fig. 3. The maximum polarization can reach 44.5 μC/cm², corresponding to a maximum induced charge of Q_M=3.5 nC. Several special electric field values are also designated in Fig. 3. The maximum voltage used in

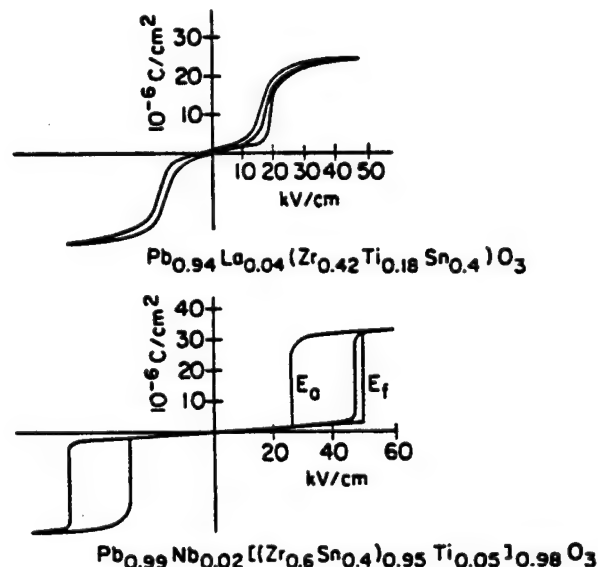


FIG. 1. Delineation of slanted and square hysteresis loop behavior, reproduced from Berlincourt (see Ref. 4).

^{a)}Corresponding author. Electronic mail: bxx2@psu.edu

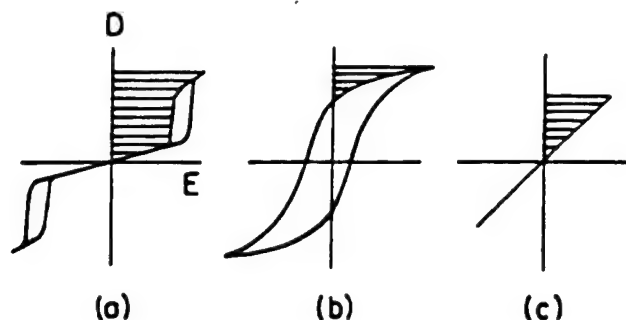


FIG. 2. Hysteresis and energy storage figures for (a) a soft antiferroelectric, (b) a normal ferroelectric, and (c) a linear capacitor. The shaded area denotes the discharge energy [after Jaffe (see Ref. 1)].

Fig. 3 is $V_M = 15$ V, corresponding to an electric field of $E_M = 375$ kV/cm. The switching fields have been determined by extrapolating the two steepest sections of the hysteresis loops and obtaining their intersections with the horizontal axis. The forward switching field E_F and backward switching field E_{AF} are 220 and 140 kV/cm, respectively, corresponding to the voltage $V_F = 8.8$ V and $V_{AF} = 5.6$ V. Focusing on the backward arm of the hysteresis loop, it can be found that with decreasing of the electric field from E_M , the curve is rather flat at first (the slope is small) then becomes very steep (the slope is very large). We define the electric field at which the slope of the hysteresis loop changes from flat to steep as E'_{AF} , and its value is 250.0 kV/cm. The corresponding voltage is $V'_{AF} = 10.0$ V.

The block diagram of the measuring system is shown in Fig. 4. The principle of the measurement can be described as follows: first a dc voltage of 15 V was applied to the sample, charging the sample and inducing the antiferroelectric to ferroelectric phase switching so that the maximum polarization was reached. Then the applied voltage was removed quickly, simultaneously short circuiting the sample (including the small resistor R_2 which is in series with the sample) so that the sample can be discharged and brought back to the original antiferroelectric phase. The discharge (switching) current was determined by measuring the voltage across the small resistor R_2 . In the actual measurement system, a mercury wetted relay was used to change the conditions of the sample from charged, induced ferroelectric state to discharged, original antiferroelectric state, and the relay was controlled by a function generator with 10 Hz square wave output. A special probe made from a short segment of indium wire was used to touch the top electrode of the sample because the soft indium metal formed a relatively large contact area which is necessary for the high peak current. The high speed part of the circuit was compactly assembled on a piece of copper clad circuit board and a 1.2 Ω surface mounting resistor was used for R_2 in order to keep the wires as short as possible and reduce the circuit parasitics caused by the wires. The bandwidth of the setup is mainly determined by the oscilloscope, which is 400 MHz.

Figure 5 shows the measurement results. Channel 1 (lower curve) is the trace of applied voltage versus time and channel 2 (upper curve) is the trace of the voltage across R_2 versus time, which can be viewed as discharge current versus time. Figure 5(a) is the situation when the circuit was fully assembled but the probe contact to the sample was not com-

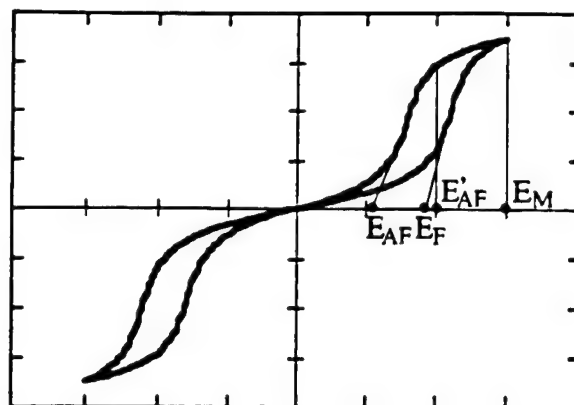


FIG. 3. Hysteresis loop of the antiferroelectric thin films. Several special electric field values are also designated in the figure. X axis: driving voltage, 5 V/division, or electric field, 125 (kV/cm)/division. Y axis: induced charge, 1 nC/division, or polarization, 12.7 ($\mu\text{C}/\text{cm}^2$)/division.

pleted. The small current fluctuation around zero after switching to short state (upper curve) was caused by the circuit parasitics but the net charge is close to zero. This proved that, except for the sample, there are no significant sources in the system contributing to charge release during measurement. On the other hand, the lower curve indicates that the switching time of the system from open to short state is not larger than approximately 1 ns, which verified the system can measure the discharge current in nanosecond range. Figure 5(b) shows the switching current caused by the sample. It demonstrates that the maximum switching current value can reach 0.74 A, which is equivalent to a current density of more than 9400 A/cm² (the electrode area is 0.1 mm in diameter). The area between the time axis and the current curve represents the released charge. Calculating the area from $t = 0$ to $t = 10$ ns indicates that the charge released in 10 ns is about 1.98 nC. Figure 3 shows the total stored charge is 3.5 nC. Therefore, 56.6% of the stored charge can be released in 10 ns.

Typical switching current curves of the bulk materials show two distinctive current peaks, as observed in Pan's work.¹¹ The first peak corresponds to the released charge when the applied voltage drops from V_M to V'_{AF} and the second peak corresponds to the released charge when the applied voltage drops from V'_{AF} to V_{AF} . The switching time is defined as the time in which the current decreases to 10% of the value from the second maximum.^{11,12} However, just one distinctive current peak can be found in Fig. 5 (the small peaks in the "fall" part of the current curve are caused by

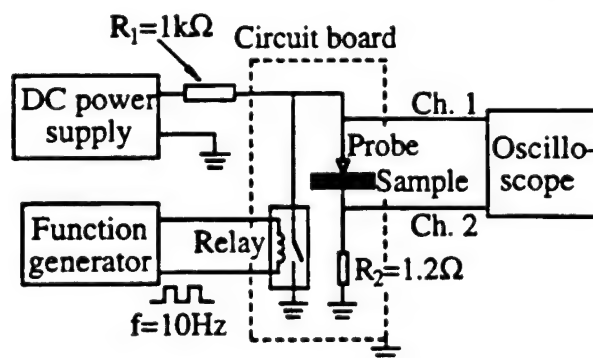


FIG. 4. Block diagram of the switching current-time measurement setup.

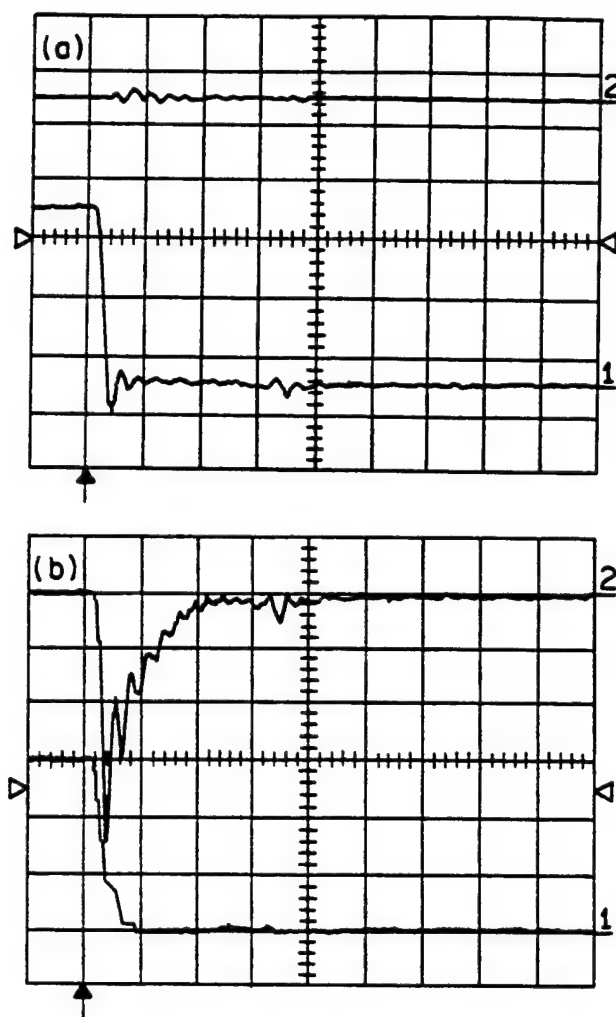


FIG. 5. Switching current of the antiferroelectric thin film sample. X axis: time, 5 ns/division. Y axis: channel 1 (lower curve), applied voltage, 5 V/division. channel 2 (upper curve), voltage across the 1.2 Ω resistor, 0.2 V/division, or switching current, 0.167 A/division. (a) The situation when the probe did not touch the sample, the upper curve proving that the current caused by circuit parasitics is very small. (b) The situation when the sample was connected in the circuit, the upper curve representing the switching current of the sample.

the circuit parasitics). This is possibly because the time interval between these two peaks is so short for the thin films that it cannot be resolved due to the limited time response of the measurement setup. About 0.52 nC charge is released before the current peaks appear according to Fig. 5(b). Figure 3 shows that 0.5 nC charge should be released when the applied voltage decreases from V_M to V'_{AF} . This means that even if there were two current peaks in the thin films studied, they would appear to be one peak because of overlapping in the present time scale. Using the same definition of the switching time as in bulk materials, the switching time for these thin films is found to be about 6 ns, which is three orders of magnitude smaller than in bulk materials.

According to the results on bulk materials,¹¹ the switching time decreases with increasing of backward switching field because higher backward switching field means a larger driving force for the recovery of the antiferroelectric phase from a field induced ferroelectric phase. The highest backward switching field in their samples was 30 kV/cm.¹¹ The present thin film sample has the backward switching field value of 140 kV/cm, which is much higher than that of the bulk materials. This is one of the reasons that the backward switching time of the thin film sample is much shorter. Another factor, which may be more important, is the effect of the substrate. Due to the phase transition strain, at the thin film-substrate interface the film tends to change its dimensions while the substrate tries to maintain the original dimensions, causing a substantial stress in the interface. This contributes to an extra driving force making the backward switching time of thin films much shorter than that of bulk materials under stress-free mechanical boundary conditions.

In summary, the switching current of antiferroelectric thin films from a field induced ferroelectric phase to antiferroelectric phase upon release of the applied electric field was measured with the time range as small as nanoseconds. The charge release speed and backward phase transition time have been determined from the switching current-time curve. The maximum switching current density was more than 9400 A/cm², and more than half of the stored charge could be released in 10 ns. The backward phase switching time is about 6 ns, and the high phase switching fields and stress induced by the phase transition at the interface between film and substrate are probably responsible for the very short backward phase switching time. These antiferroelectric thin films are very promising for decoupling capacitor applications in high speed multichip modules.

The authors would like to thank the Office of Naval Research for the financial support and Dr. Qiming Zhang for his valuable discussions.

- ¹B. Jaffe, Proc. IRE 49, 1264 (1961).
- ²D. Berlincourt, H. Jaffe, H. H. A. Krueger, and B. Jaffe, Appl. Phys. Lett. 3, 90 (1963).
- ³D. Berlincourt, H. H. A. Krueger, and B. Jaffe, J. Phys. Chem. Solids 25, 659 (1964).
- ⁴D. Berlincourt, IEEE Trans. Sonics Ultrason. SU-13, 116 (1966).
- ⁵K. Uchino and S. Nomura, Ferroelectrics 50, 191 (1983).
- ⁶W. Y. Pan, C. Q. Dam, Q. M. Zhang, and L. E. Cross, J. Appl. Phys. 66, 6014 (1989).
- ⁷K. G. Brooks, J. Chen, K. R. Udayakumar, and L. E. Cross, J. Appl. Phys. 75, 1699 (1994).
- ⁸S. S. Sengupta, D. Roberts, J. F. Li, M. C. Kim, and D. A. Payne, J. Appl. Phys. 78, 1171 (1995).
- ⁹C. J. Gaskey, K. R. Udayakumar, H. D. Chen, and L. E. Cross, J. Mater. Res. 10, 2764 (1995).
- ¹⁰B. Xu, N. G. Pai, and L. E. Cross, Mat. Lett. (to be published).
- ¹¹W. Y. Pan, W. Y. Gu, and L. E. Cross, Ferroelectrics 99, 185 (1989).
- ¹²E. Fazzu and W. J. Merz, Phys. Rev. 116, 61 (1959).

APPENDIX 90

Lanthanum Doped Lead Zirconate Titanate Stannate Antiferroelectric Thin Films From Acetic Acid-based Sol-gel Method

Baomin Xu*, Neelesh G. Pai, and L. Eric Cross

Intercollege Materials Research Laboratory, Pennsylvania State University,
University Park, PA 16802, USA

Abstract

Lanthanum doped lead zirconate titanate stannate antiferroelectric thin films with "square" hysteresis loops and zero remanant polarization were prepared, for the first time, from acetic acid-based sol-gel processing. The method has the advantages of simple procedure in solution preparation, less sensitivity to moisture, and the potential to make thick films. The thin films obtained have very distinctive phase transition fields, and the saturated polarization value of $37\mu\text{C}/\text{cm}^2$, which are suitable for high-energy-storage or decoupling capacitor applications in advanced multichip modules, as well as microactuation applications.

Keywords: Lanthanum doped lead zirconate titanate stannate; Antiferroelectrics; Thin films; Sol-gel method; Decoupling capacitors

1. Introduction

Antiferroelectric ceramic materials of lead zirconate titanate stannate ($\text{Pb}(\text{Zr},\text{Sn},\text{Ti})\text{O}_3$) and further modified forms have been studied many years for the applications of high-

* Corresponding author. E-mail: BXX2@PSU.EDU

energy-storage-capacitors and transducers [1,2,3]. In these materials, switching from one phase to another is possible by the application of a reasonable electric field because of the small free energy difference between the antiferroelectric and ferroelectric phases. Berlincourt found two different types of P-E hysteresis loops in the doped $\text{Pb}(\text{Zr},\text{Sn},\text{Ti})\text{O}_3$ system, that is, “slanted” and “square” types of loops [4]. The “slanted” loop materials have much less hysteresis, lower transition fields, smaller volume differences between antiferroelectric and ferroelectric phases, and wider temperature ranges over which the phase transition can be forced by the electric field. The “slanted” loop materials exhibit a small remanent polarization at zero field, while the “square” loop materials do not. Representative P-E hysteresis traces for the slanted and square loop compositions are shown in Fig. 1. According to Jaffe’s work [5], only the materials with “square” hysteresis loop behavior are suitable for high-energy-storage-capacitor applications.

Thin films of $\text{Pb}(\text{Zr},\text{Sn},\text{Ti})\text{O}_3$ antiferroelectric materials have been studied since the early 1990s, with the applications as microactuators in microelectromechanical systems (MEMS) [6]. Up to date, nearly all of the $\text{Pb}(\text{Zr},\text{Sn},\text{Ti})\text{O}_3$ antiferroelectric thin films are made by the sol-gel method using 2-methoxyethanol as solvent [6,7]. Recently, our group reported [8] that $\text{Pb}(\text{Zr},\text{Sn},\text{Ti})\text{O}_3$ antiferroelectric thin films with “square” hysteresis loops can be prepared by 2-methoxyethanol based sol-gel method, which is very promising for the power plane decoupling capacitor application in multichip modules.

In 1988, G. Yi et al reported [9] that ferroelectric PZT thin films can be made from the sol-gel method using acetic acid as solvent. Furthermore, acetic acid not only acts as a solvent, but also acts as a chelating agent which imparts solubility to a growing metal oxide cluster, extending the time to the gel point [10], hence this method is also called hybrid solution synthesis [11]. Compared to the 2-methoxyethanol process, acetic acid process offers the advantages of relatively simple solution synthesis, less sensitivity to moisture and easier to thick film preparation [11,12], but there are no reports to prepare the $(\text{Pb},\text{La})(\text{Zr},\text{Sn},\text{Ti})\text{O}_3$ antiferroelectric thin films by this method. In this paper, we will

report, for the first time, that lanthanum doped lead zirconate titanate stannate antiferroelectric thin films with "square" hysteresis loop behavior can be made through the acetic acid-based sol-gel processing.

2. Experimental Procedure

The composition used in this work is $\text{Pb}_{0.97}\text{La}_{0.02}(\text{Zr}_{0.85}\text{Sn}_{0.13}\text{Ti}_{0.02})\text{O}_3$ (hereafter abbreviated as PLZST), which is located in the orthorhombic region in the $(\text{Pb},\text{La})(\text{Zr},\text{Sn},\text{Ti})\text{O}_3$ system phase diagram [4]. The flow chart for the sol-gel processing is shown in Fig. 2. The elemental precursors used are lead acetate trihydrate, lanthanum acetate hydrate, tin acetate, zirconium n-propoxide, and titanium isopropoxide, and all of them are from the Aldrich Chemical Company. Lead acetate trihydrate, lanthanum acetate hydrate, and tin acetate are initially dissolved in acetic acid, and the water is removed during a period of distillation at 105°C . After cooling to room temperature, the solution is added with zirconium and titanium alkoxides and mixed in the flask. Ethylene glycol and deionized water are also added to control the viscosity and concentration of the solution. The concentration of the final solution is adjusted to be about 0.4M.

Thin films were prepared through a multiple layer spin-coating procedure. The solution was filtered through a $0.2\mu\text{m}$ filter and deposited on a substrate, which was spun at 3000rpm for approximately 30 seconds on a commercial resist spin-coater. The substrate is n-type, (100) oriented silicon wafer with $0.5\mu\text{m}$ thick thermally grown SiO_2 layer, $0.02\mu\text{m}$ thick sputtered titanium layer, and $0.15\mu\text{m}$ thick sputtered platinum bottom electrode. After the deposition of each layer, the films were pyrolyzed at 600°C to remove organics and allowed to cool to room temperature. Subsequent layers were applied until a thickness of about $0.4\mu\text{m}$ was achieved. The films were then annealed at 700°C for one hour in a conventional box furnace.

Platinum top electrodes with diameters of 1.6mm were deposited by rf sputtering method. The thickness of the films were determined from surface profilometer traces. The polarization-electric field (P-E) hysteresis loops were measured using a modified Sawyer-Tower circuit at room temperature. Samples were driven with a 15 - 20V, 60Hz signal. The low field dielectric constant and loss tangent of the films were measured at room temperature using an HP4274A LCR meter with an oscillating field of about 1mV/ μ m and a frequency of 1kHz. Capacitance as a function of DC bias was measured with an HP4192A impedance analyzer, and the oscillating voltage and frequency were set at 10mV and 1kHz, respectively.

3. Results and Discussions

Fig. 3 shows the P-E hysteresis loop of the PLZST films with the thickness of 0.40 μ m. It exhibits a typical antiferroelectric-ferroelectric switching characteristics with the “square” hysteresis loop. The forward and reverse switching fields are quite distinctive, and the remanent polarization is nearly zero at zero applied field. The saturated polarization value reaches 37 μ C/cm². Focusing on the ferroelectric-antiferroelectric phase transition arm of the double hysteresis loop in Fig. 3, a polarization charge of 20 μ C/cm² can be released for a small voltage change of 0.75V; this corresponds to a differential capacitance per unit area of 27 μ F/cm², more than one order of magnitude higher than the 1 μ F/cm² requirement projected for the decoupling capacitor applications. Therefore, the antiferroelectric thin films reported here will be very valuable as dielectrics for power and ground plane decoupling capacitors in advanced multichip modules (MCM's).

Fig. 4 shows the capacitance as a function of slowly varying DC bias. The presence of the “double butterfly” variation, a general characteristics of “soft” antiferroelectric materials, corresponds to the forward and reverse switching fields of the phase transition. Generally, the magnitudes of the phase switching fields can be determined both from the

peaks of the C-V curves, and from the intersections of the tangents drawn to the steepest portions of the P-E curves. For these PLZST thin films, the values of the forward and reverse switching fields are 250kV/cm and 165kV/cm from the P-E hysteresis loops, while the corresponding values determined from the C-V curves are 225kV/cm and 175kV/cm, respectively, hence the values determined from these two methods are in good agreement.

The electrical properties of the antiferroelectric PLZST thin films are summarized in Table 1. Compared to the thin films with the same composition but prepared from the 2-methoxyethanol based sol-gel method [13], the maximum polarization values of the two kinds of films are almost the same, but the phase transition field of the films from acetic acid method is a little smaller than that of the films from 2-methoxyethanol method, which may be attributed to the effect of different processing.

4. Summary

Lanthanum doped lead zirconate titanate stannate antiferroelectric thin films have been prepared from the sol-gel processing using acetic acid as solvent. The method has the advantages of simple procedure to make solutions, relatively less sensitivity to moisture, and the potential to make thick films. The thin films demonstrate "square" hysteresis loop behavior with very distinct phase transition field and zero remanant polarization value at zero field, and are very promising for decoupling capacitor applications in advanced multichip modules.

Acknowledgments

The authors would like to thank Drs. K. K. Li, H. D. Chen and Mr. C. J. Gaskey for their help at the initial stage of this work, and Dr. Q. M. Zhang for his valuable

discussions. This work is supported by the Office of Naval Research under the contract No. N00094-96-1-1066.

References

1. B. Jaffe, W. R. Cooke, Jr., and H. Jaffe, *Piezoelectric ceramics* (Academic, London, 1971).
2. D. Berlincourt, H. Jaffe, H. H. A. Krueger, and B. Jaffe, *Appl. Phys. Lett.*, **3** (1963) 90.
3. W. Y. Pan, C. Q. Dam, Q. M. Zhang, and L. E. Cross, *J. Appl. Phys.*, **66** (1989) 6014.
4. D. Berlincourt, *IEEE Trans. Sonics Ultrason.*, **SU-13** (1966) 116.
5. B. Jaffe, *Proc. IRE*, **49** (1961) 1264.
6. K. G. Brooks, J. Chen, K. R. Udayakumar, and L. E. Cross, *Mater. Res. Soc. Symp. Proc.*, **243** (1992) 443.
7. S. S. Sengupta, D. Roberts, J. F. Li, M. C. Kim, and D. A. Payne, *J. Appl. Phys.*, **78** (1995) 1171.
8. C. J. Gaskey, K. R. Udayakumar, H. D. Chen, and L. E. Cross, *J. Mater. Res.*, **10** (1995) 2764.
9. G. Yi, Z. Wu, and M. Sayer, *J. Appl. Phys.*, **64** (1988) 2717.
10. C. D. Chandler, C. Roger, and M. J. Hampden-Smith, *Chem. Rev.*, **93** (1993) 1205.
11. B. A. Tuttle and R. W. Schwartz, *MRS Bulletin*, **21** (6) (1996) 49.
12. H. D. Chen, K. R. Udayakumar, C. J. Gaskey, and L. E. Cross, *J. Am. Ceram. Soc.*, **79** (1995) 2189.
13. C. J. Gaskey, K. R. Udayakumar, H. D. Chen, and L. E. Cross, in *Proceedings of the Eighth IEEE International Symposium of Ferroelectrics* (IEEE Catalog No. 90CH3080-9, 1992), 416.

Captions of Figures

Fig. 1. Delineation of slanted and square hysteresis loop behavior, reproduced from Berlincourt [4]. Also indicated are definitions of forward and backward switching fields, E_f and E_b .

Fig. 2. Flow chart for the sol-gel processing of PLZST thin films.

Fig. 3. Hysteresis loop behavior of the PLZST thin films.

X: Voltage, 5 V/division; or electric field, 125 (kV/cm)/division.

Y: Polarization, 10 ($\mu\text{C}/\text{cm}^2$)/division.

Fig. 4. Dependence of capacitance on DC bias.

Table 1. Electrical properties of the PLZST thin films

Film thickness (μm)	ϵ_r at 1 kHz	$\tan\delta$ (%)	E_{AF-F} (kV/cm)	E_{F-AF} (kV/cm)	P_{max} ($\mu\text{C}/\text{cm}^2$)
0.40	210	1.50	250	165	37

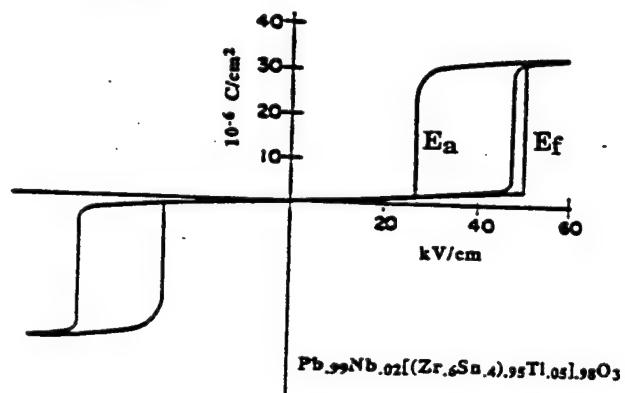
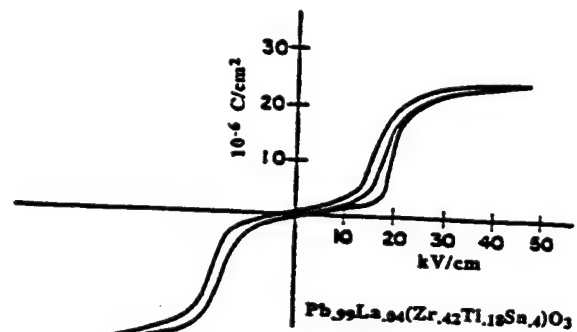


Fig. 1.

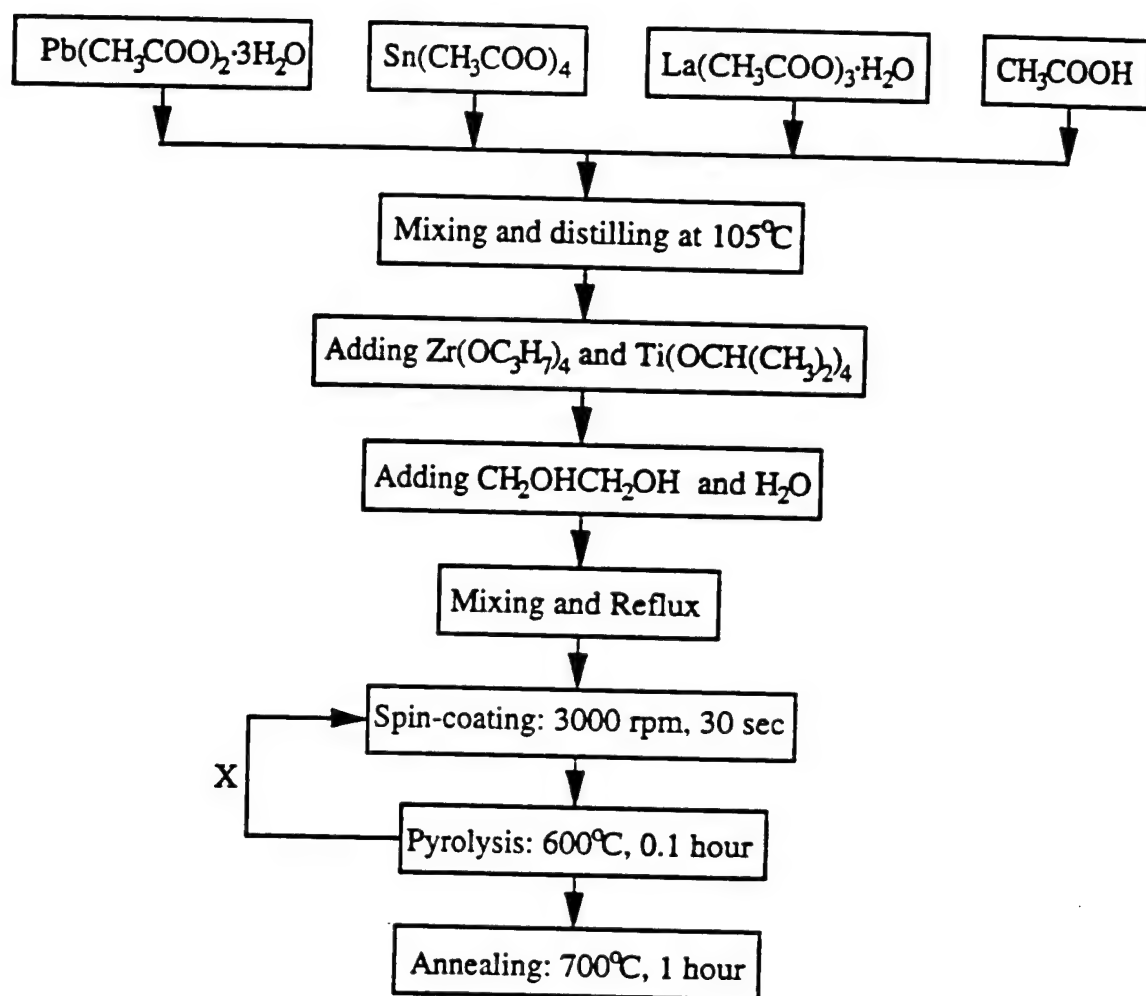


Fig. 2.

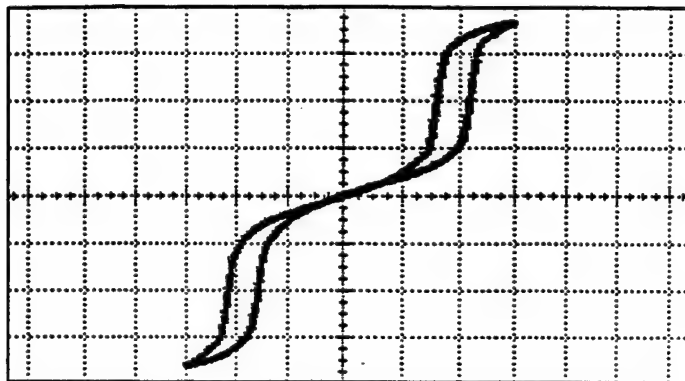


Fig. 3

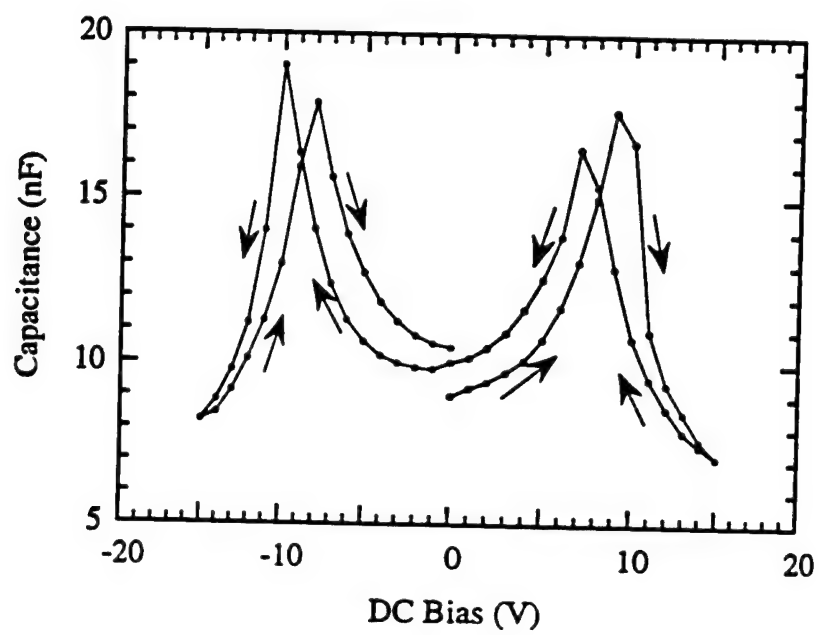


Fig. 4

APPENDIX 91

ANTIFERROELECTRIC THIN FILMS FOR DECOUPLING CAPACITOR AND MICROACTUATOR APPLICATIONS

BAOMIN XU, NEELESH G. PAI, PAUL MOSES, AND L. ERIC CROSS
Intercollege Materials Research Laboratory, Pennsylvania State University, University Park,
PA 16802

ABSTRACT

Lanthanum-doped or niobium-doped lead zirconate titanate stannate antiferroelectric thin films with the thickness of about 0.4 μm have been prepared from acetic acid-based or 2-methoxyethanol-based sol-gel method. All the films have the maximum polarization larger than 30 $\mu\text{C}/\text{cm}^2$ and show zero remanent polarization. By choosing appropriate compositions, we can make the films have "square" hysteresis loops with very sharp phase transition or "slanted" hysteresis loops with very small hysteresis. The properties that are important for decoupling capacitor and microactuator applications are characterized. For decoupling capacitor applications, films having square hysteresis loops with energy storage density of up to 7 J/cm^3 can be made, which release more than half of their stored charge in 10 ns with a maximum current density of more than 9400 A/cm^2 . For microactuator applications, the films can either have a strain level of 0.32% with very small hysteresis or have a strain level of 0.42% with moderate hysteresis.

INTRODUCTION

Since antiferroelectric materials can have higher energy storage density and larger strain levels as compared to ferroelectric materials [1-4], antiferroelectric thin films have been studied since the 1990s for applications such as microactuators in microelectromechanical systems (MEMS) and decoupling capacitors in high speed multichip modules (MCMs) [5-8]. It has been found that in bulk materials, the antiferroelectric to ferroelectric phase transition can occur as a step function of electric fields or change gradually with electric fields, which are characterized by "square" and "slanted" hysteresis loops [2]. However, most antiferroelectric thin films have slanted type hysteresis loops with some remanent polarization, showing that their ferroelectric properties are not as good as bulk materials [5,7].

In this paper, we will report that both lanthanum-doped and niobium-doped lead zirconate titanate stannate antiferroelectric thin films can be prepared from acetic acid-based or 2-methoxyethanol-based sol-gel method. All these films demonstrate zero remanent polarization after the electric field is removed. Depending on compositions, the films can have square hysteresis loops with sharp phase transition or slanted hysteresis loops with very small hysteresis. The most important properties for decoupling capacitor and actuator applications, that is, the charge release speed and phase transition strain of these films, have been characterized.

EXPERIMENT

The compositions used in this work are $\text{Pb}_{0.97}\text{La}_{0.02}(\text{Zr}_{0.85}\text{Sn}_{0.13}\text{Ti}_{0.02})\text{O}_3$ (abbreviated as PL-1), $\text{Pb}_{0.97}\text{La}_{0.02}(\text{Zr}_{0.65}\text{Sn}_{0.31}\text{Ti}_{0.04})\text{O}_3$ (abbreviated as PL-2) and $\text{Pb}_{0.99}\text{Nb}_{0.02}(\text{Zr}_{0.35}\text{Sn}_{0.13}\text{Ti}_{0.02})_{0.98}\text{O}_3$ (abbreviated as PN-1). The PL-1 and PL-2 samples are prepared from acetic acid-based method and the PN-1 samples are prepared from 2-methoxyethanol-based method. The flow charts of these two methods are given in Fig. 1 and Fig. 2 respectively. For acetic acid-based method, lead acetate trihydrate, lanthanum ethoxide, and tin acetate were initially dissolved in acetic acid, and the associated water was removed during a period of distillation at 150°C for 2 min. After cooling to room temperature, titanium isopropoxide and zirconium n-propoxide were added to the solution and mixed in the flask at 105°C for 1 h. Ethylene glycol and deionized water were also added during reflux to control the concentration and viscosity of the solution. For the 2-methoxyethanol-based method, lead acetylacetonate, titanium isopropoxide, zirconium n-propoxide, tin acetate, and niobium ethoxide were added to 2-methoxyethanol and the mixture was refluxed at 115°C for 12h.

The solution was then cooled to room temperature and 4% formamide was added to promote proper drying. All the solutions were adjusted to a 0.4 M concentration.

Thin films were prepared through a multiple spin coating procedure. The substrate is n-type, (100) oriented silicon wafer with 0.5 μm thick thermally grown SiO_2 layer, 0.02 μm thick sputtered titanium layer, and 0.15 μm thick sputtered platinum bottom electrode. For the acetic acid-based method, the films were pyrolyzed at 600°C for 0.1 h in a commercial box furnace after the deposition of each layer and annealed at 700°C for 1 h after the final layer deposition. For the 2-methoxyethanol-based method, the pyrolysis condition is 400°C for 5 min on a hot plate and the annealing condition is 700°C for 15 min.

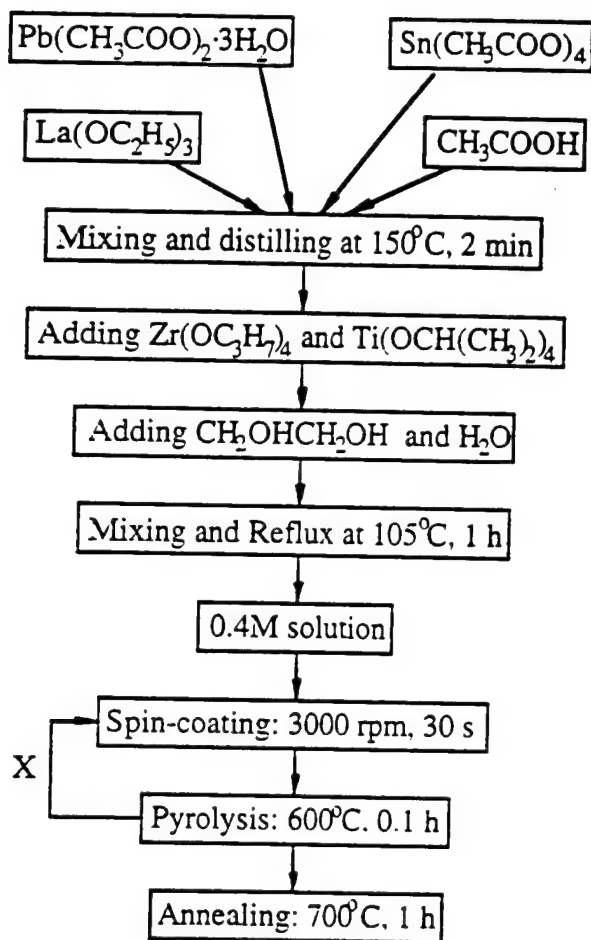


Fig. 1. Flow chart to make the thin films using acetic acid-based method

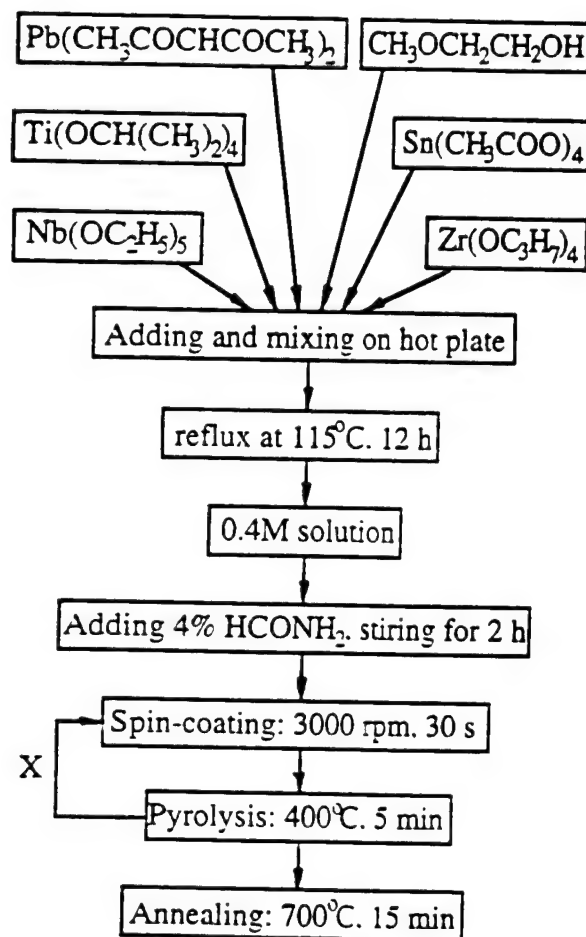


Fig. 2. Flow chart to make the thin films using 2-methoxyethanol-based method

For the general electrical characterization of the films, platinum top electrodes with a diameter of 1.6 mm were deposited by rf sputtering method. The thickness of the films were determined from surface profilometer traces. The low field dielectric properties were measured using an HP4274A LCR meter with an oscillating field of about 2 mV/ μm and a frequency of 1 kHz. The hysteresis loops were measured using a modified Sawyer-Tower circuit with a 50 Hz, triangular waveform driving signal. The measurements for charge release and phase transition strains are explained later in this paper.

RESULTS AND DISCUSSION

Dielectric and Ferroelectric Properties

The hysteresis loops of the samples are given in Fig. 3, and the electric property data are summarized in Table I. It can be seen that all the films have relatively low dielectric loss (lower than 2.0% for Samples PL-1 and PN-1 and lower than 3.0% for Sample PL-2) and maximum polarization larger than $30 \mu\text{C}/\text{cm}^2$. Samples PL-1 and PN-1 have square hysteresis loops and zero remanent polarization. Their phase transition fields were determined by extrapolating the steepest sections of the hysteresis loops and obtaining their intersections with the horizontal axis. The energy storage density values were obtained by calculating the area between the vertical axis and the backward arm of the hysteresis loop. These two kinds of samples (especially Sample PL-1) are very promising for decoupling capacitor applications as well as microactuator applications. Sample PL-2 has a slanted hysteresis loop with zero remanent polarization and small hysteresis, which is ideal for microactuation applications. The phase transition field values of Sample PL-2 can not be given because of the gradual phase transition.

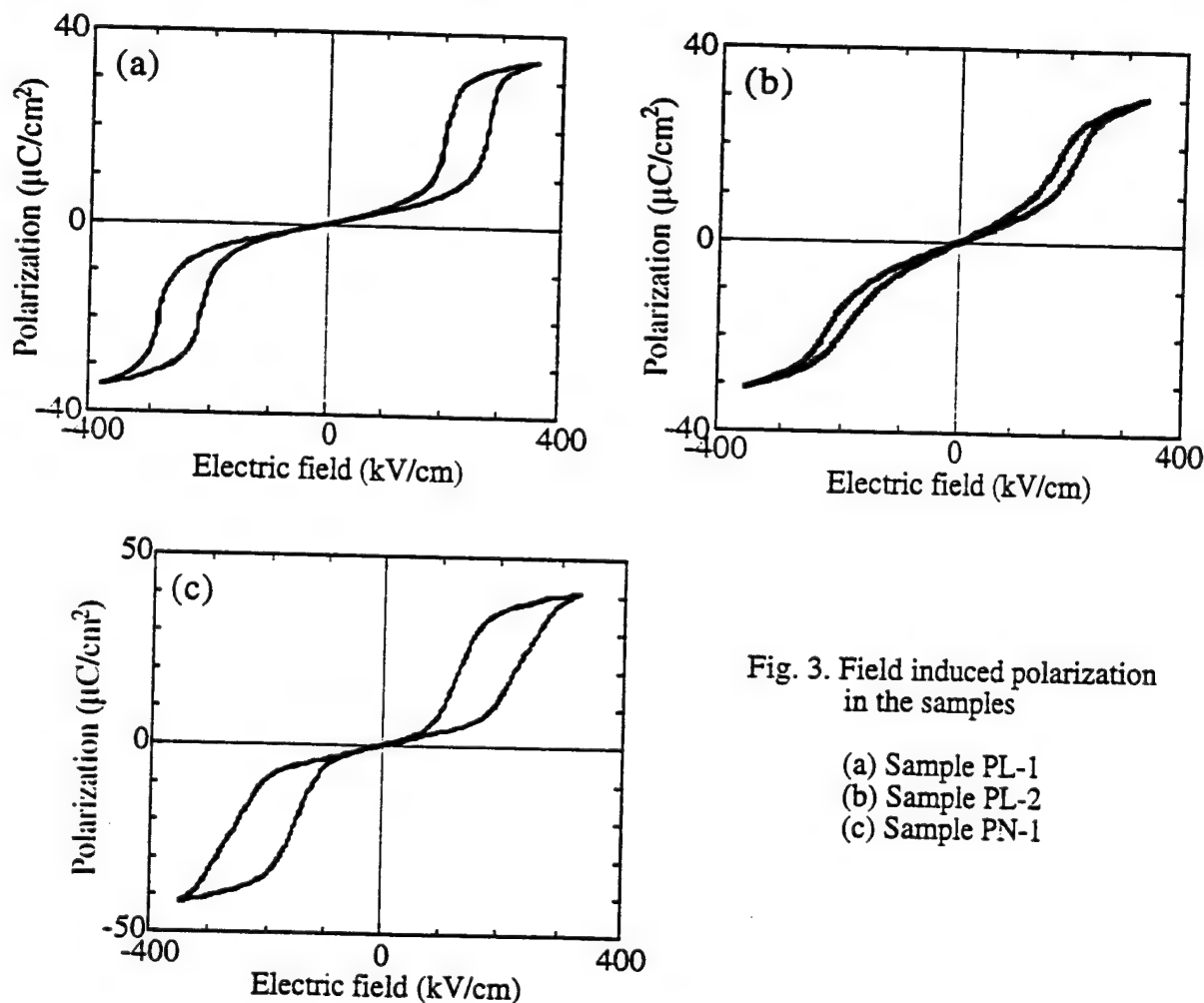


Fig. 3. Field induced polarization in the samples

- (a) Sample PL-1
- (b) Sample PL-2
- (c) Sample PN-1

Table I. Electrical Properties of the Thin Films

Sample Notation	Thickness (μm)	ϵ_r	$\tan\delta$ (%)	$E_{AF \rightarrow F}$ (kV/cm)	$E_{F \rightarrow AF}$ (kV/cm)	P_{\max} ($\mu\text{C}/\text{cm}^2$)	Energy storage density (J/cm^3)
PL-1	0.40	210	1.46	250	175	35	7.0
PL-2	0.36	360	2.75	—	—	30	—
PN-1	0.43	280	1.97	160	75	41	5.8

Charge Release and Backward Phase Transition

Charge release speed is very important for the decoupling capacitors used in high speed MCMs. The charge release speed of Sample PL-1 was characterized by measuring the discharge or switching current in nanoseconds range. For this measurement, the platinum top electrode with 0.1 mm in diameter was used considering the possibility of large switching current in the films. The field induced charge in the films with diameter = 0.1 mm electrodes are shown in Fig. 4. The block diagram of the measurement setup are given in Fig. 5. The measurement principle is that, first a DC voltage of 15V was applied to the sample, charging the sample and inducing the antiferroelectric to ferroelectric phase transition hence the maximum polarization was reached. Then the applied voltage was removed quickly, simultaneously short-circuiting the sample so that the sample can be discharged and brought back to the original antiferroelectric phase. The charge and discharge conditions were controlled through the relay and the switching current was determined by measuring the current through the small resistor R_2 . Fig. 6 shows the measurement result. Channel 1 (lower curve) is the trace of applied voltage vs time and channel 2 (upper curve) is the trace of voltage across R_2 vs time, which can be viewed as discharge current vs time. It demonstrates that the maximum current value can reach 0.74 A, which is equivalent to a current density of more than 9400 A/cm². The area between the time axis and the current curve represents the released charge. Calculating the area from $t = 0$ to $t = 10$ ns indicates that the charge released in 10 ns is about 1.98 nC. Fig. 4 shows the total stored charge is 3.5 nC. Therefore, 56.6% of the stored charge can be released in 10 ns.

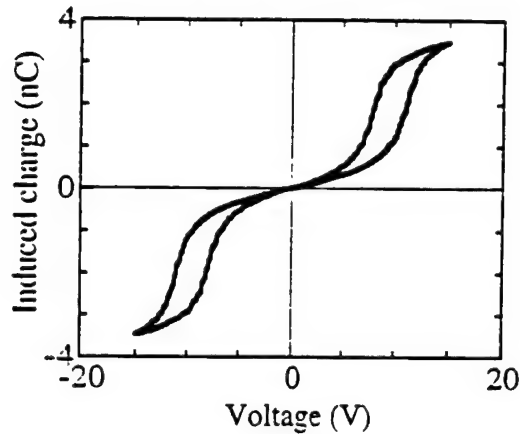


Fig. 4. Field (voltage) induced charge in Sample PL-1 ($\phi = 0.1$ mm electrode)

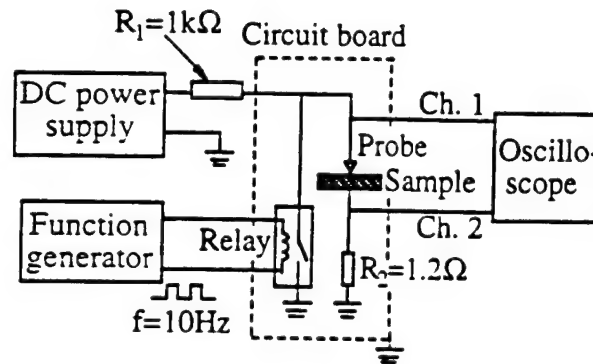


Fig. 5. Switching current measurement setup

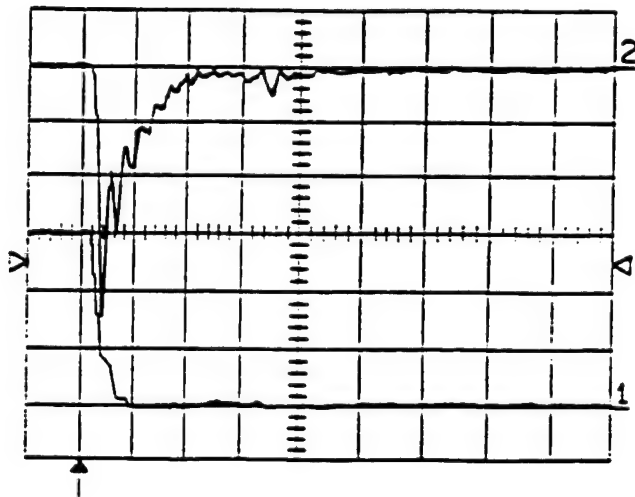


Fig. 6. Switching current of the Sample PL-1 ($\phi = 0.1$ mm electrode)

X axis: time, 5 ns/division.

Y axis:

Channel 1(lower curve), applied voltage, 5 V/division.

Channel 2 (upper curve), voltage across the 1.2 Ω resistor, 0.2 V/division; or switching current, 0.167 A/division.

The backward phase transition time can be defined as the time at which the switching current decreases to 10% of the peak value [9,10]. From Fig. 6 it can be determined to be about 6 ns for Sample PL-1. Typical bulk materials have transition times of 2 μ s [10], hence the backward phase transition time of thin films is about three orders of magnitude smaller than that of bulk materials. This may be caused by the effect of substrate. Due to the phase transition strain, at the thin film-substrate interface the film tends to change its dimensions while the substrate tries to remain its original dimensions, causing a substantial stress in the interface. This contributes to an extra driving force making the backward phase transition time of thin films much shorter than that of bulk materials under the stress-free mechanical boundary condition.

Phase Transition Strain

The phase transition strains of Samples PL-2 and PN-1 were measured by using the sensitive double beam laser interferometer. The top electrode area is 1.6 mm in diameter. The description of the measurement setup can be found in Refs. [11] and [12], but an oscilloscope is used as the final data output instead of lock-in amplifier because of the nonlinear relationship between the driving field and phase transition strain. The oscilloscope is controlled by a computer. A driving voltage with 100 Hz, triangular waveform was used. The phase transition strain curves of these two samples are given in Fig. 7. The maximum strain levels can reach 0.32% for Sample PL-2 and 0.42% for sample PN-1. This is comparable to most bulk materials which have strain levels of around 0.4% [4].

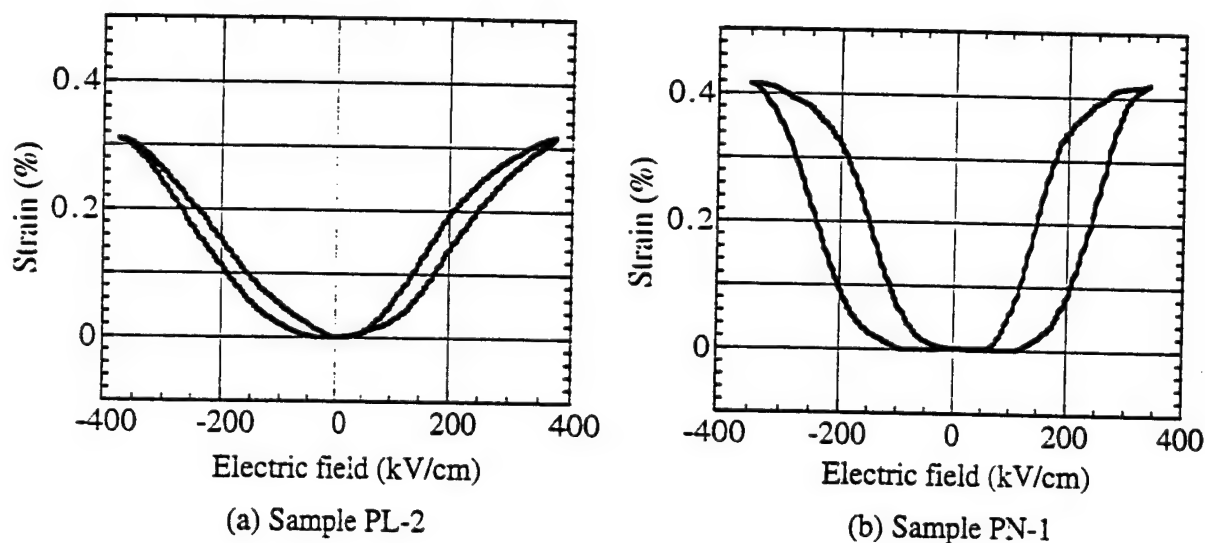


Fig. 7. Field induced strains of the samples

Corresponding to the shape of the hysteresis loops, the strain curve of Sample PL-2 has very small hysteresis and the strain increases gradually with electric field, which is suitable for analog mechanical response applications. The strain curve of Sample PN-1 has a moderate hysteresis, and the strain begins to be generated only when the applied electric field is larger than 100 kV/cm, showing a digital response character to some extent. The strain levels shown in Fig. 7 are much larger than the data reported before, such as 0.16% in refs. [5] and [7], which can be attributed to several factors. First, the present samples have much larger maximum polarization, which greatly enhances the polarization strain. Secondly, the zero remanent polarization, implying no retention of the ferroelectric phase in these films, may indicate that there is much less internal stress in the films, and this internal stress is a factor believed to retard the antiferroelectric to ferroelectric phase transition and reduce the phase transition strain [5]. Thirdly, electric fields of more than 300 kV/cm are used here, which is much larger than the electric fields used in the earlier reports (225 kV/cm in [5] and 160 kV/cm in [7]).

CONCLUSIONS

Lanthanum-doped or niobium-doped lead zirconate titanate stannate antiferroelectric thin films with zero remanent polarization and either square or slanted hysteresis loops were prepared from acetic acid-based or 2-methoxyethanol-based sol-gel method. All the films have maximum polarization larger than $30 \mu\text{C}/\text{cm}^2$. For decoupling capacitor applications, the energy storage density of the films can reach $7 \text{ J}/\text{cm}^3$, and more than half of the stored charge can be released in 10 ns with the maximum current density larger than $9400 \text{ A}/\text{cm}^2$. For actuator applications, the phase transition strain can reach 0.32% for the films with very small hysteresis or 0.42% for the films with moderate hysteresis.

ACKNOWLEDGMENT

The authors gratefully acknowledge Dr. Qiming Zhang for his valuable discussion and the Office of Naval Research for the financial support.

REFERENCES

1. B. Jaffe, *Proc. IRE*, **49**, 1264 (1961).
2. D. Berlincourt, *IEEE Trans. Sonics. Ultrason.*, **13**, 116 (1966).
3. W. Y. Pan, C. Q. Dam, Q. M. Zhang, and L. E. Cross, *J. Appl. Phys.*, **66**, 6014 (1989).
4. K. Markowski, S. E. Park, S. Yoshikawa, and L. E. Cross, *J. Am. Ceram. Soc.*, **79**, 3297 (1996).
5. K. G. Brooks, J. Chen, K. R. Udayakumar, and L. E. Cross, *J. Appl. Phys.*, **75**, 1699 (1994).
6. K. K. Li, F. Wang, and G. H. Haerting, *J. Mat. Sci.*, **30**, 1386 (1995).
7. S. S. Sengupta, D. Roberts, J. F. Li, M. C. Kim, and D. A. Payne, *J. Appl. Phys.*, **78**, 1171 (1995).
8. C. J. Gaskey, K. R. Udayakumar, H. D. Chen, and L. E. Cross, *J. Mat. Res.*, **10**, 2764 (1995).
9. E. Fatuzzo and W. J. Merz, *Phys. Rev.*, **116**, 61 (1959).
10. W. Y. Pan, W. Y. Gu, and L. E. Cross, *Ferroelectrics*, **99**, 185 (1989).
11. Q. M. Zhang, W. Y. Pan, and L. E. Cross, *J. Appl. Phys.*, **63**, 2492 (1988).
12. W. Y. Pan and L. E. Cross, *Rev. Sci. Instrum.*, **60**, 2701 (1989).

Domain Studies

APPENDIX 92

Direct Observation of Ferroelectric Domains in LiTaO₃ Using Environmental Scanning Electron Microscopy

Shining Zhu* and Wenwu Cao

Intercollege Materials Research Laboratory, The Pennsylvania State University, University Park, Pennsylvania 16802
(Received 31 March 1997)

Direct observation of ferroelectric domain structures in LiTaO₃ crystal, without etching or surface coating, has been realized by using environmental scanning electron microscopy in secondary electron emission mode. The new method can nondestructively provide domain contrast image at submicron resolution, and the domain contrast image is very stable. Conditions for best domain contrast of LiTaO₃ crystals have been established. [S0031-9007(97)04101-X]

PACS numbers: 77.80.Dj, 61.16.Bg, 61.72.Mm, 77.22.Ej

In recent years, scanning electron microscopy (SEM) has found applications in the study of ferroelectric domain structures [1–4]. Using low accelerating voltage a contrast between antiparallel ferroelectric domains can be imaged on an unmetalized polar crystal surface in secondary electron emission mode. The technique does not need special treatment of the sample surface and is nondestructive. It has been successfully used to study domain structures of several ferroelectric crystals [5–7].

In the SEM method, the key is to avoid surface charge accumulation onto an insulating crystal. The experimental conditions are very strict; particularly, the choice of probe current and accelerating voltage is very critical, and no contrast can be found if the parameters are not properly chosen. Moreover, the contrast image is short lived; i.e., it disappears under the influence of electron beam after a few seconds to a few minutes. The observation time for the contrast shortens with the increase of accelerating voltage and magnification. Consequently, it is not possible to obtain a stable contrast image with high resolution and magnification [1,2].

In this Letter we report a new secondary electron image (SEI) technique of observing ferroelectric domains by using environmental scanning electron microscopy (ESEM). Because the ESEM [8,9] can operate at pressures 10 000 times higher than that of standard SEM, the free ions which are created by collisions between moving electrons and neutral gas molecules can be used to provide a conducting path for beam-deposited surface charges, which allows one to examine unprepared, uncoated insulating samples. The results show that one can obtain *stable* domain contrast under relatively high accelerating voltage, large beam current, and slow scan rate using ESEM. Because higher accelerating voltage can be used, higher resolution than the conventional SEM is expected. The technique has been applied to a LiTaO₃ crystal with uncoated surface. A clear stable secondary electron image of the domain structures was obtained.

The spontaneous polarization P_s of LiTaO₃ can be reversed by a pulse electric field at room temperature [10]. Using different electrode pattern LiTaO₃ crystals can be

poled into periodic and quasiperiodic domain structures which have been widely used in acoustics [11], nonlinear optics, and solid state laser devices [12–16]. Preliminary examination of the domain structure in a poled LiTaO₃ sample was made by optical microscopy on an etched surface. The destructive method of etching often affects further experiments on the sample. Therefore, it is desirable to develop new convenient nondestructive methods for the observation of domain patterns on an unprepared surface of a poled LiTaO₃ crystal.

In this work we used *c*-cut LiTaO₃ crystal wafers. The domain structures in the wafers were engineered by field poling method at room temperature. Two kinds of aluminum electrodes were fabricated: one is periodic and the other is uniform plane. During pulse poling using the above two kinds of electrodes two types of domain morphology, stripe and triangular shape, were produced.

The domain observations were performed using an ESEM (ElectroScan Model E-3, Wilmination, MA) in secondary electron emission mode. Figure 1 is a schematic diagram of the experimental arrangement and crystal orientation. A periodically poled sample was etched in a solution containing 2 parts HNO₃ and 1 part HF for 15 h at room temperature, and was attached to an aluminum sample mount using double faced tape for observation. The sample mount was grounded. The electric potential of the detector was set at +0.5 kV. Water vapor was chosen as the imaging gas. Under normal observation condition of wet mode, chamber pressure 3–3.5 Torr, accelerating voltage 15 kV, condenser 40, scan rate 8–30 sec/frame, and aperture size 30 μ m, we got a topographic image of the periodic domain pattern on the \bar{c} surface, which is [001] orientation, as shown in Fig. 2(a). In the image the surfaces of negative domains are lower than those of positive domains. The formation of the surface steps is due to different etching rates of positive and negative domains in the acid. A wider stripe and some island domains shown in the figure are attributed to imperfect poling. One can see that the contrast only appears in domain boundaries which are brighter than the interior of domains, reflecting the fact

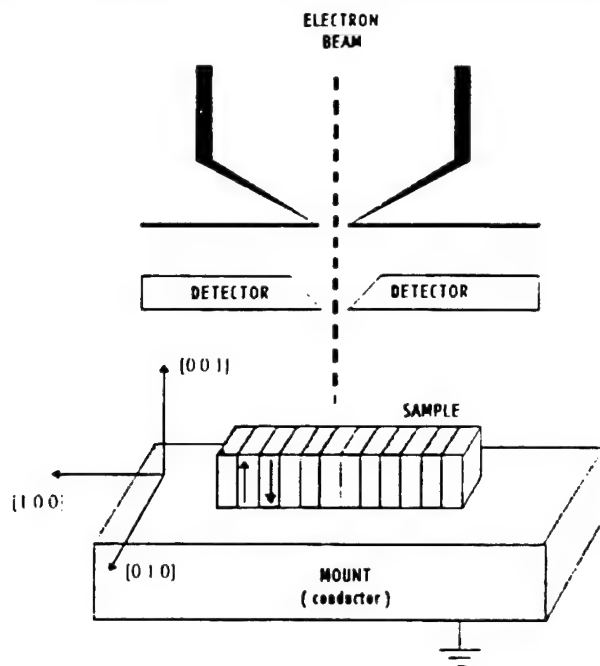


FIG. 1. Schematic diagram of the experimental arrangement.

that more secondary electrons are emitted at the edges of the etching steps. No contrast was revealed between the positive and negative domains due to the screening of the polarization P_s by the probing current. In other words, the positive and negative domains have nearly equal secondary electron emission rate.

After the first observation, the etched sample was taken out of the chamber and the [001] surface was polished. When the polished sample was reexamined using ESEM under the same condition, nothing interesting was seen except some polishing scratches on the surface. However, after the experiment parameters were changed by decreasing the chamber pressure, increasing the probe current by decreasing the condenser current and increasing the aperture, and increasing the accelerating voltage, contrast stripes began to appear [shown in Fig. 2(b)]. The locations and shapes of the contrast patterns in Fig. 2(b) exactly match the etched patterns in Fig. 2(a). This confirms that the contrast stripes originated from the antiparallel domains.

Optimum contrast was obtained under the following conditions: accelerating voltage, 30 kV; chamber pressure, 2 Torr; aperture size, 50 μm (maximum for the E-3 system); condenser, 10 (lowest of the E-3 system); and scan rate, 17–30 sec/frame. The positive domains were sufficiently brighter than the negative domains, indicating that the secondary electron emission from positive domains exceeds that from negative ones. The contrast is very stable in time, no change was observed over a period of 4 h which was the longest observation time used in our experiments. This is a marked advance from the conventional SEM method in which the contrast can only be kept for a few seconds to a few minutes [1,2].

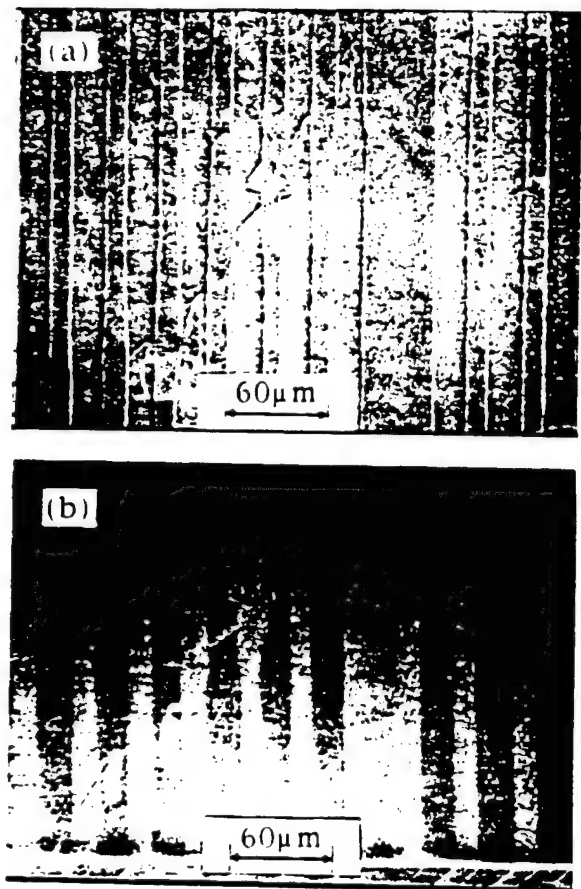


FIG. 2. Comparison of ESEM images of a surface portion in a c-cut LiTaO₃ with antiparallel domains. (a) Etched surface: voltage = 15 kV, condenser = 40, pressure = 3.0 Torr, and aperture = 30 μm . (b) Polished surface: voltage = 30 kV, condenser = 10, pressure = 2.0 Torr, and aperture = 50 μm .

With a slight tilt of the sample, we could simultaneously observe the previously etched patterns of the periodic domain structure on the [010] surface of the sample which was not polished [see the bottom of Fig. 2(b)]. The image patterns on the two adjacent [001] and [010] faces are consistent. However, if we tilt the sample to the [0 $\bar{1}$ 0] surface which was polished, no contrast stripes were found. This means that only the polar surfaces can show the domain contrast images.

We found that although higher contrast domain images could be obtained under the optimum conditions mentioned above, the experimental conditions are not very critical. With an aperture of 50 μm , domain contrast could appear in the range of accelerating voltages from 20–30 kV, condenser current setting from 10–30, scan rates from 4–60 sec/frame, and chamber pressure from 1.0–3.0 Torr. In all cases the positive domains were always brighter than the negative ones.

The visualization of domain contrast is also independent of surface roughness. We could clearly observe the contrast image of domains on a crack surface with appropriate conditions as shown in Fig. 3. The sample in

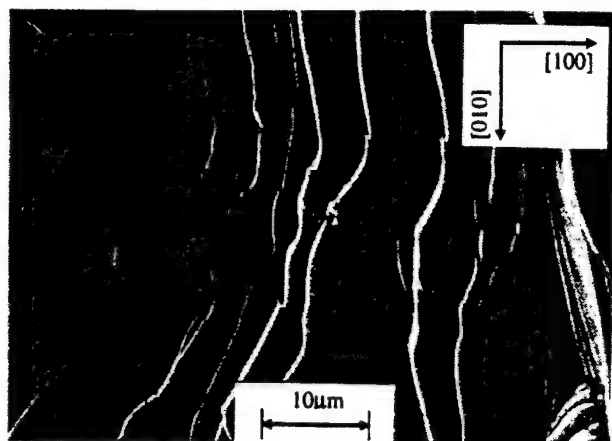


FIG. 3. ESEM image of a crack surface of LiTaO_3 crystal with nearly $[001]$ orientation. The sample was partially poled by a poling field of $E = 21 \text{ kV/cm}$. The triangular antiparallel domains with positive polarity are shown as brighter regions on the darker background. Image conditions: voltage = 30 kV, condenser = 10, pressure = 2.0 Torr, and aperture = 50 μm .

Fig. 3 was partially poled under a pair of plane aluminum electrodes. After poling, the electrodes were removed in NaOH solution which only resolves the aluminum but not the LiTaO_3 crystal. In Fig. 3 some triangular domains with positive polarity are shown as lighter regions on the dark background of negative polarity. Generally speaking, the morphology of the inverted domains depends on the symmetry of the crystal as well as the intensity of the poling field. The polarization direction of LiTaO_3 is parallel to its triad axis. Using a moderate field of $E = 21 \text{ kV/mm}$, the triangular shape inverted domains can be formed under plane electrode in a partial poling process. The sides of the triangle corresponding to domain walls are parallel to crystallographic x directions. Domains grow by gradually extending the domain walls along crystallographic y directions during poling. This is a typical growth morphology of the antiparallel domains of LiTaO_3 in a quasiequilibrium process through two-dimensional nucleation [17]. The domains in Fig. 3 have different sizes, which reveals that the polarization reversal in the crystal is through multisite nucleation and growth: i.e., a large number of inverted domains are nucleated first, then they grow and coalesce to complete the switching process.

The domain contrast in Fig. 3 is better than that in Fig. 2(b) which has to be contrast enhanced by computer. This is because a depolarization layer is produced on the polished surface, while the cracked surface has much less mechanical artifact; thus a better contrast image can be obtained. This phenomenon is also found in the domain contrast image observation using conventional SEM [1,2].

Le Bihan [1] proposed a theoretical model to explain the domain contrast of triglycine sulfate (TGS) crystal using conventional SEM under low voltage condition. It was assumed that the contrast of ferroelectric domains is

caused by polarization charges, hence the surface of positive domain should be darker than that of a negative domain. However, this is in contradiction with our results here. Generally speaking, for an insulating sample, surface electric charge equilibrium is the fundamental principle for producing these contrast images. In conventional SEM technique, the charge neutralization relies on the exact balance of surface input and output currents. The samples need to be slightly conductive or coated with a conducting layer in order to accomplish this task under vacuum. For the ESEM this charge balance is achieved by neutralizing surface electron buildup with positive ions under finite vapor pressure.

The secondary electron emission rate depends on the level of interaction between the electron beam and the surface layer of ferroelectric crystal. Although it is not clear if the probing current is sufficient to instantly screen the charge on the sample surface at each frame, there is definitely a charge balance after a short period of time. Therefore, the polarization charges cannot be the main cause of contrast due to the large amount of ionic composition under finite vapor pressure. Because the technique is new, the exact mechanism for the image formation is still under investigation.

In conclusion, for the first time we have successfully observed *stable contrast image* of antiparallel domains in poled LiTaO_3 crystals using ESEM technique. This technique is very promising since it allows us to directly observe antiparallel domains in an unetched and uncoated insulating sample surface. The condition for obtaining the contrast image is not very strict and the domain image for LiTaO_3 crystal is stable for several hours. From our experience, better image can be produced with higher voltage, lower condenser current, and larger aperture (more electrons). Because the ions produce a conducting path to neutralize the surface charge accumulation, the technique allows the use of higher accelerating voltage with higher magnification; therefore, submicron resolution can be obtained.

This research was sponsored by the NSF and the Office of Naval Research.

*Permanent address: Physics Department, Nanjing University, Nanjing 210093, People's Republic of China.

- [1] R. Le Bihan, *Ferroelectrics* **97**, 19 (1989).
- [2] A. A. Sogor, *Ferroelectrics* **97**, 47 (1989).
- [3] T. Ozaki, K. Fujii, and S. Aoyagi, *J. Appl. Phys.* **80**, 1697 (1996).
- [4] G. Rosenman *et al.*, *J. Appl. Phys.* **80**, 7166 (1996).
- [5] B. Hlilczar, L. Szczesniak, and K. P. Meyer, *Ferroelectrics* **97**, 59 (1989).
- [6] D. V. Roshchupkin and M. Brunel, *Scanning Microsc.* **7**, 543 (1993).
- [7] A. S. Oleinik and V. A. Bokov, *Sov. Phys. Solid State* **17**, 560 (1975).

-
- [8] G.D. Danilatos, *Adv. Electron. Electron Phys.* **71**, 109 (1988).
 - [9] G.D. Danilatos, *Adv. Electron. Electron Phys.* **78**, 1 (1989).
 - [10] S.N. Zhu *et al.*, *J. Appl. Phys.* **77**, 5481 (1995).
 - [11] Y.F. Chen, S.N. Zhu, Y.Y. Zhu, and N.B. Ming, *Appl. Phys. Lett.* **70**, 592 (1997).
 - [12] C. Baron, H. Cheng, and M.C. Gupta, *Appl. Phys. Lett.* **68**, 481 (1996).
 - [13] R.L. Byer, *Nonlinear Opt.* **7**, 234 (1994).
 - [14] S.N. Zhu *et al.*, *Appl. Phys. Lett.* **67**, 320 (1995).
 - [15] K.S. Abedin, T. Tsuritani, M. Sato, and H. Ito, *Appl. Phys. Lett.* **70**, 10 (1997).
 - [16] S.N. Zhu, Y.Y. Zhu, Y.Q. Qin, H.F. Wang, C.Z. Ge, and N.B. Ming, *Phys. Rev. Lett.* **78**, 2752 (1997).
 - [17] V.Y. Shur and E.L. Rumyantsev, *Ferroelectrics* **151**, 171 (1994).

APPENDIX 93



GRAIN SIZE AND DOMAIN SIZE RELATIONS IN BULK CERAMIC FERROELECTRIC MATERIALS

WENWU CAO and CLIVE A. RANDALL

Materials Research Laboratory, Pennsylvania State University, University Park, PA 16802, U.S.A.

(Received 13 March 1995; accepted 6 September 1995)

Abstract—A study of the ferroelastic domain size variations with grain sizes in $\text{Pb}(\text{Zr,Ti})\text{O}_3$ [PZT] ferroelectric ceramic has been conducted. Experimental results determined by a transmission electron microscopy (TEM) study on hard and soft PZT ceramics indicate that it is possible to observe a bulk metastable domain configuration in a thinned foil. The transmission electron microscopy observations demonstrate that the domain structures formed at the paraelectric-ferroelectric phase transition are strongly dependent on the elastic boundary conditions and crystallite sizes. Statistical analysis of the domain size distributions in PZT reveals that the traditional parabolic relation between grain size and domain size is only good for a limited size range of 1–10 μm . For grains size $> 10 \mu\text{m}$, the exponent tends to be smaller than 1/2, while for grain size $< 1 \mu\text{m}$ the exponent is larger than 1/2. We also report the analysis on poled ceramics which reveals for the first time direct evidence for transgranular domain switching mechanisms.

Keywords: A. ceramics, A. interfaces, C. electron microscopy, D. ferroelectricity, D. microstructures.

INTRODUCTION

Domain structures are generated during a structural phase transition to recover the lost symmetry operations [1, 2]. In ferroic materials, these domain structures can be switched by external (elastic, electric, or magnetic) fields. The domain population distribution is strongly affected by these fields, which in effect gives the extrinsic contributions.

Stable domain configurations in ferroic materials are the result of an energy balance. In the case of a ferroelectric system, stable domain configurations reflect the balance of anisotropy energy, domain wall energy, electric and elastic energies. Previous theoretical investigations considered the energy balance of elastic interactions between the system and a semi-infinite medium and that of the domain walls, which leads to a parabolic scaling ($m = 1/2$) of the grain-domain size relation [3–8],

$$\text{Domain Size} \propto (\text{Grain Size})^m. \quad (1)$$

Most previous domain size studies have focused on ceramic BaTiO_3 . One of the major reasons for studying this system is the strong macroscopic dielectric constant enhancement observed in the tetragonal ferroelectric phase of 1.0 μm grain materials compared to coarse grain ceramics and single crystals. The change of the dielectric constant with grain size has been accounted for in terms of the different stresses created under the spontaneous deformation at the cubic-tetragonal phase transition [9].

Arlt re-examined the domain size distributions in BaTiO_3 ceramic and showed the departure of the domain size grain size relation from the parabolic relation for grain size below 1 μm and about 10 μm [7]. Domain density is higher than the value predicted using the parabolic relation for submicron grains as shown in Fig. 1. For grain sizes larger than 10 μm , the exponent in eqn. (1), m , is found to be close to 1/3 in his experimental results. The slope becomes steeper as the grain size decreases. When the whole range of domain and grain sizes are considered, the fitting to the $m = 1/2$ is very poor as shown in Fig. 1. The current work is in part triggered by this observation. Our intention is to find out if the parabolic relation could hold for the PZT systems.

In practice, the size effect of domain structures is of importance to the future application trends in ferroelectric based materials. In the last few years there have been rapid advances in the ability to fabricate thin and thick films for applications such as memories, micromotors, thermal imaging, multilayer capacitors, and actuators [10, 11]. The miniaturization of ferroelectric based electroceramic components is accompanied by the necessity of the reduction of grain sizes. Consequently, the domain sizes, domain configurations, and domain wall mobility will all be changed with the size reduction.

Owing to the large contribution of the elastodielectric properties from the extrinsic mechanisms, i.e. domain walls motion, it is imperative to advance the

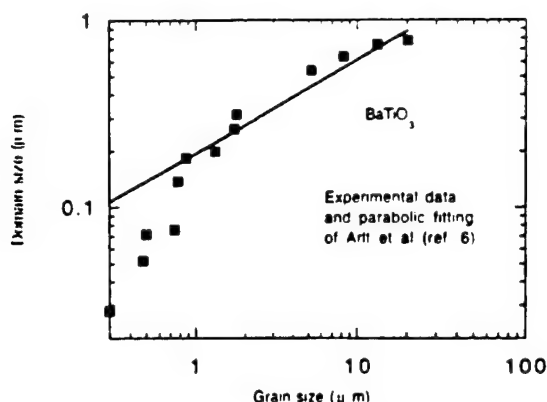


Fig. 1. Domain size vs grain size for BaTiO_3 ceramics, experimental results compared to parabolic relation (after Ref. [7]).

understanding of domain size effects in the submicron grain size ceramics [12, 13]. In this paper, we present some experimental studies on the domain size distributions in poled and unpoled PZT ceramics. In addition, thermally cycling effects on the domain populations in the thin foil samples used in the TEM experiments were also examined.

EXPERIMENTAL

Ceramic processing

Morphotropic phase boundary composition PZT has been investigated in sintered ceramics with a grain size variation from 0.2 to 14 μm . Starting powder size variations were obtained from solid state reactions using conventional and reactive calcination techniques [14, 15]. Grain size variations were obtained by controlling densification and grain growth during the sintering process. The submicron grain size ceramics were fabricated using hot pressing techniques; namely, hot uniaxial pressure (HUP) and hot isostatic pressure (HIP). The larger grain size ceramics ($>1 \mu\text{m}$) were sintered using conventional methods by varying temperature and time in closed crucibles and controlling the lead atmosphere with PbZrO_3 sources.

Two systems with the morphotropic composition were investigated in this study: one is undoped $\text{Pb}(\text{Zr}_{0.52}\text{Ti}_{0.48})\text{O}_3$, and the other is Nb-doped PZT based on compositional formula of $\text{Pb}_{0.988}(\text{Zr}_{0.52}\text{Ti}_{0.48})_{0.976}\text{Nb}_{0.024}\text{O}_3$ [16]. The undoped PZT is naturally a hard piezoelectric material owing to the superoxidation processes creating an excess of acceptor lead vacancies over oxygen vacancies. The Nb-donor doping is commonly used in commercial soft PZT for piezoelectric applications and is therefore regarded as a model system for this study.

Transmission electron microscopy

The domain size distributions and structures were investigated using analytical transmission electron microscopy (TEM); Phillips-420 STEM operated at 120 kV. TEM is most suited for microstructural investigations in the nanometer to micrometer size regime. Ferroelectric domains can be directly imaged using diffraction contrast imaging techniques [17, 18]. The observations were made on dense ($>95\%$ theoretical density) ceramic samples which were cut and polished to a thickness of 70 μm . Samples were epoxied to 3 mm copper grids before ion-beam thinning a 3 kV, with a 12°C glancing angle until electron transparent. The poled samples were prepared after exposure to a poling field of 40 kV/cm in a heated oil bath at 120°C for 20 min. Samples were prepared with the poling direction in the plane of the thin foil. A Gatan single tilt hot stage was used to heat thinned samples through the transition temperature to re-equilibrate the domain configurations in the foils used for TEM studies.

RESULTS AND DISCUSSION

In the nature of this experiment we must ensure that the obtained domain sizes by the TEM technique are representative of the bulk ceramic but not the ion-beam thinned foils. We found that in order for this to be true, the ferroelectric material must have a moderately high transition temperature compared with sample preparation and observation temperatures. The thermal and mechanical stresses have to be kept to a minimum during the cutting, polishing and ion-beam thinning processes. Under these conditions, samples prepared may preserve the bulk domain structures (which are metastable configurations in the thin foil).

Two tests were performed in the PZT samples to verify this fact. First, poled Nb-doped piezoelectric ceramics were thinned and shown to preserve an aligned domain configuration which is expected only in poled sample, as shown in Fig. 2 (a-c), indicating there were no major redistribution of the domains during the sample preparation procedure. Second, unpoled ceramic samples were analyzed for domain size distribution after ion beam thinning and later after being heated and cooled slowly through the transition temperature inside the TEM with a hot stage. A difference in the mode and shape of the distribution function of the domain sizes was observed before and after the foils were heated through the transition temperature. The domain sizes are shifted to multimodal distributions with the majority of domains smaller in the thin foil samples after the

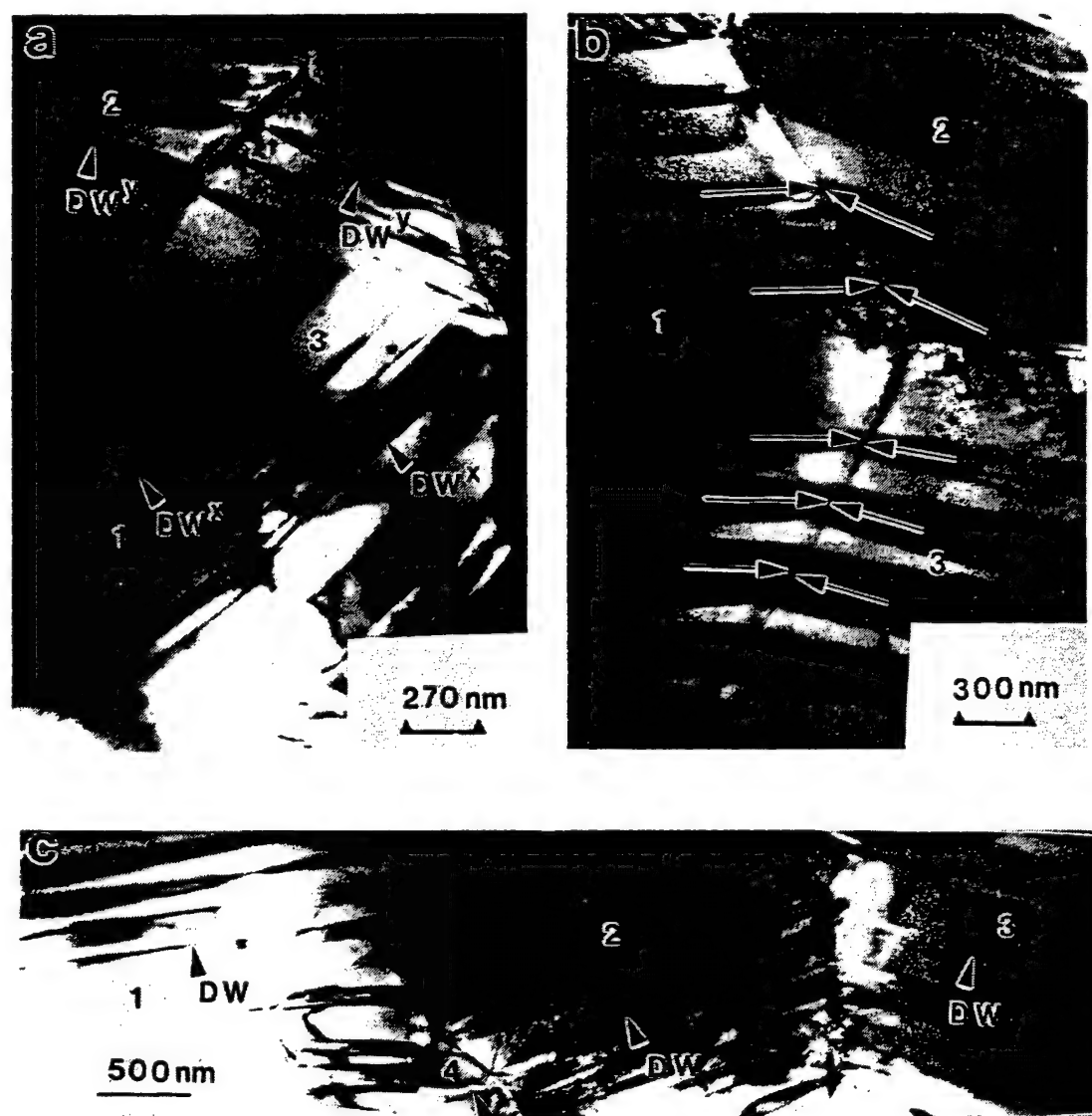


Fig. 2. (a)–(c) Multi-beam bright field TEM images of domain structures in a poled PZT ceramic foil. RAIN SIZE IN BULK

heat treatment, suggesting the domain patterns before heating are metastable. These test results support the claim that carefully prepared TEM samples can preserve domain structures representative of the bulk ceramic in systems with moderately high transition temperatures.

Figure 3 shows a selection of domain structures in a variety of grain size for PZT piezoelectric ceramics. We note in the finer grain ceramics ($0.2\mu\text{m}$) the domain walls generally have preferred orientations. In other words, the number of variants becomes less within each grain. The domain walls are generally periodic as shown in Figure 3(a) and transverse across the entire grain to pin on the grain boundaries. Figure 3(b) shows a typical domain structure for the soft PZT with a mean grain size $0.8\mu\text{m}$. Figure 3(c) shows a multimodal domain size distribution in soft PZT with

$1.8\mu\text{m}$ mean grain size after the thinned TEM foil was heated above the transition temperature and then slowly cooled in the microscope. Figure 3(d) is a typical complex multiple variant domain configuration for larger grain sized PZT.

A statistical analysis of the grain and domain sizes is determined directly by measuring scanning electron microscope (SEM) micrographs of etched ceramics and TEM micrographs, respectively. The domains measured were limited to those tilted such that no δ fringes are observed; i.e. domain wall planes are parallel to the electron beam direction [17, 18]. The histograms for the grain size are in general symmetric and therefore the mode and the mean are almost the same as observed in the typical histograms [see Fig. 4(a)]. However, the histograms of the domain size distributions are often skewed, an example is given in

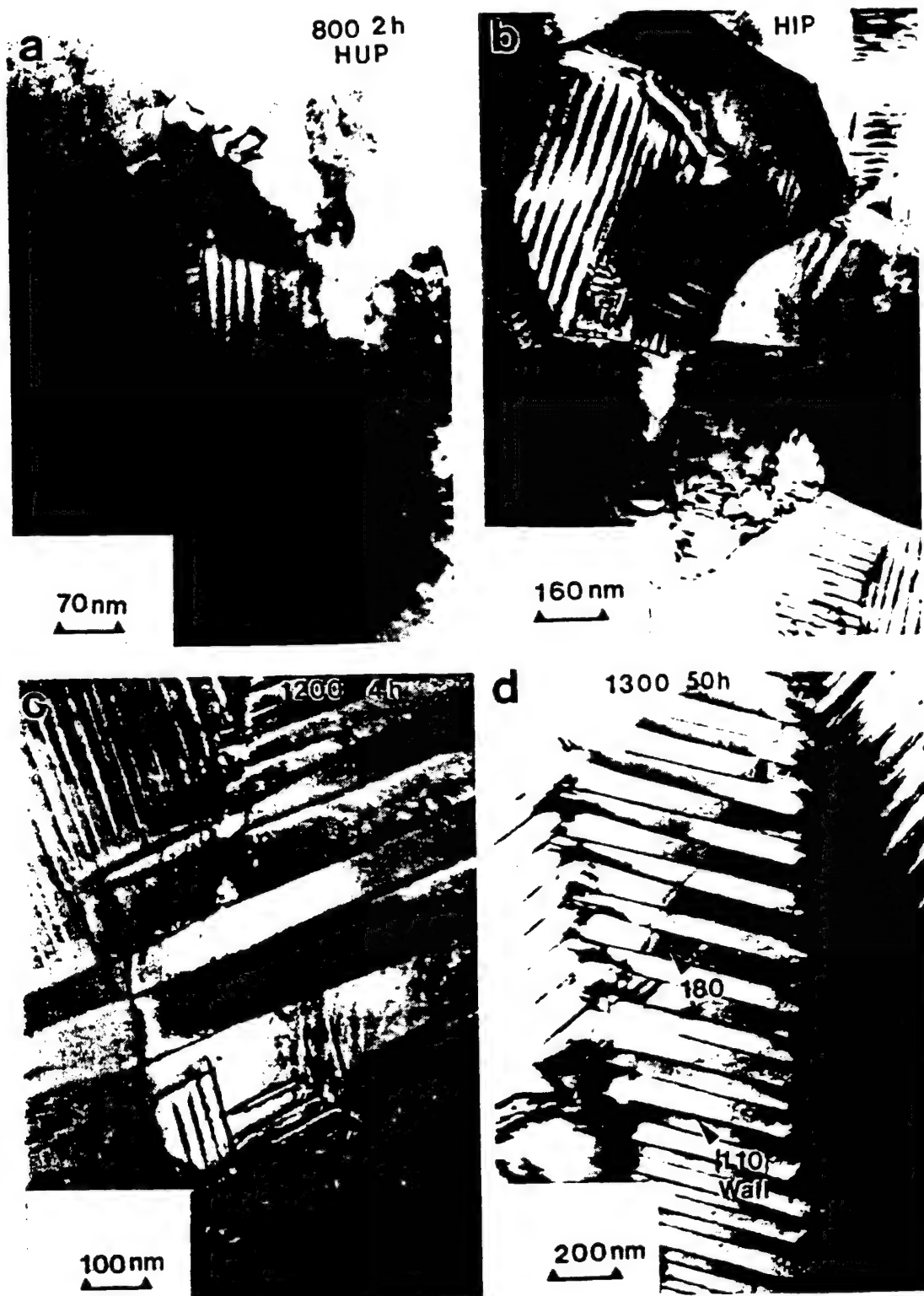


Fig. 3. Typical bright field images of ferroelectric domain structures in (a) 0.2 μm , (b) 0.8 μm , (c) 1.8 μm , and (d) 14 μm bulk ceramics.

Fig. 4(b), therefore, the modes of the domain distribution are selected for comparison. The mode in the distribution corresponding to the most probable domain size as indicated in Fig. 4(a), but not the

mean value. The mode values and the errors based on a full width half maximum distribution are listed in Table 1.

The experimental values for the domain sizes are

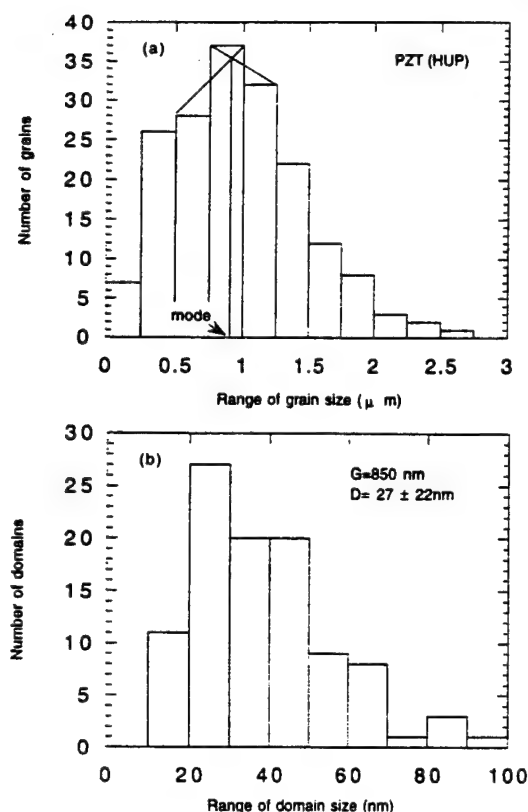


Fig. 4. Typical histograms of (a) grain size distribution of undoped PZT, $G_{\text{mode}} = 0.8 \mu\text{m}$ and (b) domain size distribution of Nb-doped PZT, $D_{\text{mode}} = 0.2 \mu\text{m}$.

plotted against the corresponding grain sizes in Fig. 5(a) and (b) for Nb-doped and undoped PZT, respectively. For both compositions of grain sizes between $1.0 \mu\text{m}$ and $10 \mu\text{m}$ the exponent is found to be approximately $m \approx 0.5 \pm 0.03$, consistent with previous bulk ceramic studies. However, the domain size in the

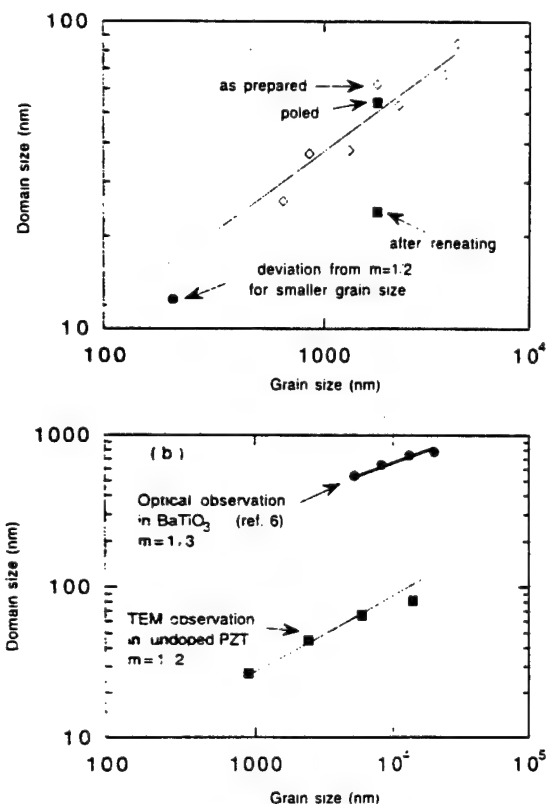


Fig. 5. (a) Logarithmic plot of measured domain size vs grain size for Nb-doped PZT ceramics and the parabolic relation. (b) Comparison of the domain size grain size relation in undoped PZT and large grain BaTiO_3 . The exponent, m , for BaTiO_3 of large grains is $\sim 1/3$ while for PZT is $\sim 1/2$ except the largest grain sample which shows deviation to higher domain density (not in the figure).

$0.1 \mu\text{m}$ grain sample shows departure from the $m = 1/2$ curve as shown in Fig. 6(a). Similar departures have been reported for domain structures in the

Table 1. Sintering conditions for the PZT samples, and the measured grain size, domain size and the estimated errors

Firing conditions	Mean grain size (μm)	Mode grain size (μm)	Standard error of grain size (μm)	Mode domain size (nm)	Estimated domain size error in mode (\pm nm)	Comments
Nb-doped PZT						
800°C 2 hr	0.17	0.16	0.005	12	3	Hot Pressed
970°C 4 hr	0.64	—	0.020	30	15	Conventional & HIP
900°C 2 hr	—	—	—	—	—	—
1000°C 4 hr	0.85	0.78	0.020	37	22	Conventional
1100°C 4 hr	1.32	1.30	0.025	38	10	Conventional
1200°C 4 hr	1.82	—	0.030	63	12.5	Conventional
1250°C 4 hr	2.30	—	0.038	53	8.5	Conventional
1300°C 50 hr	3.95	3.85	0.230	67	11	Conventional
Unknown*	4.5†	—	—	85	—	—
Undoped PZT						
800°C 2 hr	0.98	0.82	0.037	26	9.5	Hot pressed
1000°C 4 hr	2.4	2.2	0.12	49	20	Conventional
1200°C 4 hr	5.9	—	0.19	66	10	Conventional
1300°C 50 hr	14.3	12.5	0.59	82	13	Conventional

* Commercial soft PZT, † Grain size determined from line intercept

fine grain thin film ferroelectrics [19]. The departure to higher domain densities in submicron grains may be associated with the inhomogeneous strain fields, which also have been found to increase the domain densities in highly defective coelastic crystals [4]. With higher domain densities, one might expect a larger extrinsic contribution to elastodielectric properties, but this is found not to be the case in both PZT fine grain bulk ceramics and thin film studies [20,21]. One possible reason for this is a decrease in the domain mobility and the number of variants in each grain as the grain size decreases. In the case of grain sizes larger than $10\text{ }\mu\text{m}$ our data are limited to one composition and one grain size but it is noted that this point also departs from the parabolic relation in a manner consistent with the coarsened grain BaTiO_3 ceramics [see the upper curve in Fig. 6(b)], i.e. domain density becomes higher than the $m = 1/2$ relation.

The domain structures observed in the poled PZT ceramics are shown to be strongly influenced by the domain structures in neighboring grains, both with regard to domain wall spacing and orientations. Figure 2 (a) and (b) clearly shows a transgranular elastic coupling, which can only be explained through cooperative intra- and trans-granular domain switching. Figure 2 (a) shows grain #3 with two sets of periodic ferroelastic twins, DW^x and DW^y , which couple, respectively, to domain configurations in the adjacent grains labeled #1 and #2, respectively. Figure 2 (b) also shows transgranular coupling of poled domain structures. This micrograph shows that the grain boundary between grains #2 and #3 perturbs the periodicity of domain structure in grain #1. Transgranular coupling is also of practical importance for fine grained thin film piezoelectric materials for devices such as micromotors. Grain boundary phases must be kept at a minimum to maximize the transgranular coupling. The transgranular coupling and their relation to elastodielectric properties will be the focus of future investigations in the domain structures of PZT ceramics.

CONCLUSIONS

With the semi-infinite medium approximation, one can derive the exponent in eqn (1) to be $1/2$. However, experimental data supporting the parabolic relationship are scarce in the literature. The main reason for this is due to the strong influence of boundary conditions during the formation of domains. We have roughly estimated a situation of limited deformable medium with one side fixed and found that the exponent becomes $1/3$ [22]. Through the experimental results reported here we show that in hard and soft PZT systems the parabolic relation ($m = 1/2$) is

roughly obeyed only for grain size between 1.0 and $10\text{ }\mu\text{m}$. For grain size $> 10\text{ }\mu\text{m}$ and $< 1\text{ }\mu\text{m}$, deviation is found from the parabolic relation to higher domain densities. Because the problem is very complex for the ceramic system with a finite size, there is no sound theory with proper treatment of the boundary conditions to account for the domain size grain size relation at this point. We are currently pursuing numerical analysis using finite element method and hopefully will resolve some of the key issues in the near future.

One of the important contributions from our experimental works is the confirmation of the TEM technique as a valid method for domain size assessment in bulk ceramics. Using poled samples and heating cycles, we conclude that the domain size obtained in the TEM reflects that of the bulk ceramic if the samples were prepared at temperatures much below the transition temperature. Domain redistribution reflecting the new boundary conditions of the thin foil was found only after the samples were heated to temperatures near T_c .

Additionally, it was noted that fine grain ferroelectrics ($< 1\text{ }\mu\text{m}$) often contain one or two sets of simple twin bands, while larger grains can have many cross hatching twin band structures. The result of fine grains having simple domain structures implies a reduction in the degrees of freedom a fine grain can readily deform while the system is undergoing the paraelectric-ferroelectric phase transition. The reduced variants combined with the surface pinning of the domain walls may be the cause for the reduction of domain wall mobility and hence the associated extrinsic elasto-dielectric properties for fine grain PZT ceramics and thin films.

The poled ceramic samples reveal direct evidence of the domain switching process involving both intra-granular and trans-granular cooperation. The trans-granular switching indicates that the non- 180° domains have strong semi-coherent elastic coupling across grain boundaries which in turn complicates the measure of effective grain size in the calculation of domain size.

Acknowledgements—We wish to thank Drs T. R. Shrout and N. Kim for the supplying of the ceramic samples in the TEM studies. The authors are also wish to acknowledge many insightful conversations with Drs L. E. Cross, R. E. Newham, and T. R. Shrout. This research is supported by the National Science Foundation under Grant MRG DMR-92-23847.

REFERENCES

1. Fousek J. and Janovec V., *J. Appl. Phys.* **40**, 135 (1969).
2. Sapriel J., *Phys. Rev.* **B12**, 5182 (1975).
3. Khachaturyan A. G., *Theory of Structural Transformations in Solids*. John Wiley, New York (1983).

4. Salje E., *Phase Transitions in Ferroelastic and Coelastic Crystals*. Cambridge University Press (1990).
5. Kittel C., *Phys. Rev.* **70**, 965 (1946).
6. Mitsui T. and Furuichi J., *Phys. Rev.* **90**, 193 (1953).
7. Arlt G., *Ferroelectrics* **104**, 217 (1990).
8. Chenskii E. V., *Sov. Phys. Solid-State* **14**, 1940 (1973).
9. Buessem W. R., Cross L. E. and Goswami A. K., *J. Am. Ceram. Soc.* **49**, 33 (1966).
10. Swartz S. L., *IEEE Trans. Elect. Insulator* **25**, 935 (1990).
11. Whatmore R. W., Patel A., Shorrocks N. M. and Ainger F. W., *Ferroelectrics* **104**, 269 (1990).
12. Cross L. E. (private communication).
13. Randall C. A., Rossetti G. A. and Cao W., *Ferroelectrics* **150**, 163 (1993).
14. Philippe P., Dougherty J. P. and Shrout T. R., *J. Mater. Res.* **5**, 2901 (1990).
15. Shrout T. R., *Proc. 1st Int. Meeting on Chem. of Electron. Ceram. Mater.* (1990).
16. Jaffe B., Cook W. R. and Jaffe H., *Piezoelectric Ceramics*. Academic Press (1971).
17. Gevers R., Blank H. and Amelinckx S., *Phys. Stat. Sol.* **13**, 449 (1966).
18. Randall C. A., Barber D. J. and Whatmore R. W., *J. Mater. Sci.* **22**, 925 (1987).
19. Tuttle B., Voigt J., Headley T. J., Potter B. G., Dimos D., Schwartz R. W., Duggan M. T., Michael J., Nasby R. D., Garino T. J. and Goodnow D. C., *Ferroelectrics* **151**, 11 (1994).
20. Demartin M., Carry C. and Setter N., *Proc. 4th Int. Conf. on Electron. Ceram. and Applications*, P. 393 (1994).
21. Eatough M., Dimos D. and Tuttle B., *MRS Fall Meeting* (1994).
22. Cao W., *Ferroelectrics*, **172**, 31 (1995).

APPENDIX 94

Characterization of ferroelectric lead zirconate titanate films by scanning force microscopy

Genaro Zavala and Janos H. Fendler^{a)}
Department of Chemistry, Syracuse University, Syracuse, New York 13244-4100

Susan Trolier-McKinstry
Materials Research Laboratory, The Pennsylvania State University, University Park, Pennsylvania 16802

(Received 27 December 1996; accepted for publication 20 February 1997)

Scanning force microscopy (SFM) has been used for the determination of friction, phase transformation, piezoelectric behavior (in the contact mode), polarization state, and dielectric constant (in the noncontact mode) of nanometer regions of lead zirconate titanate (PZT) films. The use of the SFM tip in the contact mode, to polarize different nanoregions of the PZT film and to apply an oscillating field thereon, led to effective piezoelectric coefficients and piezoelectric loops. The measured effective piezoelectric coefficient was shown to depend appreciably on both the tip contact force and the quality of the tip-to-film electrical contact. In the noncontact mode, application of an ac signal (with a frequency ω) across the tip—PZT film—electrode system produced an oscillation of the tip at frequencies ω (fundamental or first harmonic) and 2ω (second harmonic). The signals at ω and 2ω were related to the state of polarization and the dielectric constant of the PZT film, respectively. Analysis of the combined contact, noncontact and friction force microscopic data provided insight into the structure and into the dielectric, ferroelectric, and piezoelectric properties of distinct nanoregions of the PZT film. © 1997 American Institute of Physics. [S0021-8979(97)00211-9]

I. INTRODUCTION

Ferroelectric thin films are currently being investigated for applications including nonvolatile memory elements, high volumetric efficiency capacitors, nonlinear optical elements, electromechanical actuators for microelectromechanical systems, and pyroelectric detectors.¹ One of the principal attractions for thin films in each of these devices is the degree of miniaturization and integration which can be achieved relative to designs based on bulk ceramics. As such devices are made, however, it becomes increasingly important to develop means of characterizing the properties of the ferroelectric films on a microscopic scale in order to investigate both the local properties and the homogeneity of the films. In this work, scanning force microscopy (SFM) was used to investigate the dielectric and piezoelectric properties of lead zirconate titanate (PZT) thin films prepared by the sol-gel technique on the morphotropic phase boundary between PbTiO_3 and PbZrO_3 .

Scanning force microscopy,²⁻¹¹ both in the contact³⁻⁶ and in the noncontact⁸⁻¹⁰ mode, as well as scanning tunneling microscopy^{2,7} have been fruitfully employed for the characterization of ferroelectric materials. In general, it is assumed that the surface-to-tip interactions are due to the local electric fields (associated with the spontaneous polarization or with the domain walls),⁸⁻¹⁰ or to the electromechanical response to an applied field (via piezoelectricity or electrostriction),²⁻⁷ or to the dielectric permittivity⁴⁻⁶ of the ferroelectric film or, indeed, to the combination of all these factors. An understanding of the mechanism of the interaction between the SFM tip and ferroelectric films requires a direct comparison of the observed macroscopic properties,

using large area electrodes, and the behavior of the same samples, probed in nanodomains. We have, therefore, undertaken such a comparison and report here our initial results.

II. EXPERIMENT

A. Sample preparation and macroscopic characterization

The PZT films were prepared using a sol-gel process, following a route adapted from Budd, Dey, and Payne.¹² Lead acetate trihydrate was dissolved in 2-methoxyethanol, and the water of hydration was removed by distillation at 125 °C under flowing Ar. Ti isopropoxide and Zr-*n*-propoxide were added in a dry box in the correct ratio for a Zr-Ti composition of 52:48. No excess Pb was added. The solution was then refluxed at 90 °C for 4 to 5 h under a flowing Ar blanket. After cooling, 1.5 moles of H_2O to 1 mole of PZT were added to the sol in order to provide partial hydrolysis. At the same time, 4 vol % of formamide was added to promote crack-free drying.

Silicon substrates with a thick thermal SiO_2 barrier layer, 200 Å of Ti and 1500 Å of Pt (supplied by Nova Electronics) were used. The liquid was then dispensed onto the substrate through a 0.2 μm filter and spun at 3000 rpm. Each layer was dried and pyrolyzed on a hot plate at 300 °C for one minute. Additional layers were spun and pyrolyzed until a total thickness of nearly 3000 Å was built up. The film was then crystallized using rapid thermal annealing (RTA) at 700 °C for 30 s (AG Associates HeatPulse 210).

Structural and electrical characterizations were performed on the films. X-ray diffraction showed a well-crystallized perovskite film. For electrical measurements, an array of 0.3 mm diameter Au top electrodes were sputtered onto the film. Contact to the bottom electrode was made by

^{a)}Electronic mail: jfendler@summon.syr.edu

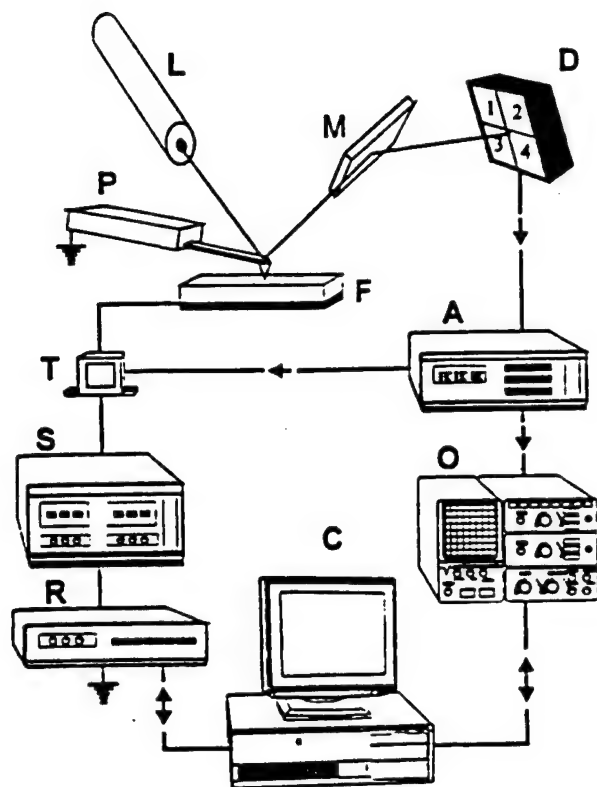


FIG. 1. Experimental set-up. The laser (L) beam was directed to the cantilever (P) and reflected to a detector (D) through a mirror (M). The film (F) movement was detected by the signal $(1-2)-(3+4)$ on the detector and was used as an input to a lock-in amplifier. The internal signal reference of the lock-in amplifier (A) was applied to the film through a transformer (T) with a dc source (S) or a function generator (R) in series. The magnitude and phase of the lock-in output were seen in an oscilloscope (O) and saved in a computer (C). For electric measurements, the function generator was not used.

etching off a corner of the film using a dilute HF solution. Hysteresis loops were measured using a Radiant Technologies RT66A Ferroelectrics tester on one of the same films that was subsequently characterized by SFM. Dielectric constant measurements were made using an HP 4275A LCR bridge. Piezoelectric measurements were also made on 1.5 mm diameter electrodes using double beam interferometry. As has been described elsewhere,^{13,14} this method is capable of resolving longitudinal displacements of 10^{-2} Å, while eliminating errors associated with flexure of the substrate.

Additional samples were prepared using a similar procedure at the Army Research Laboratory at Fort Monmouth, New Jersey. Circular gold electrodes were patterned on the film top surface using a lift-off technique. The electrode diameters were on the order of 1 μm. This was done to provide electrodes on the same order in size as the SFM interaction area.

A commercial Topometrix Explorer System provided the basics for all SFM in the contact and in the noncontact mode. This basic system was supplemented by an EG&G PARC 5301 lock-in amplifier, a Hewlett Packard P8116A pulse/function generator, a dc Tektronix PS 280 power supply, a Zenith Z-100 computer, and a Hewlett Packard 54510A digitizing oscilloscope to perform piezoelectric, polarization, and capacitance measurements (see Fig. 1).

B. Topography and friction force microscopy (FFM) measurements

The SFM system was set to acquire topography in the contact mode in the micro and nanolevel range. The reflection laser technique was used to measure friction forces.¹⁵ A four-part detector, which measured lateral changes in the laser beam as well as vertical movements, was used. The perpendicular scanning direction was used (scanning perpendicularly to the direction of the longitude of the cantilever). The lateral signals for the forward and the backward directions, in the contact mode, were obtained.^{16,17} The lateral image in the backward direction was subtracted from the one in the forward direction to obtain a friction coefficient image.¹⁷

C. Piezoelectric measurements

Piezoelectric measurements of the PZT films were carried out by using the attachments to a Topometrix Explorer System (see Fig. 1). A grounded silicon tip (with a spring constant of 50 N/m), with an insulating layer on the surface that prevented contact electrification,⁶ was used. The tip was brought into feedback position in the contact mode. The position of the reflected beam on the cantilever surface was detected by a four-segment detector. The signal $(1+2)-(3+4)$ which detected any vertical movement, was taken to the lock-in amplifier. The amplifier internal signal reference was applied to the bottom electrode of the film through a transformer to drive mechanical movements (i.e., from piezoelectric response) of the film. The signal applied to the bottom electrode was a 5 KHz sinewave, 0.5 V rms. To polarize the film, either the function generator or the dc power supply was connected in series with the transformer to the bottom electrode. The piezoelectric constant was calculated by dividing the thickness oscillation amplitude (from the detector signal) by the driving voltage (ac signal applied to the film). To obtain the movement in meters, the sensor response (the relation between the detector signal and the cantilever vertical movement) for a specific tip was measured.

A piezoelectric loop was measured by a computer controlled experiment. The computer controlled the magnitude of a step voltage signal produced by the generator connected in series (see Fig. 1). This signal was applied to polarize the film. The magnitude was changed in each cycle by two volts from -16 to +16 V and from +16 to -16 V. In each step, when the voltage was zero, the computer saved the magnitude and phase of the piezoelectric response. The results were plotted in a ferroelectric-loop style curve.

The effect of stress was determined by changing the force applied by the silicon tip on the surface. The tip was brought into the contact mode and a dc voltage was applied to polarize the area. An ac signal was applied to drive mechanical movements of the film. The piezoelectric response was measured by the lock-in amplifier for different applied forces. The area of interaction between the tip and the film was assessed by sensing the piezoelectric behavior as a function of distance from the polarization point. After applying the polarization voltage, the piezoelectric response was measured at different distances from the polarization place.

Piezoelectric microscopy was performed on the film. A region was scanned with a silicon tip while applying a dc voltage to polarize the entire area. The piezoelectric behavior of the region was then obtained by scanning the same area in order to measure the piezoelectric constant.

D. Electrical measurements

Polarization and capacitance experiments were made by the SFM in the noncontact mode with a platinum coated silicon tip (5 N/m). As in piezoelectric measurements, a dc voltage was applied in the contact mode to the bottom electrode to polarize the film. In the noncontact mode, an ac signal (at frequency ω) was applied. This signal was of a frequency high enough (2.5 KHz, 0.5 V rms) to suppress the feedback circuit but it was smaller than the cantilever resonance frequency (~ 70 KHz) to avoid interference with the feedback loop. The laser detector signal, $(1+2)-(3+4)$, was taken to the lock-in amplifier (see Fig. 1). The magnitude of the signal (the cantilever oscillation) was measured at frequencies ω (first harmonic) and 2ω (second harmonic). The first harmonic signal (ωs) was related to the polarization state and the second harmonic signal ($2\omega s$) was related to the capacitance between the tip and the electrode supporting the film.

Point spectroscopy on the film was performed. Both harmonics, ωs and $2\omega s$, were measured while the tip was approaching the film. The obtained data were plotted as a function of distance from the film and fitted to a proposed mathematical model to interpret the results. From ωs , the polarization, the apparent radius of the tip for capacitance interaction, and the area of polarization interaction were calculated. From $2\omega s$, the capacitance, the apparent radius of the tip for capacitance interaction, and the dielectric constant were assessed.

The PZT film was polarized by applying positive and negative dc voltages to the bottom electrode while placing the grounded tip in different locations. This polarization (ωs magnitude) was imaged by scanning in the noncontact mode. Positive and negative polarizations were obtained and distinguished.

To obtain a polarization loop, polarizing voltages from -16 to $+16$ V were applied in the contact mode. After the application of the desired polarizing voltage, the tip was brought into the noncontact mode to measure ωs . The maximum fundamental signal magnitude in each measurement was plotted in a ferroelectric-loop style curve as a function of applied polarizing voltage.

Values for ωs and $2\omega s$ were also measured in the nanoregions of the PZT films. No poling voltage was applied at this time. Images of polarization, capacitance, and dielectric constant as a function of grain size were obtained.

III. RESULTS AND DISCUSSION

A. Macroscopic characterization

The film showed a well-defined hysteresis loop (see Fig. 2) with a remanent polarization (P_r) of $32 \mu\text{C}/\text{cm}^2$ and a coercive voltage (V_c) of ~ 3 V. The dielectric properties of comparable films gave measured dielectric constants be-

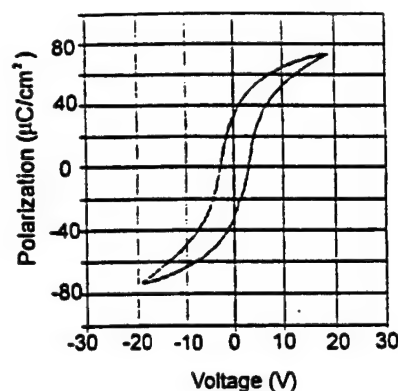


FIG. 2. Measured hysteresis loops using a Radiant Technologies RT66A Ferroelectrics tester. The remanent polarization (P_r) is $32 \mu\text{C}/\text{cm}^2$ and the coercive voltage (V_c) is 3 V.

tween 800 and 1000 and loss tangents of 3%–5%.^{18,19} The piezoelectric d_{33} coefficient of similar films was ~ 70 – $80 \text{ pC}/\text{N}$ ²⁰ as measured by double beam interferometry under zero field bias.

B. Topography

A typical SFM image of a ferroelectric film, taken in the contact mode with a silicon nitride tip (0.064 N/m) using 4.4 nN force in air, is illustrated in Fig. 3(a). The rms roughness of the image was 6.5 nm. This value is in a good agreement with that measured previously by spectroscopic ellipsometry.²¹ The film had some hills and valleys on the otherwise flat surface. A nanorange image of the same film was taken in the noncontact mode [see Fig. 3(b)]. The grains or clusters on the surface were clearly observed and measured to be about 50 nm. Similar grains were obtained on RTA-treated films deposited by rf-magnetron sputtering.²² Larger grains (100–200 nm) have been observed on sol-gel prepared films with conventional firing.^{23–25} This indicated that RTA suppressed grain growth.

C. Surface friction characterization

Topographic and friction coefficient images in micro- and nanosized regions of a typical ferroelectric film, obtained by FFM, are shown in Fig. 4. In the friction images, the

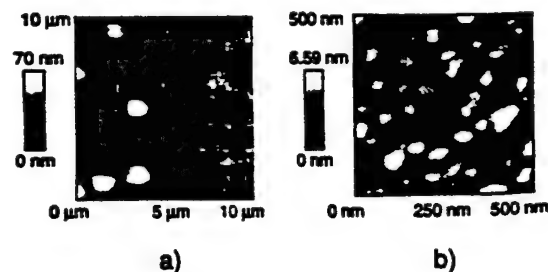


FIG. 3. (a) 10 micrometer topography image of the sample taken in the contact mode with a silicon nitride tip (0.064 N/m spring constant) in air. There are a number of hills and valleys of the order of 1 micrometer size. (b) 500 nm topography image taken in the noncontact mode with a silicon tip. The film grains or clusters are resolved. They are 50 nm in size.

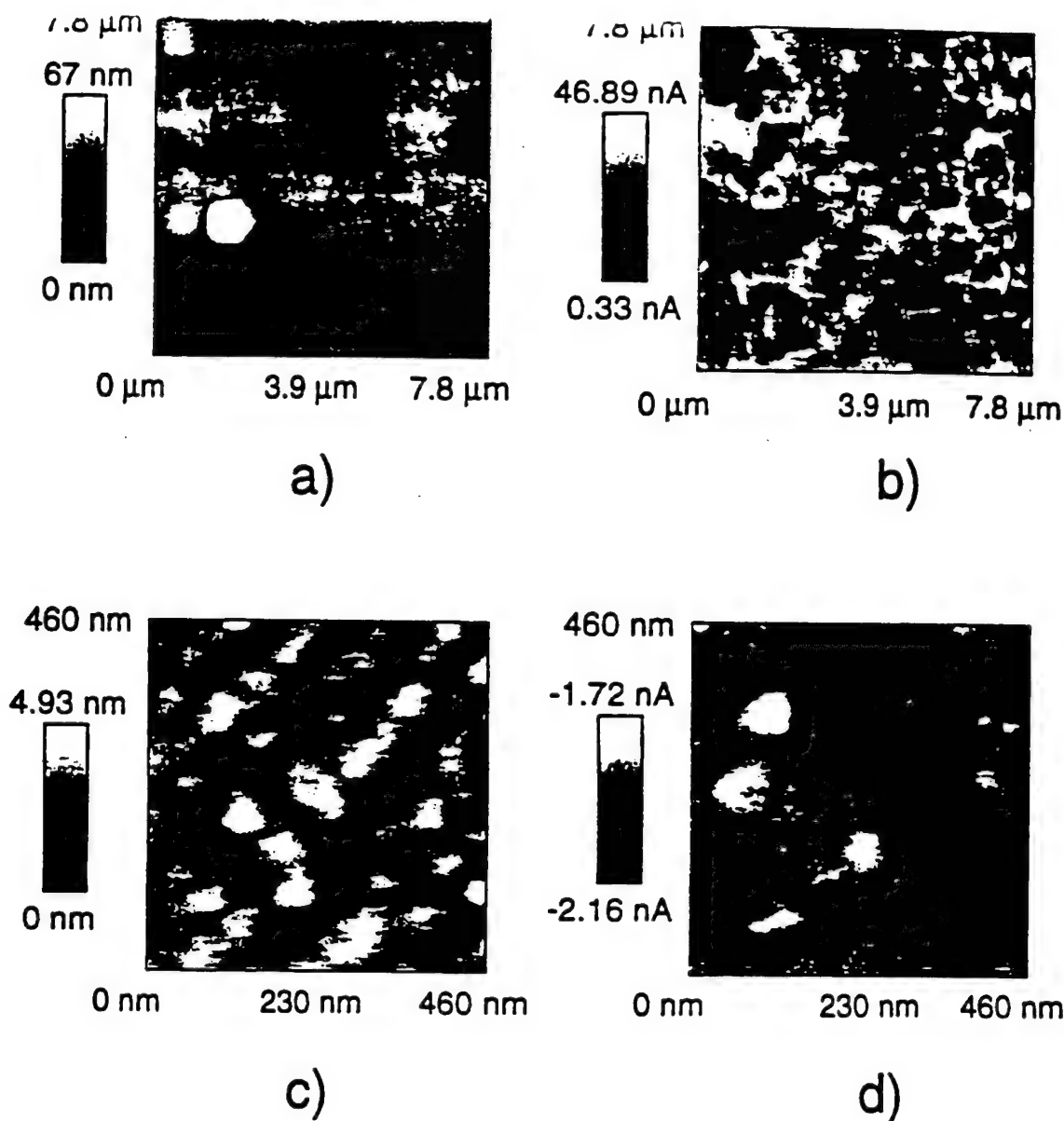


FIG. 4. Friction measurements. Topography (a) and friction coefficient (b) images of a microlevel area. Hills and valleys in (a) had the same friction coefficient which differed from the rest of the area. (c) Topography and (d) friction coefficient images in a nanoscale area. Some grains had a different friction coefficient than that of the rest of the grains.

brightness is scaled to the measured friction coefficient. As can be seen in Fig. 4(a), both hills and valleys appeared as regions where the friction coefficient was smaller than the rest of the film. A three-line profile of the friction coefficient image, shown in Fig. 4(b), was obtained (see Fig. 5). It showed that the friction coefficient in the hills and valleys was constant (2.8 ± 1.4 nA), where nA is just a relative unit that is proportional to the actual friction coefficient. On the rest of the area, the friction coefficient was higher (35.6 ± 12.4 nA). The difference in friction coefficient between hills and valleys and the value in the rest of the area was approximately the same for all lines measured. These results imply that the hills and valleys were of the same material and different from the rest of the ferroelectric film.

PZT films sometimes have problems with the residual pyrochlore phase.^{26,27} Since the performed friction measurements indicated that there were regions of different friction

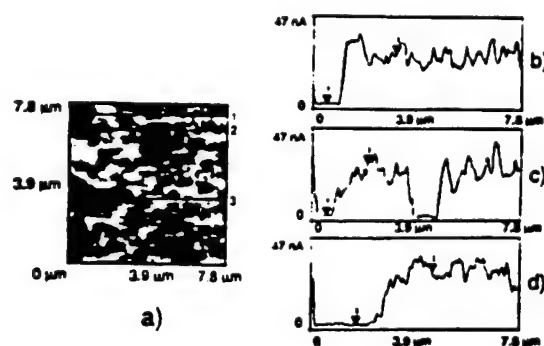


FIG. 5. (a) Three friction line profiles of a friction coefficient image. (b)–(d) are lines 1, 2, and 3, respectively. Note that the difference in friction coefficient between hills and valleys (2.8 ± 1.4 nA) and the average value in the rest of the area (35.6 ± 12.4 nA) was the same regardless of the line measured.

coefficient, these regions might correspond to either a lead deficient pyrochlore phase at the film surface or to an incompletely transformed intermediate phase.

At the nanolevel [Figs. 4(c) and 4(d)], it can be seen that some grains had a different friction coefficient from the majority of grains, the matrix. It was observed that, opposite what is found in the microscopic level [Figs. 4(a) and 4(b)], the friction coefficient of those grains was larger than that of the matrix. Thus, this behavior strongly supports the idea that the friction coefficient difference on grains is related to domain orientation. The tip could be charged and the contrast of the image could be due to the interaction of this charge and the domain of the grain.

Friction force microscopy can, therefore, be used as for the characterization of ferroelectric films in terms of their uniformity and phase changes in the microscaled scale and for domain orientation in the nanosized scale.

D. Microscopic piezoelectric measurements by the contact mode SFM

The thickness of a ferroelectric film is expected to increase when it is polarized by a poling voltage of either sign. Once the film is polarized, its thickness will change when a voltage is applied between the bottom and top electrodes (via the inverse piezoelectric effect, $e = dE$ or $\Delta t = dV$, where e is strain, d is piezoelectric constant, E electric field, V voltage, and Δt the change in thickness). For an oscillating voltage, the thickness oscillates at the same frequency. The response to an ac signal changes with different states of polarization. When the applied voltage is parallel to the polarization, the film thickness should increase, while for a small field opposite to the sense of the original polarization, the sample thickness will decrease.

The SFM tip was used as a top electrode to polarize and apply an ac signal to the film (see experimental section and Fig. 1). The film was positively and negatively polarized in different regions. When an ac signal was applied, the tip oscillated, following the change in film thickness. In a positive polarization region, the positive part of the ac signal increased the thickness, so the detected signal was in phase with the ac signal. In a negatively polarized region, the positive part of the ac signal decreased the thickness, so the detected signal was 180° out of phase with respect to the ac signal.

1. Piezoelectric loop

A piezoelectric loop (see Fig. 6) was obtained by means of a computer controlled experiment as described in the experimental section. The piezoelectric constant (d_{33}) was set to be negative when the phase obtained was 180° and positive when the phase obtained was 0° . The resulting curve had all the features of a hysteresis loop; d_{33} values came to a saturation point around 13 V and the coercive voltage (V_c) was around 3 to 4 V (compare to a ferroelectric loop obtained on the same film, see Fig. 2). The difference between the present measurements and a similar loop obtained elsewhere² was that the present loop was taken with no dc voltage applied. It is important to point out that all piezoelectric measurements using the SFM tip were taken with just the ac

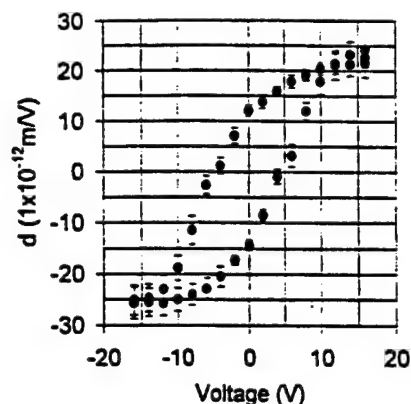


FIG. 6. Piezoelectric loop. The polarizing voltage was changed in two volt steps. For each step the magnitude and phase of the piezoelectric response was recorded. Negative magnitude values indicate that the phase at that step is 180° and positive magnitude values indicate that the phase at that step is 0° . Note that the curve has a hysteresis-like shape. It has a saturation point around 13 V and a coercive voltage around 3 to 4 V.

signal applied. A dc voltage was applied to polarize the film but was reduced to zero for each piezoelectric measurement. Therefore, the actual remanent piezoelectricity was measured since this experiment did not have any additional interactions produced by a dc field, such as an additional stress.⁶ Piezoelectric measurements can, therefore, be performed and piezoelectric loops can be obtained by the SFM tip on given nanoregions, grains, and grain boundaries as a function of temperature and/or pressure.

The piezoelectric constant obtained using the SFM tip was found to be tip dependent and smaller ($5\text{--}22 \times 10^{-12}$ m/V for positive polarization and $6\text{--}26 \times 10^{-12}$ m/V for negative polarization) than those obtained with macroscopic techniques for these films ($\sim 70\text{--}80 \times 10^{-12}$ m/V by double beam interferometry). There are several potential reasons for this behavior. In particular, the possibility of poor electrical contact between the tip and the film leading to inefficient excitation, clamping of the small excited region by the surrounding matrix, and clamping of the piezoelectric response by the contact force of the tip itself need to be considered. Consequently, a set of experiments was performed to separate the relative importance of these different factors.

In order to investigate the role of the contact force in mechanically clamping the piezoelectric response, the effective piezoelectric coefficient d_{33} was measured at different values of the contact force. The data in Fig. 7(a) show a monotonic decrease in the measured values with increasing stress over the range measured. It was found that increasing the constant force from 4 to 28 μN leads to a $\sim 60\%$ drop in the measured effective d_{33} value.

It is interesting to compare these data to similar work on bulk ceramics exposed to uniaxial stresses. To do so, as a first approximation it was assumed that the contact force was applied over an area $\sim 400\text{--}500$ nm in diameter [see Fig. 7(b)], and that the loading could be treated as roughly uniaxial. The resulting compressive stress for the higher contact force is thus $\sim 140\text{--}220$ MPa. The film was also as-

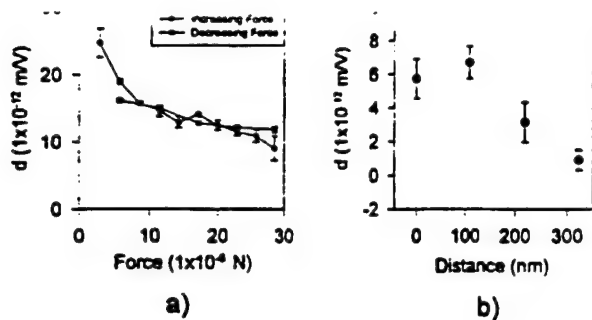


FIG. 7. (a) Stress effect on piezoelectric response. The piezoelectric constant (d_{33}) decreased from 17×10^{-12} to 13×10^{-12} m/V as the force was increased (from 10.2 to 25.5 μ N). d_{33} was reversible as the stress was taken back to its previous value indicating that the change in d_{33} is stress related and not due to depoling of the film. (b) A typical measurement of the lateral distance dependence of d_{33} is shown. The magnitude shows a maximum around 100 nm that is related to the stress applied at the contact point where the voltage was applied.

sumed to behave much like a hard PZT ceramic, as it is undoped. Many publications on the stress dependence of piezoelectric properties have been reported, the work of Zhang *et al.*²⁸ was chosen here for comparison. These authors report that for hard PZT compositions the d_{33} value initially increases as uniaxial pressure is applied, it then goes through a maximum, and subsequently decreases for stress levels of 150 MPa. The enhanced d_{33} observed at modest stress levels was attributed to deaging the ceramic sample, so that non-180° domain walls were freed to contribute to the observed response. The fact that this was not observed in the thin undoped PZT films measured in this study implies that it was not possible to engender appreciable non-180° domain wall motion for the stress levels applied. The observed decrease in the piezoelectric response of the material under load could then be attributed to either a shift in the morphotropic phase boundary composition with stress or to clamping of the response by the applied stress.

Another interesting point apparent in Fig. 7(a) is that on decreasing the load, the effective piezoelectric coefficient of the films approximately retraces the curve measured on increasing load. In soft PZT ceramics loaded parallel to the poling direction, there is appreciable hysteresis in the piezoelectric coefficients on unloading after application of a large uniaxial stress due to domain reorientation.^{28,29} That is, domains which were originally parallel to the applied load can be reoriented ferroelastically under stress. On removing the stress, there is little driving force to restore these domains to their original configuration. As a result of the decrease in the remanent polarization, the measured d_{33} value also decreases hysteretically. Hard PZT ceramics show less ferroelastic depoling and hysteresis, since the local defect dipoles act to stabilize the domain structure. In this work, even accounting for the approximations inherent in the stress calculations for the SFM measurements on films, the observed nonhysteretic film response measured here strongly suggests that non-180° twin walls are immobile in these films. This is in agreement with measurements made on similar sol-gel PZT films exposed to large in-plane biaxial stresses.³⁰ It is also interesting that a decrease in the twin wall mobility is ob-

served in the thin films, where the grain size is reduced below 1 μ m.^{31,32} Thus, in the thin films, where the grain size is typically under 0.1 μ m, it is not surprising that low domain wall mobilities are observed. In any event, it is clear that in order to measure the effective d_{33} coefficient of films using the SFM, it is preferable to use minimal loading conditions. This is consistent with the observation of Gruverman *et al.*¹¹ that piezoelectric coefficients measured by SFM should be performed at low loads.

A second factor which was investigated to account for the low measured effective d_{33} values was the electric field/charge delivery. To investigate this, a new film was prepared with an array of ~ 1 μ m diameter gold top electrodes. The piezoelectric properties were then measured both on and off the electrodes using a conductive SFM tip. It was observed that measurements made on an electroded array were approximately three times larger than those made on the bare film surface (59 to 18 pm/V, respectively). This observation implies that variations in the local electric field due to poor electrical contact is responsible for the majority of the discrepancies between d_{33} values measured on the ferroelectric films by SFM and that observed macroscopically.

2. Polarization area

The size of the interaction area accessed by the SFM tip was established by determining the piezoelectric constant as a function of distance from the polarization point [see Fig. 7(b)]. The error bars for each experimental point were taken from the variation of the signal with time. The area of interaction was found to have a radius of around 250 nm. This area can be related either to the effective tip radius or to the film thickness.³ An interesting behavior in Fig. 7(b) was that the d_{33} value first increased and then decreased to zero as the tip was moved away from the poling position. This behavior could be related to stress. At the point of contact, where the dc voltage was applied, the stress exerted was greater than that on areas nearby where the contact was made just for the measurement of the piezoelectric response. This greater stress was due to the applied additional stress on the film produced by the dc voltage.⁶

3. Piezoelectric scanning image

A piezoelectric scanning experiment was performed by FFM on a region of the ferroelectric film which had a hill with a different friction coefficient from the matrix (see Fig. 8). The region was scanned with a silicon tip applying -16 V to polarize the entire area. Then, the area was scanned measuring the piezoelectric response. The hill had a significantly lower piezoelectric response than that of the matrix. It can be concluded that the hill was nonpiezoelectric.

The presence of secondary phases degrades the properties in ferroelectric films.³³ Consequently, it is useful to be able to detect even small amounts of such phases. X-ray diffraction (XRD) has been used to detect second phase regions.²⁷ However, XRD is limited either when there is little of the second phase present ($<1\%$ – 5%) or when the second phase is poorly crystallized or amorphous.³⁴ Friction

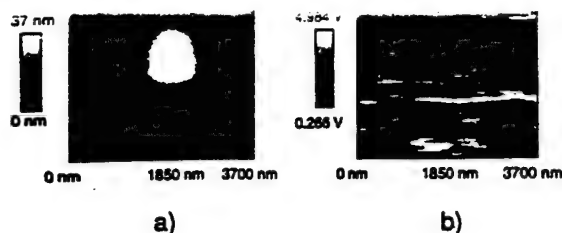


FIG. 8. Piezoelectric response in a hill. With the help of friction microscopy, a region (a) of a hill with smaller friction coefficient was chosen. The entire area was previously polarized at -16 V. The hill had a lower piezoelectric constant (b) than the matrix and its phase changed from 180° to zero.

and piezoelectric measurements can easily overcome this limitation, particularly for phases present primarily in the near surface region.

E. Microscopic polarization measurements by noncontact SFM

An SFM tip was used to polarize submicron-sized regions of the film. The polarization produced surface and volume bound charge on the film and induced an electric field (E) over the film surface. This induced electric field produced a charge and a force on the tip (Q_p and F).

$$F = Q_p E. \quad (1)$$

where F is attractive for both remanent polarization directions. In the noncontact mode, an ac signal was applied ($V_0 \sin \omega t$) to the bottom electrode (see Fig. 1) to produce an additional induced charge (Q_e) on the tip given by,

$$Q_e = -CV_0 \sin \omega t, \quad (2)$$

where C is the tip-to-film capacitance. This charge interacted with E producing an oscillatory force, given by

$$F_\omega = -E_z CV_0 \sin \omega t, \quad (3)$$

where E_z is the z direction of E . F_ω was modulated at the frequency ω . It was in phase when E_z was negative and 180° out of phase when E_z was positive. This force made the tip oscillate and this oscillation was measured by a lock-in amplifier. The phase of the tip oscillation depended on the polarization state of the film (through E_z). The magnitude depended on E_z , the tip-film capacitance C , and the voltage applied magnitude V_0 .

The first harmonic signal, ωs , was measured as a function of applied voltage, V_0 [see Fig. 9(a)]. As can be seen, ωs was linearly dependent on V_0 as predicted by Eq. (3). At higher applied voltages, there was a deviation in linearity. This effect can be due to a strong capacitance interaction between the tip and the bottom electrode producing a non-modulated attractive force on the tip.^{5,6,35} At higher ac voltages, this attractive force could reduce the tip-to-surface distance and produce higher ωs breaking the linearity of the experiment. To avoid this strong force interaction, all polarization experiments were performed on the linear part of the curve.

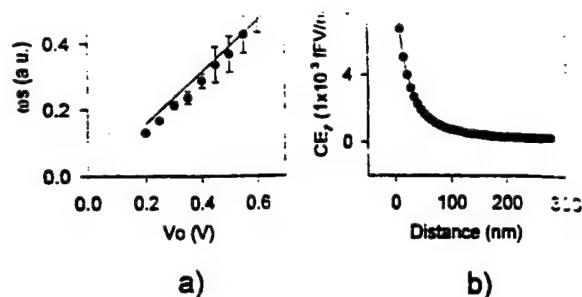


FIG. 9. (a) Polarization magnitude (ωs) as a function of voltage amplitude (V_0) applied. The response was linear as expected. (b) Fundamental signal depended on capacitance and polarization. The experimental curve was fitted to a mathematical model to obtain a physical meaning for the curve. From the fitting curve, some parameters were obtained: The remanent polarization was obtained to be $22.1 \mu\text{C}/\text{cm}^2$ compared to $30 \mu\text{C}/\text{cm}^2$ obtained macroscopically. The apparent radius of the tip was 16.4 nm which is in close agreement with capacitance measurements. The radius of the polarized area by the tip was 410.8 nm which is very close to the value measured experimentally.

1. Point spectroscopy of ωs

Point spectroscopy of ωs was performed [see Fig. 9(b)] by allowing the tip to approach the surface while ωs was measured. Prior to point spectroscopy, -16 V was applied to the bottom electrode to polarize the film. To interpret ωs , a model was proposed. The model determined the polarization induced by the tip, the apparent radius of the tip for capacitance interaction, and the polarization interaction area by fitting ωs to $E_z C$ [see Eq. (3)]. E_z and C were the only two quantities that were tip-film distance dependent. For C , the capacitance between an infinite plane and a sphere was used.³⁶

$$C(z) = \frac{2\pi\epsilon_0 R^2}{\frac{r}{K} + z + R}, \quad (4)$$

where R was the apparent radius of the tip, r and K were the thickness and the dielectric constant of the film, respectively. To calculate E_z , the polarization P was approximated by

$$P = P_0 \left(\frac{r_0 - r}{r_0} \right), \quad (5)$$

where P_0 is the maximum of polarization and r_0 was a parameter representing the radius of a circular area of polarization. The resulting equation calculated with this polarization was

$$E_z = \frac{P_0}{2\epsilon_0} \left[1 - \frac{z}{r_0} \ln \left(\frac{r_0 + \sqrt{r_0^2 + z^2}}{z} \right) \right]. \quad (6)$$

Using Eqs. (4) and (6), the experimental points of Fig. 9(b) were fitted with three parameters given by

$$CE_z = \frac{b_1 b_2^2}{\frac{r}{K} + b_2 + z} \left[1 - \frac{z}{b_3} \ln \left(\frac{b_3 + \sqrt{b_3^2 + z^2}}{z} \right) \right]. \quad (7)$$

R , and b_3 was proportional to r_0 .

The fitting curve showed that the model was qualitatively appropriate [see Fig. 9(b)]. Parameter b_1 was obtained to be 6.9×10^{-17} FV/nm². From b_1 , P_0 was calculated to be $22.1 \mu\text{C}/\text{cm}^2$. This remanent polarization value was reasonably close to the macroscopically obtained value, $32 \mu\text{C}/\text{cm}^2$ (see Fig. 2) and is consistent with the fact that there appeared to be some contact problems when no top electrodes were used in the piezoelectric measurements. Parameter b_2 was 16.4 nm. This parameter can be interpreted as the apparent radius of the tip for capacitance measurements. Parameter b_3 was related to the dimension of the polarized area. This value was 410.8 nm, which is in close agreement with the polarized region size obtained as described below.

The unpolarized film acted as if it had a homogeneous charge on the surface as previously reported.³⁷ A nanometer-scale scanning experiment, in which both the topography and ωs were measured, was performed on an unpolarized region

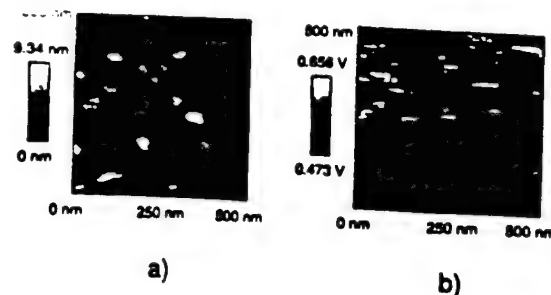


FIG. 10. Topography (a) and magnitude of first harmonic (b) for an unpolarized region. Note that first harmonic magnitude was grain dependent.

of the film (see Fig. 10). The image showed that ωs was grain dependent. In nonferroelectric films, the first harmonic signal has been reported to be due to surface potential.^{35,38,39} Therefore, there could be two reasons for this grain-dependent behavior. One is that the surface potential in ferroelectric materials is dependent on crystalline direction of the

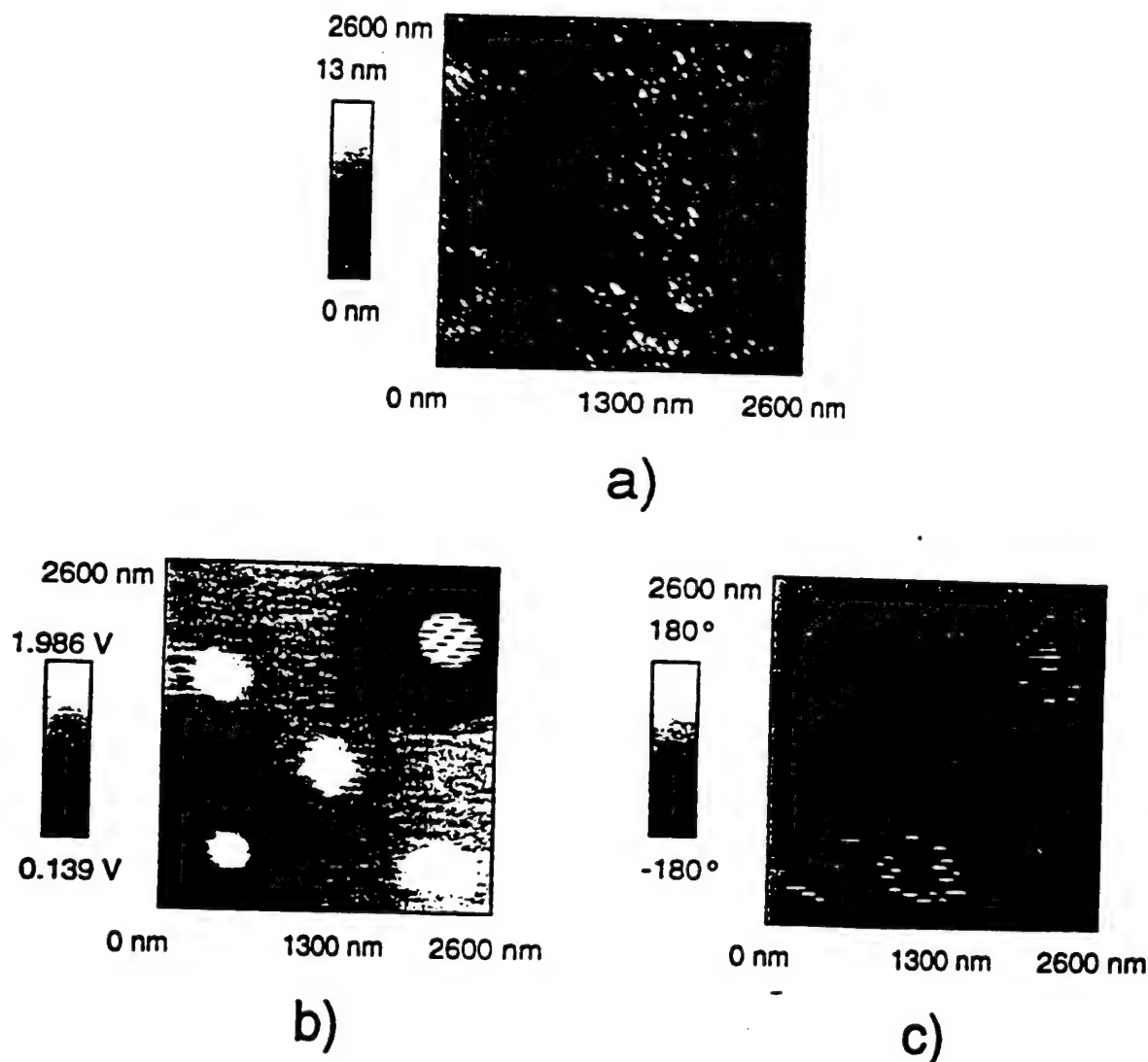


FIG. 11. (a) Topography, (b) magnitude, and (c) phase of the polarization signal for a region where 5 points were polarized 1, 2, and 3 in (b) are positive-voltage-applied points. 4 and 5 in b are negative-voltage-applied points. The phase of 180° of points 4 and 5 is clearly seen. The phase of points 1, 2, and 3, 0° , is not resolved since the matrix has a 0° phase as well. Note that the voltage applied does not have any effect in topography.

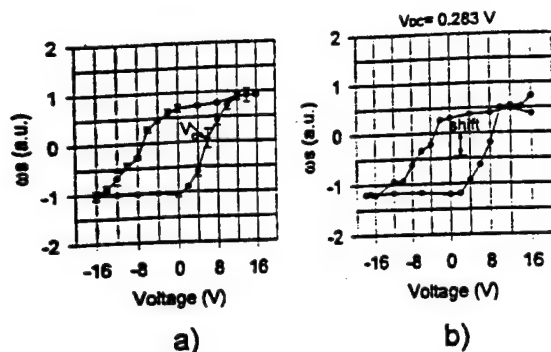


FIG. 12. Polarization Loops. (a) Negative values were set for 180° phase and positive for 0° phase. Note that the saturation point is around 12 V and the coercive voltage is around 6 V, greater than expected. (b) The image was taken with a small bias voltage applied ($V_{bc}=0.283$ V). The loop is shifted with respect to the one in a.

grain. The other is that the signal shows the spontaneous polarization of grains.

2. Polarization areas

Nanoregions of the ferroelectric film were polarized by applying either positive or negative voltages by the SFM tip. A typical experiment is illustrated (see Fig. 11). Three points with positive voltage were applied [points 1, 2, and 3 in Fig. 11(b)] and two points with negative voltages [points 4 and 5 in Fig. 11(b)]. After the voltage was applied, the region was scanned by measuring the magnitude and phase of the first harmonic signal along with the topography. In Fig. 11(b), the five points are clearly shown. In Fig. 11(c), the three positive-voltage-applied points did not appear since they showed a zero phase. As was noted previously, the matrix of the film showed a zero phase as well. The phase of positive-voltage-applied points suggested a negative surface charge. Negative-voltage-applied points showed 180° out of phase signals suggesting surface positive charge. This behavior indicated that the charges seen by the tip in the noncontact mode were of a neutralization or a compensating type. Notice from Figs. 11(b) and 11(c) that the polarized area agreed in size with point spectroscopy measurements.

3. Polarization loop

Signals measured by this technique in nonferroelectric (ceramic and polymer) materials have been previously reported to be due simply to charge transfer.^{37,40-43} To rule out this possibility, a polarization loop experiment was performed [see Fig. 12(a)]. The polarization voltage was changed from -16 to 16 V. For each voltage point, the dc voltage was reduced to zero to measure the fundamental signal. A negative value on the polarization was assigned when the phase was 180°. Although the coercive voltage measured was 6 instead of 3 V as given by ferroelectric and piezoelectric loops, the curve showed hysteresis and a saturation point around 12 V. The charge observed might be composed of two parts: One, the charge transfer from electrification contact; and the other, compensating charges at the surface due to the bounded charge of polarization. For voltages greater than but close to the coercive voltage, the polarization charge

might be very small and the remaining charge from higher voltages could overshadow the new compensating charge, giving as a result, a larger apparent coercive field.³⁷ It has also been reported that the charge transfer is reduced considerably when zero voltage is applied.^{37,40,41} For each point in Fig. 12(a), the last voltage applied was zero and the signal was not reduced. This supports that the signal in voltages higher than V_c are due to polarization rather than charge transfer.

Applying a small bias voltage while in the noncontact mode is known to reduce to zero the inherent first harmonic signal produced by the surface potential in nonferroelectric materials.³⁷ In these experiments, different values of negative and positive voltages were applied to the surface by the SFM tip in the contact mode. For each voltage applied, the first harmonic signal in the noncontact mode was measured with the small bias voltage applied. The obtained results were symmetric with the voltage. Similarly, in the present experiment, the polarization loop with small bias voltage applied was obtained [see Fig. 12(b)]. In contrast to the results published elsewhere,³⁷ the first harmonic signal loop was shifted (not symmetric) with respect to the same loop with no bias applied [see Fig. 12(a)]. This result strongly supports that the first harmonic signal is due to polarization and the loop is a polarization loop.

F. Nanoscopic capacitance measurements

The second harmonic signal (the signal at 2ω) was assumed to be a result of the interaction between the tip and the bottom electrode through their capacitance. When a voltage ($V_0 \sin \omega t$) was applied between the tip and the bottom electrode system, a force ($F_{2\omega}$) between these two electrodes is created.⁴⁴

$$F_{2\omega} = \frac{1}{2} V_0^2 \frac{dC}{dZ} = \frac{1}{2} V_0^2 \sin^2 \omega t \frac{dC}{dZ}$$

$$F_{2\omega} = \frac{1}{4} V_0^2 \frac{dC}{dZ} - \frac{1}{4} V_0^2 \cos 2\omega t \frac{dC}{dZ} \quad (8)$$

where C is the tip-to-bottom electrode capacitance and Z is the tip-to-film distance. This force made the tip oscillate. The oscillation of the tip was modulated at two times the frequency of the applied signal (2ω). This modulation was measured by the lock-in amplifier and was called the second harmonic signal or $2\omega s$. $2\omega s$ depended mainly on the square of the magnitude of the voltage applied (V_0) and the derivative of the capacitance with respect to the distance from the film (dC/dZ).

The magnitude of $2\omega s$ was measured as a function of V_0 from a constant tip-film distance [see Fig. 13(a)]. As predicted by Eq. (8), $2\omega s$ depends on the square of V_0 for low voltages. At higher V_0 , the second power dependence was lost. This was likely produced by the nonmodulated attractive force indicated in Eq. (8). This nonmodulated force can reduce the tip-film distance and produce higher signal measurements breaking the second order dependence of the experiment. To avoid this strong force interaction, all the second harmonic experiments were performed on the quadratic part of the curve.

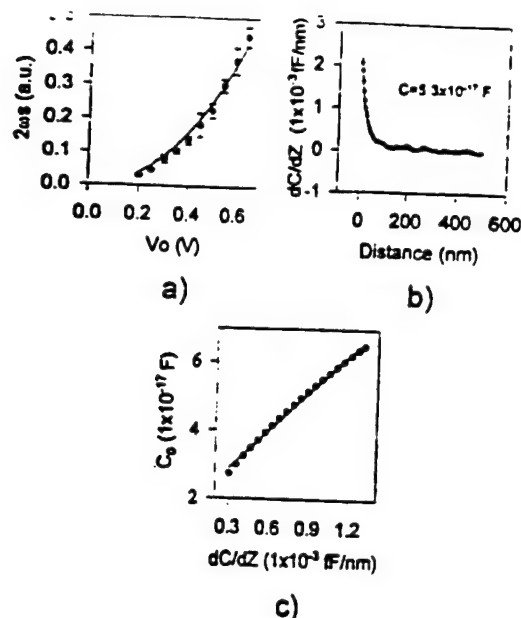


FIG. 13. (a) Second harmonic signal ($2\omega s$) magnitude as a function of the applied ac voltage (V_0). As expected, a second order function was obtained. (b) Point spectroscopy of calculated capacitance derivative (from the magnitude of the second harmonic) as a function of distance from the surface. Points are the experimental data and the line is the fitted curve. The capacitance (5.3×10^{-17} F) was obtained by calculating the area under the curve. (c) Capacitance at the surface vs capacitance derivative at the noncontact distance. The range in $dC(Z_n)/dZ$ was taken from the actual range in capacitance derivative values in a scanning image [Fig. 14(b)]. It shows that in the range of $dC(Z_n)/dZ$, $C(0)$ is linear. Therefore, capacitance images can be calculated from the second harmonic image with simple arithmetic operations.

1. Point spectroscopy of $2\omega s$

Point spectroscopy of $2\omega s$ was performed [see Fig. 13(b)] by allowing the tip to approach the surface while $2\omega s$ was measured. V_0 was kept constant during each measurement, resulting in a dC/dZ curve as a function of tip-to-film distance. The capacitance was obtained by calculating the area under the curve. The capacitance was different from point to point. It varied between 4 and 6×10^{-17} F. Since the tip used was the same for all the measurements, the difference in capacitance was produced by the film. To obtain a physical meaning of Fig. 13(b), the experimental values of the spectroscopy data were fitted to the derivative of the capacitance between an infinite plane and a sphere.³⁶

$$|dC/dZ| = \frac{2\pi\epsilon_0 R^2}{\left(Z + \frac{t}{K} + R\right)^2} \quad (9)$$

R represented the apparent tip radius, t and K the thickness and the dielectric constant of the film, respectively. The thickness and the dielectric constant were not chosen as parameters of the fitting curve since t/K is very small compared to R . Equation (10) was used as a model with two parameters:

$$|dC/dZ| = \frac{b_1 b_2^2}{\left(Z + \frac{t}{K} + b_2\right)^2} \quad (10)$$

where b_2 was the important parameter representing the apparent tip radius for capacitance interaction. Fitting Eq. (10) to the spectroscopy data in Fig. 13(b), the b_2 value obtained was 26.4 nm. The apparent radius of the tip was comparable to the one obtained in polarization measurements (16.4 nm) and to what is expected for this kind of probe (20–30 nm).

2. Capacitance and dielectric constant images

Since the capacitance was point-to-point dependent, the capacitance for an image can be qualitatively obtained for a given area. From Eqs. (4) and (10), the capacitance $C(0)$ of a point at the surface ($Z=0$) can be calculated knowing the derivative value $dC(Z_n)/dZ$ in that point at the noncontact distance ($Z=Z_n$), assuming that this tip-to-film distance (Z_n) is known.

$$C(0) = \frac{b_1 b_2^2}{\frac{b_1^{1/2} b_2}{[dC(Z_n)/dZ]^{1/2}} Z_n} \quad (11)$$

b_1 and b_2 and Z_n were used as calibration parameters. b_1 and b_2 were taken from the values calculated previously, and Z_n was measured experimentally by measuring the fundamental and second harmonic in the noncontact mode and then comparing that value to the spectroscopy curve. The value obtained was 8.5 nm. With these parameters, a scanning taking $2\omega s$ and calculating $dC(Z_n)/dZ$ along with topography was performed. In order to obtain the capacitance value from the $dC(Z_n)/dZ$ image, arithmetic operations were performed using Eq. (11). Although this equation is not linear with respect to $dC(Z_n)/dZ$, for the range obtained in $dC(Z_n)/dZ$ image, it can be assumed to be linear [see Fig. 13(c)]. The resulting image for capacitance [see Fig. 14(b)] revealed that C was grain and grain boundary dependent. In general, grain boundaries had greater capacitance than grains, although among grains also differences in capacitances were found. The capacitance on the film image depended on basically three factors: The geometric form of the tip, which was constant throughout all the experiment, the thickness of the sample, which was measured by topography, and dielectric constant, which was assessed on the next section.

From capacitance images, the dielectric constant (K) can be qualitatively obtained. To obtain K from this capacitance image, the simple parallel-plate capacitor was chosen as a model.

$$K = \frac{C(0)t}{\epsilon_0 A} \quad (12)$$

$C(0)$ can be obtained from the capacitance image, t , the film thickness, can be obtained from topography image, and A , the area, can be calculated from R , the tip apparent radius (26.4 nm as calculated in point spectroscopy). The calculation of K image was performed by taking the product of two images, capacitance, and topography [Figs. 14(a) and 14(b)] and a constant (A).

The dielectric constant image [see Fig. 14(c)], normalized to K of the film (800), revealed that it was grain and grain boundary dependent. The dielectric constant in grain

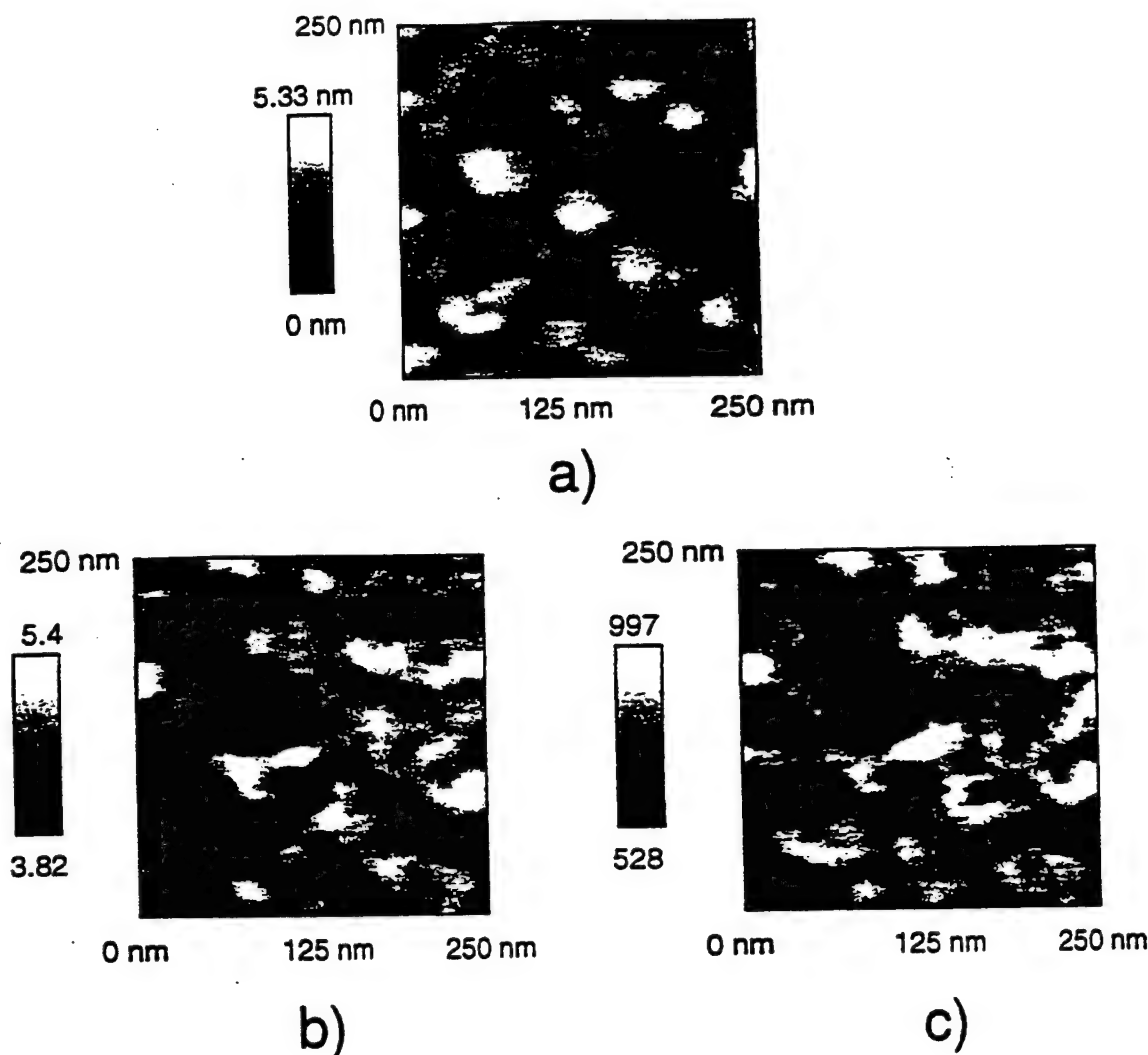


FIG. 14. Topography (a) capacitance (b) and dielectric constant (c) images in a 250 nm range. The units in (b) are 1×10^{-17} F. It was observed that: the capacitance is grain and grain boundary dependent. In general, the measured capacitance in grain boundaries was greater than that in grains, although differences were found from grain to grain. The capacitance in these images depended on three factors, the geometrical form of the tip, which was constant in the image; the thickness, and the dielectric constant. The dielectric constant in c was calculated from the capacitance and topography images. In general, the measured dielectric constant was greater in the grain boundaries than in grains.

boundaries appeared to be greater than that within grains. Two possibilities could account for these differences. In the first place, it was found that the SFM-measured dielectric constant of individual grains was dependent on grain size, with smaller grains showing larger K values. Thus, it is possible that the contrast seen in Fig. 14(c) is in part, size dependent. In the second place, the measured capacitance may be affected by dielectric loss, which could easily be different between grains and grain boundaries. It was observed that the capacitance image and the dielectric constant image were very similar. This was expected given the small surface roughness.

IV. CONCLUSIONS

The limit of phase detection by x-ray diffraction is about 1% (in volume) depending on the phases involved. Friction measurements by SFM can easily overcome this limitation. It was shown that in micro-sized regions, friction microscopy was able to reveal a second phase and with the help of pi-

ezoelectric measurements, this second phase can be tested for ferroelectricity. Therefore, the insight gained can be used to improve ferroelectric thin film processing. Also, FFM can be used to characterize domain orientation in nanosized regions, since it was found that friction coefficient varied from grain to grain.

It was proven in the present work that piezoelectric measurements can be performed by SFM on nanodomains. The smaller values of piezoelectric response compared to macroscopic measurements were shown to be due to poor electric contact between the tip and the film leading to an inefficient excitation of the film and clamping of the piezoelectric response by the applied stress. Therefore, piezoelectric measurements by SFM should be performed at low loads. Also, it was shown that non-180° domain walls do not contribute appreciably to the measured piezoelectric response at any level of applied stress and that the mobility of this domain walls is low. This is in agreement to what could be expected for 50 nm grain size film. These conclusions strongly support

that these studies will lead to a better understanding of piezoelectricity in films.

Polarization loops were obtained in noncontact SFM leading to a new way of characterizing ferroelectric films. From point spectroscopy analysis, polarization, polarization area, and capacitance interaction area were assessed. The values assessed were in close agreement with the experimental results. Thus a new technique to calculate remanent polarization in films in noncontact mode has been developed.

Capacitance and dielectric constants were assessed in the present work in the nanometer range. This technique can be used to assess not only ferroelectric films, but also any dielectric film.

ACKNOWLEDGMENTS

Support of this work by the National Science Foundation is gratefully acknowledged. One of the authors (G.Z.) wants to thank CONACYT, Mexico (National Council of Science and Technology) for their support.

- ¹ See, for example, MRS Proceedings: Ferroelectric Thin Films I-V; Integrated Ferroelectrics (unpublished), Vols. 1-11.
- ² H. Birk, J. Glaz-Reichenbach, Li-Jie, E. Schreck, and K. Dransfeld, *J. Vac. Sci. Technol. B* 9, 1162 (1991).
- ³ P. Guthner and K. Dransfeld, *Appl. Phys. Lett.* 61, 1137 (1992).
- ⁴ K. Franke, J. Besold, W. Haessler, and C. Seegebarth, *Surf. Sci. Lett.* 302, L283 (1994).
- ⁵ K. Franke and M. Weihnacht, *Ferroelectr. Lett. Sect.* 19, 25 (1995).
- ⁶ K. Franke, *Ferroelectr. Lett. Sect.* 19, 35 (1995).
- ⁷ Li-Jie, C. Baur, B. Koslowski, and K. Dransfeld, *Physica B* 204, 318 (1995).
- ⁸ F. Saurenbach and B. D. Terris, *Appl. Phys. Lett.* 56, 1703 (1990).
- ⁹ R. Luthi, H. Haefke, P. Grutter, H.-J. Guntherodt, L. Szczesniak, and K. P. Meyer, *Surf. Sci. Lett.* 285, L498 (1993).
- ¹⁰ R. Luthi, H. Haefke, K. P. Meyer, E. Meyer, L. Howald, and H.-J. Guntherodt, *J. Appl. Phys.* 74, 7461 (1993).
- ¹¹ A. Gruverman, O. Auciello, and H. Tokumoto, *J. Vac. Sci. Technol. B* 14, 602 (1996).
- ¹² K. D. Budd, S. K. Dey, and D. A. Payne, *Br. Ceram. Proc.* 36, 107 (1985).
- ¹³ A. L. Kholkin, Ch. Wutrich, D. V. Taylor, and N. Setter, *Rev. Sci. Instrum.* 67, 1935 (1996).
- ¹⁴ H. D. Chen, K. R. Udayakumar, C. J. Gaskey, and L. E. Cross, *Appl. Phys. Lett.* 67, 3411 (1995).

- ¹⁵ G. Meyer and N. M. Amer, *Appl. Phys. Lett.* 57, 2089 (1990).
- ¹⁶ J. Ruan and B. Bhushan, *Trans. ASME* 116, 378 (1994).
- ¹⁷ C. Ascoli, F. Dinelli, C. Frediani, D. Petracchi, M. Saleno, M. Labardi, M. Allegrini, and F. Fuso, *J. Vac. Sci. Technol. B* 12, 1642 (1994).
- ¹⁸ P. Aungkavattana and S. Troler-McKinstry (unpublished).
- ¹⁹ B. J. Gibbons, S. Troler-McKinstry, J. Chen, and L. E. Cross (unpublished).
- ²⁰ F. Xu and S. Troler-McKinstry (unpublished).
- ²¹ P. Aungkavattana, Ph.D. Thesis, the Pennsylvania State University, 1996.
- ²² S. Yamauchi, H. Tamura, M. Yoshimaru, and M. Ino, *Jpn. J. Appl. Phys.* 32, 4118 (1993).
- ²³ K. Amanuma, T. Mori, T. Hase, T. Sakuma, A. Ochi, and Y. Miyasaka, *Jpn. J. Appl. Phys.* 32, 4150 (1993).
- ²⁴ L. E. Sanchez, S.-Y. Wu, and I. K. Naik, *Appl. Phys. Lett.* 56, 2399 (1990).
- ²⁵ K. Aoki, Y. Fukuda, and A. Nishimura, *Jpn. J. Appl. Phys.* 32, 4147 (1993).
- ²⁶ M. Labardi, M. Allegrini, F. Leccabue, B. E. Watts, C. Ascoli, and C. Frediani, *Solid State Commun.* 91, 59 (1994).
- ²⁷ B. A. Tuttle, R. W. Schwartz, D. H. Dougherty, and J. A. Voigt, *Mater. Res. Soc. Symp. Proc.* 200, 159 (1990).
- ²⁸ Q. M. Zhang, J. Z. Zhao, K. Uchino, and J. H. Zheng (unpublished).
- ²⁹ H. A. Krueger, *J. Acoust. Soc. Am.* 42, 636 (1967).
- ³⁰ J. F. Shepard Jr., S. Troler-McKinstry, M. A. Hendrickson, and R. Zeto (unpublished).
- ³¹ W. Cao and C. A. Randall, *J. Phys. Chem. Solids* 57, 1499 (1996).
- ³² N. Kim, Ph.D. Thesis, The Pennsylvania State University, 1994.
- ³³ A. Iembo, F. Fuso, M. Allegrini, E. Arimondo, V. Berardi, N. Spinelli, F. Leccabue, B. E. Watts, G. Franco, and G. Chiorboli, *Appl. Phys. Lett.* 63, 1194 (1993).
- ³⁴ B. D. Cullity, *Elements of X-Ray Diffraction* (Addison-Wesley, Reading, MA, 1978).
- ³⁵ H. Yokoyama and T. Inoue, *Thin Solid Films* 242, 33 (1994).
- ³⁶ P. Lorrain and D. Corson, *Electromagnetic Fields and Waves* (Freeman and Company, New York, 1970), p. 150.
- ³⁷ F. Saurenbach and B. D. Terris, *IEEE Trans. Ind. Appl.* 28, 256 (1992).
- ³⁸ O. Vatel and M. Tanimoto, *J. Appl. Phys.* 77, 2358 (1995).
- ³⁹ T. Inoue and H. Yokoyama, *Thin Solid Films* 243, 399 (1994).
- ⁴⁰ T. Uchihashi, T. Okusako, T. Tsuyuguchi, Y. Sugawara, M. Igarashi, R. Kaneko, and S. Morita, *Jpn. J. Appl. Phys.* 33, 5573 (1994).
- ⁴¹ T. Uchihashi, T. Okusako, J. Yamada, Y. Fukano, Y. Sugawara, M. Igarashi, R. Kaneko, and S. Morita, *Jpn. J. Appl. Phys.* 33, L374 (1994).
- ⁴² R. C. Barrett and C. F. Quate, *J. Appl. Phys.* 70, 2725 (1991).
- ⁴³ C. Schonenberger, *Phys. Rev. B* 45, 3861 (1992).
- ⁴⁴ Y. Martin, D. W. Abraham, and H. K. Wickramasinghe, *Appl. Phys. Lett.* 52, 1103 (1988).

Electrostriction

APPENDIX 95

ELECTROSTRICTION - NONLINEAR ELECTROMECHANICAL COUPLING IN SOLID DIELECTRICS.

R. E. Newnham, V Sundar, R. Yimnirun, J. Su and Q.M. Zhang
Intercollege Materials Research Laboratory, The Pennsylvania State University, University Park, PA 16802.

ABSTRACT

Electrostriction is the basis of electromechanical coupling in all insulators. The quadratic electrostrictive strain x_{ij} associated with induced polarization components P_k and P_l is given by $x_{ij} = Q_{ijkl} P_k P_l$. Two converse electrostrictive effects may also be defined. In this paper, some trends in structure-property relationships that govern electrostriction are identified, along with the problems that limit our understanding of this fundamental electromechanical property. Electrostrictive coefficients range from the $\sim 10^{-3} \text{m}^4/\text{C}^2$ in relaxor ferroelectrics to $\sim 10^3 \text{m}^4/\text{C}^2$ in some polymers. High sensitivity techniques such as interferometry or compressometry are necessary to accurately measure electrostrictive effects in most insulators. But even in low-K dielectrics, electrostrictive stresses may initiate breakdown in high field environments such as microelectronic components with small dimensions, high voltage insulators or in high power lasers. In polymeric materials, charge injection mechanisms may produce local electric field concentrations that can cause large electrostrictive strains. The electromechanical properties in polymers have also been observed to vary with the thickness of the specimen. A brief description of the anharmonic nature of electrostriction and its frequency dependence is included.

INTRODUCTION

Many of the recent innovations in the field of electroceramics have exploited the nonlinearities of material properties with factors such as electric field, frequency, or temperature. The nonlinear dielectric behavior of ferroelectric ceramics (fig.1), for example, has opened up new market segments in electronics and communication. In these materials, the polarization increases nonlinearly to a saturation value as the applied electric field is increased¹. Polarization P_i varies with applied electric field E_j as :

$$P_i = \eta_{ij} E_j + \eta_{ijk} E_j E_k + \dots$$

where η_{ij} is the dielectric susceptibility, and η_{ijk} the higher order dielectric susceptibility. η_{ij} is related to the dielectric constant K_{ij} by the linear relation $\eta_{ij} = (K_{ij} - 1)\epsilon_0$.

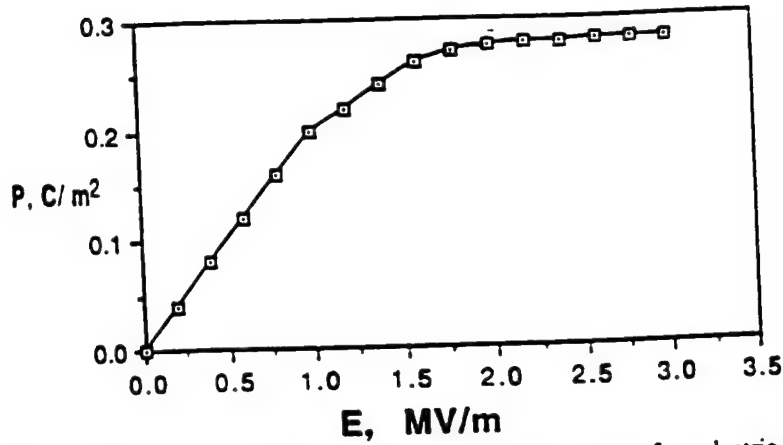


Fig. 1 : Nonlinear polarization vs. electric field behavior for the relaxor ferroelectric 0.9PMN-0.1PT in its paraelectric regime (Ref. 1).

Similarly the nonlinear elastic behavior of materials such as polymers (fig.2) has also been exploited in composite structures. In the natural vulcanized rubber shown, the strain obtained saturates as stress is increased in the low MPa range².

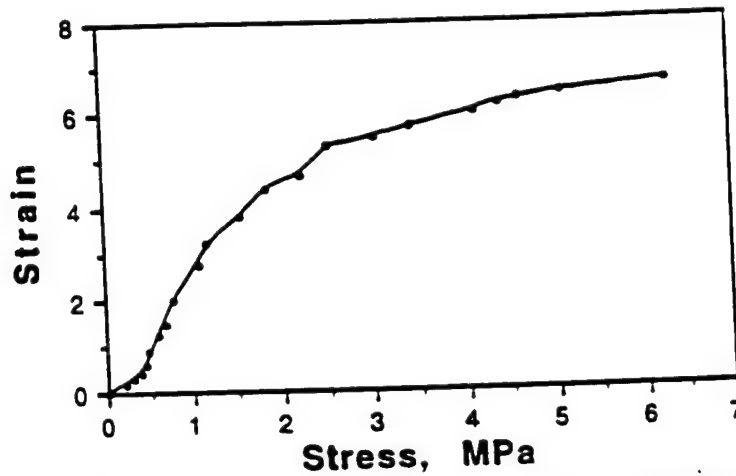


Fig. 2 : Nonlinear strain vs. stress behavior of a typical natural vulcanized rubber (Ref. 2).

Linear stress-strain behavior conforming to Hooke's law is observed only in regions of low stress. In the linear region, the strain x_{ij} is related to the stress X_{kl} by the relation $x_{ij} = s_{ijkl} X_{kl}$. Nonlinear elastic behavior in general may be described by the equation :

$$x_{ij} = s_{ijkl} X_{kl} + s_{ijklmn} X_{kl} X_{mn} + \dots$$

where s_{ijkl} is the elastic compliance, and s_{ijklmn} the higher order elastic compliance.

Materials which display large electromechanical interactions have been exploited in the areas of stress or displacement sensing and in actuating. While most

commercial electromechanical materials and structures are based on linear or piezoelectric mechanisms. nonlinear electromechanical interactions are of interest in engineering material systems and structures with tunable properties³. Strains caused by linear and nonlinear electromechanical interactions may be expressed as:

$$x_{ij} = g_{ijm} P_m + Q_{ijmn} P_m P_n + ..$$

where the linear effect is associated with the piezoelectric constants g_{ijm} and quadratic nonlinear effect with the electrostriction coefficients Q_{ijmn} . These strains may also be expressed in terms of electric field related coefficients d_{ijm} and M_{ijmn} as :

$$x_{ij} = d_{ijm} E_m + M_{ijmn} E_m E_n + ..$$

Piezoelectricity is absent in centric crystals, but electrostriction, being a tensor property of even rank, can be observed in all insulating materials. Quadratic

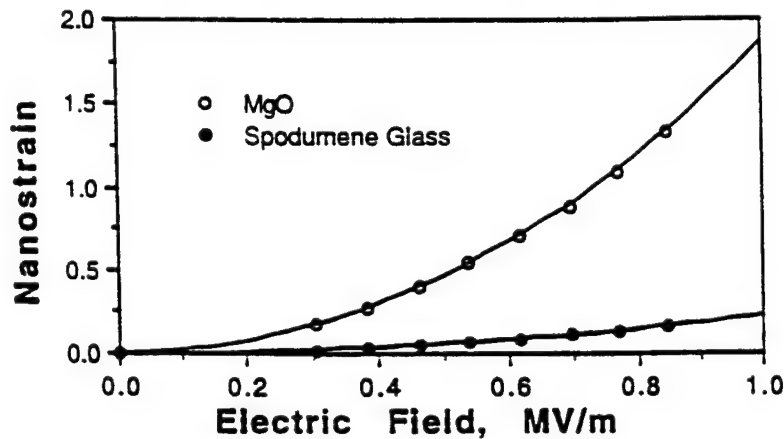


Fig. 3 : Electrostrictive strain can be observed in all insulating materials. Quadratic strain vs. electric field relationships for single crystal $\langle 100 \rangle$ oriented MgO and spodumene glass measured by interferometry are illustrated here.

electrostrictive strain in MgO and spodumene glass ($\text{Li}_2\text{O} \cdot \text{Al}_2\text{O}_3 \cdot 4\text{SiO}_2$) is illustrated in fig. 3⁴. It is also the primary electromechanical coupling mechanism in centrosymmetric materials. In this review, we look at nonlinear electromechanical interactions in the different ways in which it may be observed in materials, along with trends in structure property relationships that affect these interactions.

PHENOMENOLOGY OF ELECTROSTRICTION

Nonlinearity in electrical, elastic and electromechanical properties may be defined using the Devonshire formalism^{5,6}. The elastic Gibbs function (G) for the free energy of a material may be expressed in differential form as :

$$dG = -SdT - x_{ij}dX_{ij} + E_idP_i$$

where S is the entropy, T the temperature, x_{ij} the elastic strain tensor, X_{ij} the stress tensor, and E_i and P_i the electric field and polarization vectors. Properties relating derived variables such as S , x_{ij} or E_i to fixed variables of state such as T , X_{ij} or P_i are obtained by taking the second derivative of this free energy function. For example, the first order terms for inverse dielectric susceptibility χ_{mn} and elastic compliance s_{ijkl} may be expressed as :

$$\chi_{mn} = (dE_m/dP_n)_{X,T} = (d^2G/dP_m dP_n)_{X,T}, \text{ and}$$

$$s_{ijkl} = (dx_{ij}/dX_{kl})_{P,T} = (d^2G/dX_{ij} dX_{kl})_{P,T}$$

Cross-coupled properties can be derived by changing the differentiation variable for the second differential. The properties that introduce strain in a material are derived by differentiating the elastic Gibbs function with respect to stress. The tensor properties associated with these effects are elastic constants, linear and nonlinear thermal expansion, linear piezoelectric constants (g_{ijm}), and quadratic (Q_{ijmn}) electrostriction constants. These electromechanical interactions can be expressed in a power series to the second order (fixed X , T) as :

$$x_{ij} = g_{ijm} P_m + Q_{ijmn} P_m P_n + \dots$$

Electrostriction may be thus defined as the quadratic coupling between strain and electric field, or between strain and polarization. It is a fourth rank tensor defined by the following relationships :

$$x_{ij} = M_{ijmn} E_m E_n, \text{ or}$$

$$x_{ij} = Q_{ijmn} P_m P_n$$

where M_{ijmn} the fourth rank field related electrostriction tensor and Q_{ijmn} the fourth rank polarization related electrostriction tensor. The M and Q coefficients are equivalent in linear dielectrics. Conversions between the two coefficients are carried out using the field-polarization relationships $P_m = \eta_{mn} E_n$ and $E_n = \chi_{mn} P_m$ where η_{mn} is the dielectric susceptibility tensor, and χ_{mn} is the inverse dielectric susceptibility tensor. The need for defining a polarization related electrostriction tensor arises from the fact that ferroelectrics and other materials often show nonlinearity of dielectric properties with changing electric fields. Electrostrictive strain is not always quadratic with electric field, especially in high permittivity materials with nonlinear $P_i - E_j$ relationships (Fig. 4). Thus, it is useful to define a polarization related electrostriction coefficient Q_{ijmn} better express the quadratic nature of electrostriction in all materials.

The M coefficients are defined in units of m^2/V^2 . Their values range from about $10^{-24} m^2/V^2$ in low permittivity materials to $10^{-16} m^2/V^2$ in high permittivity actuator materials such relaxor ferroelectrics such as lead magnesium niobate - lead

titanate compositions. Large strains of the order of strains in ferroelectric piezoelectric materials such as lead zirconate titanate may be induced in these materials for similar fields. Q coefficients are defined in units of m^4/C^2 . Q values vary in an opposite way to M values. Q ranges from $10^{-3} \text{ m}^4/\text{C}^2$ in relaxor ferroelectrics to greater than the order of $10^3 \text{ m}^4/\text{C}^2$ in polyurethane films.

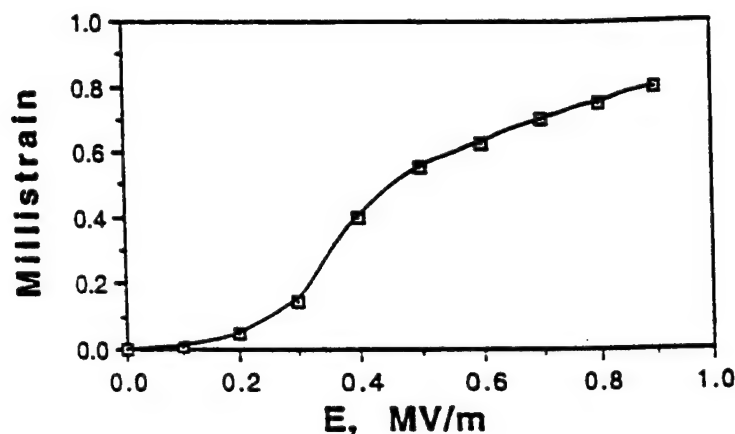


Fig. 4 : Electrostrictive strain is not always quadratic with electric field, especially for high K materials such as PMN (Ref. 1).

Fourth rank electrostriction tensors may also be expressed in collapsed Voigt notation as M_{ij} or Q_{ij} . Expressing these tensors in matrix form illustrates the effects of point group symmetry on this tensor, as applied through Neumann's principle. For example, the electrostriction matrix for cubic materials (point group $m\bar{3}m$) is :

$$\begin{array}{cccccc}
 Q_{11} & Q_{12} & Q_{12} & 0 & 0 & 0 \\
 Q_{12} & Q_{11} & Q_{12} & 0 & 0 & 0 \\
 Q_{12} & Q_{12} & Q_{11} & 0 & 0 & 0 \\
 0 & 0 & 0 & Q_{44} & 0 & 0 \\
 0 & 0 & 0 & 0 & Q_{44} & 0 \\
 0 & 0 & 0 & 0 & 0 & Q_{44}
 \end{array}$$

while the matrix for isotropic materials such as unoriented ceramics, glasses or polymers (Curie groups $\infty\infty m$ and $\infty\infty$) would be of the form :

$$\begin{array}{cccccc}
 Q_{11} & Q_{12} & Q_{12} & 0 & 0 & 0 \\
 Q_{12} & Q_{11} & Q_{12} & 0 & 0 & 0 \\
 Q_{12} & Q_{12} & Q_{11} & 0 & 0 & 0 \\
 0 & 0 & 0 & 2(Q_{11}-Q_{12}) & 0 & 0 \\
 0 & 0 & 0 & 0 & 2(Q_{11}-Q_{12}) & 0 \\
 0 & 0 & 0 & 0 & 0 & 2(Q_{11}-Q_{12})
 \end{array}$$

It is also useful to define a hydrostatic electrostriction coefficient Q_h , as the variation of susceptibility with applied hydrostatic pressure. This coefficient can be useful in comparing electrostrictive effects in materials with different anisotropy characteristics. Since applied compressive stress is by convention negative, Q_h values are positive for ceramic materials, indicating the decrease of inverse dielectric susceptibility (χ) with applied pressure. $Q_h = 0.5(d\chi/dp) = Q_{11} + 2Q_{12}$ (for materials with cubic or isotropic symmetry). The Q_h , dielectric permittivity, and elastic compliance values for some common dielectric materials⁹⁻¹⁶ are listed in Table 1.

As a consequence of the quadratic nature of the electrostriction effect, the sign of the strain produced in the material is independent of the polarity of the field. This is in contrast with linear piezoelectricity where reversing the direction of the field would cause a change in the sign of the strain.

Another consequence is that electrostrictive strain occurs at twice the frequency of an applied AC field. In acentric materials where both piezoelectric and electrostrictive strains may be observed, this fact is very useful in separating the strains arising from piezoelectricity and from electrostriction.

The electrostriction tensor can also be treated as a complex quantity, similar to the dielectric and the piezoelectric tensors. The imaginary part of the electrostriction is also a fourth rank tensor. Such a treatment could be very useful in providing a better understanding at electromechanical energy conversion in materials with relaxation mechanisms such as glasses containing alkali ions⁷ or polymeric materials⁸. In this review, though, the discussion is confined to the real part of the electrostriction tensor.

Also, electrostriction in liquid and gaseous dielectrics has been studied since late in the 19th century, when studies by Roentgen¹⁷ showed that all liquids expanded when an electric field was applied to them. In liquids, electrostriction is observed mainly as the contraction of a solvent around solute ions. Similar to solids, the electrostrictive effect in liquids is observed to be proportional to the square of the charge of the ions, inversely proportional to the ionic radius, and proportional to the value of $K^{-2}dK/dP$ for the solute¹⁸. This discussion, however, is confined to solid dielectrics.

DIRECT AND CONVERSE ELECTROSTRICTION EFFECTS

The electrostriction effect defined in the previous section, which relates the quadratic dependence of strain on applied field or induced polarization may be termed the direct electrostrictive effect. This effect may be expressed in terms of field related and polarization related electrostriction coefficients as :

$$Q_{ijmn} = (d^2 x_{ij} / dP_m dP_n) = (d^3 G / dX_{ij} dP_m dP_n) \text{ or}$$

$$M_{ijmn} = (d^2 x_{ij} / dE_m dE_n) = (d^3 G / dX_{ij} dE_m dE_n)$$

By changing the order of differentiation in the free energy term, we may derive an equivalent converse effect of electrostriction, as :

$$Q_{ijmn} = -1/2 (d \chi_{ij} / d X_{mn}) = (d^3 G / dP_i dP_j dX_{mn}) \text{ or}$$

$$M_{ijmn} = 1/2 (d \eta_{ij} / d X_{mn}) = (d^3 G / dE_i dE_j dX_{mn})$$

which is the variation of dielectric susceptibility or its inverse with applied stress.

Table 1 : List of dielectric constants, elastic constants, and electrostriction coefficients of common dielectrics.

Materials	K	S ($\times 10^{-12}$) (m ² /N)	S/K ϵ_0 ($\times 10^{-4}$) (m/FN)	Q _h (m ⁴ /C ²)	Ref
<i>Relaxor Ferroelectric</i>					
PLZT (11/65/35)	5900	9.50	1.82	0.007	9, 10, 11
BaTi _x Sn _{1-x} O ₃ (x=0.38)	10300	8.90	1.01	0.0099	
BaSr _x Ti _{1-x} O ₃ (x=0.35)	25000	4.55	0.206	0.0069	
La/PMN-PT (1/93/97)	13000	16.42	1.43	0.006	
<i>Perovskite Ferroelectric</i>					
SrTiO ₃	450	1.82	4.57	0.07	11
PbTiO ₃	270	7.81	32.6	0.03	
BaTiO ₃	1070	6.02	6.36	0.03	
Pb(Ti _{1-x} Zr _x)O ₃	1700	1.52	1.01	0.018	
<i>Glass-Ceramics</i>					
Corning 888VE	300	7.25	27.31	0.079	9
Corning 888YT	370	5.85	17.87	0.055	
Corning 888ZF	440	4.93	12.66	0.064	
<i>Linear Dielectrics</i>					
<u>Single Crystals</u>					
CaF ₂	6.8	6.92	1150	0.47	13, 4
BaF ₂	7.4	15.3	2342	0.33	
KMnF ₃	9.8	9.72	1121	0.24	
MgO	9.8	4.03	465	0.18	
<u>Ceramics</u>					
MgO-Doped Al ₂ O ₃	10.5	2.90	312	1.58	This work
AlN	9.5	3.03	360	0.318	
Si ₃ N ₄	8.7	3.13	406	1.06	
<i>Glasses</i>					
Na-Aluminosilicate	10.2	15.3	1696	0.519	12, 14
Fused-SiO ₂	3.8	14.0	4163	0.37	
Na ₂ O.3SiO ₂	11.3	16.3	1629	0.765	This work
Spodumene Glass	7.9	1.18	169	0.43	
<i>Polymers</i>					
PVDF	16	420	29660	2.4	15, 16,
VDF/TrFE	11	400	41090	2.5	
PVC	3.4	333	110700	10.1	This work
Polyurethane	6.5	25000	4346000	850	

It is also possible to define a second converse effect, in which electrostriction is defined as the variation of the piezoelectric voltage coefficient g_{ijk} with the induced polarization.

$$Q_{ijkl} = -1/2 (d g_{ijk} / dP_l)$$

ELECTROSTRICTION IN RELATION TO OTHER ANHARMONIC MATERIAL PROPERTIES

It is necessary to model anharmonic behavior to describe some macroscopic properties that cannot be modeled using the harmonic approximation in solid state theory. Some of these properties are the thermal expansion coefficient, the isothermal compressibility, its pressure coefficient, and electrostriction, all of which contribute to the macroscopic Gibbs free energy, and are typically defined like compliance coefficients.

Modeling anharmonic properties from first principles involves much effort in computational theoretical physics. However, simpler atomistic models, in combination with empirical correlations, can provide some understanding of electrostriction in relation with other anharmonic properties.

Under the action of an applied electric field, the cations and anions in a crystal structure are displaced in opposite directions by an amount Δr . This displacement is responsible for the electric polarization, the dielectric constant, and the electrostrictive strain³. To a first approximation, we may express the relation between these as :

$$Q = \chi/P^2 \sim (\Delta r)/(\Delta r)^2 = 1/\Delta r \sim 1/K$$

Plotting Q_h as a function of the dielectric permittivity (fig. 5) reveals two distinct trends, one for materials with cubic perovskite structures and another for other materials. Perovskite materials of comparable compliances follow the $Q \sim 1/K$ relation. However, linear dielectric with a large range of compliances and a small range of dielectric constants do not follow this relationship. For example, diamond is a very covalent material with a very low compliance, and has a $Q_h \sim 0.02$. Introducing a larger compliance range by including soft polymer dielectrics can further dilute this relationship.

Large strains in compliant solids such as polymers can introduce large changes in the dielectric stiffness and in anharmonic potentials. Electrostrictive strain is displacive and acts against the elastic forces in a material. Introducing the elastic compliance s into the Q vs. K relationship can better express the correlation between these properties. Through the first converse effect, electrostriction is proportional to the change of dielectric stiffness β with stress X , which may be expressed as $Q \sim (\Delta\beta)/(X) \sim \chi/(\chi/s) \sim s$

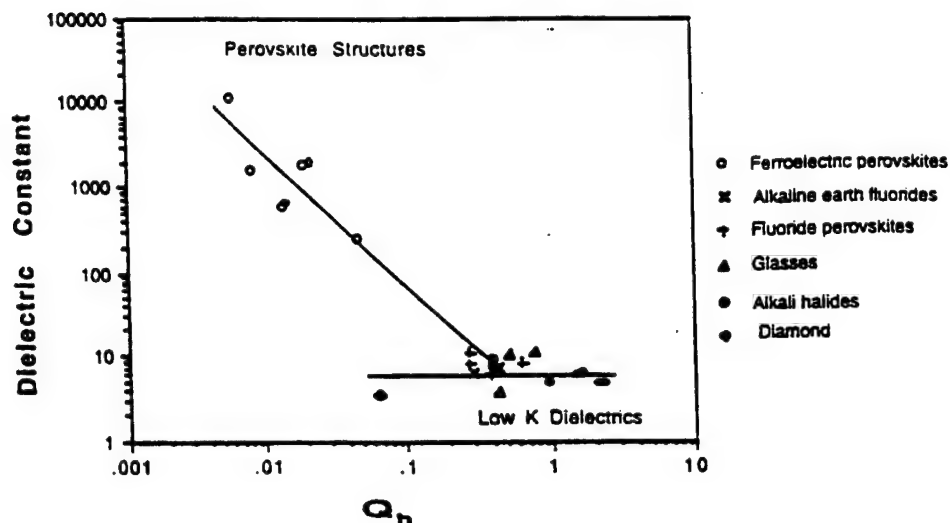


Fig. 5 : Variation of $Q_h(m^4/C^2)$ with dielectric constant for various materials.

Empirically, $\log(Q_h)$ is seen to vary nearly linearly with $\log(s/\epsilon_0 K)$ (Fig. 6). This combination of the compliance and the dielectric properties of a materials may be used as a predictor of the size of electrostriction effects in insulators.

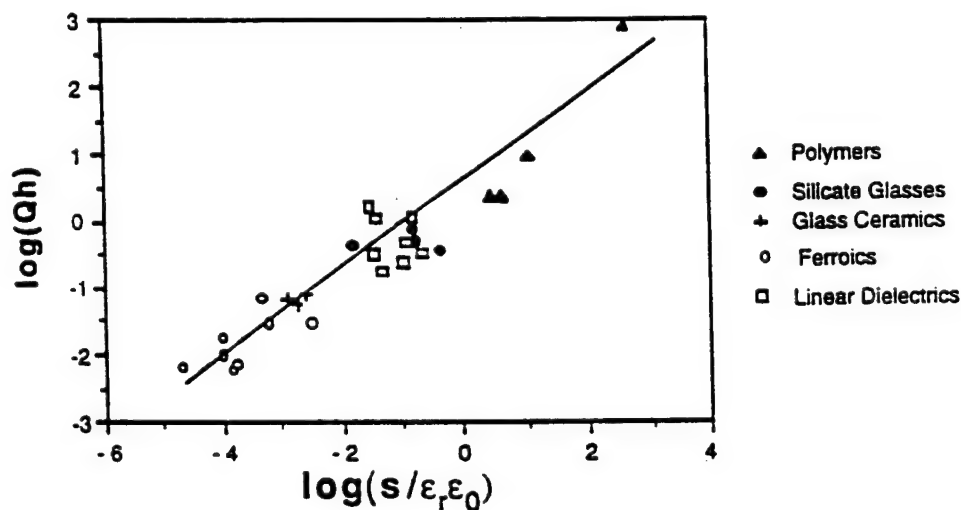


Fig. 6 : Variation of $\log Q_h(m^4/C^2)$ with $\log(s/\epsilon_r \epsilon_0)$ for various materials including polymers shows a near linear relationship

Electrostrictive coefficients have also been related to other anharmonic properties such as the thermal expansion coefficient, the isothermal volume compressibility, and the pressure derivative of the volume compressibility with comparable levels of correlation. More complicated shell models and quasiharmonic models have also been attempted for electrostriction^{19,20,21}. The development of an

a priori model to accurately predict electrostriction in linear dielectrics is held back in part by the lack of reliable and accurate measurements of electrostriction in these materials and also by the complexity of the problem.

ELECTROSTRICTION IN ANTIFERROELECTRIC AND FERROELECTRIC MATERIALS

In a ferroelectric material, that exhibits both spontaneous and induced polarizations, P^F_i and P^i_j , the strains arising from spontaneous polarizations, piezoelectricity, and electrostriction may be formulated as :

$$x_{ij} = Q_{ijkl} P^F_k P^F_l + 2 Q_{ijkl} P^F_k P^i_l + Q_{ijkl} P^i_k P^i_l$$

Leaving out the negligibly small pure electrostrictive contribution in the ferroelectric state, we may express the piezoelectric voltage coefficient g_{ijk} as :

$$g_{ijk} = dx_{ij} / dP^i_l = 2 Q_{ijkl} P^F_k$$

Electrostriction has been shown to be the origin of piezoelectricity in ferroelectric materials in conventional ceramic ferroelectrics such as barium titanate as well as in organic polymer ferroelectrics such as vinylidene fluoride copolymers (PVDF)¹⁵.

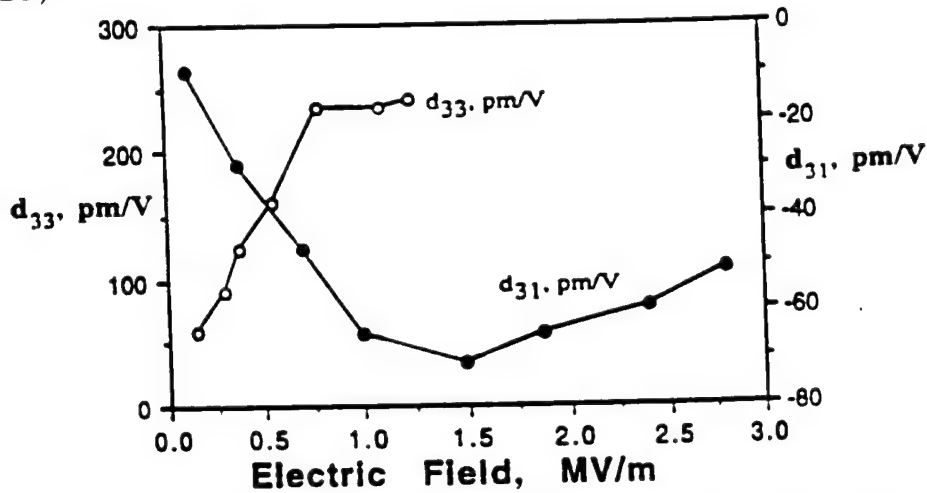


Fig. 7 : Variation of longitudinal and transverse d coefficients with applied electric field for electrostrictive PMN, 18°C (Ref. 1).

This origin of piezoelectricity in electrostriction provides us an avenue into nonlinearity. The piezoelectric coefficient and the dielectric behavior of a transducer can be tuned to desired values. The piezoelectric coefficient varies with the polarization induced in the material, and may be controlled by an applied electric field (Fig. 7). The electrostrictive element may be tuned from an inactive to a highly active state. The electrical impedance of the element may be tuned by exploiting the

dependence of permittivity on the biasing field for these materials, and the saturation of polarization under high fields^{3,21}.

Electrostrictive coupling between sublattices has also been proposed as a mechanism to explain piezoelectric anisotropy in antiferroelectric ceramics²². In a two-sublattice model, if Q_{ij} denotes the conventional electrostriction tensor, and q_{ij} the corresponding intersublattice coupling parameters, then the strains arising from spontaneous polarizations and induced polarizations P_k^F and P_k^i , in the ferroelectric state may be written in Voigt notation as :

$$x_k = (Q_{kl} + q_{kl})(P_k^F)^2 + 2(Q_{kl} + q_{kl}) P_k^F P_k^i + (Q_{kl} + q_{kl})(P_k^i)^2$$

When a spontaneous polarization is induced, the pure electrostrictive contribution from induced polarizations alone is negligible, and we may express the piezoelectric coefficient d_{kl} as $d_{kl} = dx_k / dP_k^i = 2(Q_{kl} + q_{kl}) P_k^F$.

The strains x_k^{AF} associated with the field induced transition from antiferroelectric to ferroelectric states and spontaneous strains x_k^{PF} observed at the transition from paraelectric to antiferroelectric states can be expressed in terms of the spontaneous polarization in the ferroelectric state, P_k^F , and P_k^A , the spontaneous polarization in the antiferroelectric state as :

$$x_k^{AF} = 2q_{ik}(P_k^F)^2 \text{ and } x_k^{PF} = (Q_{kl} - q_{kl})(P_k^A)^2$$

The piezoelectric anisotropy factor d_{ij}/d_{ik} may then be calculated as :

$$d_{ij}/d_{ik} = (Q_{ij} + q_{ij})/(Q_{ik} + q_{ik})$$

Estimations of q_{ij} ($\sim 0.01 \text{ m}^4/\text{C}^2$) show in antiferroelectric materials show that they are comparable to but smaller than Q_{ij} ($\sim 0.06 \text{ m}^4/\text{C}^2$) values.

SOME APPLICATIONS OF ELECTROSTRICTION

Despite the fact that electrostriction was initially relegated to the role of an esoteric, and at best secondary effect, the number of applications of the phenomenon, both theoretical and practical, has been increasing significantly since the introduction of PMN as a prototype electrostrictive material¹. Most applications take advantage of the electrostrictor as an actuator, exploiting the anhysteretic, tunable nature of the electromechanical response. Mechanical applications range from stacked actuators, through inchworms, micro angle adjusting devices, and oil pressure servo valves^{23,24}. These are in the main servo-transducers, deployed as micropositioning devices, featuring a reproducible, non-hysteretic deformation response on the application of an electric signal of suitable magnitude.

The advantages that electrostrictors have over other actuator materials include low hysteresis of the strain-field response, no remanent strain (walk off), reduced aging and creep effects, a high response speed ($<10\text{ms}$), and strain values ($>0.03\%$) achievable at realizable electric fields. Displacement ranges of several tens of microns may be achieved with $\pm 0.01\mu$ reproducibility. Most actuator

applications of electrostrictors as servo transducers and micropositioning devices take advantage of these characteristics. Mechanical applications range from stacked actuators through inchworms, microangle adjusting devices, and oil pressure servo valves. Multilayer actuators produce large displacements and high forces at low drive voltages. The linear change in capacitance with applied stress of an electrostrictor can be used as a capacitive stress gage²⁵. Electrostrictors may also be used as used in field tunable piezoelectric transducers. Recently, electrostrictive materials have been integrated into ultrasonic motors and novel flexensional transducers.

Electrostrictors have also been integrated into "smart" optical systems such as bistable optical devices, interferometric dilatometers and deformable mirrors. Electrostrictive correction of optical aberrations is a significant tool in active optics. Electrostrictors also find applications in "very smart" systems such as sensor-actuator active vibration suppression elements. A shape memory effect arising from inverse hysteretic behavior and electrostriction in PZT family antiferroelectrics is also of interest.

In selecting electrostrictive relaxor ferroelectrics for actuator and sensor applications, the following criteria are commonly used. A large dielectric constant and field stability in the K vs. E relations are useful in achieving large electrostrictive strains. These criteria also lead to large induced polarizations and large induced piezoelectric coefficients through the second converse effect. Broad dielectric transitions allow for a large operating temperature range. Minimal E-P hysteresis and no remanent polarization are useful in achieving a low loss material that is not susceptible to Joule heating effects. These factors are listed in Table 2.

Table 2 : Selection Criteria for Ceramics for Electrostrictive Devices.

Desirable Properties	Material Behavior
<ul style="list-style-type: none"> • Large strain, induced polarization, and induced piezoelectricity • Large operating temperature range • Low loss, low joule heating, minimal hysteresis, no remanent polarization 	<ul style="list-style-type: none"> • Large dielectric constants • Broad dielectric transition • Operation in paraelectric regime ($T > T_{max}$)

As a fundamental effect, electrostriction may prove to be an important factor in the design of sub-micron electronic devices. The present focus is on synthesis of materials with large electrostriction effects. The other extreme of the scale may prove to be of interest, too. As microelectronic devices are taken to smaller dimensions, the increased field levels on the materials can cause quadratic electrostrictive effects ($x \propto E^2 - 1/t^2$) to predominate over inear piezoelectric effects ($x \propto E - 1/t$). This effect is illustrated for silica, using the piezoelectric d coefficients of quartz ($d \sim 10^{-12}$ m/V) and electrostrictive M coefficients of silica glass ($M \sim 10^{-21}$ m²/V²) in fig.8. An applied voltage of 10V is assumed, and piezo and electrostrictive strains are plotted for devices of various thicknesses. Oxide layers in semiconductors are typically a few hundreds of angstroms thick. Around

thicknesses of 100Å, the electrostrictive strain can be larger than the piezoelectric contribution, and close to breakdown strains for ceramics. It is then tempting to consider designing a material with zero electrostriction coefficients, for applications in areas where field induced damage is a significant risk. Other, more benign options are also offered by the effect in an increasing array of novel sensor and actuator applications, that make it well worth further study.

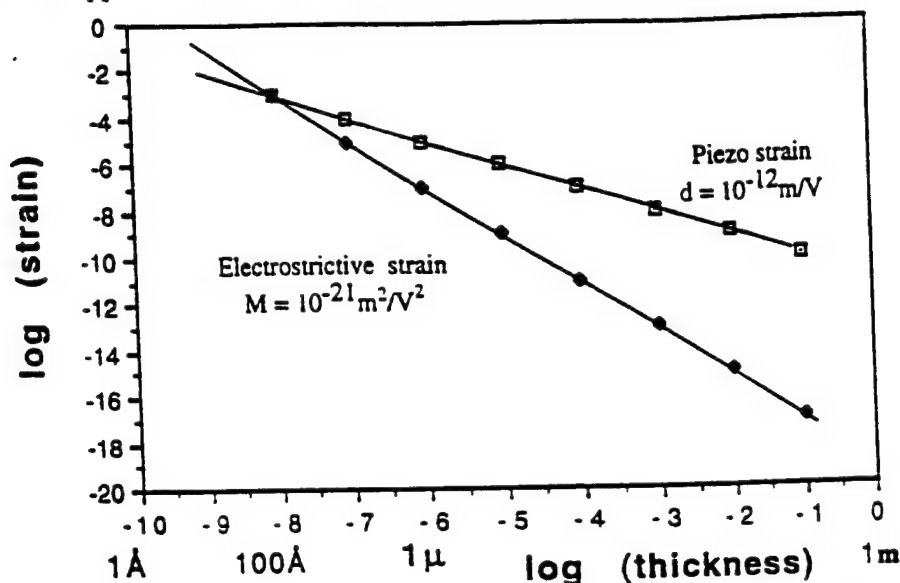


Fig.8 : Strains from piezoelectric quartz and electrostrictive amorphous silica glass for devices of varying thickness, with a voltage of 10V across the device. A typical d coefficient $\sim 10^{-12} \text{ m/V}$ and M coefficient $\sim 10^{-21} \text{ m}^2/\text{V}^2$ were assumed.

MEASURING A RANGE OF ELECTROSTRICTIVE EFFECTS

A variety of experimental methods have been employed to measure a wide range of electrostrictive effects in dielectric materials. The direct and converse electrostriction effects are of importance in that they offer two independent and equivalent techniques of measuring electrostriction in a material :

- by measuring the strains induced in materials in response to applied fields or induced polarizations, using the direct effect, and
- measuring the change in permittivity (via the change in capacitance) under an appropriate stress using the converse effect.

The detection of small electrostrictive strains and the accurate evaluation of electrostrictive properties in most low permittivity materials is a necessarily intricate process. For a field strength of 10^6 V/m , the typical induced strain in a centric ionic material is of the order of 10^{-9} . This translates into a displacement of 10^{-12} m , or 0.01 Å for a sample 1 mm thick. However, experiments to measure electrostrictive effects have been carried out since the turn of the 20th century. An early review of electrostriction by Cady²⁶ cites several measurements of electrostriction in insulators such as gases, oils, rubbers, glasses and cements. These effects were

measured by evaluating the expansion or the contraction of a condenser - probably a Leyden jar in the case of early measurements.

Widely used experimental techniques include the strain gauge method in which the output from a strain gauge (usually pasted on the displacing sample) is used to measure the displacement in a given direction. The increased sensitivity and available in linear voltage displacement transformers (LVDTs) and potentiometers have made them another tool to measure displacements in electrostrictive materials²⁵. The strain gauge and LVDT techniques are typically used for materials with larger strains, typically of the order of 10^{-4} or greater. The technique of capacitance dilatometry involves measuring the change in capacitance arising from the electrostrictive displacement of one face of a parallel plate capacitor. The accuracy of early capacitance dilatometry measurements may have been limited by the unavailability of phase locking and sophisticated electronic feedback loops incorporated into the system to compensate for thermal drift^{28,29}.

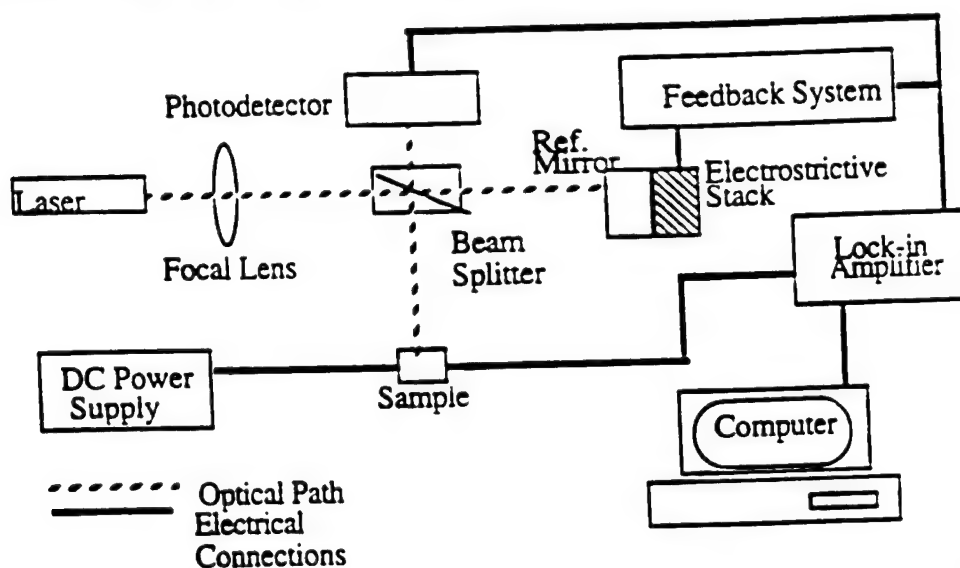


Fig. 9 : Schematic of a typical interferometric ultradilatometer, showing system components, optical paths and electrical connections (Ref. 33)

Homodyne and heterodyne laser ultradilatometers based on Michelson interferometers have been used since the 1930s to measure very small displacements^{30,31,32,33}. These instruments detect the shifts in interference fringes caused by changes in path length of two laser beams, one of which is reflected from the surface of a sample under an ac field. Using phase locking and feedback loops to stabilize the system, interferometers are capable of resolutions of 10^{-3}\AA or better, and usually operate in the range of 1kHz to 100kHz (Fig.9). Typical results from interferometry measurements for MgO and spodumene glass are shown in fig.3.

Recently, a bimorph based dilatometer similar in principle to an atomic force microscope has been introduced. This instrument is capable of measuring

displacements of the order of 0.01\AA in a frequency range of 1 to 100kHz, and is useful in studying electrostriction in thin films (Fig.10)³⁴.

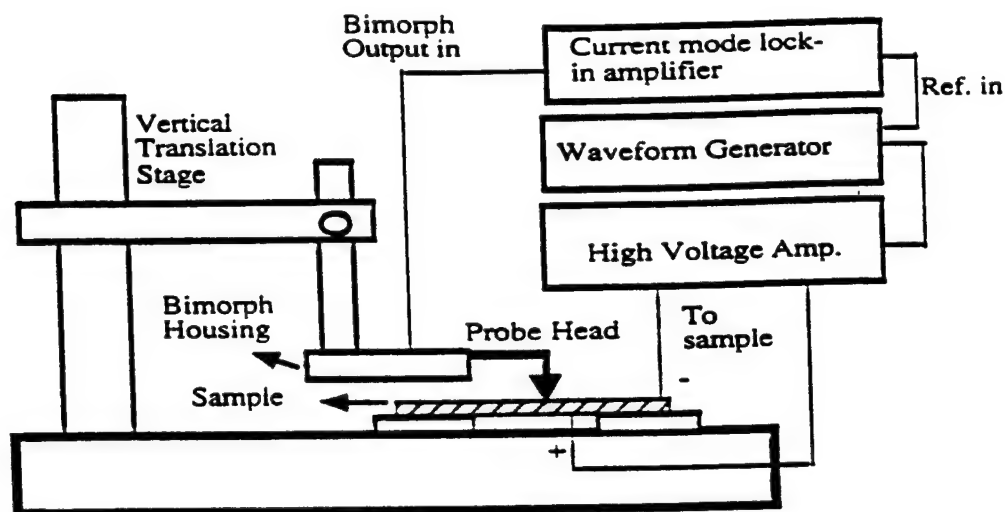


Fig. 10 : Schematic of the bimorph dilatometer for measuring electromechanical response in polymer thin films (Ref. 34)

In most direct effect measurements, the electrostatic attractive stress between opposite charged faces of a dielectric material can contribute to the dimensional change. This stress is called the Maxwell stress, and the corresponding strain x_M is dependent on the dielectric and elastic properties of the material. With all quantities being measured in the direction of the field, x_M is given by³⁵ :

$$x^M = -0.5 \epsilon_0 \epsilon_r s E^2$$

This correction is significant mainly in the case of low permittivity materials where very small strains are observed and for elastically soft polymers.

Techniques for measuring the converse effect call for precision evaluation of dielectric properties. small capacitance changes of the order of $10^{-16} - 10^{-15}$ F need to be resolved for applied stresses of the order of 0.1MPa for low permittivity ceramic materials. Other requirements are stable temperature control and the establishment of 'true' stress systems - completely hydrostatic if the hydrostatic Q_h coefficients are being measured and truly uniaxial stresses in compressometry (Fig. 11a)^{7,36}.

Modifications to compressometric systems are aimed mainly at improving sensitivity or uniaxiality for accurate evaluation of the separated components of the electrostriction tensor^{37,38}. A correction corresponding the capacitance change due to the geometric shape change of the dielectric from elastic strain has to be performed to calculate accurate Q_{ij} values in low permittivity dielectrics when the

converse method is used. Results from compressometry measurements for some common ceramics are illustrated in fig.11b.

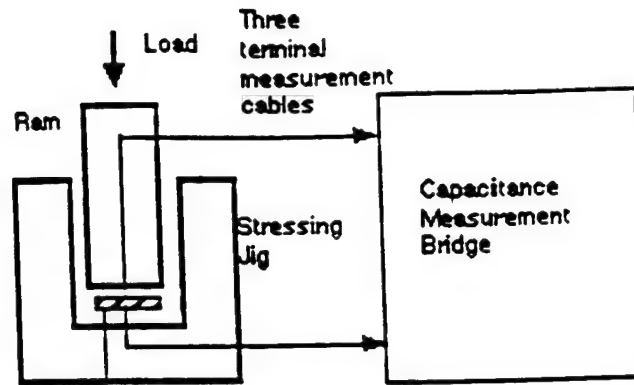


Fig. 11a : Schematic of a converse method measurement system. The sample is shown shaded (Ref. 48).

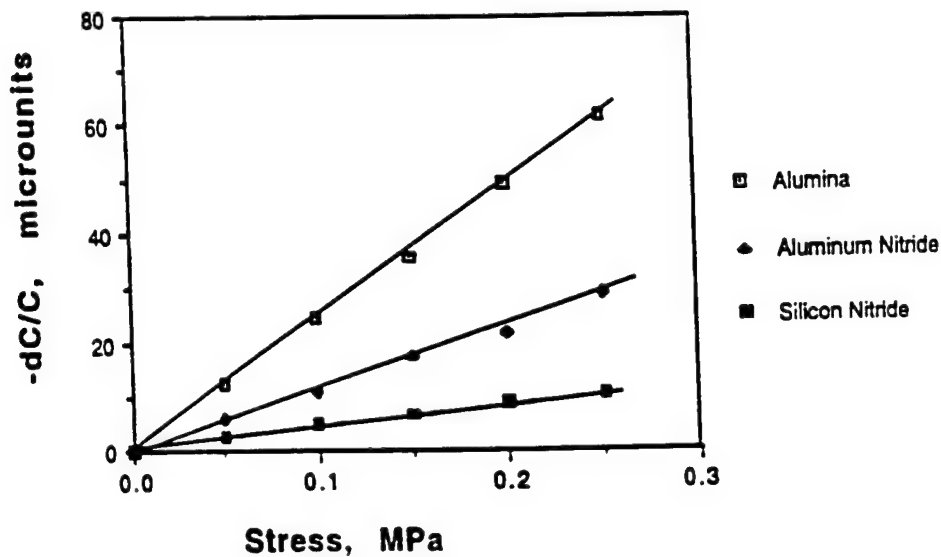


Fig. 11b : Compressometry results for ceramic alumina, aluminum and silicon nitride.

In the case of low permittivity materials, it is necessary to measure electrostriction by both direct and converse methods to calculate reliable and accurate Q or M values (Table 3).

Some recent studies on quartz have used the change in resonant frequency of the vibration modes of the material caused by a dc field³⁹, or the dc field induced variations in the transit times of ultrasonic pulses in the material⁴⁰. These methods are used to calculate combinations of the electroelastic and the electrostrictive

constants of quartz, as well as the nonlinear-piezoelectricity and the permittivity tensors. While the method yields accurate results for the piezoelectricity, the electrostriction values show poorer agreement with values in the literature.

Table 3 : Comparison of direct and converse method measurement results for a variety of dielectric materials. These values agree to within $\pm 5\%$ (Refs. 4, 12)

Material		Direct $Q_{11} \text{ m}^4/\text{C}^2$	Converse $Q_{11} \text{ m}^4/\text{C}^2$
BaF ₂	Q ₁₁	-0.33	-0.31
	Q ₁₂	-0.29	-0.29
	Q ₄₄	1.46	1.48
Spodumene Glass (Li ₂ O·Al ₂ O ₃ ·4SiO ₂)		0.43	0.46
KMnF ₃	Q ₁₁	0.51	0.49
	Q ₁₂	-0.09	-0.10
	Q ₄₄	1.16	1.15
CaF ₂	Q ₁₁	-0.48	-0.49
	Q ₁₂	-0.48	-0.48
	Q ₄₄	1.99	2.01
LiF		0.79	0.57
888 VE Corning Glass Ceramic		0.081	0.079
MgO		0.33	0.34
BeO		1.45	1.48
SrF ₂	Q ₁₁	-0.33	-0.33
	Q ₁₂	0.38	0.39
	Q ₄₄	2.01	1.90
3% Ca / PMN-PT		0.00289	0.00333
Calcite		1.20	1.19

ELECTROSTRICTION AND POLARIZATION MECHANISMS

The basic mechanisms contributing to the polarization in dielectric materials have been identified and treated extensively⁴¹. Electrostriction is a polarization related effect defined as $x_{ij} = Q_{ijkl}P_kP_l$. An understanding of the mechanisms of polarization, especially the ionic and electronic can offer further insight into the underlying mechanisms, and is useful in discerning trends in the electrostrictive behavior, especially in low permittivity linear dielectrics. Electrostriction measurements on most crystalline materials have been performed only over limited frequency ranges (10^5Hz and below). Little variation of the Q coefficients with the frequency of measurement is seen for most crystalline ionic solids. Measurements over wider ranges of frequencies may be necessary to directly study the frequency dependence of electrostriction.

The variation of the low frequency dielectric constants with temperature and pressure has been a subject for analysis by physicists for several decades^{42,20}. Several studies review the changes in refractive index of solids with pressure, and attempt to explain these changes in terms of the polarizabilities of ions^{43,44}. These two sets of data may be combined to analyze the electronic and ionic contributions to electrostriction. The electronic and ionic contributions to electrostriction may be compared for some well characterized oxide and fluoride materials. Results from studies on hydrostatic Q_h electrostriction coefficients of low permittivity fluorides⁴⁵ are used in this analysis, along with measurements of the change of refractive index of solids with pressure^{46,47}.

The electrostrictive contribution from both ionic and electronic polarization mechanisms at low frequencies is proportional to the ratio $1/\epsilon_r (d\epsilon_r/dp)$. Using the approximation $n^2 \sim \epsilon_e$ where n is the refractive index of the material and ϵ_e the electronic or high frequency dielectric constant we may calculate $1/\epsilon_r (d\epsilon_e/dp) \sim 1/\epsilon_r (dn^2/dp)$ from the dn/dp data. To compare the relative contributions of the electronic and ionic polarizations at low frequencies, the same low frequency (1kHz) value for ϵ_r was used in both $1/\epsilon_r (d\epsilon_e/dp)$ and $1/\epsilon_r (d\epsilon_r/dp)$ ratios. The data used here was measured at pressures of 1kbar and less so that no nonlinearity was apparent in dn/dp or $d\epsilon_r/dp$. The results are listed in Table 4 for eight oxide and fluoride materials.

Table 4 : $1/\epsilon_r (dn^2/dp)$ and $1/\epsilon_r (d\epsilon_r/dp)$ for some oxides and fluorides.

Material	$1/\epsilon_r (d\epsilon_r/dp)$	m^2/N	$1/\epsilon_r (dn^2/dp)$	m^2/N
KMnF ₃	-4.39×10^{-11}		8.79×10^{-13}	
CaF ₂	-3.42×10^{-11}		1.5×10^{-12}	
BaF ₂	-4.29×10^{-11}		3.8×10^{-12}	
LiF	-5.08×10^{-11}		4.2×10^{-13}	
MgO	-2.58×10^{-11}		-9.5×10^{-13}	
KTaO ₃	-1.38×10^{-10}		-6.7×10^{-14}	
SrTiO ₃	-2.74×10^{-10}		-2.9×10^{-14}	
Silica Glass	-1.5×10^{-11}		1.03×10^{-13}	

It may be seen that most of the oxides in this analysis show a decrease in refractive index with pressure. This is true also for α -Al₂O₃, ZnO, stoichiometric and nonstoichiometric MgAl₂O₄ spinels, α -ZnS and α -CdS⁴⁴. Most fluorides on the other hand show an increase in n with pressure. Low frequency dielectric

constants decrease with pressure for both oxide and fluoride materials. The differing behaviors at different frequencies are caused by the relative magnitude of the electronic and ionic polarizations to electrostriction. In general the ionic contribution to electrostriction is at least two orders of magnitude greater than the electronic contribution, neglecting sign. The polarization effects caused by the relative shifting of the anion sublattice with respect to the cation sublattice in the crystal dominates the change in electronic polarizabilities of the various ions with pressure.

Both positive and negative values of dn/dp are observed. This holds out the tantalizing possibility of manipulating electrostriction values. By choosing materials with predominantly electronic polarizability contributions, and probably combining or doping them, it may be possible to achieve specific (especially zero) electrostrictive responses in materials. This would involve further research into the variation of electrostrictive effects with frequency, and possible mixing rules for electrostriction. The possibility of achieving zero electrostriction through the manipulation of crystal anisotropy has been discussed in an earlier work⁴⁸.

ELECTROSTRICTION IN POLYMER DIELECTRICS

Piezoelectric and electromechanical coupling properties have been well characterized for ferroelectric polyvinylidene fluoride (PVDF) and its copolymers with trifluoroethylene (TRFE). Their applications have been limited mainly by their lower electromechanical activity when compared to conventional ceramic actuator materials. Recently, there has been renewed interest in nonferroelectric polyurethane elastomers because of their large field induced strain response, which is primarily electrostrictive. These materials could have promising applications in sensor, actuator and microelectromechanical systems technology^{8,49,27}.

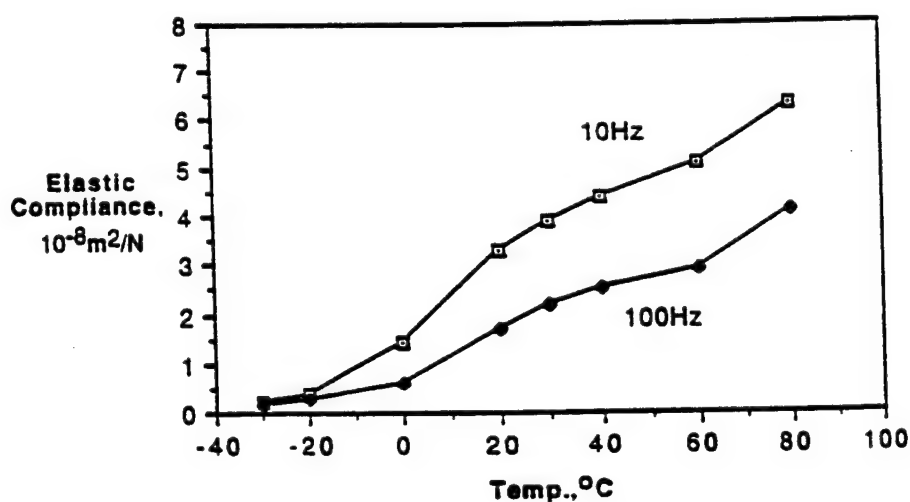


Fig. 12 : Elastic compliance vs. temperature curves for Dow 2105-80AE polyurethane elastomers at 10 and 100Hz (Ref. 50)

Some unusual effects have been observed in these polymer electrostrictors. The first is the large strain response. Strains of the order of 0.25% have reproducibly been achieved in these polymer systems for fields of the order of 1MV/m. In discussing these materials, it may be more practical to define an effective field induced strain coefficient R_e ($x = R_e E^2$), to calculate the large strains achieved in these materials.

A strong temperature effect is observed, as may be expected from the nonlinear temperature dependence of the compliance of this polymer (Fig.12). The Maxwell stress induced strain in these materials is given by :

$$x_M = -0.5 s \epsilon_0 K E^2$$

A Maxwell strain coefficient R_m similar to R_e can be defined to calculate the percentage of Maxwell stress contribution. Below the glass transition temperature T_g , the Maxwell stress contributions are fairly small (~10%) while above T_g , the Maxwell stress contribution to the field induced strain response increases to about 35-50%. A strong frequency dependence is also observed (Fig. 13a).

One effect that may help explain the large field induced strain in these materials is the thickness dependence of R_e . The induced strain and correspondingly, R_e , initially increased with increasing thickness and then decreases (Fig. 13b). Experiments with different electrode materials and thermally stimulated discharging current measurements support the hypothesis that effects related to charge injection, or interfacial charge may cause these dependencies.

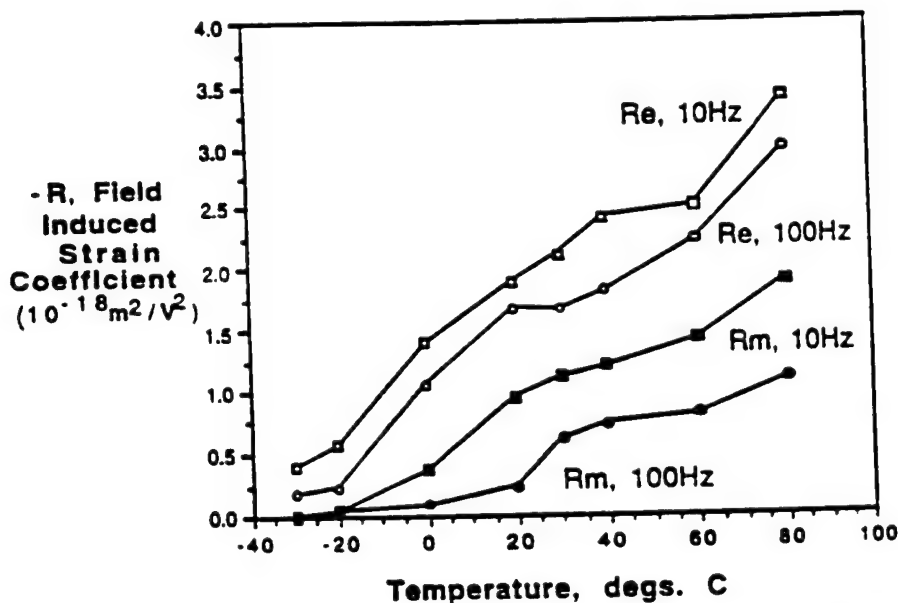


Fig. 13a : Field induced strain coefficient R_e and Maxwell strain coefficient R_m for unfiltered polyurethane thin films, at RT, 10 and 100Hz, through the glass transition for Dow 2105-80AE polyurethane elastomer (Ref. 50).

Some unusual effects have been observed in these polymer electrostrictors. The first is the large strain response. Strains of the order of 0.25% have reproducibly been achieved in these polymer systems for fields of the order of 1MV/m. In discussing these materials, it may be more practical to define an effective field induced strain coefficient R_e ($x = R_e E^2$), to calculate the large strains achieved in these materials.

A strong temperature effect is observed, as may be expected from the nonlinear temperature dependence of the compliance of this polymer (Fig.12). The Maxwell stress induced strain in these materials is given by :

$$x_M = -0.5 s \epsilon_0 K E^2$$

A Maxwell strain coefficient R_m similar to R_e can be defined to calculate the percentage of Maxwell stress contribution. Below the glass transition temperature T_g , the Maxwell stress contributions are fairly small (~10%) while above T_g , the Maxwell stress contribution to the field induced strain response increases to about 35-50%. A strong frequency dependence is also observed (Fig. 13a).

One effect that may help explain the large field induced strain in these materials is the thickness dependence of R_e . The induced strain and correspondingly, R_e , initially increased with increasing thickness and then decreases (Fig. 13b). Experiments with different electrode materials and thermally stimulated discharging current measurements support the hypothesis that effects related to charge injection, or interfacial charge may cause these dependencies.

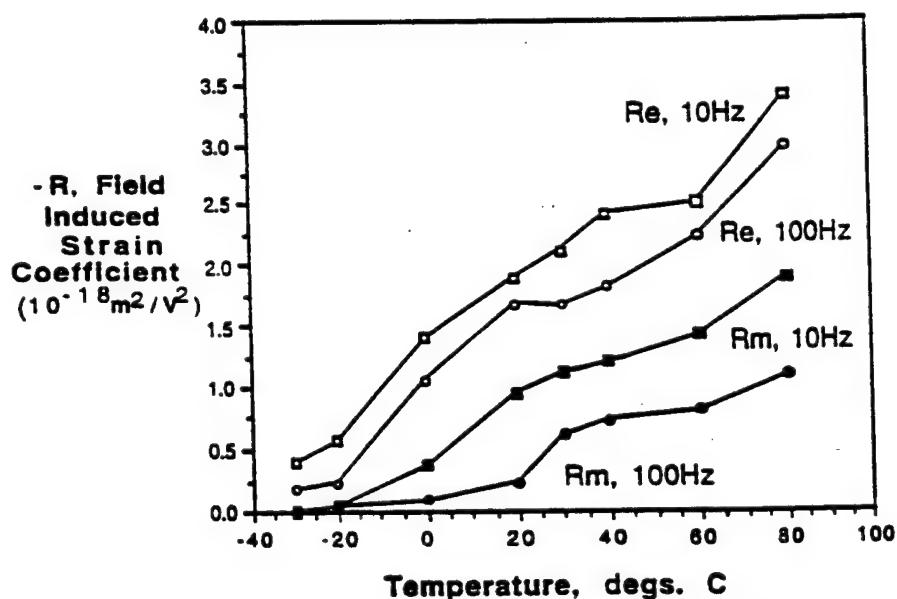


Fig. 13a : Field induced strain coefficient R_e and Maxwell strain coefficient R_m for unfiltered polyurethane thin films, at RT, 10 and 100Hz, through the glass transition for Dow 2105-80AE polyurethane elastomer (Ref. 50).

When a polymer dielectric with metal electrodes is subjected to a high voltage, charge injection can occur in this material. Injected charges can then be trapped in various sites such as defects, interfaces etc., and their effects can show a strong thickness and frequency dependence. Filtering polyurethane polymers before solution casting markedly reduces the field induced strain observed in these materials (Fig. 13b) and the frequency dispersion as well, supporting the charge injection hypothesis. The dielectric and elastic properties are not significantly changed by filtering.

Injected charges can also cause enhanced nonuniform local electric fields, depending on the film thickness. The depth of the region of the polymer with enhanced local fields from charge injection is determined by the transport coefficients of the charges in the polymer film under an electric field. The volume fraction of the polymer with enhanced local fields increases with a decrease in sample thickness. After a critical thickness, though, charge neutralization and homogenization processes reduces the local field enhancement. The strain responses correspondingly decrease⁵⁰.

The nonlinear compliance behavior of these polyurethane elastomers, combined with unusual polarization behavior from interfacial charge effects, can make for large induced strains that are thickness dependent. Further work in this area may identify the specific chemistry responsible for the large strains associated with charge injection, and their applications in sensor and actuator areas.

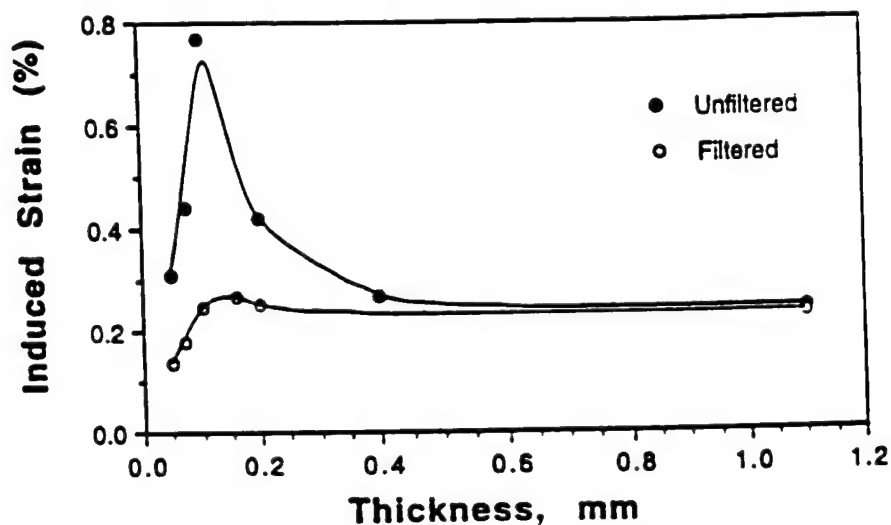


Fig. 13b : Induced strain as a function of thickness (using identical applied electric fields) for filtered and unfiltered electrostrictive polyurethane thin films, at RT, 10Hz (Ref. 50).

SUMMARY

As a summary, some common misconceptions about electrostriction to describe the key ideas set out in this paper are listed here.

1. *Electrostrictive strain is proportional to the square of the applied electric field* : For most low permittivity dielectrics, P is proportional to the applied field E , and therefore this statement is true. However, for high fields, polarization can saturate for high permittivity materials, especially in ferroelectric ceramics. A linear

relationship is observed when strain is plotted as a function of the square of polarization for these materials, but not as a function of the electric field. So it is more accurate to say that electrostrictive strain is proportional to the square of the induced polarization.

2. *Large voltages are required to observe electrostriction* : Two factors have made this a misconception. The introduction of thick and thin film capacitors has enabled high field levels to be achieved even in low permittivity materials at low voltages. Also, the introduction of high dielectric constant relaxor ferroelectrics have raised polarization levels to new heights, further contributing to large electrostrictive strains with relatively modest voltages.

3. *Electrostriction constants are about the same size for all materials, and materials with larger electrostriction coefficients produce the largest strains* : Q constants measured for solids vary from the order of $10^{-3} \text{m}^4/\text{C}^2$ for relaxor ferroelectrics to 1 for low permittivity insulators. Larger Q values have been observed for polymer materials. The induced electrostrictive strain is proportional to the square of the polarization, which implies the square of the relative permittivity is introduced in the strain - electric field relation. For similar electric fields, materials with large dielectric constants produce the larger strains.

4. *Thermal expansion effects make electrostrictive micropositioners and stress gauges impractical* : This statement is true for low permittivity oxide ceramics but not relaxor ferroelectrics. For PMN type ceramics, $Q \sim 0.01 \text{m}^4/\text{C}^2$, $K \sim 10,000$ and the thermal expansion coefficient $\alpha \sim 10^{-6} \text{K}^{-1}$. The electrostrictive strain in these ceramics for a field around 1MV/m is 10^{-3} , which corresponds to a 1000°C change in temperature! Relaxor ferroelectrics can also have abnormally low thermal expansion coefficients near their diffuse phase transitions, where K values are quite large.

In conclusion, though electrostriction effects can be very small in common materials, experimental techniques using phase and frequency selection can help in achieving accurate and reliable measurements of M and Q coefficients. Being a nonlinear effect, electrostriction may be applied smart systems requiring tunable properties. Electrostriction is a significant electromechanical coupling mechanism in many high field situations. Investigating the variation of electrostriction with frequency can reveal the contributions of various polarization mechanisms to electrostrictive effects. In areas such as polymer thin films, the effects of charge injection and defects can produce anomalously large strains that are worth further investigation. Electrostriction still poses a range of problems and challenges in the areas of modeling, and in terms of a fundamental understanding of a well known effect.

ACKNOWLEDGMENTS

This study was sponsored by the National Science Foundation through contract DMR 9634101, Electrostriction in Ceramics and Glasses.

REFERENCES

- ¹Jang, S.J., Ph.D. Thesis, Pennsylvania State University, Univ. Park, PA, 1979.
- ²McCrum, N.G., Read, B.E., Williams, G., *Anelastic and Dielectric Effects in Polymeric Solids*, Dover Publications, Mineola, NY, 1991.
- ³Newnham, R.E., *Chemistry of Electronic Ceramic Materials*, Proc. Int. Conf., Jackson, WY, 1990; NIST Special Publication 804, 39, 1991.
- ⁴Sundar, V., Li, J-F., Viehland, D., Newnham, R.E., *Mat. Res. Bull.*, **31**, p555, 1996.
- ⁵Cross, L.E., *Phil. Mag.*, **1**, 76, 1956.
- ⁶Devonshire, A.F., *Adv. Phys.*, **3**, 94, 1954.
- ⁷Pan, W.Y., Cross, L.E., *Rev. Sci. Instrum.*, **60**, 2701, 1989.
- ⁸Zhenyi, M., Scheinbeim, J.I., Lee, J.W., Newman, B.A., *J. Polymer Sci. Part B: Polymer Phys.*, **32**, p2721, 1994
- ⁹Sundar, V., WaGachigi, K., McCauley, D., Markowski, K.A., Newnham, R.E., *Proc. ISAF* 1994.
- ¹⁰Landolt-Bornstein, *Num. Data on Func. Relns. in Sci. and Tech., New Srs., Gp. III. 24*, Springer-Verlag, New York, NY, 1990.
- ¹¹Uchino, K., Cross, L.E., *Jpn. J. Ap. Phys.*, **19**, L171, 1980
- ¹²Sundar, V., Newnham, R.E., *Mat. Res. Bull.*, **31**, p545, 1996.
- ¹³Simmons, G., Wang, H., *Single Crystal Elastic Consts. and Calculated Aggregate Properties: A Handbook*, MIT Press, Cambridge, MA, 1971.
- ¹⁴Sun, Y., Cao, W.W., Cross, L.E., *Mater. Lett.*, **4**, p329, 1986.
- ¹⁵Furukawa, T., Seo, N., *Jap. J. Appl. Phys.*, **29**, p675, 1990
- ¹⁶Brandrup, J., Immergut, E.H., *Polymer Handbook*, Interscience Pub., New York, NY, 1966.
- ¹⁷Roentgen, W., *Annalen der Physik*, **11**, p780, 1880.
- ¹⁸Hamann, S.D., *Rvw. Phys. Chem. of Japan*, **50**, p147, 1980.
- ¹⁹Srinivasan R., and Srinivasan, K., *J. Phys. Chem. Solids*, **33**, p1079, 1971
- ²⁰Woods, A.D.B., Cochran, W., Brockhouse, B.N., *Phys. Rev.*, **119**, p980, 1960.
- ²¹Zhang, Q.M., Zhao, J., Shrout, T., Kim, N., Cross, L.E., Newnham, R.E., Amin, A., and Kulwicki, B.M., *J. Ap. Phys.*, **77**, p2549, 1995.
- ²²Uchino, K., Oh, K.Y., *J. Am. Ceram. Soc.*, **74**, p1131, 1991.
- ²³Nakajima, Y., Hayashi, T., Hayashi, I., Uchino, K., *Jpn. J. Appl. Phys.*, **24**, p235, 1985.
- ²⁴Nomura, S., Tonooka, K., Kuwata, J., Cross, L.E., Newnham, R.E., *Proc. 2nd Mtg. on Ferroelectric Matrls. and Applications*, Kyoto, p133, 1979.
- ²⁵Sundar, V., Newnham, R.E., *Ferroelectrics*, **135**, p31, 1992.
- ²⁶Cady, W.G., in *"International Critical Tables"*, **6**, p207, 1929

- 27 Elhamy, K., Gauthier-Manuel, B., Manceau, J.F., Bastien, F., *J. App. Phys.*, **77**, p3987, 1995.
- 28 Burkard, H., Kanzig, W., Rossinelli, M., *Helvetica Physica Acta*, **49**, p12, 1976
- 29 Legg, G.J., Lanchester, P.C., *J. Phys. C, Sol. State Phys.*, **13**, p6547, 1980.
- 30 Osterberg, H., and Cookson, *Rev. Sci. Instrum.*, **6**, p347, 1935.
- 31 Luymes, B.J., *Rev. Sci. Instrum.*, **54**, p90, 1983.
- 32 van Sterkenburg, S.W.P., *J. Phys D., App. Phys.*, **25**, p996, 1992.
- 33 Li, J-F, Moses, P., Viehland, D., *Rev. Sci. Instrum.*, **65**, p1089, 1994.
- 34 Su, J., Zhang, Q.M., Kim, C.H., Ting, R.Y., Capps, R., in print, *J. Appl. Polym. Sci.*, 1997.
- 35 Juretschke, H.J., *Am. J. Phys.*, **45**, p277, 1977.
- 36 Bohaty, L., Hassuhl, S., *Acta Cryst.*, **A 33**, p114, 1977
- 37 Balakrishnan, G., Srinivasan, K., Srinivasan, G., *J. App. Phys.*, **54**, p2875, 1983
- 38 Meng, Z.Y., Sun, Y.M., Cross, L.E., *Mater. Letters*, **2**, p544, 1984
- 39 Hruska, C.K., Brendel, R., *J. Appl. Phys.*, **67**, p1676, 1990.
- 40 Kittinger, E., Tichy, J., Freidel, W., *J. Appl. Phys.*, **60**, p1465, 1986.
- 41 von Hippel, A.R., *Dielectrics and Waves*, John Wiley & Sons, New York, NY, 1956.
- 42 Shanker, J., Dixit, S., *Phys. Stat. Sol. (a)*, **123**, p17, 1991.
- 43 Bogardus, E.H., *J. Appl. Phys.*, **36**, p2504, 1965.
- 44 Vedam, K., Davis, T.A., *J. Appl. Phys.*, **33**, p4555, 1967.
- 45 Rittenmyer, K., Ph.D. Thesis, Pennsylvania State University, Univ. Park, PA 1984.
- 46 Vedam, K., Schmidt, E.D.D., Kirk, J.L., Schneider, W.C., *Mat. Res. Bull.*, **4**, p573, 1969.
- 47 Vedam, K., Schmidt, E.D.D., *Phys. Rev.*, **v146**, p548, 1966.
- 48 Sundar, V., Newnham, R.E., *J. Mat. Sci. Lett.*, **13**, p799, 1994.
- 49 Wang, H., Zhang, Q.M., Cross, L.E., Ting, R., Coughlin, C., Rittenmyer, K., *Proc. Int. Symp. Appl. Ferroelectrics*, **9**, p182, 1994.
- 50 Su, J., Zhang, Q.M., in print, *Appl. Phys. Lett.*, 1997.

APPENDIX 96

ELECTROSTRICTION IN DIELECTRIC MATERIALS

R. E. Newnham, V Sundar, R. Yimnirun, J. Su and Q.M. Zhang
Materials Research Laboratory, The Pennsylvania State University, University
Park, PA 16802.

ABSTRACT

Electrostriction is the basis of electromechanical coupling in all insulators. The quadratic electrostrictive strain x_{ij} associated with induced polarization components P_k and P_l is given by $x_{ij} = Q_{ijkl} P_k P_l$. Two converse electrostrictive effects may also be defined. In this paper, some trends in structure-property relationships that govern electrostriction are identified, along with the problems that limit our understanding of this fundamental electromechanical property. Electrostrictive coefficients range from the $\sim 10^{-3} \text{m}^4/\text{C}^2$ in relaxor ferroelectrics to $\sim 10^3 \text{m}^4/\text{C}^2$ in some polymers. High sensitivity techniques such as interferometry or compressometry are necessary to accurately measure electrostrictive effects in most insulators. But even in low-K dielectrics, electrostrictive stresses may initiate breakdown in high field environments such as microelectronic components with small dimensions, high voltage insulators or in high power lasers. In polymeric materials, charge injection mechanisms may produce local electric field concentrations that can cause large electrostrictive strains. The electromechanical properties in polymers have also been observed to vary with the thickness of the specimen. A brief description of the anharmonic nature of electrostriction and its frequency dependence is included.

INTRODUCTION

Many of the recent innovations in the field of electroceramics have exploited the nonlinearities of material properties with factors such as electric field, frequency, or temperature. The nonlinear dielectric behavior of ferroelectric ceramics (fig.1), for example, has opened up new market segments in electronics and communication. In these materials, the polarization increases nonlinearly to a saturation value as the applied electric field is increased¹. Polarization P_i varies with applied electric field E_j as :

$$P_i = \eta_{ij} E_j + \eta_{ijk} E_j E_k + \dots$$

where η_{ij} is the dielectric susceptibility, and η_{ijk} the higher order dielectric susceptibility. η_{ij} is related to the dielectric constant K_{ij} by the linear relation $\eta_{ij} = (K_{ij} - 1)\epsilon_0$.

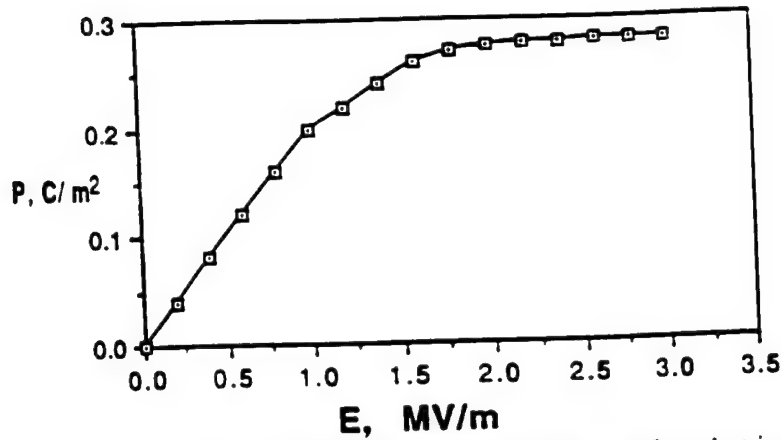


Fig. 1 : Nonlinear polarization vs. electric field behavior for the relaxor ferroelectric 0.9PMN-0.1PT in its paraelectric regime (Ref. 1).

Similarly the nonlinear elastic behavior of materials such as polymers (fig.2) has also been exploited in composite structures. In the natural vulcanized rubber shown, the strain obtained saturates as stress is increased in the low MPa range².

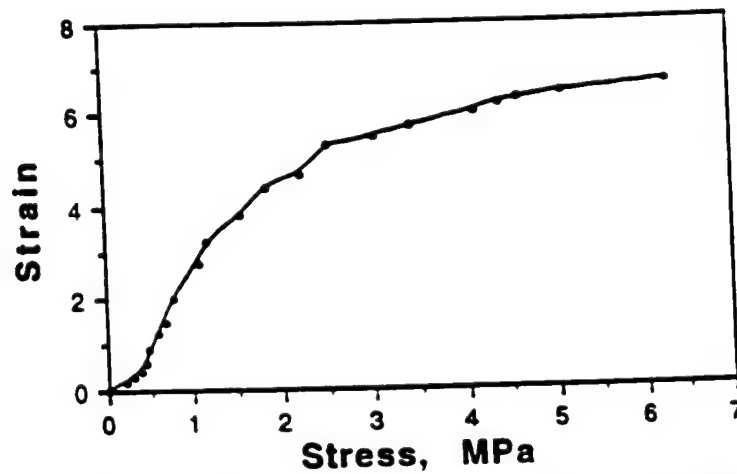


Fig. 2 : Nonlinear strain vs. stress behavior of a typical natural vulcanized rubber (Ref. 2).

Linear stress-strain behavior conforming to Hooke's law is observed only in regions of low stress. In the linear region, the strain x_{ij} is related to the stress X_{kl} by the relation $x_{ij} = s_{ijkl} X_{kl}$. Nonlinear elastic behavior in general may be described by the equation :

$$x_{ij} = s_{ijkl} X_{kl} + s_{ijklmn} X_{kl} X_{mn} + \dots$$

where s_{ijkl} is the elastic compliance, and s_{ijklmn} the higher order elastic compliance.

Materials which display large electromechanical interactions have been exploited in the areas of stress or displacement sensing and in actuating. While most

commercial electromechanical materials and structures are based on linear or piezoelectric mechanisms. nonlinear electromechanical interactions are of interest in engineering material systems and structures with tunable properties³. Strains caused by linear and nonlinear electromechanical interactions may be expressed as:

$$x_{ij} = g_{ijm} P_m + Q_{ijmn} P_m P_n + ..$$

where the linear effect is associated with the piezoelectric constants g_{ijm} and quadratic nonlinear effect with the electrostriction coefficients Q_{ijmn} . These strains may also be expressed in terms of electric field related coefficients d_{ijm} and M_{ijmn} as :

$$x_{ij} = d_{ijm} E_m + M_{ijmn} E_m E_n + ..$$

Piezoelectricity is absent in centric crystals, but electrostriction, being a tensor property of even rank, can be observed in all insulating materials. Quadratic

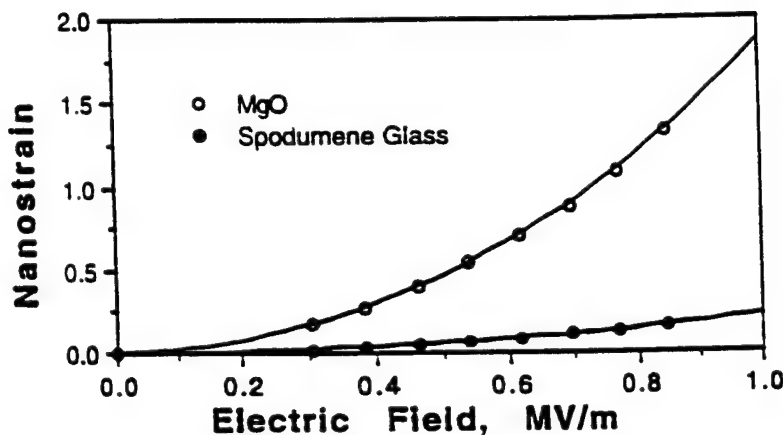


Fig. 3 : Electrostrictive strain can be observed in all insulating materials. Quadratic strain vs. electric field relationships for single crystal $\langle 100 \rangle$ oriented MgO and spodumene glass measured by interferometry are illustrated here.

electrostrictive strain in MgO and spodumene glass ($\text{Li}_2\text{O} \cdot \text{Al}_2\text{O}_3 \cdot 4\text{SiO}_2$) is illustrated in fig. 3⁴. It is also the primary electromechanical coupling mechanism in centrosymmetric materials. In this review, we look at nonlinear electromechanical interactions in the different ways in which it may be observed in materials, along with trends in structure property relationships that affect these interactions.

PHENOMENOLOGY OF ELECTROSTRICTION

Nonlinearity in electrical, elastic and electromechanical properties may be defined using the Devonshire formalism^{5,6}. The elastic Gibbs function (G) for the free energy of a material may be expressed in differential form as :

$$dG = -SdT - x_{ij}dX_{ij} + E_i dP_i$$

where S is the entropy, T the temperature, x_{ij} the elastic strain tensor, X_{ij} the stress tensor, and E_i and P_i the electric field and polarization vectors. Properties relating derived variables such as S , x_{ij} or E_i to fixed variables of state such as T , X_{ij} or P_i are obtained by taking the second derivative of this free energy function. For example, the first order terms for inverse dielectric susceptibility χ_{mn} and elastic compliance s_{ijkl} may be expressed as :

$$\chi_{mn} = (dE_m/dP_n)_{X,T} = (d^2G/dP_m dP_n)_{X,T}, \text{ and}$$

$$s_{ijkl} = (dx_{ij}/dX_{kl})_{P,T} = (d^2G/dX_{ij} dX_{kl})_{P,T}$$

Cross-coupled properties can be derived by changing the differentiation variable for the second differential. The properties that introduce strain in a material are derived by differentiating the elastic Gibbs function with respect to stress. The tensor properties associated with these effects are elastic constants, linear and nonlinear thermal expansion, linear piezoelectric constants (g_{ijm}), and quadratic (Q_{ijmn}) electrostriction constants. These electromechanical interactions can be expressed in a power series to the second order (fixed X , T) as :

$$x_{ij} = g_{ijm} P_m + Q_{ijmn} P_m P_n + \dots$$

Electrostriction may be thus defined as the quadratic coupling between strain and electric field, or between strain and polarization. It is a fourth rank tensor defined by the following relationships :

$$x_{ij} = M_{ijmn} E_m E_n, \text{ or}$$

$$x_{ij} = Q_{ijmn} P_m P_n$$

where M_{ijmn} the fourth rank field related electrostriction tensor and Q_{ijmn} the fourth rank polarization related electrostriction tensor. The M and Q coefficients are equivalent in linear dielectrics. Conversions between the two coefficients are carried out using the field-polarization relationships $P_m = \eta_{mn} E_n$ and $E_n = \chi_{mn} P_m$ where η_{mn} is the dielectric susceptibility tensor, and χ_{mn} is the inverse dielectric susceptibility tensor. The need for defining a polarization related electrostriction tensor arises from the fact that ferroelectrics and other materials often show nonlinearity of dielectric properties with changing electric fields. Electrostrictive strain is not always quadratic with electric field, especially in high permittivity materials with nonlinear $P_i - E_j$ relationships (Fig. 4). Thus, it is useful to define a polarization related electrostriction coefficient Q_{ijmn} better express the quadratic nature of electrostriction in all materials.

The M coefficients are defined in units of m^2/V^2 . Their values range from about $10^{-24} m^2/V^2$ in low permittivity materials to $10^{-16} m^2/V^2$ in high permittivity actuator materials such relaxor ferroelectrics such as lead magnesium niobate - lead

titanate compositions. Large strains of the order of strains in ferroelectric piezoelectric materials such as lead zirconate titanate may be induced in these materials for similar fields. Q coefficients are defined in units of m^4/C^2 . Q values vary in an opposite way to M values. Q ranges from $10^{-3} \text{ m}^4/\text{C}^2$ in relaxor ferroelectrics to greater than the order of $10^3 \text{ m}^4/\text{C}^2$ in polyurethane films.

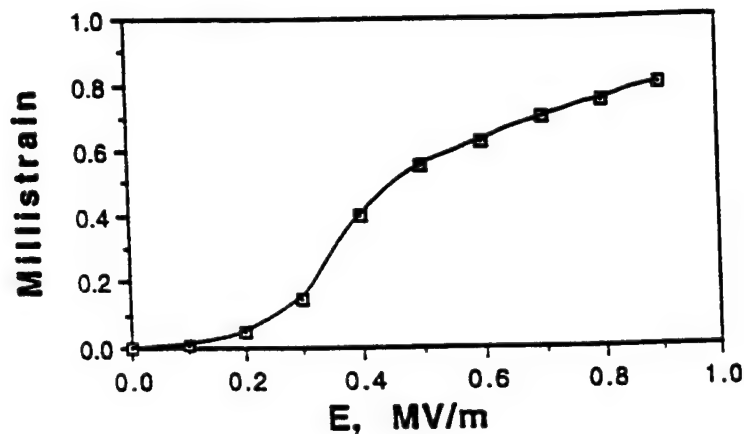


Fig. 4 : Electrostrictive strain is not always quadratic with electric field, especially for high K materials such as PMN (Ref. 1).

Fourth rank electrostriction tensors may also be expressed in collapsed Voigt notation as M_{ij} or Q_{ij} . Expressing these tensors in matrix form illustrates the effects of point group symmetry on this tensor, as applied through Neumann's principle. For example, the electrostriction matrix for cubic materials (point group $m\bar{3}m$) is :

Q_{11}	Q_{12}	Q_{12}	0	0	0
Q_{12}	Q_{11}	Q_{12}	0	0	0
Q_{12}	Q_{12}	Q_{11}	0	0	0
0	0	0	Q_{44}	0	0
0	0	0	0	Q_{44}	0
0	0	0	0	0	Q_{44}

while the matrix for isotropic materials such as unoriented ceramics, glasses or polymers (Curie groups $\infty\infty m$ and $\infty\infty$) would be of the form :

Q_{11}	Q_{12}	Q_{12}	0	0	0
Q_{12}	Q_{11}	Q_{12}	0	0	0
Q_{12}	Q_{12}	Q_{11}	0	0	0
0	0	0	$2(Q_{11}-Q_{12})$	0	0
0	0	0	0	$2(Q_{11}-Q_{12})$	0
0	0	0	0	0	$2(Q_{11}-Q_{12})$

It is also useful to define a hydrostatic electrostriction coefficient Q_h , as the variation of susceptibility with applied hydrostatic pressure. This coefficient can be useful in comparing electrostrictive effects in materials with different anisotropy characteristics. Since applied compressive stress is by convention negative, Q_h values are positive for ceramic materials, indicating the decrease of inverse dielectric susceptibility (χ) with applied pressure. $Q_h = 0.5(d\chi/dp) = Q_{11} + 2Q_{12}$ (for materials with cubic or isotropic symmetry). The Q_h , dielectric permittivity, and elastic compliance values for some common dielectric materials⁹⁻¹⁶ are listed in Table 1.

As a consequence of the quadratic nature of the electrostriction effect, the sign of the strain produced in the material is independent of the polarity of the field. This is in contrast with linear piezoelectricity where reversing the direction of the field would cause a change in the sign of the strain.

Another consequence is that electrostrictive strain occurs at twice the frequency of an applied AC field. In acentric materials where both piezoelectric and electrostrictive strains may be observed, this fact is very useful in separating the strains arising from piezoelectricity and from electrostriction.

The electrostriction tensor can also be treated as a complex quantity, similar to the dielectric and the piezoelectric tensors. The imaginary part of the electrostriction is also a fourth rank tensor. Such a treatment could be very useful in providing a better understanding at electromechanical energy conversion in materials with relaxation mechanisms such as glasses containing alkali ions⁷ or polymeric materials⁸. In this review, though, the discussion is confined to the real part of the electrostriction tensor.

Also, electrostriction in liquid and gaseous dielectrics has been studied since late in the 19th century, when studies by Roentgen¹⁷ showed that all liquids expanded when an electric field was applied to them. In liquids, electrostriction is observed mainly as the contraction of a solvent around solute ions. Similar to solids, the electrostrictive effect in liquids is observed to be proportional to the square of the charge of the ions, inversely proportional to the ionic radius, and proportional to the value of $K^{-2}dK/dP$ for the solute¹⁸. This discussion, however, is confined to solid dielectrics.

DIRECT AND CONVERSE ELECTROSTRICTION EFFECTS

The electrostriction effect defined in the previous section, which relates the quadratic dependence of strain on applied field or induced polarization may be termed the direct electrostrictive effect. This effect may be expressed in terms of field related and polarization related electrostriction coefficients as :

$$Q_{ijmn} = (d^2 x_{ij} / dP_m dP_n) = (d^3 G / dX_{ij} dP_m dP_n) \text{ or}$$

$$M_{ijmn} = (d^2 x_{ij} / dE_m dE_n) = (d^3 G / dX_{ij} dE_m dE_n)$$

By changing the order of differentiation in the free energy term, we may derive an equivalent converse effect of electrostriction, as :

$$Q_{ijmn} = -1/2 (d \chi_{ij} / d X_{mn}) = (d^3 G / dP_i dP_j dX_{mn}) \text{ or}$$

$$M_{ijmn} = 1/2 (d \eta_{ij} / d X_{mn}) = (d^3 G / d E_i d E_j d X_{mn})$$

which is the variation of dielectric susceptibility or its inverse with applied stress.

Table 1 : List of dielectric constants, elastic constants, and electrostriction coefficients of common dielectrics.

Materials	K	S ($\times 10^{-12}$) (m^2/N)	S/K ϵ_0 ($\times 10^{-4}$) (m/FN)	Q _h (m^4/C^2)	Ref
<i>Relaxor Ferroelectric</i>					
PLZT (11/65/35)	5900	9.50	1.82	0.007	9, 10, 11
BaTi _{1-x} Sn _x O ₃ (x=0.38)	10300	8.90	1.01	0.0099	
BaSr _x Ti _{1-x} O ₃ (x=0.35)	25000	4.55	0.206	0.0069	
La/PMN-PT (1/93/97)	13000	16.42	1.43	0.006	
<i>Perovskite Ferroelectric</i>					
SrTiO ₃	450	1.82	4.57	0.07	11
PbTiO ₃	270	7.81	32.6	0.03	
BaTiO ₃	1070	6.02	6.36	0.03	
Pb(Ti _{1-x} Zr _x)O ₃	1700	1.52	1.01	0.018	
<i>Glass-Ceramics</i>					
Corning 888VE	300	7.25	27.31	0.079	9
Corning 888YT	370	5.85	17.87	0.055	
Corning 888ZF	440	4.93	12.66	0.064	
<i>Linear Dielectrics</i>					
<u>Single Crystals</u>					
CaF ₂	6.8	6.92	1150	0.47	13, 4
BaF ₂	7.4	15.3	2342	0.33	
KMnF ₃	9.8	9.72	1121	0.24	
MgO	9.8	4.03	465	0.18	
<u>Ceramics</u>					
MgO-Doped Al ₂ O ₃	10.5	2.90	312	1.58	This work
AlN	9.5	3.03	360	0.318	
Si ₃ N ₄	8.7	3.13	406	1.06	
<i>Glasses</i>					
Na-Aluminosilicate	10.2	15.3	1696	0.519	12, 14
Fused-SiO ₂	3.8	14.0	4163	0.37	
Na ₂ O.3SiO ₂	11.3	16.3	1629	0.765	This work
Spodumene Glass	7.9	1.18	169	0.43	
<i>Polymers</i>					
PVDF	16	420	29660	2.4	15, 16, This work
VDF/TrFE	11	400	41090	2.5	
PVC	3.4	333	110700	10.1	
Polvurethane	6.5	25000	4346000	850	

It is also possible to define a second converse effect, in which electrostriction is defined as the variation of the piezoelectric voltage coefficient g_{ijk} with the induced polarization.

$$Q_{ijkl} = -1/2 (d g_{ijk} / dP_l)$$

ELECTROSTRICTION IN RELATION TO OTHER ANHARMONIC MATERIAL PROPERTIES

It is necessary to model anharmonic behavior to describe some macroscopic properties that cannot be modeled using the harmonic approximation in solid state theory. Some of these properties are the thermal expansion coefficient, the isothermal compressibility, its pressure coefficient, and electrostriction, all of which contribute to the macroscopic Gibbs free energy, and are typically defined like compliance coefficients.

Modeling anharmonic properties from first principles involves much effort in computational theoretical physics. However, simpler atomistic models, in combination with empirical correlations, can provide some understanding of electrostriction in relation with other anharmonic properties.

Under the action of an applied electric field, the cations and anions in a crystal structure are displaced in opposite directions by an amount Δr . This displacement is responsible for the electric polarization, the dielectric constant, and the electrostrictive strain³. To a first approximation, we may express the relation between these as :

$$Q = \chi/P^2 \sim (\Delta r)/(\Delta r)^2 = 1/\Delta r \sim 1/K$$

Plotting Q_h as a function of the dielectric permittivity (fig. 5) reveals two distinct trends, one for materials with cubic perovskite structures and another for other materials. Perovskite materials of comparable compliances follow the $Q \sim 1/K$ relation. However, linear dielectric with a large range of compliances and a small range of dielectric constants do not follow this relationship. For example, diamond is a very covalent material with a very low compliance, and has a $Q_h \sim 0.02$. Introducing a larger compliance range by including soft polymer dielectrics can further dilute this relationship.

Large strains in compliant solids such as polymers can introduce large changes in the dielectric stiffness and in anharmonic potentials. Electrostrictive strain is displacive and acts against the elastic forces in a material. Introducing the elastic compliance s into the Q vs. K relationship can better express the correlation between these properties. Through the first converse effect, electrostriction is proportional to the change of dielectric stiffness β with stress X , which may be expressed as $Q \sim (\Delta\beta)/(X) \sim \chi/(\chi/s) \sim s$

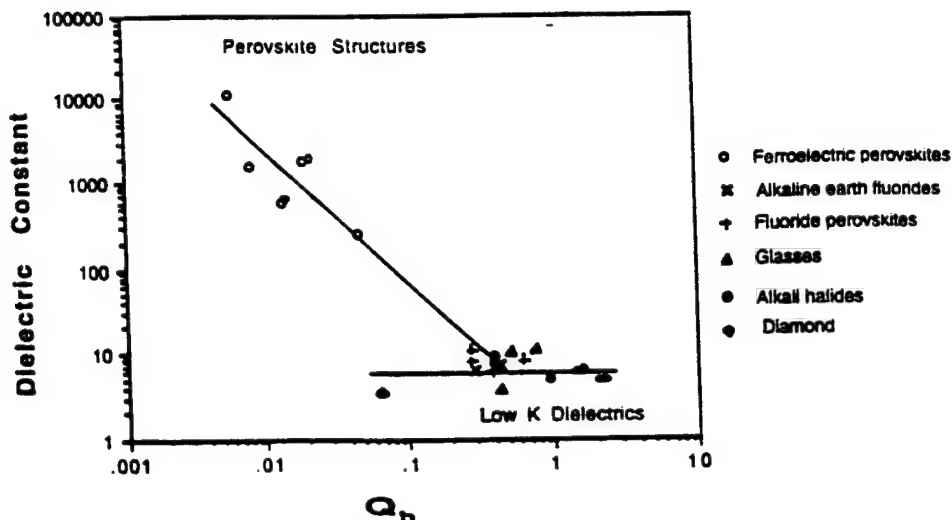


Fig. 5 : Variation of $Q_h(m^4/C^2)$ with dielectric constant for various materials.

Empirically, $\log(Q_h)$ is seen to vary nearly linearly with $\log(s/\epsilon_0 K)$ (Fig. 6). This combination of the compliance and the dielectric properties of a materials may be used as a predictor of the size of electrostriction effects in insulators.

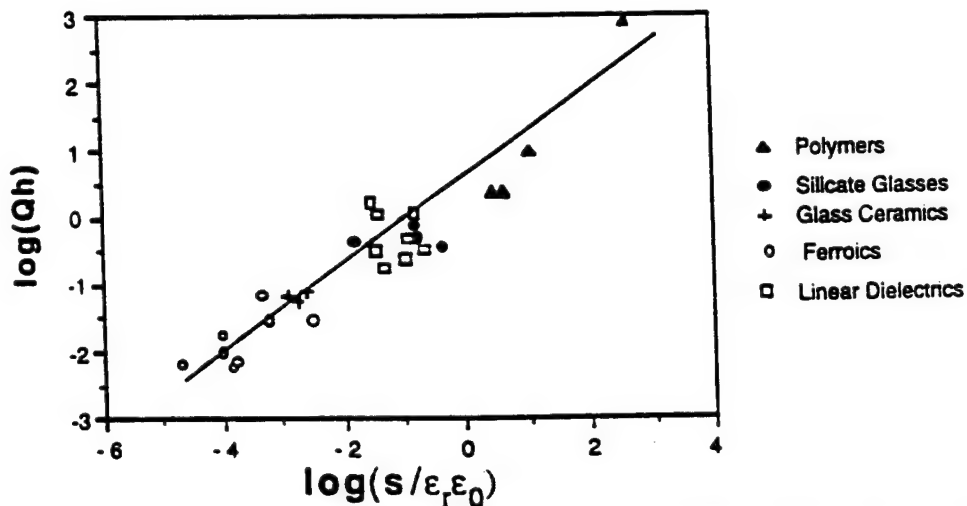


Fig. 6 : Variation of $\log Q_h(m^4/C^2)$ with $\log(s/\epsilon_r \epsilon_0)$ for various materials including polymers shows a near linear relationship

Electrostrictive coefficients have also been related to other anharmonic properties such as the thermal expansion coefficient, the isothermal volume compressibility, and the pressure derivative of the volume compressibility with comparable levels of correlation. More complicated shell models and quasiharmonic models have also been attempted for electrostriction^{19,20,21}. The development of an

a priori model to accurately predict electrostriction in linear dielectrics is held back in part by the lack of reliable and accurate measurements of electrostriction in these materials and also by the complexity of the problem.

ELECTROSTRICTION IN ANTIFERROELECTRIC AND FERROELECTRIC MATERIALS

In a ferroelectric material, that exhibits both spontaneous and induced polarizations, P^F_i and P^i_j , the strains arising from spontaneous polarizations, piezoelectricity, and electrostriction may be formulated as :

$$x_{ij} = Q_{ijkl} P^F_k P^F_l + 2 Q_{ijkl} P^F_k P^i_l + Q_{ijkl} P^i_k P^i_l$$

Leaving out the negligibly small pure electrostrictive contribution in the ferroelectric state, we may express the piezoelectric voltage coefficient g_{ijk} as :

$$g_{ijk} = dx_{ij} / dP^i_l = 2 Q_{ijkl} P^F_k$$

Electrostriction has been shown to be the origin of piezoelectricity in ferroelectric materials in conventional ceramic ferroelectrics such as barium titanate as well as in organic polymer ferroelectrics such as vinylidene fluoride copolymers (PVDF)¹⁵.

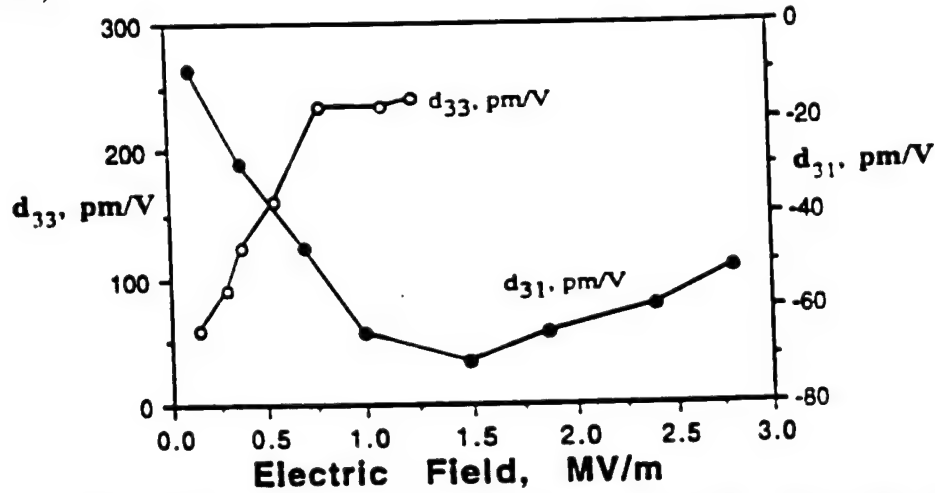


Fig. 7 : Variation of longitudinal and transverse d coefficients with applied electric field for electrostrictive PMN, 18°C (Ref. 1).

This origin of piezoelectricity in electrostriction provides us an avenue into nonlinearity. The piezoelectric coefficient and the dielectric behavior of a transducer can be tuned to desired values. The piezoelectric coefficient varies with the polarization induced in the material, and may be controlled by an applied electric field (Fig. 7). The electrostrictive element may be tuned from an inactive to a highly active state. The electrical impedance of the element may be tuned by exploiting the

dependence of permittivity on the biasing field for these materials, and the saturation of polarization under high fields^{3,21}.

Electrostrictive coupling between sublattices has also been proposed as a mechanism to explain piezoelectric anisotropy in antiferroelectric ceramics²². In a two-sublattice model, if Q_{ij} denotes the conventional electrostriction tensor, and q_{ij} the corresponding intersublattice coupling parameters, then the strains arising from spontaneous polarizations and induced polarizations P_k^F and P_k^i , in the ferroelectric state may be written in Voigt notation as :

$$x_k = (Q_{kl} + q_{kl})(P_k^F)^2 + 2(Q_{kl} + q_{kl}) P_k^F P_k^i + (Q_{kl} + q_{kl})(P_k^i)^2$$

When a spontaneous polarization is induced, the pure electrostrictive contribution from induced polarizations alone is negligible, and we may express the piezoelectric coefficient d_{kl} as $d_{kl} = dx_k / dP_k^i = 2(Q_{kl} + q_{kl}) P_k^F$

The strains x_k^{AF} associated with the field induced transition from antiferroelectric to ferroelectric states and spontaneous strains x_k^{PF} observed at the transition from paraelectric to antiferroelectric states can be expressed in terms of the spontaneous polarization in the ferroelectric state, P_k^F , and P_k^A , the spontaneous polarization in the antiferroelectric state as :

$$x_k^{AF} = 2q_{lk}(P_k^F)^2 \text{ and } x_k^{PF} = (Q_{kl} - q_{kl})(P_k^A)^2$$

The piezoelectric anisotropy factor d_{ij}/d_{ik} may then be calculated as :

$$d_{ij}/d_{ik} = (Q_{ij} + q_{ij})/(Q_{ik} + q_{ik})$$

Estimations of q_{ij} ($\sim 0.01 \text{ m}^4/\text{C}^2$) show in antiferroelectric materials show that they are comparable to but smaller than Q_{ij} ($\sim 0.06 \text{ m}^4/\text{C}^2$) values.

SOME APPLICATIONS OF ELECTROSTRICTION

Despite the fact that electrostriction was initially relegated to the role of an esoteric, and at best secondary effect, the number of applications of the phenomenon, both theoretical and practical, has been increasing significantly since the introduction of PMN as a prototype electrostrictive material¹. Most applications take advantage of the electrostrictor as an actuator, exploiting the anhysteretic, tunable nature of the electromechanical response. Mechanical applications range from stacked actuators, through inchworms, micro angle adjusting devices, and oil pressure servo valves^{23,24}. These are in the main servo-transducers, deployed as micropositioning devices, featuring a reproducible, non-hysteretic deformation response on the application of an electric signal of suitable magnitude.

The advantages that electrostrictors have over other actuator materials include low hysteresis of the strain-field response, no remanent strain (walk off), reduced aging and creep effects, a high response speed ($<10\text{ms}$), and strain values ($>0.03\%$) achievable at realizable electric fields. Displacement ranges of several tens of microns may be achieved with $\pm 0.01\mu$ reproducibility. Most actuator

applications of electrostrictors as servo transducers and micropositioning devices take advantage of these characteristics. Mechanical applications range from stacked actuators through inchworms, microangle adjusting devices, and oil pressure servo valves. Multilayer actuators produce large displacements and high forces at low drive voltages. The linear change in capacitance with applied stress of an electrostrictor can be used as a capacitive stress gage²⁵. Electrostrictors may also be used as used in field tunable piezoelectric transducers. Recently, electrostrictive materials have been integrated into ultrasonic motors and novel flextensional transducers.

Electrostrictors have also been integrated into "smart" optical systems such as bistable optical devices, interferometric dilatometers and deformable mirrors. Electrostrictive correction of optical aberrations is a significant tool in active optics. Electrostrictors also find applications in "very smart" systems such as sensor-actuator active vibration suppression elements. A shape memory effect arising from inverse hysteretic behavior and electrostriction in PZT family antiferroelectrics is also of interest.

In selecting electrostrictive relaxor ferroelectrics for actuator and sensor applications, the following criteria are commonly used. A large dielectric constant and field stability in the K vs. E relations are useful in achieving large electrostrictive strains. These criteria also lead to large induced polarizations and large induced piezoelectric coefficients through the second converse effect. Broad dielectric transitions allow for a large operating temperature range. Minimal E-P hysteresis and no remanent polarization are useful in achieving a low loss material that is not susceptible to Joule heating effects. These factors are listed in Table 2.

Table 2 : Selection Criteria for Ceramics for Electrostrictive Devices.

Desirable Properties	Material Behavior
<ul style="list-style-type: none"> • Large strain, induced polarization, and induced piezoelectricity • Large operating temperature range • Low loss, low joule heating, minimal hysteresis, no remanent polarization 	<ul style="list-style-type: none"> • Large dielectric constants • Broad dielectric transition • Operation in paraelectric regime ($T > T_{max}$)

As a fundamental effect, electrostriction may prove to be an important factor in the design of sub-micron electronic devices. The present focus is on synthesis of materials with large electrostriction effects. The other extreme of the scale may prove to be of interest, too. As microelectronic devices are taken to smaller dimensions, the increased field levels on the materials can cause quadratic electrostrictive effects ($x \propto E^2 \sim 1/t^2$) to predominate over linear piezoelectric effects ($x \propto E \sim 1/t$). This effect is illustrated for silica, using the piezoelectric d coefficients of quartz ($d \sim 10^{-12}$ m/V) and electrostrictive M coefficients of silica glass ($M \sim 10^{-21}$ m²/V²) in fig.8. An applied voltage of 10V is assumed, and piezo and electrostrictive strains are plotted for devices of various thicknesses. Oxide layers in semiconductors are typically a few hundreds of angstroms thick. Around

thicknesses of 100Å, the electrostrictive strain can be larger than the piezoelectric contribution, and close to breakdown strains for ceramics. It is then tempting to consider designing a material with zero electrostriction coefficients, for applications in areas where field induced damage is a significant risk. Other, more benign options are also offered by the effect in an increasing array of novel sensor and actuator applications, that make it well worth further study.

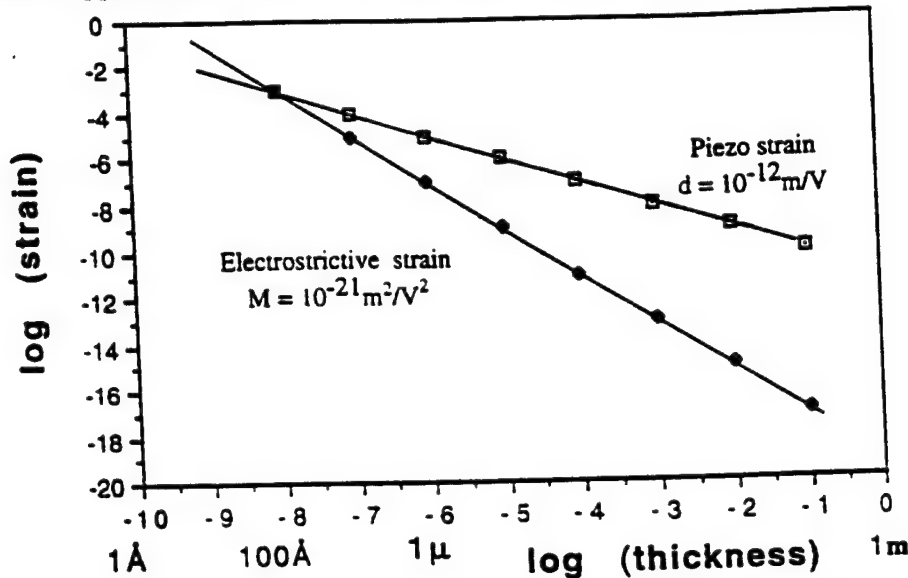


Fig.8 : Strains from piezoelectric quartz and electrostrictive amorphous silica glass for devices of varying thickness, with a voltage of 10V across the device. A typical d coefficient $\sim 10^{-12} \text{m/V}$ and M coefficient $\sim 10^{-21} \text{m}^2/\text{V}^2$ were assumed.

MEASURING A RANGE OF ELECTROSTRICTIVE EFFECTS

A variety of experimental methods have been employed to measure a wide range of electrostrictive effects in dielectric materials. The direct and converse electrostriction effects are of importance in that they offer two independent and equivalent techniques of measuring electrostriction in a material :

- by measuring the strains induced in materials in response to applied fields or induced polarizations, using the direct effect, and
- measuring the change in permittivity (via the change in capacitance) under an appropriate stress using the converse effect.

The detection of small electrostrictive strains and the accurate evaluation of electrostrictive properties in most low permittivity materials is a necessarily intricate process. For a field strength of 10^6 V/m , the typical induced strain in a centric ionic material is of the order of 10^{-9} . This translates into a displacement of 10^{-12} m , or 0.01 Å for a sample 1 mm thick. However, experiments to measure electrostrictive effects have been carried out since the turn of the 20th century. An early review of electrostriction by Cady²⁶ cites several measurements of electrostriction in insulators such as gases, oils, rubbers, glasses and cements. These effects were

measured by evaluating the expansion or the contraction of a condenser - probably a Leyden jar in the case of early measurements.

Widely used experimental techniques include the strain gage method in which the output from a strain gage (usually pasted on the displacing sample) is used to measure the displacement in a given direction. The increased sensitivity and available in linear voltage displacement transformers (LVDTs) and potentiometers have made them another tool to measure displacements in electrostrictive materials²⁵. The strain gage and LVDT techniques are typically used for materials with larger strains, typically of the order of 10^{-4} or greater. The technique of capacitance dilatometry involves measuring the change in capacitance arising from the electrostrictive displacement of one face of a parallel plate capacitor. The accuracy of early capacitance dilatometry measurements may have been limited by the unavailability of phase locking and sophisticated electronic feedback loops incorporated into the system to compensate for thermal drift^{28,29}.

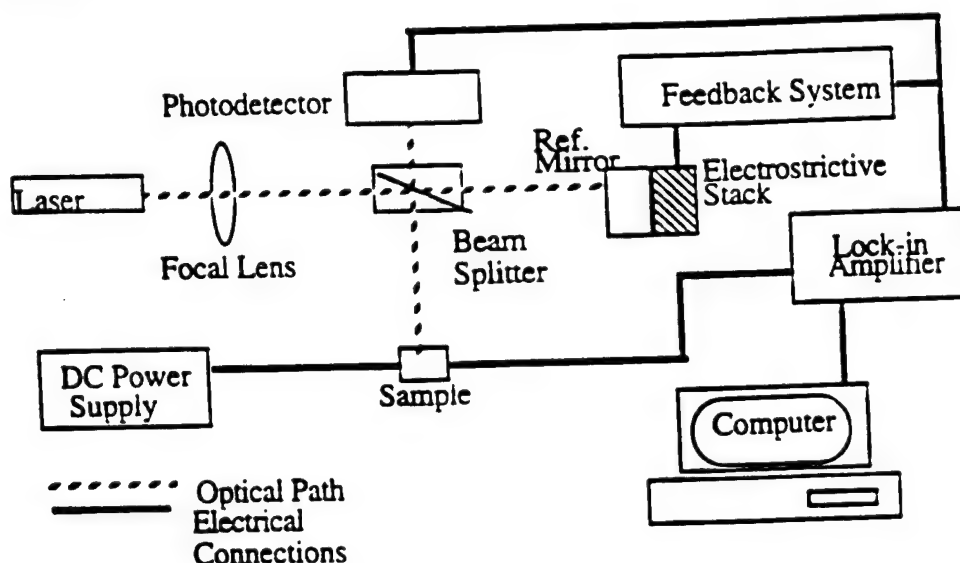


Fig. 9 : Schematic of a typical interferometric ultradilatometer, showing system components, optical paths and electrical connections (Ref. 33)

Homodyne and heterodyne laser ultradilatometers based on Michelson interferometers have been used since the 1930s to measure very small displacements^{30,31,32,33}. These instruments detect the shifts in interference fringes caused by changes in path length of two laser beams, one of which is reflected from the surface of a sample under an ac field. Using phase locking and feedback loops to stabilize the system, interferometers are capable of resolutions of 10^{-3}\AA or better, and usually operate in the range of 1kHz to 100kHz (Fig.9). Typical results from interferometry measurements for MgO and spodumene glass are shown in fig.3.

Recently, a bimorph based dilatometer similar in principle to an atomic force microscope has been introduced. This instrument is capable of measuring

displacements of the order of 0.01\AA in a frequency range of 1 to 100kHz, and is useful in studying electrostriction in thin films (Fig.10)³⁴.

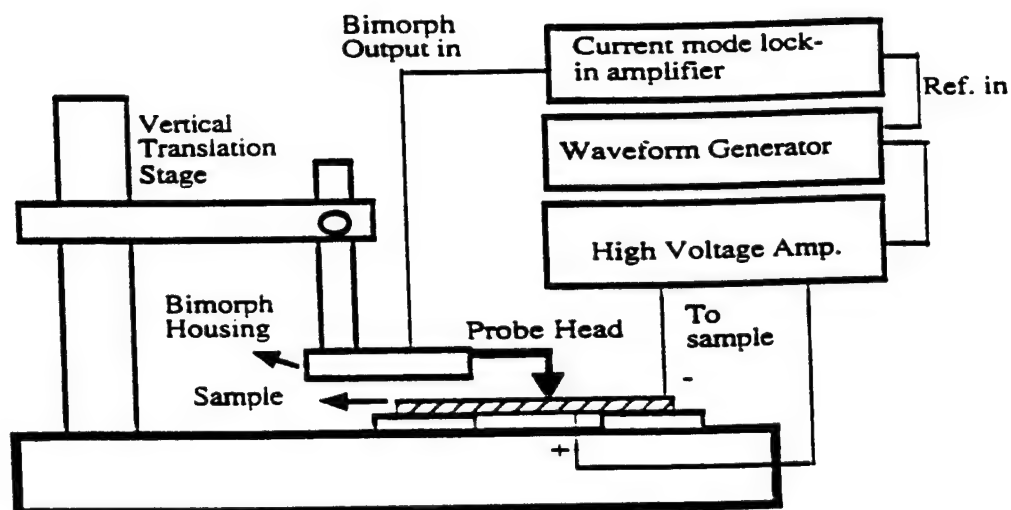


Fig. 10 : Schematic of the bimorph dilatometer for measuring electromechanical response in polymer thin films (Ref. 34)

In most direct effect measurements, the electrostatic attractive stress between opposite charged faces of a dielectric material can contribute to the dimensional change. This stress is called the Maxwell stress, and the corresponding strain x_M is dependent on the dielectric and elastic properties of the material. With all quantities being measured in the direction of the field, x_M is given by³⁵ :

$$x_M = -0.5 \epsilon_0 \epsilon_r s E^2$$

This correction is significant mainly in the case of low permittivity materials where very small strains are observed and for elastically soft polymers.

Techniques for measuring the converse effect call for precision evaluation of dielectric properties. small capacitance changes of the order of 10^{-16} - 10^{-15} F need to be resolved for applied stresses of the order of 0.1MPa for low permittivity ceramic materials. Other requirements are stable temperature control and the establishment of 'true' stress systems - completely hydrostatic if the hydrostatic Q_h coefficients are being measured and truly uniaxial stresses in compressometry (Fig. 11a)^{7,36}.

Modifications to compressometric systems are aimed mainly at improving sensitivity or uniaxiality for accurate evaluation of the separated components of the electrostriction tensor^{37,38}. A correction corresponding the capacitance change due to the geometric shape change of the dielectric from elastic strain has to be performed to calculate accurate Q_{ij} values in low permittivity dielectrics when the

converse method is used. Results from compressometry measurements for some common ceramics are illustrated in fig.11b.

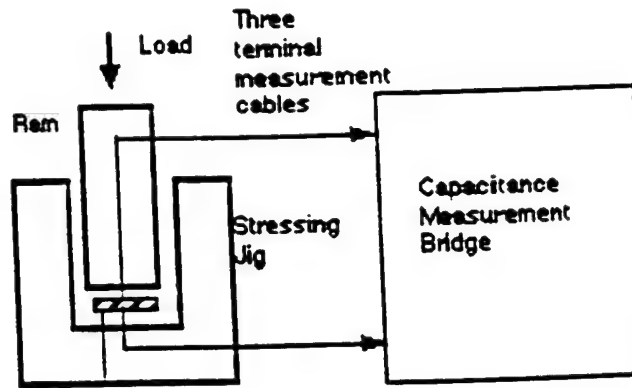


Fig. 11a : Schematic of a converse method measurement system. The sample is shown shaded (Ref. 48).

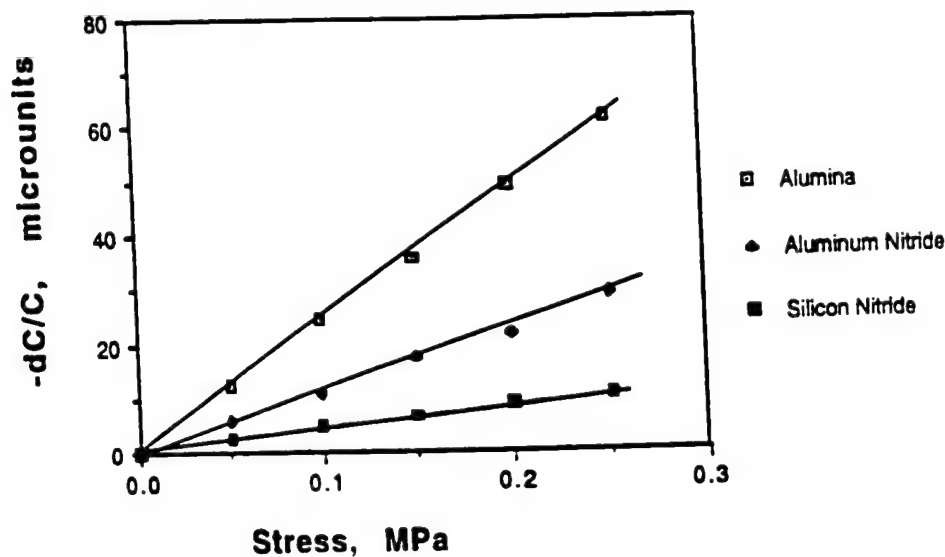


Fig. 11b : Compressometry results for ceramic alumina, aluminum and silicon nitride.

In the case of low permittivity materials, it is necessary to measure electrostriction by both direct and converse methods to calculate reliable and accurate Q or M values (Table 3).

Some recent studies on quartz have used the change in resonant frequency of the vibration modes of the material caused by a dc field³⁹, or the dc field induced variations in the transit times of ultrasonic pulses in the material⁴⁰. These methods are used to calculate combinations of the electroelastic and the electrostrictive

constants of quartz, as well as the nonlinear piezoelectricity and the permittivity tensors. While the method yields accurate results for the piezoelectricity, the electrostriction values show poorer agreement with values in the literature.

Table 3 : Comparison of direct and converse method measurement results for a variety of dielectric materials. These values agree to within $\pm 5\%$ (Refs. 4, 12)

Material	Direct $Q_{11} \text{ m}^4/\text{C}^2$	Converse $Q_{11} \text{ m}^4/\text{C}^2$
BaF ₂ Q ₁₁	-0.33	-0.31
	Q ₁₂	-0.29
	Q ₄₄	1.48
Spodumene Glass (Li ₂ O·Al ₂ O ₃ ·4SiO ₂)	0.43	0.46
KMnF ₃ Q ₁₁	0.51	0.49
	Q ₁₂	-0.10
	Q ₄₄	1.15
CaF ₂ Q ₁₁	-0.48	-0.49
	Q ₁₂	-0.48
	Q ₄₄	2.01
LiF	0.79	0.57
888 VE Corning Glass Ceramic	0.081	0.079
MgO	0.33	0.34
BeO	1.45	1.48
SrF ₂ Q ₁₁	-0.33	-0.33
	Q ₁₂	0.39
	Q ₄₄	1.90
3% Ca / PMN-PT	0.00289	0.00333
Calcite	1.20	1.19

ELECTROSTRICTION AND POLARIZATION MECHANISMS

The basic mechanisms contributing to the polarization in dielectric materials have been identified and treated extensively⁴¹. Electrostriction is a polarization related effect defined as $x_{ij} = Q_{ijkl}P_kP_l$. An understanding of the mechanisms of polarization, especially the ionic and electronic can offer further insight into the underlying mechanisms, and is useful in discerning trends in the electrostrictive behavior, especially in low permittivity linear dielectrics. Electrostriction measurements on most crystalline materials have been performed only over limited frequency ranges (10^5Hz and below). Little variation of the Q coefficients with the frequency of measurement is seen for most crystalline ionic solids. Measurements over wider ranges of frequencies may be necessary to directly study the frequency dependence of electrostriction.

The variation of the low frequency dielectric constants with temperature and pressure has been a subject for analysis by physicists for several decades^{42,20}. Several studies review the changes in refractive index of solids with pressure, and attempt to explain these changes in terms of the polarizabilities of ions^{43,44}. These two sets of data may be combined to analyze the electronic and ionic contributions to electrostriction. The electronic and ionic contributions to electrostriction may be compared for some well characterized oxide and fluoride materials. Results from studies on hydrostatic Q_h electrostriction coefficients of low permittivity fluorides⁴⁵ are used in this analysis, along with measurements of the change of refractive index of solids with pressure^{46,47}.

The electrostrictive contribution from both ionic and electronic polarization mechanisms at low frequencies is proportional to the ratio $1/\epsilon_r (d\epsilon_r/dp)$. Using the approximation $n^2 \sim \epsilon_e$ where n is the refractive index of the material and ϵ_e the electronic or high frequency dielectric constant we may calculate $1/\epsilon_r (d\epsilon_e/dp) \sim 1/\epsilon_r (dn^2/dp)$ from the dn/dp data. To compare the relative contributions of the electronic and ionic polarizations at low frequencies, the same low frequency (1kHz) value for ϵ_r was used in both $1/\epsilon_r (d\epsilon_e/dp)$ and $1/\epsilon_r (d\epsilon_r/dp)$ ratios. The data used here was measured at pressures of 1kbar and less so that no nonlinearity was apparent in dn/dp or $d\epsilon_r/dp$. The results are listed in Table 4 for eight oxide and fluoride materials.

Table 4 : $1/\epsilon_r (dn^2/dp)$ and $1/\epsilon_r (d\epsilon_r/dp)$ for some oxides and fluorides.

Material	$1/\epsilon_r (d\epsilon_r/dp) \quad m^2/N$	$1/\epsilon_r (dn^2/dp) \quad m^2/N$
KMnF ₃	-4.39×10^{-11}	8.79×10^{-13}
CaF ₂	-3.42×10^{-11}	1.5×10^{-12}
BaF ₂	-4.29×10^{-11}	3.8×10^{-12}
LiF	-5.08×10^{-11}	4.2×10^{-13}
MgO	-2.58×10^{-11}	-9.5×10^{-13}
KTaO ₃	-1.38×10^{-10}	-6.7×10^{-14}
SrTiO ₃	-2.74×10^{-10}	-2.9×10^{-14}
Silica Glass	-1.5×10^{-11}	1.03×10^{-13}

It may be seen that most of the oxides in this analysis show a decrease in refractive index with pressure. This is true also for α -Al₂O₃, ZnO, stoichiometric and nonstoichiometric MgAl₂O₄ spinels, α -ZnS and α -CdS⁴⁴. Most fluorides on the other hand show an increase in n with pressure. Low frequency dielectric

constants decrease with pressure for both oxide and fluoride materials. The differing behaviors at different frequencies are caused by the relative magnitude of the electronic and ionic polarizations to electrostriction. In general the ionic contribution to electrostriction is at least two orders of magnitude greater than the electronic contribution, neglecting sign. The polarization effects caused by the relative shifting of the anion sublattice with respect to the cation sublattice in the crystal dominates the change in electronic polarizabilities of the various ions with pressure.

Both positive and negative values of dn/dp are observed. This holds out the tantalizing possibility of manipulating electrostriction values. By choosing materials with predominantly electronic polarizability contributions, and probably combining or doping them, it may be possible to achieve specific (especially zero) electrostrictive responses in materials. This would involve further research into the variation of electrostrictive effects with frequency, and possible mixing rules for electrostriction. The possibility of achieving zero electrostriction through the manipulation of crystal anisotropy has been discussed in an earlier work⁴⁸.

ELECTROSTRICTION IN POLYMER DIELECTRICS

Piezoelectric and electromechanical coupling properties have been well characterized for ferroelectric polyvinylidene fluoride (PVDF) and its copolymers with trifluoroethylene (TRFE). Their applications have been limited mainly by their lower electromechanical activity when compared to conventional ceramic actuator materials. Recently, there has been renewed interest in nonferroelectric polyurethane elastomers because of their large field induced strain response, which is primarily electrostrictive. These materials could have promising applications in sensor, actuator and microelectromechanical systems technology^{8,49,27}.

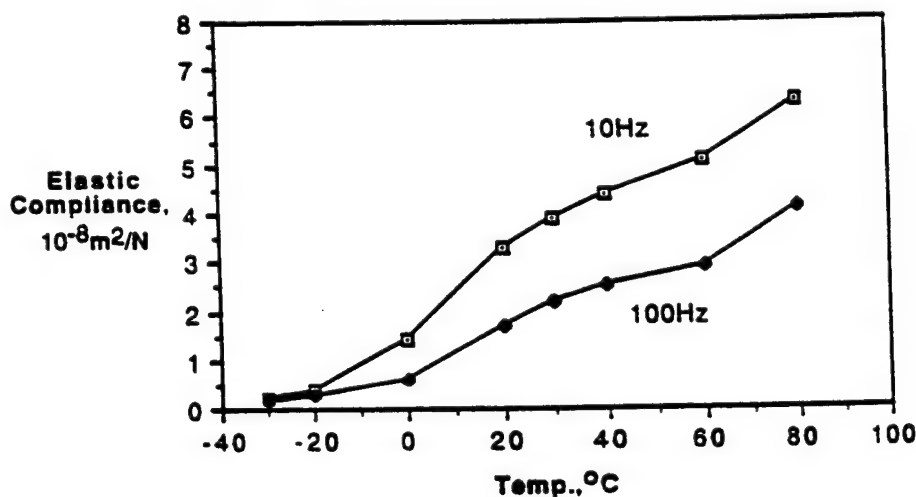


Fig. 12 : Elastic compliance vs. temperature curves for Dow 2105-80AE polyurethane elastomers at 10 and 100Hz (Ref. 50)

Some unusual effects have been observed in these polymer electrostrictors. The first is the large strain response. Strains of the order of 0.25% have reproducibly been achieved in these polymer systems for fields of the order of 1MV/m. In discussing these materials, it may be more practical to define an effective field induced strain coefficient R_e ($x = R_e E^2$), to calculate the large strains achieved in these materials.

A strong temperature effect is observed, as may be expected from the nonlinear temperature dependence of the compliance of this polymer (Fig.12). The Maxwell stress induced strain in these materials is given by :

$$x_M = -0.5 s \epsilon_0 K E^2$$

A Maxwell strain coefficient R_m similar to R_e can be defined to calculate the percentage of Maxwell stress contribution. Below the glass transition temperature T_g , the Maxwell stress contributions are fairly small (~10%) while above T_g , the Maxwell stress contribution to the field induced strain response increases to about 35-50%. A strong frequency dependence is also observed (Fig. 13a).

One effect that may help explain the large field induced strain in these materials is the thickness dependence of R_e . The induced strain and correspondingly, R_e , initially increased with increasing thickness and then decreases (Fig. 13b). Experiments with different electrode materials and thermally stimulated discharging current measurements support the hypothesis that effects related to charge injection, or interfacial charge may cause these dependencies.

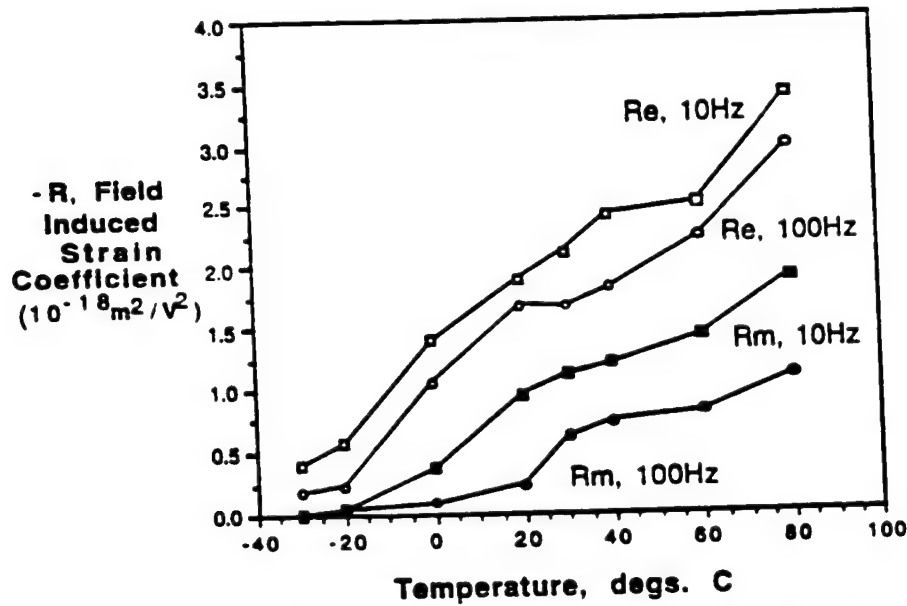


Fig. 13a : Field induced strain coefficient R_e and Maxwell strain coefficient R_m for unfiltered polyurethane thin films, at RT, 10 and 100Hz, through the glass transition for Dow 2105-80AE polyurethane elastomer (Ref. 50).

Some unusual effects have been observed in these polymer electrostrictors. The first is the large strain response. Strains of the order of 0.25% have reproducibly been achieved in these polymer systems for fields of the order of 1MV/m. In discussing these materials, it may be more practical to define an effective field induced strain coefficient R_e ($x = R_e E^2$), to calculate the large strains achieved in these materials.

A strong temperature effect is observed, as may be expected from the nonlinear temperature dependence of the compliance of this polymer (Fig.12). The Maxwell stress induced strain in these materials is given by :

$$x_M = -0.5 s \epsilon_0 K E^2$$

A Maxwell strain coefficient R_m similar to R_e can be defined to calculate the percentage of Maxwell stress contribution. Below the glass transition temperature T_g , the Maxwell stress contributions are fairly small (~10%) while above T_g , the Maxwell stress contribution to the field induced strain response increases to about 35-50%. A strong frequency dependence is also observed (Fig. 13a).

One effect that may help explain the large field induced strain in these materials is the thickness dependence of R_e . The induced strain and correspondingly, R_e , initially increased with increasing thickness and then decreases (Fig. 13b). Experiments with different electrode materials and thermally stimulated discharging current measurements support the hypothesis that effects related to charge injection, or interfacial charge may cause these dependencies.

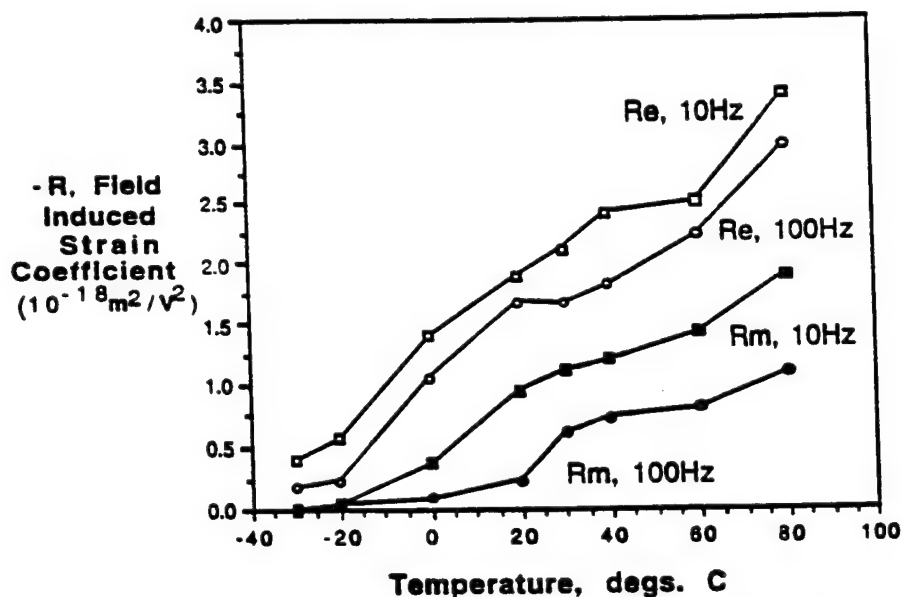


Fig. 13a : Field induced strain coefficient R_e and Maxwell strain coefficient R_m for unfiltered polyurethane thin films, at RT, 10 and 100Hz, through the glass transition for Dow 2105-80AE polyurethane elastomer (Ref. 50).

When a polymer dielectric with metal electrodes is subjected to a high voltage, charge injection can occur in this material. Injected charges can then be trapped in various sites such as defects, interfaces etc., and their effects can show a strong thickness and frequency dependence. Filtering polyurethane polymers before solution casting markedly reduces the field induced strain observed in these materials (Fig. 13b) and the frequency dispersion as well, supporting the charge injection hypothesis. The dielectric and elastic properties are not significantly changed by filtering.

Injected charges can also cause enhanced nonuniform local electric fields, depending on the film thickness. The depth of the region of the polymer with enhanced local fields from charge injection is determined by the transport coefficients of the charges in the polymer film under an electric field. The volume fraction of the polymer with enhanced local fields increases with a decrease in sample thickness. After a critical thickness, though, charge neutralization and homogenization processes reduces the local field enhancement. The strain responses correspondingly decrease⁵⁰.

The nonlinear compliance behavior of these polyurethane elastomers, combined with unusual polarization behavior from interfacial charge effects, can make for large induced strains that are thickness dependent. Further work in this area may identify the specific chemistry responsible for the large strains associated with charge injection, and their applications in sensor and actuator areas.

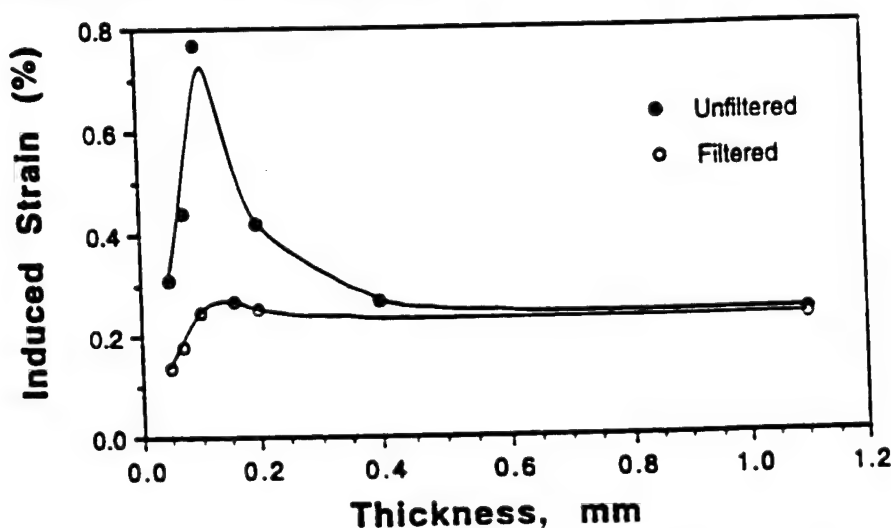


Fig. 13b : Induced strain as a function of thickness (using identical applied electric fields) for filtered and unfiltered electrostrictive polyurethane thin films, at RT, 10Hz (Ref. 50).

SUMMARY

As a summary, some common misconceptions about electrostriction to describe the key ideas set out in this paper are listed here.

1. *Electrostrictive strain is proportional to the square of the applied electric field* : For most low permittivity dielectrics, P is proportional to the applied field E , and therefore this statement is true. However, for high fields, polarization can saturate for high permittivity materials, especially in ferroelectric ceramics. A linear

relationship is observed when strain is plotted as a function of the square of polarization for these materials, but not as a function of the electric field. So it is more accurate to say that electrostrictive strain is proportional to the square of the induced polarization.

2. *Large voltages are required to observe electrostriction* : Two factors have made this a misconception. The introduction of thick and thin film capacitors has enabled high field levels to be achieved even in low permittivity materials at low voltages. Also, the introduction of high dielectric constant relaxor ferroelectrics have raised polarization levels to new heights, further contributing to large electrostrictive strains with relatively modest voltages.

3. *Electrostriction constants are about the same size for all materials, and materials with larger electrostriction coefficients produce the largest strains* : Q constants measured for solids vary from the order of $10^{-3} \text{m}^4/\text{C}^2$ for relaxor ferroelectrics to 1 for low permittivity insulators. Larger Q values have been observed for polymer materials. The induced electrostrictive strain is proportional to the square of the polarization, which implies the square of the relative permittivity is introduced in the strain - electric field relation. For similar electric fields, materials with large dielectric constants produce the larger strains.

4. *Thermal expansion effects make electrostrictive micropositioners and stress gauges impractical* : This statement is true for low permittivity oxide ceramics but not relaxor ferroelectrics. For PMN type ceramics, $Q \sim 0.01 \text{m}^4/\text{C}^2$, $K \sim 10,000$ and the thermal expansion coefficient $\alpha \sim 10^{-6} \text{K}^{-1}$. The electrostrictive strain in these ceramics for a field around 1MV/m is 10^{-3} , which corresponds to a 1000°C change in temperature! Relaxor ferroelectrics can also have abnormally low thermal expansion coefficients near their diffuse phase transitions, where K values are quite large.

In conclusion, though electrostriction effects can be very small in common materials, experimental techniques using phase and frequency selection can help in achieving accurate and reliable measurements of M and Q coefficients. Being a nonlinear effect, electrostriction may be applied smart systems requiring tunable properties. Electrostriction is a significant electromechanical coupling mechanism in many high field situations. Investigating the variation of electrostriction with frequency can reveal the contributions of various polarization mechanisms to electrostrictive effects. In areas such as polymer thin films, the effects of charge injection and defects can produce anomalously large strains that are worth further investigation. Electrostriction still poses a range of problems and challenges in the areas of modeling, and in terms of a fundamental understanding of a well known effect.

ACKNOWLEDGMENTS

This study was sponsored by the National Science Foundation through contract DMR 9634101, Electrostriction in Ceramics and Glasses.

REFERENCES

- ¹Jang, S.J., Ph.D. Thesis. Pennsylvania State University, Univ. Park, PA. 1979.
- ²McCrum, N.G., Read, B.E., Williams, G., *Anelastic and Dielectric Effects in Polymeric Solids*, Dover Publications, Mineola, NY, 1991.
- ³Newnham, R.E., *Chemistry of Electronic Ceramic Materials*, Proc. Int. Conf., Jackson, WY, 1990; NIST Special Publication 804, 39, 1991.
- ⁴Sundar, V., Li, J-F., Viehland, D., Newnham, R.E., *Mat. Res. Bull.*, **31**, p555, 1996.
- ⁵Cross, L.E., *Phil. Mag.*, **1**, 76, 1956.
- ⁶Devonshire, A.F., *Adv. Phys.*, **3**, 94, 1954.
- ⁷Pan, W.Y., Cross, L.E., *Rev. Sci. Instrum.*, **60**, 2701, 1989.
- ⁸Zhenyi, M., Scheinbeim, J.I., Lee, J.W., Newman, B.A., *J. Polymer Sci. Part B: Polymer Phys.*, **32**, p2721, 1994
- ⁹Sundar, V., WaGachigi, K., McCauley, D., Markowski, K.A., Newnham, R.E., *Proc. ISAF* 1994.
- ¹⁰Landolt-Bornstein, *Num. Data on Func. Relns. in Sci. and Tech., New Srs., Gp. III*, **24**, Springer-Verlag, New York, NY, 1990.
- ¹¹Uchino, K., Cross, L.E., *Jpn. J. Ap. Phys.*, **19**, L171, 1980
- ¹²Sundar, V., Newnham, R.E., *Mat. Res. Bull.*, **31**, p545, 1996.
- ¹³Simmons, G., Wang, H., *Single Crystal Elastic Consts. and Calculated Aggregate Properties: A Handbook*, MIT Press, Cambridge, MA, 1971.
- ¹⁴Sun, Y., Cao, W.W., Cross, L.E., *Mater. Lett.*, **4**, p329, 1986.
- ¹⁵Furukawa, T., Seo, N., *Jap. J. Appl. Phys.*, **29**, p675, 1990
- ¹⁶Brandrup, J., Immergut, E.H., *Polymer Handbook*, Interscience Pub., New York, NY, 1966.
- ¹⁷Roentgen, W., *Annalen der Physik*, **11**, p780, 1880.
- ¹⁸Hamann, S.D., *Rvw. Phys. Chem. of Japan*, **50**, p147, 1980.
- ¹⁹Srinivasan R., and Srinivasan, K., *J. Phys. Chem. Solids*, **33**, p1079, 1971
- ²⁰Woods, A.D.B., Cochran, W., Brockhouse, B.N., *Phys. Rev.*, **119**, p980, 1960.
- ²¹Zhang, Q.M., Zhao, J., Shrout, T., Kim, N., Cross, L.E., Newnham, R.E., Amin, A., and Kulwicki, B.M., *J. Ap. Phys.*, **77**, p2549, 1995.
- ²²Uchino, K., Oh, K.Y., *J. Am. Ceram. Soc.*, **74**, p1131, 1991.
- ²³Nakajima, Y., Hayashi, T., Hayashi, I., Uchino, K., *Jpn. J. Appl. Phys.*, **24**, p235, 1985.
- ²⁴Nomura, S., Tonooka, K., Kuwata, J., Cross, L.E., Newnham, R.E., *Proc. 2nd Mtg. on Ferroelectric Matrls. and Applications*, Kyoto, p133, 1979.
- ²⁵Sundar, V., Newnham, R.E., *Ferroelectrics*, **135**, p31, 1992.
- ²⁶Cady, W.G., in "International Critical Tables", **6**, p207, 1929

- 27Elhamy, K., Gauthier-Manuel, B., Manceau, J.F., Bastien, F., J. App. Phys., 77, p3987, 1995.
- 28Burkard, H., Kanzig, W., Rossinelli, M., Helvetica Physica Acta, 49, p12, 1976
- 29Legg, G.J., Lanchester, P.C., J.Phys. C, Sol. State Phys., 13, p6547, 1980.
- 30Osterberg, H., and Cookson, Rev. Sci. Instrum., 6, p347, 1935.
- 31Luymes, B.J., Rev. Sci. Instrum., 54, p90, 1983.
- 32van Sterkenburg, S.W.P., J. Phys D., App. Phys., 25, p996, 1992.
- 33Li, J-F, Moses, P., Viehland, D., Rev. Sci. Instrum., 65, p1089, 1994.
- 34Su, J., Zhang, Q.M., Kim, C.H., Ting, R.Y., Capps, R., in print, J. Appl. Polym. Sci., 1997.
- 35Juretschke, H.J., Am. J. Phys., 45, p277, 1977.
- 36Bohaty, L., Hassuhl, S., Acta Cryst., A 33, p114, 1977
- 37Balakrishnan, G., Srinivasan, K., Srinivasan, G., J. App. Phys., 54, p2875, 1983
- 38Meng, Z.Y., Sun, Y.M., Cross, L.E., Mater. Letters, 2, p544, 1984
- 39Hruska, C.K., Brendel, R., J. Appl. Phys., 67, p1676, 1990.
- 40Kittinger, E., Tichy, J., Freidel, W., J. Appl. Phys., 60, p1465, 1986.
- 41von Hippel, A.R., Dielectrics and Waves, John Wiley & Sons, New York, NY, 1956.
- 42Shanker, J., Dixit, S., Phys. Stat. Sol. (a), 123, p17, 1991.
- 43Bogardus, E.H., J. Appl. Phys., 36, p2504, 1965.
- 44Vedam, K., Davis, T.A., J. Appl. Phys., 33, p4555, 1967.
- 45Rittenmyer, K., Ph.D. Thesis, Pennsylvania State University, Univ. Park, PA 1984.
- 46Vedam, K., Schmidt, E.D.D., Kirk, J.L., Schneider, W.C., Mat. Res. Bull., 4, p573, 1969.
- 47Vedam, K., Schmidt, E.D.D., Phys. Rev., v146, p548, 1966.
- 48Sundar, V., Newnham, R.E., J. Mat. Sci. Lett., 13, p799, 1994.
- 49Wang, H., Zhang, Q.M., Cross, L.E., Ting, R., Coughlin, C., Rittenmyer, K., Proc. Int. Symp. Appl. Ferroelectrics, 9, p182, 1994.
- 50Su, J., Zhang, Q.M., in print, Appl. Phys. Lett., 1997.

APPENDIX 97

Pre-Print

Structure-Property Relationships in the Electrostriction Response of Low Permittivity Silicate Glasses

V Sundar, R. Yimnirun, Bruce T. Aitken* and R.E. Newnham
IMRL, The Pennsylvania State University, University Park, PA 16802
*Corning Glass R & D Center, Corning, NY

Abstract

Some of the polarization mechanisms that affect the dielectric and electrostrictive responses of low dielectric permittivity glasses are examined in this work. Electrostriction is the basic electromechanical coupling mechanism in all insulators. It is defined as $x_{ij} = Q_{ijkl}P_kP_l$ where x_{ij} is the strain tensor, Q_{ijkl} the electrostriction tensor, and P_k the induced polarization. The electrostriction constant Q_{11} (in Voigt notation) for glasses containing sodium decreases with frequency in the range 0.1 - 10kHz. Q_{11} decreases with frequency from 0.95 to 0.55m⁴/C² for sodium trisilicate glass and from 0.6 to 0.45m⁴/C² for sodium aluminosilicate glass. In contrast, the Q_{11} for two samples of silica glass remains nearly constant at ~ 0.4m⁴/C² in this frequency range. The role played by the Na⁺ ion and that of silicate coordination shells in different electrostrictive responses of these glasses is analyzed.

1. Introduction

The basic mechanisms contributing to the polarization in dielectric materials have been identified and treated extensively [1]. Their individual contributions are illustrated by the frequency dispersion of the linear dielectric response, that separates the contributions from the different mechanisms. Space charge effects and defects contribute to interfacial polarization, that has a frequency regime of typically 10⁵Hz and below. Orientation or dipolar polarization may be seen in materials that have permanent dipoles, in the range 10⁵-10¹⁰Hz. Ionic or atomic polarization occurs from the relative displacement of the ions in the material, in the range 10¹⁰-10¹³Hz. Electronic polarization arises from the distortions of the charge distributions around the ions of the material, in the optical frequency ranges of 10¹⁴Hz and above.

Electrostriction is a polarization related effect defined as $x_{ij} = Q_{ijk}P_kP_l$. An understanding of the mechanisms of polarization that contribute to electrostrictive strain is thus of fundamental interest. Of the mechanisms outlined above, the effects of the ionic and electronic contributions are of primary concern. The separation of the contributions arising from these effects offers further insight into the underlying mechanisms, and is useful in discerning trends in the electrostrictive behavior, especially in low permittivity linear dielectrics.

Electrostriction measurements on most crystalline materials have been performed only over limited frequency ranges (10⁵Hz and below). Little variation of the Q coefficients with the frequency of measurement is seen for most crystalline ionic solids. Measurements over wider ranges of frequencies may be necessary to directly study the frequency dependence of electrostriction. However, by choosing materials and methods carefully, it may be possible to gain more insight into the polarization contributions to electrostriction.

In this study, the contribution of polarization mechanisms to electrostriction is examined. The effect of Na⁺ ion response to electric fields is analyzed for four silicate glasses. The frequency of measurement of both dielectric and electrostrictive properties is varied, and the effects of the ion responses at various frequencies is analyzed..

2. Ion Responses to Electric Fields in Glasses

Some silicate glasses show dielectric relaxations in the 10Hz - 10kHz frequency range. The effects of ion vibrations and the silicate 'cage' structures can affect the electrostrictive response of these materials. The dielectric and electrostrictive properties of a group of four silicate glasses were measured and are discussed in this section.

2.1 Glass Samples

The amorphous structure and metastability in glasses make them interesting for study. Random but continuous networks of (SiO₄)⁴⁻ tetrahedra make up the basic silica glass structure. One sample of Corning 7940 silica glass and one sample of fused silica (General Electric) were chosen for measurement. Two sodium trisilicate (Na₂O.3SiO₂) and sodium aluminosilicate glass samples obtained from the R&D Division of Corning Glass Works were the other two samples studied here. The samples were in the form of disks 22-25mm in diameter and 1.5 - 3.2mm in thickness. They were polished to optical finishes.

Aluminum electrodes were evaporated on to these samples. Guard gaps 0.1mm wide and 16-17mm in diameter were scribed on the low electrodes. The compositions of the glasses are given in table 1.

Table 1 : Compositions of Glasses Studied, in wt% (Refs. 2,6)

Glass	SiO ₂	Al ₂ O ₃	Na ₂ O	Other
Trisilicate	74.4	0	25.6	0
Aluminosilicate	65	25	10	0
Corning 7940	99.9	0	0	0.1% H ₂ O
Fused Silica	98-99%	0	0	~ 1% CaO

2.2 Dielectric Properties.

A plot of the real and imaginary parts of the dielectric constant for sodium aluminosilicate glass is shown in Fig. 1-a. At low frequencies, the real part is expected to approach a fairly constant value K_0 . However, interfacial (electrode) polarization effects can dominate at frequencies of 40Hz and less. To eliminate this, the inverse dielectric constants G' and G'' are plotted as a function of frequency.

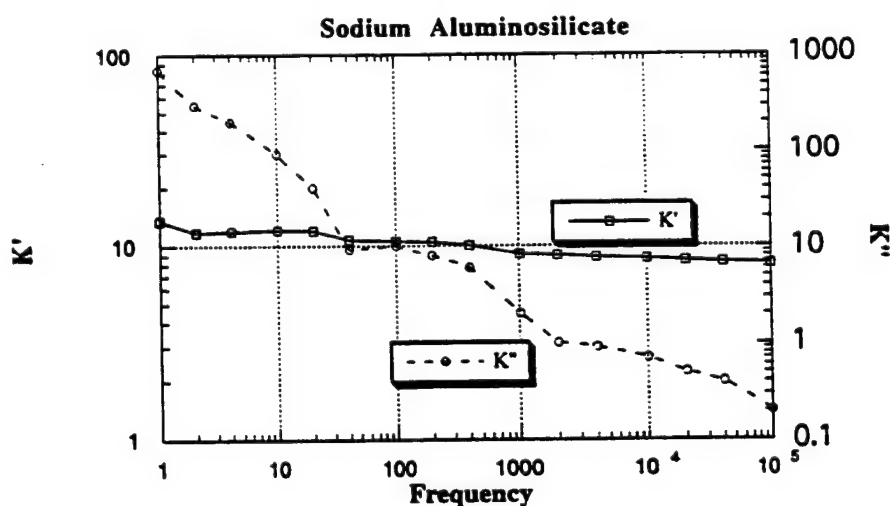


Fig. 1-a : Real and imaginary parts of the dielectric permittivity of sodium aluminosilicate glass.

The inverse dielectric constants are defined by $G^* = 1/K^* = 1/(K' - iK'') = G' + iG''$.

As may be seen in Fig. 1-b, the G'' vs. frequency plots show a peak maximum around 100Hz for both glasses. This is an ionic relaxation peak arising from Na^+ ion movements in the various silicate cages. The peak is too broad to be a single dipole relaxation, and is also asymmetric with respect to the peak maximum. In contrast, the dielectric constants of Corning 7940 glass ($\epsilon_r = 3.842$) and the fused silica ($\epsilon_r = 3.861$) are constant in the frequency range 10Hz - 10kHz.

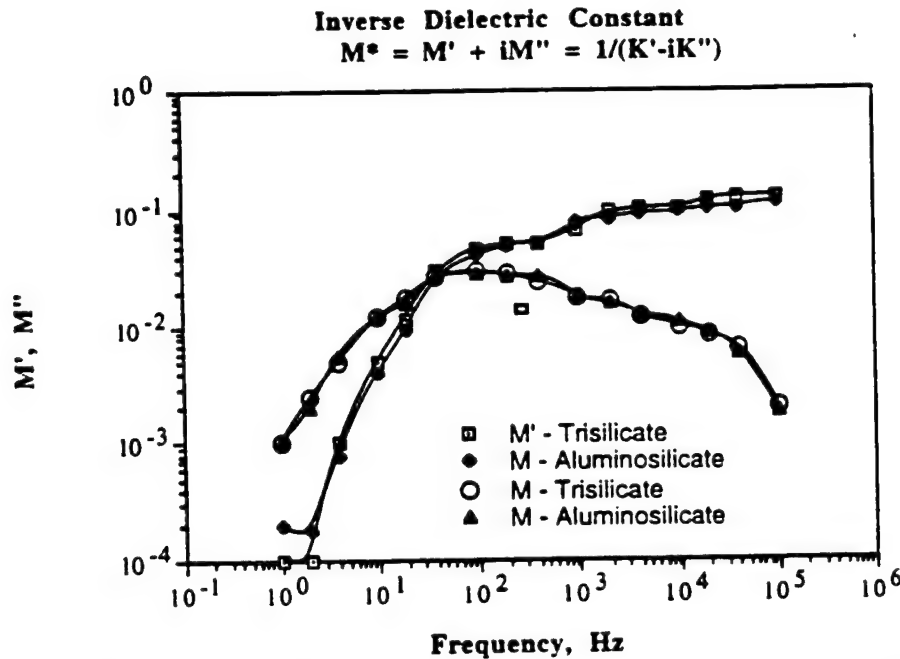


Fig. 1b M' and M'' as functions of frequency for sodium trisilicate and aluminosilicate glasses

Typically, glasses show loss curves as shown in Fig. 2-a. The curve A shows the overall loss vs. frequency plot. Losses arising from DC conduction losses (B), localized conduction (C), vibration of heavy ions (D) and IR vibration modes (E) are possible. The mechanisms associated with these loss curves are illustrated in Fig. 3-b.

DC conduction by alkali ions moving through the silicate channels is a common low frequency loss mechanisms in the 1-100Hz frequency range. Localized conduction is associated with space charge effects in the 1- 10^5 Hz frequency range, which is the range of interest in this study. Alkali ions can move by 'hopping' between positions in network coordination shells.

Losses associated with the vibrations of heavy ions such as Ba^{2+} or Pb^{2+} against the network cages are observed at even higher frequencies, centered around 10^7 Hz. Infrared

frequency vibration modes of the silicate groups themselves contribute to losses at 10^{10} Hz and above.

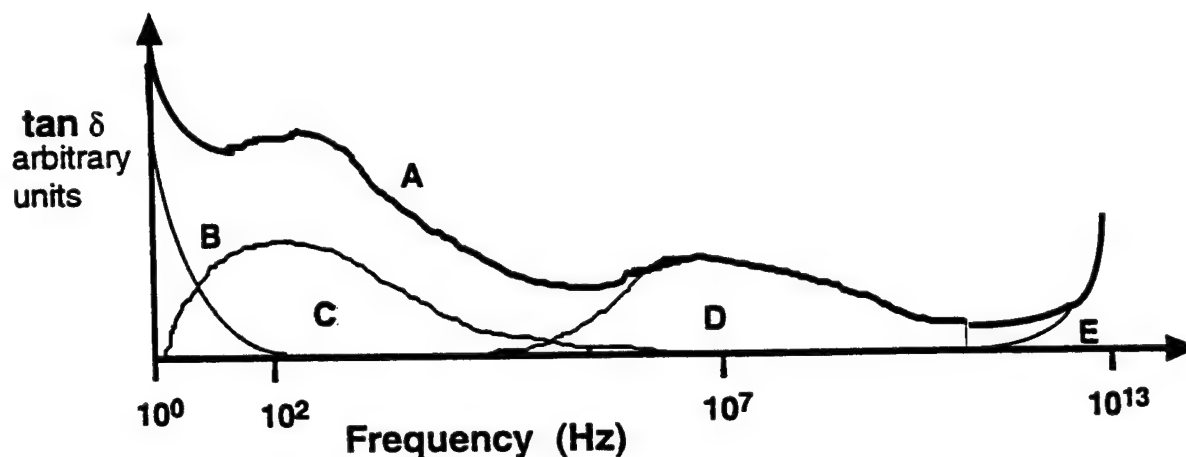


Fig. 2-a : Dielectric Loss in Glasses

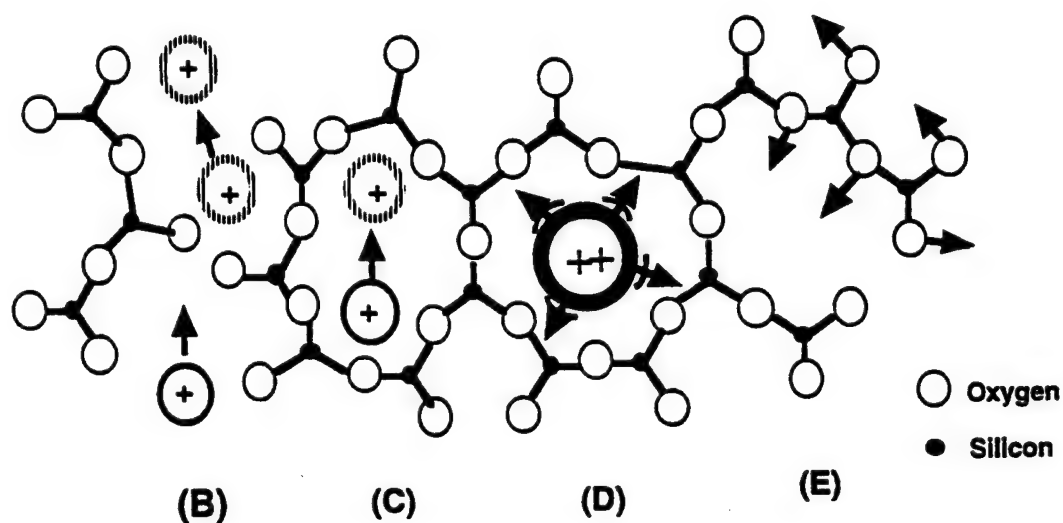


Fig. 2-b : Mechanisms associated with dielectric loss in glasses. B : DC conduction losses, C : localized conduction and D: vibration of heavy ions and E : IR vibration modes.

The trisilicate and aluminosilicate glasses do not have any such heavy ions in them. Thus, the resonance effects seen are most likely due to the localized movement of alkali ions. This behavior of the alkali ions was also seen to affect the variation of the Q coefficients with frequency.

3. Electrostriction Measurements

A General Radio 1621 capacitance bridge with a resolution of 0.1 aF (10^{-19} F) in capacitance was used to measure the dielectric and electrostrictive properties of the glasses. The compressometer cell shown schematically in Fig.3 was used for electrostriction measurements.

The compressometer is designed for the application of a homogeneous pressure on the sample surface from a completely uniaxial loading with tilt and thrust bearings in the load line. The error in load measurement is less than 0.5% . The dielectric susceptibility changes linearly with applied stress, and inhomogenieties in applied stress are averaged out by a comparatively large sample diameter and further diluted by the linear relationship. The thermal mass of the compression jig is large enough to smooth out minor drifts in ambient temperature. The drift in the fractional change in capacitance is less than 3 ppm/min under quiet conditions.

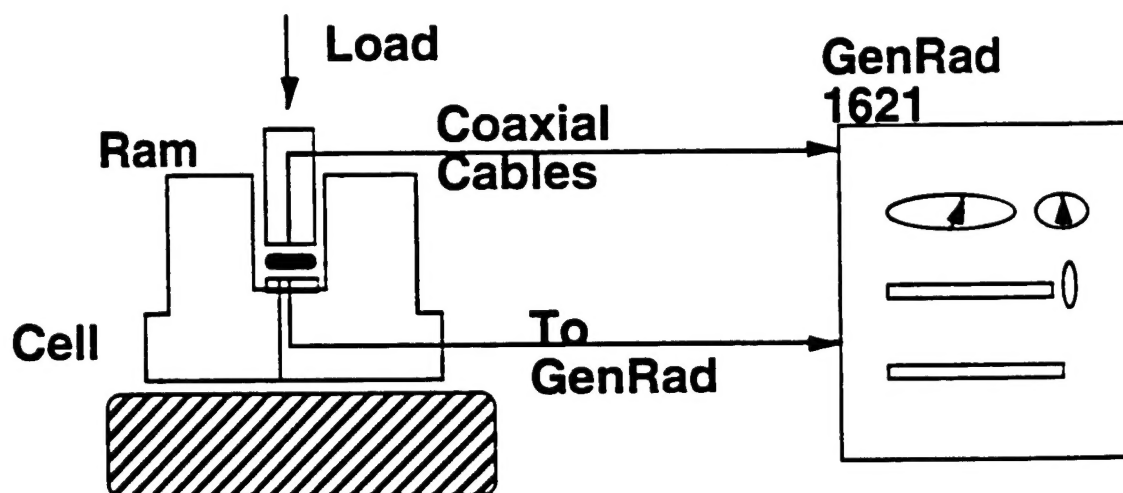


Fig. 3 : Schematic of compressometer cell design.

The electrical stability of the system is also of a high order. The capacitance of the sample holder itself is less than 20 aF . Care is taken to ensure that the only capacitance path is through the sample itself, and all signal leads are coaxial and electrically guarded. The capacitance measurement is done in a three-terminal mode using a General Radio 1621 Capacitance Measurement System capable of measuring down to 0.1 aF . The capacitance resolution is on the whole better than 1 ppm , and the resolution in change in capacitance is less than 2 aF , even as estimated in a worst case analysis. This system is a powerful

technique to establish the signs and magnitudes of the electrostriction constants of even low permittivity, low Q value materials.

3.1 Electrostriction Results

For parallel plate capacitors such as the disks used in this study, the capacitance C is given by the following equation, where A is the area of the sample, and t its thickness.

$$C = \epsilon_0 \epsilon_r A / t$$

The change of permittivity with uniaxial applied stress X is related to both the change in capacitance and the capacitance change (Σ) due to geometric deformation under stress.

$$d \ln \epsilon_r / dX = (C^{-1} dC / dX - \Sigma),$$

where Σ is given by $\Sigma = - (s_{11} - 2s_{12}) = (1/9K - 2/3\mu)$ for isotropic glasses. The bulk modulus K and the shear modulus μ are of the order of 10^8 N/m^2 for these glasses. Elastic data were taken from Karapetyan et al. [5].

The fractional change in capacitance $\Delta C/C$ is plotted as a function of stress to measure electrostriction. Corrections are made for the change in capacitance due to the elastic shape change of the samples. A typical correction for sodium trisilicate glass is shown as an example. At 1kHz, $\epsilon_r = 11.3$, $K = 365 \times 10^8 \text{ N/m}^2$ and $\mu = 252 \times 10^8 \text{ N/m}^2$. This gives a fractional change in permittivity with applied stress of $-2.339 \times 10^{-11} \text{ m}^2/\text{N}$. $C^{-1} dC/dX$ is $10.4 \times 10^{-11} \text{ m}^2/\text{N}$ for sodium trisilicate glass at 1kHz. It is very important to correct for geometric changes in capacitance for glasses and other low permittivity materials.

Q_{11} vs. frequency plots are shown for all four glasses in Fig. 4. The Q value for the trisilicate glass is within 5% of that obtained by Meng and Cross [2]. Both the fused silica and the Corning 7940 silica glass sample show a fairly constant Q_{11} vs. frequency trend in the 100-10,000 Hz range. The Corning 7940 glass has a Q_{11} value of $0.44 \text{ m}^4/\text{C}^2$ and the fused silica sample $0.38 \text{ m}^4/\text{C}^2$ at 100Hz. The Q values for silica glass represent the electrostrictive response of the unmodified silicate network.

For both the sodium trisilicate and aluminosilicate glass, the largest observed values of Q_{11} occur at 100Hz, where the ionic relaxation was observed. Q_{11} decreases with frequency

from 0.95 to $0.55 \text{ m}^4/\text{C}^2$ for sodium trisilicate glass and from 0.6 to $0.45 \text{ m}^4/\text{C}^2$ for sodium aluminosilicate glass. This reflects the decreasing response of the Na^+ ion oscillations with increasing frequency. Around 10^5 Hz , the Q_{11} values for both glasses tend towards the value for silica glass. It can safely be inferred that the Na^+ ion polarizability causes the larger (nearly doubled at 100 Hz) electrostrictive response of the sodium trisilicate glass compared to the silica glass samples.

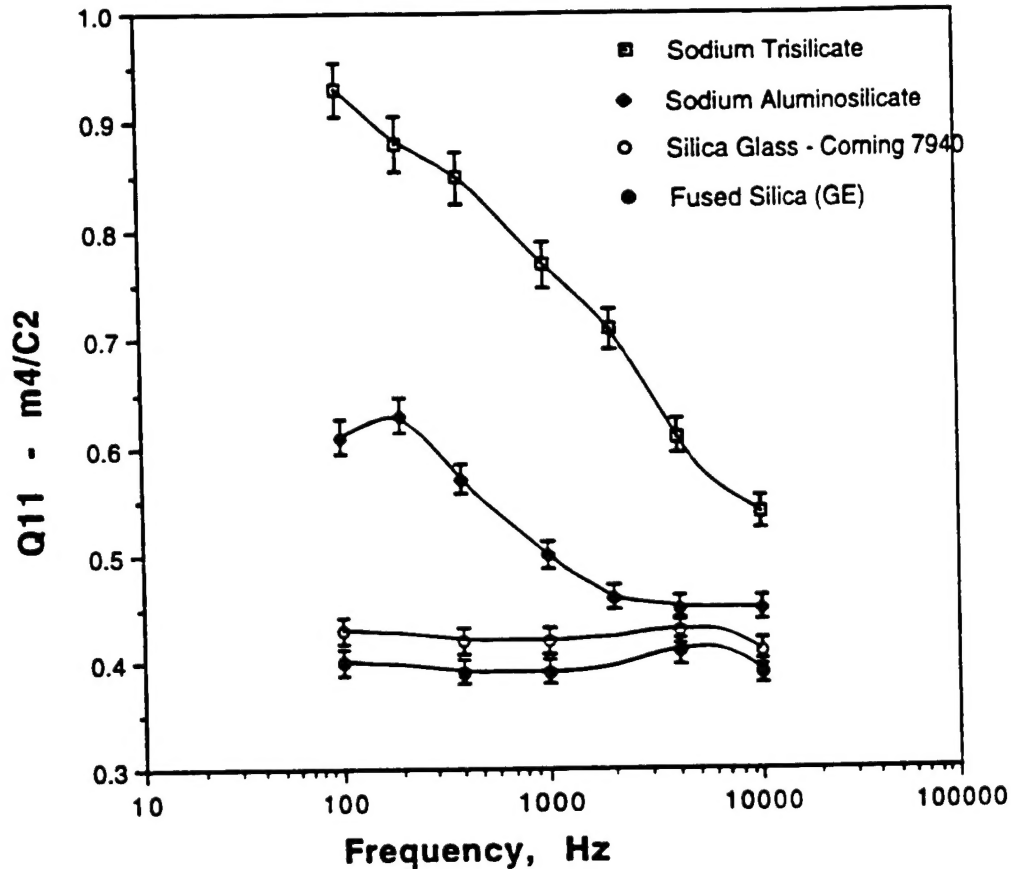


Fig. 4 : Variation of electrostriction coefficients Q_{11} with frequency for four glasses, 0.1 - 10kHz.

The Q values of the aluminosilicate glass are smaller than those of the trisilicate glass at all frequencies. The extra oxygen introduced by Na_2O is nonbridging in the sodium trisilicate structure. Sodium aluminosilicate glass has far fewer nonbridging oxygen atoms than the trisilicate glass. A reduction in the nonbridging oxygen content causes an expansion in the silicate network coordination shell around the Na^+ ion. This change in volume may be electrostatic in origin [3]. An expanded silicate cage around the Na^+ ion in the aluminosilicate is distorted less by the Na^+ ion 'hopping' in response to electric fields.

Under these circumstances, the Na^+ ion polarizability contributes less strongly to the total electrostriction for these glasses.

The contributions of Na^+ and other network modifiers to electrostriction are apparently very important for glasses. Studies on a wider variety of glasses such as borates or phosphates may reveal additional trends in their electrostrictive responses.

4. Conclusions

By choosing appropriate materials and methods, it is possible to separate the ionic and electronic contributions to electrostriction in low permittivity dielectrics. Measurements on four glasses show that the 'hopping' of alkali ions inside network cages has a significant effect on electrostriction at low frequencies. With increasing frequency, the effect of this localized conduction mechanism decreases. The network cage also has a significant effect on the electrostrictive response.

Acknowledgments

The authors would like to thank Drs. K. Vedam, L.E. Cross and K. Uchino of the IMRL, Penn State for useful discussions and suggestions, and Corning Glass Works R&D Division for some of the samples used in this study. This study was sponsored by the National Science Foundation through contract DMR 9634101, Electrostriction in Ceramics and Glasses.

References

- [1] A.R. Von Hippel, Dielectrics and Waves, John Wiley & Sons, New York, NY, 1956.
- [2] Z.Y. Meng, Y.M. Sun, L.E. Cross, Mater. Letters, v4, p5329, 1988.
- [3] J.O. Isard, Trans. Soc. Glass Tech., 43, p113, 1959.
- [4] V. Sundar and R.E. Newnham, Ferroelectrics, v 135, p 431, 1992 .
- [5] G.O. Karapetyan, Y.V. Lifshitz, D.G. Tennison, Soviet J. Glass Phys. Chem, v7, p131, 1981.
- [6] D.C. Boyd, D.A. Thompson, Kirk-Othmer Enc. of Chem. Tech., v11, p807, 1980.